# Combined Fast-Neutron $\gamma$-Ray Computed Tomography and Radiography


**Mauro Licata**

Department of Engineering
Lancaster University

This thesis is submitted in partial fulfilment for the degree of
*Doctor of Philosophy*

*Ogni giorno é l'inizio di un qualcosa di nuovo.*

# Abstract

The combination of real-time fast-neutron and $\gamma$-ray assessment for the purpose of tomography and radiography has been investigated using a number of complementary experimental techniques. The research described in this thesis comprises an extensive Monte Carlo simulation study and three experimental approaches, each of which is supported by computer simulations themselves.

In the Monte Carlo study, computed by means of MCNP6, actinide materials such as plutonium metal, plutonium oxide, uranium metal, $U_3O_8$ and $UC_2$, have been shielded with combinations of lead and high-density polyethylene, then investigated actively with a simulated beam of both fast neutrons and $\gamma$ rays produced by an americium-beryllium source, and detected by an array of liquid scintillation detectors. This Monte Carlo study demonstrates that, in terms of relative image contrast, the combination of $\gamma$ and neutron tomography yields to a better discrimination amongst plutonium metal, lead and polyethylene, as well as amongst uranium-based compounds, such as uranium metal and uranium carbide, with the same shielding materials. Less convincing contrast is instead obtained when plutonium oxide and $U_3O_8$ are concealed with the same shielding arrangement of lead and polyethylene. The study also shows that a combination of both fast neutron and $\gamma$ radiation, in several cases, led to a better spatial resolution (order of a few mm) of that achieved using fast neutrons or $\gamma$ rays in isolation.

A similar approach was performed to investigate a variety of materials often associated with conventional explosives and a lithium-based polymer (LiPo). By means of neutron tomography, LiPo and water, hydrogen peroxide, acetone, RDX, TNT, NC have been discerned from one another; whilst the $\gamma$ tomography approach helps to discern, for instance, RDX from acetone. Experimentally, this technique has been computed, albeit in terms of radiography rather than tomography, using a californium neutron source and single scintillation detector coupled to a real-time, pulse-shape discrimination system. A lithium ion laptop battery was scanned and compared with an X-ray radiograph of the battery itself. These experimental results show that the combined neutron-$\gamma$ imaging spatial information is comparable to what obtained with the X-ray. In addition, the results show that higher level of image contrast is present in the proximity of the cell batteries, suggesting the potential to identify the spatial lithium polymer distribution within the cell batteries.

Furthermore, an alternative approach to investigate a single material type subject to changes in dimension, hypothetically due to corrosion, has been explored. This was conducted assessing both the fast neutron and $\gamma$ ray flux backscattered by irradiated

steel slabs, as a function of their thickness. Such research, carried out with the objective to detect flaws in pipeline sections, not only showed the potential to estimate different thicknesses of steel in isolation, but also showed the potential to measure thicknesses of slabs covered by a layer of materials commonly used for pipelines insulation, such as polyethylene and concrete.

Finally, a Monte Carlo study has been completed for an arrangement in which a particle accelerator has been used as the neutron source, with which to explore the potential benefits of combining high-resolution $\gamma$-ray spectroscopy, neutron tomography and $\gamma$-ray tomography in the same approach. The outcome of this study showed the possibility to identify and localise the distribution of different isotopes of metals, such as $^{56}$Fe and $^{63}$Cu in a sample. The research presented associated with this aspect of the thesis has potential applications in nuclear safeguards, homeland security, contraband detection and in fields where relatively quick and non-destructive inspections are needed.

# Acknowledgements

*In primis*, I sincerely want to thank my supervisor and friend, Professor Malcolm Joyce. Malcolm has been a real guide to me, during my Ph.D. course, both from an academic point of view and, more importantly, from a merely human point of view. I thank him for having trusted me, supported, appreciated, motivated, helped and advised during the fruitful moments and especially in those less joyful, that are inevitable during a doctoral course and that sometimes, befall for causes that do not depend on ourselves. His wise teachings are a treasure that has enriched me as a researcher and as a human being.

I thank Lancaster University and the Next Generation Nuclear Centre for Doctoral Training (NGN-CDT), institutions for which I successfully completed my research work. It was a real honour for me to be part of this University and a research student of the NGN-CDT. I sincerely hope to have contributed to their growth as much as Lancaster University and NGN-CDT contributed to mine. Acknowledgements also go to the Engineering and Physical Sciences Research Council (EPSRC) and the Lloyd's Register Foundation (LFR), for funding my research. Without these, conferences, courses and workshops would not have been possible to be attended.

I would like to acknowledge Professor Colin Boxall, for the opportunities given to me through the Next Generation Nuclear Centre fo Doctoral Training and the Lloyd's Register Foundation as well as for giving me the opportunity, together with Malcolm, to be a student of the Next Generation Nuclear Centre for Doctoral Training.

I thank Dr. Frank Cave for giving me the chance to collaborate with Hybrid Instruments Ltd. The project I worked on during my Ph.D. turned out to be a game changer for my research.

A particular thank goes to Professor David Jenkins and Dr. Christopher Murphy from the Department of Physics of the University of York, as well as Dr. Jonathan Wilson and Dr. Matthieu Lebois from the Institute of Nuclear Physics of Orsay (IPNO). I thank them for the opportunity to be part of an international collaboration and for the possibility to help and collaborate in the experimental campaigns at the ALTO facility of the Institute of Nuclear Physics of Orsay (France). I also thank Benjamin Wallis, Gustavo Vega and Dr. Barbara Wasilewska for the help, advices, discussions and time passed together during the experimental measurements.

I also acknowledge Neil Roberts and Dr. Graeme Taylor for their support during the measurements performed at the National Physical Laboratory (NPL) in London.

I would like to thank Dr. Michael Aspinall, Dr. Ioannis Tsitsimpelis, Dr. Vytautas

Astromskas, Dr Manuel Bandala, Dr. Tilly Alton and Dr. Hajir Al Hamrashdi for the numerous helps, advices, discussion and chats that heavily contributed for the completion of this research work. I also thank all my colleagues of the research group and my close friends. There are so many of you and the list would be so long. Each one of you helped me and contributed, maybe even with a single smile, to complete my journey positively.

A huge thank to my family, and with *family* not only I mean my parents and my two sisters, but also my greatest loved ones. It has never mattered whether you all were in other countries or here in Lancaster, you have always been close to me with your thoughts and feelings, giving me a higher gear that has, so far, allowed me to achieve my goals.

Finally, a special thank to Anna, she helped me to find a smile I thought was lost, the same smile that gave me the strength to carry on and complete my research.

# Declaration

I hereby declare that this thesis is the product of my own work. The research here presented was carried out at Lancaster University from October 2015 to September 2019. Part of the experimental measurements were performed at the National Physical Laboratory in Teddington, London, and are the results of a collaboration with Hybrid Instruments Ltd and funded by Innovate UK. Part of this research is also the outcome of a discussion with my supervisor Malcolm Joyce, Dr A. Shippen and Dr D. Clark, from Createc Ltd, Cockermouth, Cumbria. In addition, some experimental measurements have been carried out at the ALTO facility of the Institute de Physique Nucleaire d'Orsay (IPN Orsay, Paris, France) and are the output of a collaboration with Professor David Jenkins (University of York) and Dr Jonathan N. Wilson (IPN Orsay).

Ideas, methods and experiments are, if not otherwise expressed and indicated, the outcomes of meetings, discussions, with my supervisor Professor Malcolm Joyce.

I would like to highlight that excerpts of this thesis have been published in the following journal articles and international conference proceedings:

- M. Licata and M. J. Joyce.
  ***"Concealed nuclear material identification via combined fast-neutron/$\gamma$-ray computed tomography (FNGCT): a Monte Carlo study"***.
  Journal of Instrumentation, Volume 13, February 9, 2018.
  https://iopscience.iop.org/article/10.1088/1748-0221/13/02/P02013.

- M. Licata, M. J. Joyce, I. Tsitsimpelis, D. Clark, B. A. Shippen.
  ***"The potential of real-time, fast neutron and $\gamma$ radiography for the characterization of low-mass, solid-phase media"***.
  Nuclear Instruments and Methods in Physics Research Section A: Accelerators, Spectrometers, Detectors and Associated Equipment.
  https://doi.org/10.1016/j.nima.2018.12.021.

- M. Licata and M. J. Joyce.
  "**Simultaneous, Real-Time, Fast-Neutron/$\gamma$-Ray Tomography and Radiography**".
  In proceedings of the 2018 IEEE Nuclear Science Symposium and Medical imaging Conference. 10-17 November 2018, Sydney, Australia.

- M.Licata, M. D. Aspinall, M. Bandala, F. Cave, S. Conway, D. Gerta, H. M. O. Parker, N. Roberts, G. Taylor and M.J.Joyce.
  "***Depicting corrosion-born defects in pipelines with combined neutron / $\gamma$ ray backscatter: a biomimetic approach***".
  Scientific Reports 10, 1486 (2020).
  https://www.nature.com/articles/s41598-020-58122-3.

Date..... Signature of candidate.....

I, Professor Malcolm John Joyce, hereby certify that the candidate has fulfilled the conditions of the resolution and regulations appropriate for the degree of Doctor of Philosophy at Lancaster University and that the candidate is qualified to submit this thesis in application for that degree.

Date..... Signature of supervisor.....

# Preamble

This Ph.D. thesis presents the research carried out at Lancaster University, from October 2015 to September 2019. The Ph.D. project was conducted on behalf of the EPSRC Centre for Doctoral Training in Nuclear Fission - Next Generation Nuclear (NGN-CDT); it was partially funded by the EPRSC-NGN-CDT itself and the Lloyd's Register Foundation (LRF).

The Ph.D was structured in four-years as part of a doctoral training programme. The first year was aimed to give a broad knowledge of the nuclear fuel cycle and the UK's nuclear industry, through to MSc level modules. In addition, year one included a visit to some of the UK's nuclear facilities, such as the EDF Heysham nuclear power plant, the Drigg Low Level Waste repository (LLWR) and the UK's nuclear fuel production facility (Westinghouse Springfields) in Preston. Furthermore, the first year comprised a public engagement training that aimed to develop the skills needed to communicate effectively with the general public about science, to learn about activities that can be used to successfully engage with the public, to feel the right confidence in having skills, ideas and resources to involve and get involved in public engagement activities. Training attended during the next three years, albeit in terms of conferences, workshops and short courses, are strictly related to the Ph.D. research. Years two to four were dedicated to work on this full-time doctoral level thesis project.

The research carried out at Lancaster University focuses on the study of an imaging technique with fast neutrons and $\gamma$ rays, to be applied in non-destructive tests. This method is based on the simultaneous generation and detection of both fast neutrons and $\gamma$ rays in such a way as to perform, with a single measure, respectively fast-neutron-, $\gamma$-ray- and combined fast-neutron/$\gamma$-ray- imaging. The research investigates the aforementioned concept applied to the well-known computerised axial tomography or radiography, as well as to the backscatter radiography/tomography, a relatively recent non-destructive test. In addition to these, a third, $\gamma$-ray-activation imaging technique, performed exploiting fast neutron inelastic scattering, has been investigated during the final part of the Ph.D.

# How to read this thesis

This thesis is divided into three parts: background, results and appendices. The first, is structured in four chapters, while the latter in five. The background part aims to provide the reader with a brief summary of the basic physics concepts necessary for a complete understanding of the thesis. The results part, instead, describes in detail the research carried out during the Ph.D. presenting the experimental methods used and their results. Each chapter of the results part includes a brief introduction that presents generalities, motivations and novelties of that particular chapter, as well as results and discussion. The third part comprises the appendices.

**Part I: Background**

The first chapter regards the introduction to this research and describes the hypothesis and motivations behind the work described within the thesis.

The second chapter treats the fundamentals of neutron and photon physics necessary for a better understanding of the research presented in the results section. A topic such as the detection of neutrons and photons is addressed, considering scintillation detectors, mainly used during the experimental campaigns, matter of particular focus. The chapter concludes by introducing a topic such as Pulse Shape Discrimination, i.e. the discrimination of particles by means of the analysis of different amount of light induced by themselves, into the detector

Neutron imaging is discussed in chapter 3. Being this a field that covers a broad range of topics, in this particular contest, only the principles of tomography and radiography are described, for which all the research of this thesis is focused on. Furthermore, the neutron imaging *state-of-the-art*, as well as the recent, developed techniques in combined neutron-photon imaging, are presented. This chapter concludes by describing the two main image reconstruction techniques: filtered back projection (FBP) and algebraic reconstruction techniques (ART). The reason of this discussion is that an image reconstruction algorithm was implemented during the Ph.D. Not only was this algorithm applied to the tomography and radiography system studied, but also it turned out to be useful during the experiment carried out at the ALTO facility of the Institute of Nuclear Physics in Orsay (IPNO Paris, France).

Last but not less important, chapter 4 is dedicated to a brief introduction of Monte Carlo methods and their generalities, widely used and one of key points of this research. The MCNP software / simulation code used is also presented and described in its main

features.

**Part II: Results**

The first three chapters present the results published in 3 different journal articles during the course of the Ph.D., while the fourth chapter concerns the experimental measures carried out at IPN-Orsay, and currently still under analysis and study.

Chapter 1 is an article published in the Journal of Instrumentation. It regards a Monte Carlo study entirely dedicated to show the potential of a tomographic technique that combines neutrons and $\gamma$ rays, applied in a nuclear framework.

In the second chapter, the same technique, once again supported by Monte Carlo simulations, is experimentally applied to investigate the presence of lithium inside batteries, and discriminate lithium polymers from other substances of similar densities. This research is the outcome of a discussion with Createc Ltd and was published in National Instruments and Methods A, as a peer-reviewed conference proceedings of the Symposium on Radiation Measurements and Applications (SORMA), which took place in Ann Arbor (Michigan, USA). The extension of this work was also presented later at the Nuclear Science Symposium in Sydney, Australia.

Chapter 3 describes the research carried out within a project undertaken with Hybrid Instruments Ltd and funded by Innovate UK. It presents an innovative technique to study the presence of corrosions or irregularities in steels. This technique is, to some extent, complementary to the one presented in the previous chapters, since it exploits the backscatter component of the radiation instead of that absorbed. This research was published in Scientific Reports.

The fourth chapter concerns the experimental work undertaken at IPN Orsay and presents some preliminary results and Monte Carlo simulations. This research, currently still matter of study, is the result of a collaboration with the University of York and the Institute of Nuclear Physics of Orsay. The research regards an imaging technique that allows material and isotope identification via the $\gamma$ rays generated by the nuclei excitation due to fast neutrons. Chapter 4, at the present stage, has to be intended as a proof of concept which aims to highlight the enormous potential of the presented technique. It has to be highlighted that the experimental data of this research belong to other students/researchers whilst the author individual contribution lies in the simulations study presented.

The final chapter comprises a broad discussion about the research presented and the overall results achieved, as well as suggestions for future areas of investigations. Final remarks complete this thesis.

**Part III: Appendices**

The appendices contain useful materials and data to better understand the experimental methods utilized within the experimental measures, such as MCNP6 codes, C++ and Matlab image reconstruction codes, electronic board schematics and a detailed description of the tomography control system.

# Achievements

## Journal articles

- M. Licata and M. J. Joyce. *"**Concealed nuclear material identification via combined fast-neutron/$\gamma$-ray computed tomography (FNGCT): a Monte Carlo study**"*.
  Journal of Instrumentation, Volume 13, February 9, 2018.
  https://iopscience.iop.org/article/10.1088/1748-0221/13/02/P02013.

- M. Licata, M. J. Joyce, I. Tsitsimpelis, D. Clark, B.A. Shippen. *"**The potential of real-time, fast neutron and $\gamma$ radiography for the characterization of low-mass, solid-phase media**"*.
  Nuclear Instruments and Methods in Physics Research Section A. December 2018.
  https://doi.org/10.1016/j.nima.2018.12.021.

- M.Licata, M. D. Aspinall, M. Bandala, F.Cave, S. Conway, D. Gerta, M. J. Joyce, H. M. O. Parker. **"*Depicting corrosion-born defects in pipelines with combined neutron / $\gamma$ ray backscatter: a biomimetic approach*"**.
  Scientific Reports 10, 1486 (2020).
  https://www.nature.com/articles/s41598-020-58122-3.

## Conference proceedings

- Mauro Licata, Helen M. O. Parker, Michael D. Aspinall, Manuel Bandala, Frank Cave, Sebastian Conway, Domas Gerta and Malcolm J. Joyce. ***Fast neutron and $\gamma$ ray backscatter radiography for the characterization of corrosion-born defects in oil pipelines***. EPJ Web Of Conference. In Proceedings of ANNIMA19: International conference on Advancements in Nuclear Instrumentation Measurement Methods and their Applications. Portorz, Slovenia, 17-21 June 2019.

- M. Licata and M. J. Joyce. *"**Simultaneous, Real-Time, Fast-Neutron/$\gamma$-Ray Tomography and Radiography**"*. In proceedings of the 2018 IEEE Nuclear Science Symposium and Medical imaging Conference. 10-17 November 2018, Sydney, Australia.

- H. M. O. Parker, M. Licata, F. D. Cave, M. D. Aspinall, M. J. Joyce, M. S. Bandala, D. Gerta and S. Conway. *" **Characterizing Corrosion-Born Defects***

***in Oil Pipelines Using Fast-Neutron Elastic Scattering***". In proceedings of the 2018 IEEE Nuclear Science Symposium and Medical imaging Conference. 10-17 November 2018, Sydney, Australia.

## International conference contributions

- ANNIMA19, International Conference on Advancements in Nuclear Instrumentation Measurement Methods and their Applications.
  Portroz, Slovenia. 17-21 June 2019.
  **Invited oral Presentation**: "*Fast neutron and $\gamma$ ray backscatter radiography for the characterisation of corrosion-born defects in oil pipelines*".

- IEEE NSS MIC 2018, Nuclear Science Symposium and Medical Imaging conference.
  Sydney, Australia. 10-17 November 2018.
  **Oral Presentation**: "*Simultaneous Real-Time Fast-Neutron/$\gamma$-Ray Tomography and Radiography*".
  **Poster Presentation**: "*Characterizing corrosion-born defects in oil pipelines using fast-neutron elastic scattering*".

- SORMA18, Symposium on Radiation Measurements and Applications.
  Ann Arbor, MI, USA. 11-14 June 2018.
  **Poster Presentation**: "*The potential of real-time, fast neutron and $\gamma$ radiography for the characterization of low-mass, solid-phase media*".

- IEEE NSS MIC 2017- Nuclear Science Symposium and Medical Imaging conference. Atlanta, GE, USA. 21-28 October 2017.
  **Poster Presentation**: "*Shielded nuclear material identification via combined fast-neutron/$\gamma$-ray computed tomography (FNGCT)*".

- ANNIMA17 - Advancements in Nuclear Instrumentation Measurement Methods and their Applications.
  Liege, Belgium. 19-23 June 2017.
  **Oral Presentation**: "*Combined Fast-Neutron and $\gamma$ Ray Computed Tomography: a study on the discrimination between different materials using Monte Carlo simulations.*"

- International Conference on Applications of Nuclear Techniques.
  Crete, Greece. 11-17 June 2017.
  **Oral Presentation**: "*Combined Fast-Neutron/$\gamma$-Ray Computed Tomography: a single modality with which to discern both nuclear materials and contrived shielding configurations?*".

## Other conferences, schools and forums

- 2019 Joint Nuclear Centre Winter School.
  Birmingham 8-1 January 2019
  **Oral Presentation**: "*Simultaneous, Real-Time, Fast-Neutron/$\gamma$-Ray Tomography and Radiography*".

- UNTF 2018 Universities Nuclear Technology Forum.
  Lancaster University, 10-12 July 2018
  **Oral Presentation**: "*Combined fast-neutron $\gamma$-ray computed tomography / radiography.*"

- 2018 Postgraduate Engineering Department Conference.
  Lancaster University, Engineering Department, 4-5 July 2018.
  **Oral Presentation**: "*Combined fast-neutron $\gamma$-ray computed tomography / radiography.*"
  Awarded best presentation 3rd year Ph.D. student.

- 2018 Lloyd's Register Foundation conference.
  9-10 May 2018. IET London, Savoy Place.
  **Poster Presentation**: "*Combined Fast-Neutron / $\gamma$-Ray Computed Tomography*".

- 2018 Joint Nuclear Centre Winter School.
  Birmingham 3-5 January 2018
  **Poster Presentation**: "*Shielded Nuclear Material Identification via Combined Fast-Neutron/$\gamma$-Ray Computed Tomography (FNGCT)*".

- 2017 Postgraduate Engineering Department Conference.
  Lancaster University, Engineering Department, 5-6 July 2017.
  **Oral Presentation**: "*Shielded Nuclear Material Identification via Combined Fast-Neutron/$\gamma$-Ray Computed Tomography (FNGCT).*"

- UNTF 2017 Universities Nuclear Technology Forum.
  The University of Liverpool, 4-6 April 2017.
  Conference attended.

- 2017 Joint Nuclear Centre Winter School.
  Birmingham 4-6 January 2017
  **Poster Presentation**: "*Combined fast-neutron and $\gamma$-ray computed tomography: a study on the discrimination between different materials using Monte Carlo simulation*".

- 2016 Postgraduate Engineering Department Conference.
  Lancaster University, Engineering Department, 28-29 June 2016.
  **Oral Presentation**: "*Study and development of a portable tomography system for fast-neutrons and $\gamma$ rays.*"

- UNTF 2016 Universities Nuclear Technology Forum.
  The University of Sheffield, 5-7 April 2016.
  **Oral Presentation**: "*Study and development of a portable tomography system for fast-neutrons and $\gamma$ rays.*"

- 2016 Joint Nuclear Centre Winter School.
  Birmingham 6-8 January 2016
  **Oral Presentation**: "*Study and Development of a Portable Fast Neutron Tomography System*".

## Workshops, short-courses, trainings and secondary contributions

- Radiation Protection Supervisors.
  Radman Associates and The University of Manchester, UK. April 2018.
  The University of Manchester, Centre for Radiochemistry Research. Manchester, UK.

- International Nuclear Law Course.
  The University of Manchester, UK. March 2018.
  **Essay: "*Keeping the Non Proliferation Treaty up to date*".**

- Advanced Digital Pulse Processing Techniques for Nuclear Science and Engineering Applications.
  IEEE NSS MIC Workshop. Georgia Institute of Technology, Atlanta, Georgia, USA. October 2017.

- Image Reconstruction: Theory & Practice.
  IEEE NSS MIC Short course. Atlanta, Georgia, USA. October 2017.

- The IAEA 2016 International Essay Competition on Nuclear Security for Students and Early Career Professionals.
  December 2016
  **Essay: "*The Future of Nuclear Security: Commitments and Actions*".**

- Public Engagement Training & Next Generation Nuclear, Centre for Doctoral training (NGN-CDT). The University of Manchester. August 2016.

- Visit at Springfield Fuel Ltd, nuclear fuel production installation in Preston, Lancashire. November 2015.

- Visit at Drigg: Low Level Waste Repository Ltd (LLWR). November 2015.

- Visit at EDF Heysham Nuclear Power Plant. November 2015.

- First Year Doctoral Training programme.
  EPSRC Centre for Doctoral Training in Nuclear Fission Next Generation Nuclear (NGN-CDT). The University of Manchester. October 2015 - January 2016.

# Contents

# Part I

# BACKGROUND

# Chapter 1

# Introduction

The neutron was discovered by James Chadwick in 1932, after publishing his results in the famous Nature letter "*Possible existence of a Neutron*" [1], that earned him the Nobel prize for Physics in 1935. Chadwick studied and quantified what was initially observed by Walther Bothe and Herbert Becker in 1930. They showed that beryllium, when irradiated by $\alpha$ particles emitted by polonium-210, emits a high-penetrating radiation. Furthermore, Irene Curie-Joliot and Pierre Joliot realized that, when this radiation is directed against hydrogenous targets, it causes the emission of high-energy protons with speeds of up to $3{\times}10^9$ cm/s. Chadwick proved that this radiation was caused by a "*neutron*": particle of unit mass $\sim$1u (as per the proton) and charge 0. Since then, the study of neutron physics has progressed, advancing our understanding of numerous other physical phenomena and processes, and realising many new applications in technology for use in industry.

Throughout the course of the twentieth century, attempts were made to exploit neutron beams in a similar way to how X-rays were used to achieve radiographs and tomographs and, in the last twenty-to-thirty years, this interest has increased greatly, thanks to the numerous applications that neutrons can benefit. Due to their nature, neutrons interact with matter differently than X- and $\gamma$ rays. For instance, neutrons are the ideal type of radiation to investigate thick metal layers, since they do not easily interact with the atoms comprising them, or to investigate hydrogenated materials and organic compounds, because of the contrast that can be achieved.

Although interest in neutron imaging has increased steadily over the past two decades, it has never exploded on large industrial scale to the same degree, for example, of X-ray CT. This is due, in part, to the fact that the availability of intense and properly collimated neutron beams is scarce. At present, neutron sources favoured to provide reasonable radiographs and tomographs, are nuclear reactors, spallation sources and, since a few years ago, neutron generators. Nuclear reactors and spallation sources present important issues, both from a regulatory point of view, for example important regulatory procedures need to be met to gain access and, from a logistical point of view, samples have to be moved *on-situ*, often remotely. Neutron generators, which have only recently been useable on a portable or mobile practical basis, have important radiation protection, safety and costs requirements, and they can be used only in controlled areas.

Another factor that retarded the development of neutron radiography was the spatial resolution: generally lower than that achievable with X-rays, mainly due to the size and characteristic of neutron detectors and the need to quench the energy of the neutrons to small interaction wavelengths. A further disadvantage is the fact that, some samples can be activated when irradiated by intense beams for long periods of time, which requires their storage in shielded containers to allow the activity to decay away to safe levels, before they can be reused.

Despite the aforementioned issues, however, neutron-imaging research continues to be a very active and burgeoning field. Decades of research have developed and improved a variety of techniques. In particular, cold and thermal neutron radiography is arguably the technique that has evolved and improved the most over time, achieving performances comparable to that obtained with X-rays. The reason of this development is found in the interaction properties of thermal neutrons, (i.e. low-energy neutrons), which have relatively high interaction probabilities in some materials, such as helium, boron and lithium. This has enabled the development of efficient detectors for thermal neutron detection, especially scintillation screens that, coupled with charge coupled devices (CCDs), have rendered neutron radiography and tomography competitive with other non-invasive techniques already in use. The fields of application on which radiography and tomography flourish include material science and engineering, palaeontology, archaeology, cultural heritage, geology, chemistry and biology, homeland security, contraband detection and nuclear safeguards[1]. Most of research of this type has been conducted with spallation sources and research reactors, such as the Paul Scherrer Institute [2] in Zürich (Switzerland), the NECTAR [3] facility in Munich (Germany), ANSTO [4] in Melbourne (Australia), ISIS [5] in the UK and the Institut Laue-Langevin [6] (ILL) in Grenoble (France). These facility are world leading in thermal neutron radiography research.

Whilst on the one hand (and albeit not on large scale) thermal neutron radiography and tomography have become largely consolidated over time, on the other, there is an ample margin for research regarding fast-neutron tomography and radiography. These avenues offer several advantages with respect to thermal neutron imaging. Fast neutrons can penetrate significant thicknesses of materials, especially high-density metals and compounds. Moreover, there is no need for a moderator near by the source, which therefore does not attenuate its flux and reduces the size of the system. With the advent of compact neutron generators, the use of fast neutron tomography is spreading and being used in more applications in a variety of different sectors. To cite some noteworthy research, in [7–9] fast neutron imaging has been used to inspect cargo containers, for the detection of illicit materials; a topic of significant importance nowadays [10]. Tomography systems based on compact neutron generators are also making fast neutron tomography possible to perform in-situ assessments, with transportable systems [11–14]. The *state-of-the-art* in thermal and fast neutron imaging will be addressed in detail in the third chapter of this thesis, with particular attention on the combined use of fast

[1] See section 3.3 for a more detailed description of neutron imaging applications.

neutrons and $\gamma$ rays.

Regardless the benefits mentioned above, the fact that fast neutron tomography and radiography have not evolved as quickly as the thermal neutron applications is due in the main to the fact that fast neutron detection methods are different from those used for thermal neutron energies. Thermal neutrons are detected following their capture by a material, known as converter, such as, for instance, lithium-6 and boron-10. This process is not efficient for fast neutrons, because the associated capture cross sections are very low. Fast neutrons can be detected by scintillator detectors, following the emission of light due to their elastic scattering interaction with hydrogen atoms. It is only in the past two decades that organic scintillators, both liquids and plastics, have been seen as viable alternatives to previous techniques for fast neutron detection. For instance, the deficiency of helium-3, used on a widespread basis in gas-filled $^3$He detectors, has accelerated research on scintillators in order to find new solutions for fast and efficient fast neutron detectors [15]. The scintillation process, fundamental for their detection function, has been understood for more than 50 years and is a similar physical process to that associated with photon detection. It was therefore necessary to develop techniques of signal discrimination, since neutron and photon generate a slightly different signal, and its discrimination is based on the differences in the decay time of the pulse generated in the detector by the particle. As a matter of fact, scintillators can be used in the presence of mixed radiation fields, thanks to their ability to work in the presence of $\gamma$ rays, as long as pulse shape discrimination (PSD) techniques are applied to discriminate the impulses generated by the various radiations incident upon them. The discrimination of photons and neutrons is crucial because, when dealing with neutron radiation fields, there is almost always a $\gamma$-ray component due to, for example, the neutron production process, neutron scattering in the environment, secondary $\gamma$ rays produced by neutron-induced reactions, etc. The discrimination of neutrons and $\gamma$ rays therefore allows their detection with a single detection system, which is a key advantage of itself. However, when compared to the detection rate, discrimination processes have always been slow, having always relied on analogue electronic systems. Real-time assessments were not possible, due to the inevitable requirement to post-process impulses with offline pulse-shape discrimination algorithms.

Previous research carried out at Lancaster University [16, 17] has focused on fast, real-time pulse shape discrimination, coupled with digital, fast electronic, thus allowing measurements and applications not possible before. Organic liquid scintillators, linked to these digital, pulse-shape discrimination systems (often referred to as mixed field analysers, MFA), have been used to characterize mixed radiation fields, and to compare different PSD algorithms [18]. The possibility to retain real-time information from both fast-neutrons and $\gamma$ rays opens up the potential to combine both, in such a way as to retain their simultaneous information. In [19], it has been shown that it is possible to identify mixed radiation fields simultaneously, discriminating $\gamma$ emitters from neutron emitters, and to potentially localize these sources, using a single organic liquid scintillator. This system, furthermore, has the advantage of being portable. The application

of multiple, fast and reliable imaging systems are increasingly in demand, especially for nuclear safety, nuclear safeguards applications and for radiation assessment in a nuclear decommissioning and decontamination scenarios. These studies led to real-time fast neutron spectroscopy studies [20], so as to allow the identification of different neutron sources, such as americium-beryllium and californium-252, by means of a characterization of their spectra. The discrimination of neutrons and $\gamma$ rays, as well as the relative position of the radioactive source (californium-252) was also possible in highly shielded environments [21]. This study was applied, subsequently, in remarkable research [22] to image the core of an operational TRIGA nuclear reactor from the outside, with a compact and portable radiation imaging system made of a single organic scintillator detector coupled with the aforementioned real time pulse shape discrimination system.

At present, the use of organic scintillators for the detection of fast neutrons is a consolidated technique, however, the development of digital and fast pulse-shape discrimination techniques is still matter of widespread research. Particular mention should be made of the research carried out at Lawrence Livermore National Lab [23] (LLNL), in which a fast, portable, digital electronic system has been developed. This system combines the functions of liquid scintillators, inorganic crystals and in particular plastic scintillators. This arrangement can be applied for nuclear safeguards applications [24] and for monitoring spent or reprocessed nuclear fuel, as hypothesized in the Monte Carlo simulation study [25]. This system is capable of counting and discriminating individual fast neutrons and $\gamma$ rays with time sensitivities of the order of nanoseconds. It uses an array of stilbene crystals, connected to a digitizer module for data acquisition that counts, separately, prompt and delayed fast-neutrons and $\gamma$ rays [26]. The system is also particularly suitable for correlated measurements of $\gamma$ rays and neutrons. At LLNL, portable imaging systems as well as imaging methods are also being developed, with particular focus on the measurement of neutron and photon multiplicities of fissile materials, with an associated particle imaging deuterium-tritium (API-DT) neutron generator used to actively interrogate the samples [27–29].

In a fast-neutron tomography context, [30] and [31] used the pulse shape discrimination arrangement previously mentioned [16, 17], linked to an array of liquid organic scintillation detectors (EJ-309 type), to develop a portable fast neutron tomography system. In the former, the internal structure of a concrete block with reinforced steel bars inside was investigated (by means of radiography) on the basis of the variation of the fast neutron flux transmitted. In the latter, an array of 7 organic liquid scintillators, coupled with a real time pulse shape discrimination system, was used to perform fast neutron tomography. This study used californium-252 as a neutron source, demonstrating the possibility of conducting this type of assessments *in-situ*, without the need of a reactor or a beam line, as well as without the use of scintillation screens coupled with CCDs. In both of these researches, the discrimination between neutrons and $\gamma$ rays has been exploited to retain the neutron attenuation information, that led to the final tomography and radiography. Amongst the various outcome discussions, it was suggested to investigate the integration of the $\gamma$-ray response alongside the neutron response. Such

studies were one of the starting points of the research presented in this thesis, motivated as explained in the next section.

## 1.1 Research motivations

It is well known that neutrons and photons interact differently in matter. Their probability of interaction depends on the cross section of the individual physical processes they are susceptible to. The cross sections, in turn, depend both on the energy of the particle and on the atomic number (Z) of the element with which they are interacting. Consequently, the relative attenuation of the radiations, strictly related to this probability, will be different. Several works[2] in the scientific literature carry out both thermal or fast neutron imaging alongside X-ray or $\gamma$ imaging, however, none of them have used the same source and detection system, simultaneously. The detection system made up of liquid scintillators, coupled with the real time pulse shape discrimination system developed at Lancaster University, was designed to address this opportunity. Furthermore, not only does the simultaneous performance of neutron-$\gamma$ imaging reduce times and costs, but also the scan of an identical section of the sample facilitates data fusion techniques. In such a way, neutron and $\gamma$ tomographs can be combined, so as to exploit the advantages offered by both. This approach has been used to explore different areas of research, and to investigate different experimental techniques.

- Firstly, an extensive Monte Carlo simulation study has been carried out. The motivations for this research were to explore materials (actinides) with high atomic number (Z), and shielding materials with both low-Z (polyethylene) and high-Z (lead). The aim of this research was to demonstrate whether the combination of $\gamma$ rays and fast neutrons might allow these materials to be discerned from each other, when arranged properly in such a way as to deliberately conceal the actinide compounds. This research has been collocated in a nuclear framework with the objective of recognising, identifying and discriminating special nuclear materials (SNM) used in the nuclear industry from materials that might be used for shielding purposes. This research was furthermore boosted by the potential interest in assessing such materials for national security applications. It must be emphasized that this study is a computer-based, Monte Carlo simulation study, due to the *quasi*-unfeasible option of having access to such nuclear materials.

- Secondly, the feasibility of discerning materials with similar atomic numbers has been explored. In particular, a lithium polymer was compared with different substances of similar density, such as water, water peroxide, acetone and different types of explosives. This aspect of the research has particular relevance for safety applications and was motivated by the fact that substances with similar densities can be confused with each other when they are imaged with X-rays. As a matter of fact, this is one of the reasons why, at airport screening checks, it is often

[2] See section 3.3 and 3.4 for more details.

requested that laptops are removed from bags: in addition to having high-density metal components, which might easily hide suspicious metal objects inside, laptops have also batteries made of lithium polymers, which on X-rays can result in a degree of attenuation that is similar when compared to a variety of different explosives. This study therefore sought to determine whether fast neutron radiography and the combination of fast-neutron/$\gamma$-ray radiography are able to discriminate these polymers with respect to different types of hazardous materials. Experimentally, a radiograph of a laptop lithium ion battery was carried out with objective of imaging the battery cells and the distribution of lithium ions inside the cells.

- Thirdly, an innovative imaging technique, based on the detection of elastic backscatter of fast neutrons and the Compton scattering of $\gamma$ rays, was investigated. The technique was applied to distinguish different physical characteristics of a single type of material (steel), such as the thickness of different slabs, rather than to discern different materials, as carried out in the two research studies mentioned previously. In particular, this technique uses fast neutrons to determine whether the approach might be compatible with the depiction of corrosion-related defects in steel, by measuring differences in backscatter as a result of changing steel thickness. This research was carried out in an oil & gas industry context, with one of its possible applications is an integrity assessment of the steel pipeline. Amongst the various measurements carried out in this research, the response of steel under materials selected to illustrate the presence of insulation on pipelines was also explored, including the effect of polyethylene and concrete insulation. This research, as done for the previous examples described above, is accompanied and supported by Monte Carlo simulations.

- Finally, the potential to exploit high-energy $\gamma$ rays produced by the interaction of fast neutrons, has also been investigated. This technique has been studied with the aim of combining different imaging techniques to identify particular metal isotopes, qualitatively and quantitatively. Tomography and radiography techniques yield the spatial distribution of the materials, and allows them to be discriminated qualitatively, whilst the spectroscopy technique offers the potential to identify a particular isotope, within the section under scrutiny. This technique can lead to, in principle and by means of a single measure, to three different tomographic representations of the object under scrutiny, which can in turn be combined with each other. The first two representations refer to neutron and $\gamma$-ray tomography, whilst the third, instead, is the representation produced by exploiting the high-energy $\gamma$-ray activation produced by inelastic scattering by the neutrons themselves. These are characteristic of each isotope and constitute the isotopic footprint. Moreover, using the energies of these $\gamma$ rays and combining this information with the spatial-qualitative information produced by the neutrons, it is possible to identify the spatial distribution of the isotopes within the sample.

The entire research described in this thesis is motivated by the fact that industry

requires non-destructive methods that are, increasingly, more detailed, reliable and fast. In this regard, the combination of multiple imaging techniques turns out to be useful and is a strong candidate to play a key role in the future of non-destructive imaging tests. Concepts and methods presented here combine nuclear techniques for specific applications in different fields, particularly where neutron metrology plays a fundamental role, such as in homeland security, safeguards, oil and gas, nuclear and civil engineering.

# Chapter 2

# Fundamentals of neutron and photon detection

## 2.1 Neutrons

The neutron is a subatomic particle, classified as a baryon[1] and with a mass of $1.674\times10^{-27}$ kg (939,57 MeV/c$^2$). The neutron has been found to be an unstable particle. Its half-life is 900 seconds and decays in isolation as:

$$n \rightarrow p + e^- + \bar{\nu_e} \tag{2.1}$$

which is the same reaction of the $\beta^-$ decay, that occurs in nuclei with which the neutron-proton ratio is high, making the nucleus unstable. Neutrons are subject to the four natural forces: gravitational, weak-nuclear, strong-nuclear and, despite their lack of charge, electromagnetic, as they possess an internal charge distribution and spin momentum. The characteristic of being chargeless leave neutrons free of the Coulomb interaction with protons and electrons of the atoms, a property which makes them particularly useful for the study of the atomic nucleus.

### 2.1.1 Neutron production

In nature there are no natural sources[2] of neutrons, therefore, they have to be produced artificially, exploiting nuclear reactions. In general, neutrons produced in nuclear reactions possess energies of the order of MeV. By convention, neutrons are classified according to different energy values, as shown in table 2.1.

The following paragraphs describe the most important methods and nuclear reactions exploited for neutron production.

[1] Baryons are particles constitutes by three quarks. Neutrons are composed by one quark *up*, and two quarks *down*.

[2] With the exception of uranium-238 and uranium-235, that have a very small neutron emission yield due to their negligible spontaneous fission.

| | |
|---|---|
| Ultracold | E $<$ 0.025 eV |
| Thermal or Cold | E $\sim$ 0.025 eV |
| Epithermal | E $\sim$ 1 eV |
| Slow | E $\sim$ 1 keV |
| Fast | E $\sim$ 100 keV - 10 MeV |

Table 2.1: Classification of neutrons depending on their energy [32].

### $(\alpha, n)$ reaction

This reaction led to the discovery of neutrons. Usually, an $\alpha$ emitter radioisotope is mixed with specific isotopes of beryllium, boron, lithium or other light nuclei, to give a reaction of the type:

$$\alpha + {}^{9}Be \rightarrow {}^{12}C + n \tag{2.2}$$

The vast majority of $\alpha$ emitters used are $^{210}$Po, $^{226}$Ra, and $^{241}$Am; all of them produce a different neutron spectrum, with an energy range between 1 and 14 MeV. An example is given in figure 2.1, for an Am-Be source.

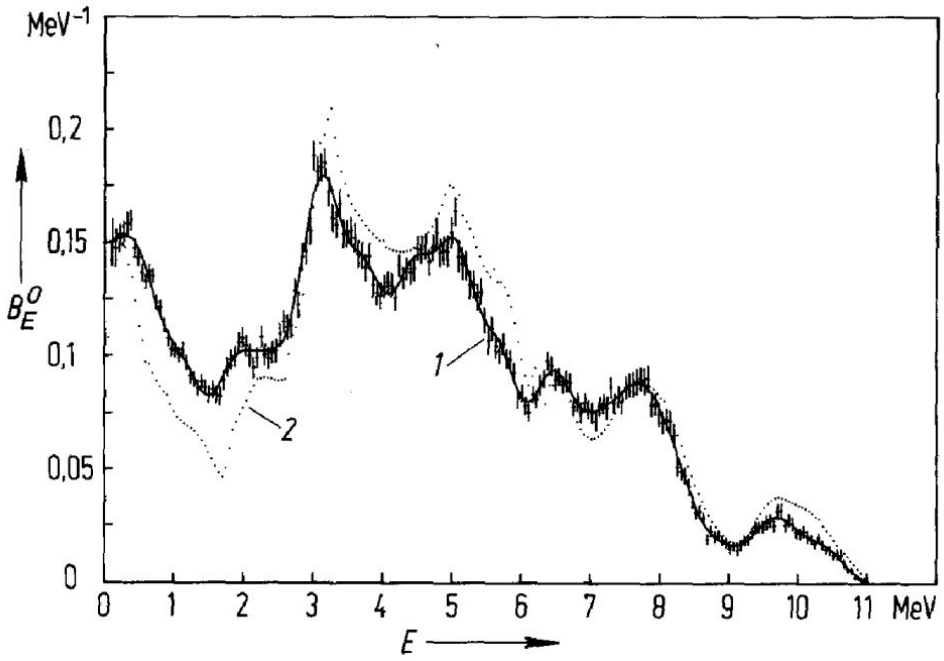


Figure 2.1: Normalised probability density ($B_E$) as a function of the energy (E), in MeV, for a $^{241}$AmBe($\alpha$,n) neutron source. The dotted line (2) represents the theoretical data whereas the black line (1) the experimental data. Image from [33].

### Spontaneous fission

Spontaneous fission (SF) is the only process capable of producing neutrons naturally. Spontaneous fission occurs only in $^{238}$U, $^{235}$U, albeit with a very low yield, and in some transuranic elements. The most noteworthy example, and closely related to the work presented in this thesis, is californium-252. Its average half-life is 2.645 years, with a

branching ratio of 96.91% $\alpha$ decay and 3.09% SF [34]. A sample of one microgram emits $1.97\times10^7$ $\alpha$ particles per second and $6.14\times10^5$ SF. The neutron yield is 0.116 n/s per Becquerel[3], considering the activity taking into account both the alpha and the spontaneous fission rate [36]. The average number of neutrons emitted per spontaneous fission (defined as multiplicity) is about 3.8[4]. The $^{252}$Cf spectrum has a typical SF shape, described by the equation:

$$\frac{dN}{dE} = A\sqrt{E}e^{-E/B} \tag{2.3}$$

and shown in figure 2.2. E is the energy, A and B are constants. Concerning californium,

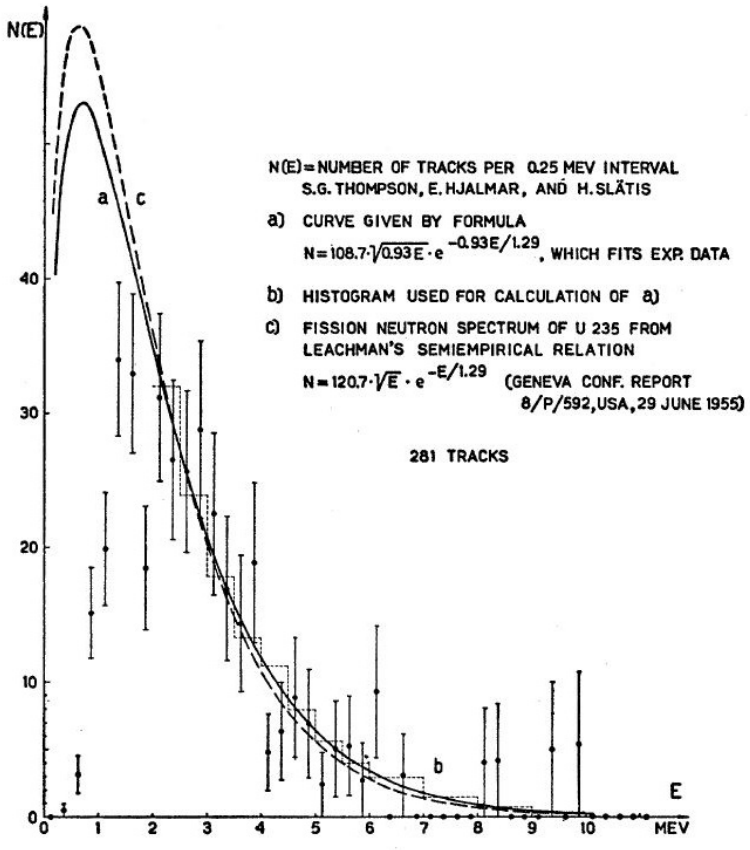


Figure 2.2: Energy spectrum of neutrons from $^{252}$Cf spontaneous fission. Image from [37].

the most probable energy is 0.7 MeV and the average energy is 2.1 MeV [38]. It has to be highlighted that each SF event produces, on average, 8 $\gamma$-ray photons, of relatively high-energy, emitted mostly within 1 ns after a SF event occurs [36].

### $(\gamma, n)$ photo-neutron production

This reaction occurs within the nucleus. The absorption of a high energy photon leaves the nucleus in an excited states; subsequently, it reaches the stability by emitting

[3]Bq: Becquerel, International System unit of radioactivity. 1 Bq corresponds to an amount of material in which one nucleus decays per second. Another common unit of radioactivity is the Ci (Curie), namely the activity of 1 g of the isotope $^{226}$Ra. 1 Curie corresponds to about 37 GBq.

[4]It was initially measured 3.55, in 1955, by Crane et al. [35].

one or more neutrons. A valid example is the isotope of sodium $^{24}$Na (half-life 15 hours): it emits a photon of 2.76 MeV, that is greater than the neutron binding energy of $^{9}$Be, with the consequent emission of a neutron, according to the reaction:

$$\gamma + {}^{9}Be \rightarrow {}^{8}Be + \mathrm{n}$$

The positive side of neutron photoproduction is the creation of a *quasi*-monoenergetic spectrum. In the aforementioned case the neutron energy is about 0.8 MeV with a yield of $2\times10^{6}$ neutrons emitted per Curie (Ci) of $^{24}$Na.

### Induced fission

In induced fission, a neutron, by interacting with a nucleus of high atomic number (usually Z>90), is absorbed[5] by the nucleus. This creates instability in the nucleus itself, that splits into two nuclei of lighter elements, called primary fission fragments. These are initially affected by high neutron/proton ratio and, as a consequence, free neutrons, $\gamma$ rays, $\beta$ and $\alpha$ particles are emitted. The two, excited fission fragments emit, on average, from 2 to 3 neutrons, depending on the atomic number of their initial parent nucleus.

In the proximity of the the core of a fission reactor, a neutron flux of the order of $10^{14}$ neutrons/cm$^2$s can be present, thus generating a constant neutron source with energy spectrum ranging from the thermal to the fast region. The neutron flux is obtained simply extracting neutrons from the shielding system of the reactor core.

### Fusion reactions

In this process two light nuclei are fused into a heavier nucleus, releasing an extremely high amount of energy. This can be done with an accelerator to provide the energies that overcome the nuclei Coulomb repulsion. The most common reactions are:

$$D + D \rightarrow {}^{3}He + n(2.45MeV) \tag{2.4}$$

$$D + T \rightarrow {}^{4}He + n(14.1MeV) \tag{2.5}$$

$$T + T \rightarrow {}^{4}He + 2n(11.3MeV) \tag{2.6}$$

To date, studies on nuclear fusion have not produced an adequate technology that allows their use in industrial applications. However, numerous research projects are progressing all over the world.

### Nuclear spallation

When high-energy particles (order of magnitude of a few GeV), such as protons or ions collide with high Z atomic nuclei (lead, tungsten), nuclear reactions occur inside the nucleus and fragments and light particles are emitted. In this particular way, neutrons are also expelled from the nucleus. On average, 20-30 neutrons are emitted per proton of 1 GeV.

[5]The probability of being absorbed by a nucleus, known as absorption cross section, is higher for low-energy neutrons.

### 2.1.2 Concepts of neutron physics

Prior to examining the reactions induced by neutrons, which are exploited for their detection and described in the following sections, it is useful to tackle some fundamental concepts of neutron physics, such as cross section, attenuation and moderation.

#### Cross section

The concept of cross section identifies the probability that a certain process or reaction will occur; for instance scattering, fission or neutron capture.

Imagine a beam of particles incident on a target, with the condition that the beam is wider than the size of the target and its distribution is uniform. The flux I of a beam is defined as the number of particles that pass throughout a unit area A, perpendicular to the direction of the beam, in the unit of time, as shown in figure 2.3. The number of

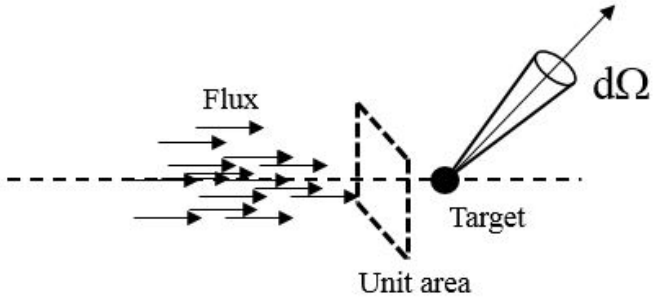


Figure 2.3: Illustration of the scattering cross section concept.

scattered particles $dN$ per unit time depends on the beam intensity, on the solid angle $d\Omega$, on the number of target diffusion centres $n$ per unit volume, and on the thickness $dx$ of the target itself, as per:

$$dN \propto I \cdot n \cdot A \cdot dx \cdot d\Omega \tag{2.7}$$

The proportionality function is known as *differential cross section*, and depends on the energy of the incident beam:

$$\sigma(E) = \frac{d\sigma}{d\Omega} \tag{2.8}$$

The total number of particles emitted per unit time is obtained by integrating over the solid angle:

$$N = \int I \cdot n \cdot A \cdot dx \cdot \frac{d\sigma}{d\Omega} d\Omega = I \cdot n \cdot A \cdot dx \cdot \sigma_{tot} \tag{2.9}$$

where

$$\sigma_{tot} = \int \frac{d\sigma}{d\Omega} d\Omega \tag{2.10}$$

The cross section has a unit of area, known as *barn*, which is equivalent to $10^{-24}$ cm$^2$. When multiplied by the diffusion centres $n$ per unit volume, the cross section becomes the macroscopic cross section $\Sigma = n\sigma$.

### Attenuation

The sum of the single reaction cross sections, is known as total cross section, and indicates the total probability of interaction of a neutron in matter:

$$\Sigma_{tot} = \Sigma_{capture} + \Sigma_{elasticscattering} + \Sigma_{inelasticscattering} + \Sigma_{fission} + \dots \tag{2.11}$$

This particular concept plays a central role when considering the attenuation of a neutron beam that passes through a thickness of material. The loss of intensity is given by:

$$dI = -I\Sigma_{tot}dx \tag{2.12}$$

Therefore, the beam intensity exponentially decreases as the material thickness increases, as per:

$$I = I_0 e^{-\Sigma_{tot}x} \tag{2.13}$$

### Moderation

Depending on the neutron energy, a certain type of reaction may become likely with respect to another. For instance, at thermal energies, neutron capture is the most probable process, whereas for fast neutrons, elastic scattering is usually the most probable interaction and the principal mechanism of neutron energy loss. Elastic scattering slows down fast neutrons and this process is known as *moderation*. Until energies up to several MeV, elastic scattering can be described non-relativistically, applying simple conservation laws. It can be shown [36] that the relationship between the energy with which the neutron hits the target and its energy after the interaction can be calculated with relationship 2.14:

$$\frac{E}{E'} = \frac{A^2 + 1 + 2Acos\theta}{(A+1)^2} \tag{2.14}$$

where $E'$ is the incident energy, A the target mass, $E$ the neutron final energy and $\theta$ the scattering angle in the reference frame of the centre of mass (see figure 2.4 for an illustration).

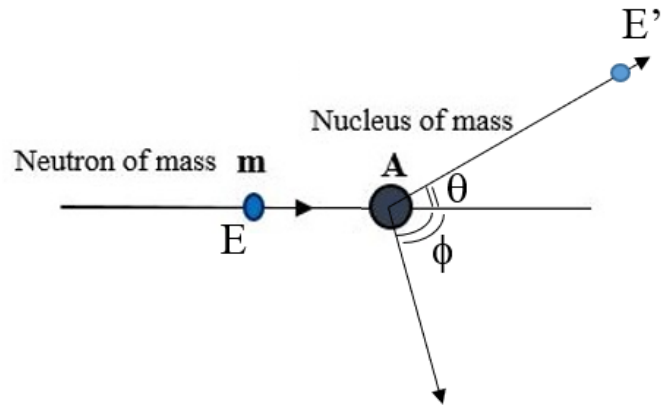


Figure 2.4: Elastic scattering of a neutron on a nucleus of mass A.

In the event of a frontal impact ($\theta$=180°), equation 2.14 becomes:

$$\frac{E}{E'} = \frac{(A-1)^2}{(A+1)^2} \tag{2.15}$$

and in case the target is an hydrogen atom, being A = 1, the $E/E'$ ratio is approximately equal to zero, i.e. the neutron has transferred all its energy to the proton. This relationship also shows that the moderation of neutrons is more efficient when compounds comprising many protons or light nuclei are used, such as water, paraffin, polyethylene, etc.

### 2.1.3 Neutron-induced reactions

Being chargeless, neutrons interact only via the strong-nuclear force with atomic nuclei. Depending on the neutron energy, different types of reaction may occur. In the case of fast neutrons, the most probable is scattering, whereas thermal neutrons are mainly absorbed via neutron capture. Interactions can be classified with the following processes:

- **Radiative capture**: The neutron is absorbed by the nucleus according to the reaction n+(Z,A)→ $\gamma$+(Z,A+1). The capture cross section depends on the inverse of the neutron energy. In certain types of elements, the capture of a neutron is followed by the emission of charged particles such protons, deuterons, tritons etc.

- **Induced fission**: a nucleus captures a neutron and then it undergoes fission. This occurs, mainly, at thermal energies. For instance, one of the possible fission reaction that uranium-235 (235U) may undertake, is described by the reaction:

$$^{235}_{92}U + n \rightarrow ^{236}_{92}U \rightarrow ^{141}_{56}Ba + ^{92}_{36}Kr + 3n \tag{2.16}$$

- **Elastic scattering**: the reaction is identified as A(n,n)A and, as shown in the previous section, it is the main mechanism of neutron energy loss in the MeV region. In this particular process, kinetic energy and momentum are conserved. The neutron does not excite the target nucleus, that remains in its fundamental state.

- **Inelastic scattering**: symbolically defined with A(n,n')A*. The target nucleus, after the interaction with n high energy neutron, typically higher than 1-2 MeV, remains in an excited state and emits high-energy $\gamma$ rays.

- **Hadron production**: For energies E>100MeV, a neutron may interact with an atomic nucleus, thus inducing a hadron shower.

### 2.1.4 Neutron detectors

By not producing ionization in matter, neutron detection is not straightforward. The devices designed for neutron detection are based on indirect methods that measure

the products of neutron-induced nuclear reactions, summarized and described in the previous paragraph. The materials used to detect neutrons are called *converters*. They act as targets in nuclear reactions in order to convert neutrons into charged particles. The most used converters are $^{10}$B, $^{6}$Li and $^{3}$He.

$$^{10}B + n \rightarrow^{7} Li + \alpha + 2.792keV(6\%) \tag{2.17}$$

$$^{10}B + n \rightarrow^{7} Li + \alpha + \gamma(0.48MeV) + 2.310keV(94\%) \tag{2.18}$$

$$^{6}Li + n \rightarrow^{3} H + \alpha + 4.78MeV \tag{2.19}$$

$$^{3}He + n \rightarrow^{3} H + p + 0.764MeV \tag{2.20}$$

The aforementioned cross-section reaction trends are shown in figure 2.5. They show higher cross sections for low energies with a trend inversely proportional to the energy. Only for these particular reactions, the inverse proportionality is regular, without any resonances up to about 100 keV. This makes these converters particularly suitable for neutron detection. This fact has also the advantage of the direct proportionality between

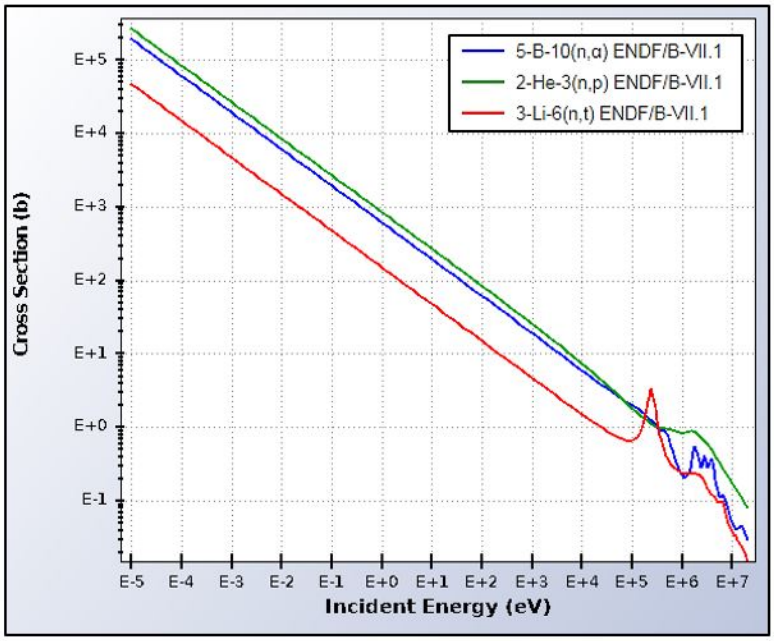


Figure 2.5: Total neutron cross section of $^{3}$He(n,p), $^{10}$B(n,$\alpha$) and $^{6}$Li(n,t). Data from [39].

the count rate and the incident neutron density on the sensitive volume of the detector, regardless the neutron speed itself. Considering a mono-energetic $E$ neutron beam, of flux $\phi$ (dimensions length$^{-2}$ time$^{-1}$), the reaction rate $R$ in the detector sensitive volume is simply the product of the neutron flux and the macroscopic cross section $\Sigma$ of the neutron-induced reaction $R = \phi\Sigma$. Generalizing for an energy-dependent neutron flux:

$$R = \int \phi(r, E)\Sigma(E)dE \tag{2.21}$$

Another important converter is the isotope $^{157}$Gd which, despite having a very high neutron capture cross section, approximately 255k barns, is not common because of the electromagnetic radiation emitted, that follows the neutron capture, which makes the detection difficult when high levels of $\gamma$ background are present.

Neutron detectors can be divided essentially in four categories: gaseous detectors, scintillation detectors, solid-state detectors and activation detectors.

### Gaseous detectors

Gas detectors exploit the ionization produced by a photon or a charged particle, within the gas. They were the first to be used in neutron physics applications. The general design is a small container filled with gas, enriched with $^{3}$He or $^{10}$B, which serves as a converter. The ion production constitutes, by means of an electrode system, an electrical signal which is converted and amplified, thus allowing the detection of the neutron.

### Scintillation detectors

Scintillation detectors base their operation on molecular processes that lead to the emission of light, using materials with luminescence properties as neutron converters. These, absorb the energy of the radiation and then re-emit it in form of light, which is collected and converted into electric signals (via photomultipliers, photodiodes, etc.) thus giving information about the incident radiation nature: intensity and the amount of photons generated depends on the type of particle interacting with the scintillation material.

These detectors will be examined in detail in the next section of this thesis, being such a concept directly related to the research work carried out.

### Solid state detectors

This group of detectors is mainly composed by crystals of silicon or germanium, which are covered on the surface by a layer of converting materials such as $^{6}$LiF, $^{6}$Li pure or $^{10}$B. Some silicon detectors have the converter homogeneously distributed in its crystalline structure. Another solid-state detector is silicon carbide, which uses a $^{6}$LiF layer as a converter.

Solid state detectors exploit the sensitivity of semiconductors to radiation. The ionizing radiation produced by the neutron converter has an energy greater than the energy gap of the detector, and thus transmits to the electrons sufficient energy to make them pass from the valence band to the conduction band. This creates electron-hole pairs that then generate the signal.

### Activation detectors

These detectors measure the $\gamma$ radioactivity that a neutron flux induces on a material with high interaction cross section. The radioactivity induced when the material is

irradiated for a certain time by a neutron flux, is measured. A disadvantages of this type of detector is that the neutron detection is not carried out *real-time* and it is not known whether the measured neutron flux is constant or not during the irradiation time. Their small dimensions and low costs are the advantages of these detectors.

None of the aforementioned types of detector has all the desirable characteristics required to be a good detector, such as high efficiency, insensitivity to $\gamma$ rays, feasibility of use in extreme conditions, reliability and low-cost. The limit of most neutron detectors is the lack of information on the energy of the incident neutron. The main reason is that it is not always possible to measure the direction of the secondary particles emitted by the nuclear reaction, and it is therefore difficult to make kinematics considerations to reconstruct the energy of the initial state.

## 2.2 Photons

Photons, like neutrons, are chargeless, and this makes inelastic collisions with atomic electrons, typical of charged particles, impossible. The main interactions of photons with matter are photoelectric effect, Compton effect, and pair production. Their probability depends on the energy of the interacting photon. The cross section of these three is smaller than most of charge particles interactions [40], and this is the reason why photons (particularly X- and $\gamma$ rays) are much more penetrating. Moreover, an important feature of photons is that when a beam passes through matter, it is only attenuated in intensity, leaving unvaried its energy spectrum. Photons interacting with the material are removed from the beam, due to either absorption processes or scattering, whereas photons that manage to pass through the material without having had any interaction, keep their initial energy.

The attenuation of the photon beam is the typical exponential attenuation law that depends on the thickness $x$ of the material:

$$I(x) = I_0 e^{-\mu x} \tag{2.22}$$

where $I_0$ is the initial intensity of the beam, $\mu$ the attenuation coefficient, characteristic of the material.

### 2.2.1 Interaction of $\gamma$ rays

Amongst the several different $\gamma$-ray interaction mechanisms, only three of them have a key role in radiation measurements. As aforementioned, these are photoelectric absorption, Compton scattering, and pair production. Their cross section strongly depends on the $\gamma$-ray energy, on the atomic number and on the electron density of the material the photon is interacting with. Figure 2.6 shows an example of a typical trend of the total interaction cross section (depicted in black) of a photon interacting in matter, in this particular case iron, as a function of its energy.

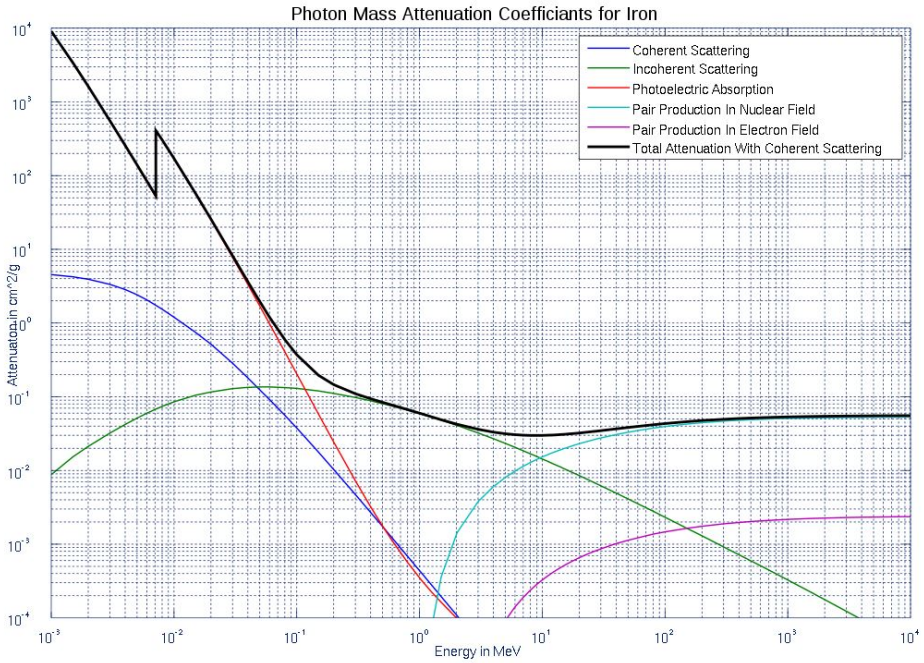


Figure 2.6: Energy dependence of different photon interaction mechanisms in iron [41]

### Photoelectric effect

The photoelectric effect is characterized by the absorption of a photon from an atomic electron. After the photon absorption, the electron is ejected. This type of interaction cannot occur with a free electron but only with those bounded to an atom. The energy $E_e$ of the emitted photoelectron is given by:

$$E_e = h\nu - E_b \tag{2.23}$$

where $E_b$ represents the binding energy of the electron in its ground shell, which is usually of the order of keV. $h\nu$ is the energy of the incident photon: $h$ is the Planck constant and $\nu$ the photon frequency. The cross section $\tau_f$ of the photoelectric effect is proportional to:

$$\tau_f \approx \frac{Z^n}{E_\gamma^{3.5}} \tag{2.24}$$

where Z is the atomic number of the material and n is an index usually between 4 and 5, depending on the energy of the $\gamma$ ray. The photoelectric effect is the process exploited for the measure of the incident $\gamma$-ray energy. All the photon energy is converted into the ejected electron kinetic energy. This is why the photoelectric effect is the most common phenomenon used in spectroscopy and particularly for the calibration of some scintillation detectors.

### Compton effect

In the Compton effect a photon interacts with an electron of the external shell, transferring part of its energy. Then, it scatters and deflects, by an angle $\theta$, that is

the angle between the direction of the incident photon and the photon direction after scattering. Applying the laws of energy conservation and momentum, the new photon

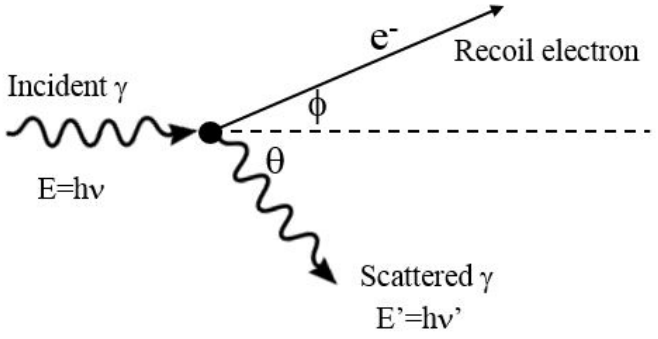


Figure 2.7: Illustration of the Compton effect.

energy can be related with the scattering angle:

$$h\nu' = \frac{h\nu}{1 + \frac{h\nu}{m_0c^2}(1 - cos\theta)} \tag{2.25}$$

while the electron energy is given by:

$$E_{e^-} = h\nu \frac{\frac{h\nu}{m_0c^2}(1 - cos\theta)}{1 + \frac{h\nu}{m_0c^2}(1 - cos\theta)} \tag{2.26}$$

The probability of Compton scattering depends on the number of electrons in the target atom-shell and it is linearly proportional with Z ( $\tau_{ec} \propto Z.$).

**Pair production**

This process involves the transformation of a photon into an electron-positron pair. It is energetically possible when the photon energy is twice the electron mass (2×511 keV: 1.022 MeV, with the mass expressed in units of eV); however, the probability that this interaction occurs remains relatively low for these energies, while it is more likely for energies of some MeV. In the interaction the photon disappears and all the energy is transformed into the pair $e^-/e^+$ and into kinetic energy.

The probability of pair production is proportional to the square of the atomic number $\tau_{pp} \propto Z^2$.

### 2.2.2 Detecting $\gamma$ rays

All of the aforementioned interactions, generate secondary electrons. Therefore ionization is the process by which gamma radiation is detected. In some $\gamma$ detectors, the signal generated by the incident radiation is proportional to the energy deposited in the detector sensitive volume; in others, such as the Geiger-Mueller (GM) counter, the energy deposited is independent of the initial $\gamma$ ray energy.

As per neutrons, $\gamma$ ray detectors can be divided into three macro-areas: scintillators detectors, gas filled detectors, and solid state detectors. Scintillation detectors will be described in detail in the next section. Within gaseous detectors it is worth mention the ionization chamber and the proportional counter, both with a response proportional to the energy deposited in the gas volume. In solid state detectors, the charge generated by $\gamma$ rays is collected directly; their energy resolution is better than scintillation detectors and they are the most common type of detectors used for spectroscopy measurements, above all high purity germanium detectors (HPGe).

## 2.3 Scintillation detectors

When radiation interacts with a scintillant, it may transfer all or part of its energy, exciting the molecules of this material. When returning to the ground state, they emit fluorescence photons, particularly in the visible and ultraviolet region of the electromagnetic spectrum. The emitted photons are known as scintillation photons, they must be collected and converted into an electric signal, that will be the footprint of the interacting particle. This conversion occurs by means of a *phototube*, which comprises a photocathode, responsible for the photon-electron conversion and photo-electrodes called dynodes where the electron multiplication takes place. The result is an output signal with a measurable amplitude.

There are many types of scintillating materials, however not all of them are suitable for radiation detectors. A scintillator must meet several characteristics, such as: capability of converting the energy released into scintillation light (the higher the better), a small emission time (order of magnitude of nanoseconds), transparency to the wavelength of its own emission, so as to avoid the self-absorption of scintillation photons, and finally linearity of response so that the quantity of light produced is proportional to the energy deposited in the material.

The property of emitting energy in form of visible light when irradiated with heat, radiation or light itself, is called *luminescence*. If the light is emitted immediately ($\sim 10^{-8}s$) the process is called *fluorescence*, whereas when the emission of light is delayed (from microseconds to hours), due to some metastable excited state, the phenomenon is called *phosphorescence* [40]. The light emission process can be described with a two-component exponential law, as per:

$$N = A \cdot exp(\frac{-t}{\tau_f}) + B \cdot exp(\frac{-t}{\tau_s}) \tag{2.27}$$

where N is the number of photons emitted at a certain time t, $\tau_s$ and $\tau_f$ are respectively the *slow* and *fast* decay constants (see figure 2.8a), A and B are constants that depend on the scintillation material.

Different types of radiation have different ionization powers, therefore they may excite the scintillation medium via different mechanisms. As a consequence, the slow and fast components of the time decay can be different depending on the particle interacting with the scintillator (figure 2.8b). Different particles can thus be detected and identified on

this basis. This technique is called *pulse-shape-discrimination* (PSD).

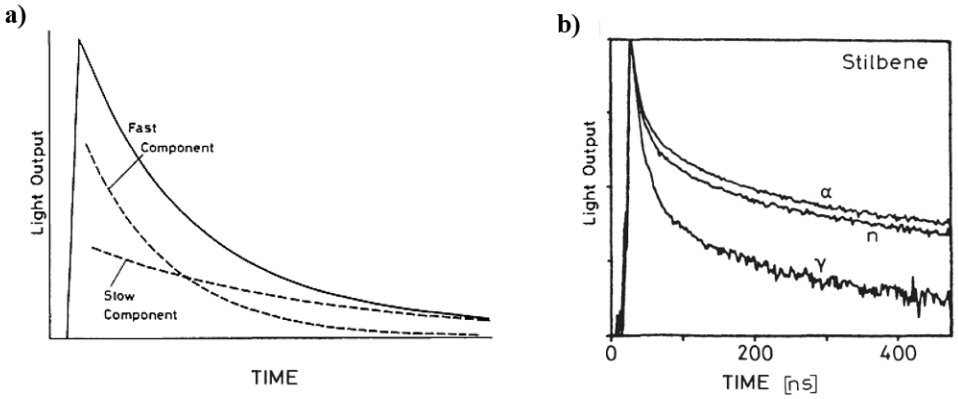


Figure 2.8: **a)** Qualitative illustration of the light output as a function of the time in scintillators, with a comparison between fast and slow component. **b)** Different light outputs for neutrons, $\alpha$ particles and $\gamma$ rays in a stilbene detector. Images from [40].

### 2.3.1 Inorganic scintillation detectors

Inorganic scintillators are crystals with impurities that act as activators. They are mostly alkali, halides and pyrosilicates. Common examples are NaI(Tl), CsI(Tl), CsI(Na), or crystals of BGO (bismuth germanate) and $CdWO_4$ or cerium-activated crystals such as $CeBr_3$, $LaBr_3$. Inorganic scintillation materials are insulators or semiconductors, therefore their light emission mechanism is based on the discrete bands of energy within their crystal lattice.

When radiation passes through these crystals, it deposits a certain amount of energy, thus elevating electrons from the valence band to the conduction band (figure 2.9). These electrons, when returning into their ground states located in the valence band, may release their energy in terms of photon emission. However, this process is inefficient and the the photon emitted is not in the visible range of the electromagnetic spectrum. For this particular reason, impurity activators are inserted in the lattice structure of the inorganic material: they modify the crystal band gap creating intermediate energy states with energies less than the forbidden gap, allowing transitions that give visible photons. Since the energy of the emitted photons is less than the difference in energy between the two bands, inorganic crystals are transparent to their own fluorescence light. In general, inorganic crystals have a response of the order of 200 ns, greater than organic crystals. One of the drawbacks of most inorganic crystals is that they are hygroscopic; this generally requires special protection measures. Amongst the advantages of inorganic scintillators is the high stopping power due to the high density and high atomic number. These type of scintillators also have the highest light-emission outputs and moreover, thanks to their relatively high atomic number and density, they are suitable for the detection of high-energy $\gamma$ rays, electrons and positrons.

Other types of inorganic scintillation materials are noble gas scintillators as well as and glasses, such as like cerium-activated lithium glasses.

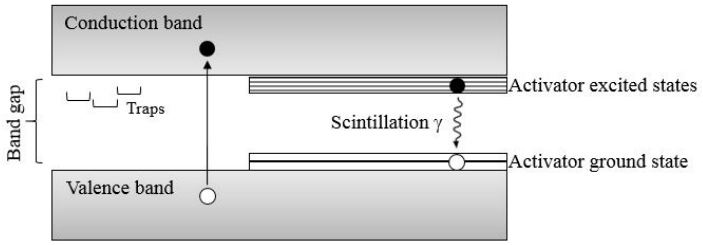


Figure 2.9: Schematic illustration of the energy band structure of an activated scintillation crystal [36].

### 2.3.2 Organic scintillation detectors

Organic scintillation detectors are hydrocarbon compounds containing the benzene-ring structure, that gives them properties typical of aromatic hydrocarbons and decay time of a few nanoseconds. The valence electrons of aromatic molecules are de-localised and not associated with a particular atom of the molecule. The structure of vibrational and electronic atomic levels ($\pi$-orbitals) is an intrinsic property of aromatic molecules and does not depend on its physical state. These $\pi$-electrons can be found in singlet states (spin 0, $S_0$, $S_1$, $S_2$, $S_3$ figure 2.10) or in triplet states (T1, T2, T3, figure 2.10) At room temperature the molecules are in the $S_0$ state. The radiation-induced excitation and ionization process brings electrons to levels $S_1$, $S_2$ and/or $S_3$. Almost immediately these pass by *internal degradation* from the highest energy states to the excited states of $S_1$. From the states $S_1$ to the fundamental vibrational states $S_0$ there is a high probability that this passage takes place with light emission. Re-absorption phenomena occur only through direct transitions from the state $S_{10}$ to $S_{00}$. Therefore organic scintillators are transparent to their own emission spectrum.

Another phenomenon that can arise is the conversion of a singlet state to a triplet state, called *intersystem crossing*. The lifetime of a triplet state is greater than that of a singlet, so that there will be emission of delayed light, of the order of milliseconds, classified as phosphorescence.

The most common organic crystals are anthracene, stilbene and naphthalene. These last two crystals have a scintillation lifetime of a few nanoseconds. Due to the anisotropic emission (channelling effect), however, the decay time may depend on the orientation of the crystal, as well as the scintillator response. Anthracene has a higher light emission, by convention 100%.

Organic liquids are solutions of two components: solvent and solute. The most famous solutes are terphenyl, PBD, PPO, POPOP. Among the solvents, the most famous are xylene, benzene and toluene. Typical concentrations are 3 g of solute per litre of solvent. The response time of these is very fast, of the order of 3-4 ns. They have the advantage that they can be used with other materials, such as boron or lithium. Plastic scintillators are probably the most used for their versatility and particularly

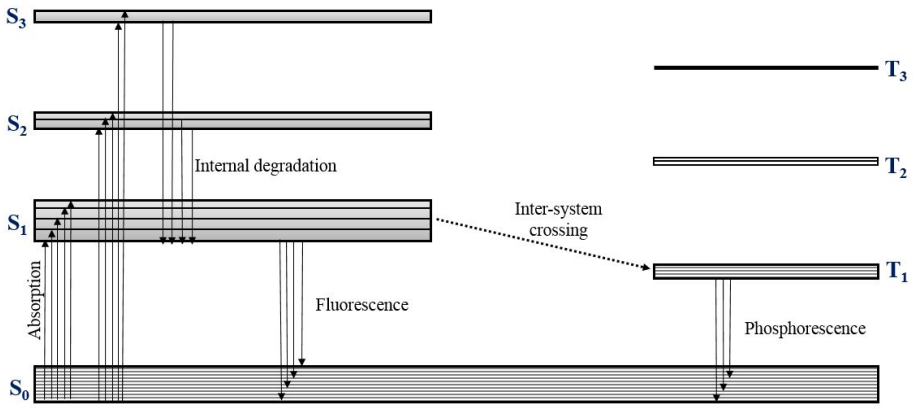


Figure 2.10: Illustration of the scintillation mechanism in organic materials [36].

suitable for pulse shape discrimination [15]. They are like liquid detectors, however the solvent is solid after being subjected to polymerization. The most common are PBD and PBO. Typical concentrations are 10 g/L. The response time is very fast, around 2-3 nanoseconds and they provide a high output light yield. One of the biggest advantages is their flexibility, as they can be easily shaped, however they degrade and can be of variable quality.

### 2.3.3 Light output

The light output of a scintillator refers more specifically to its ionization energy in photons. This is a key quantity and determines the efficiency and resolution of a scintillator. It can be assumed that the fluorescence light is proportional to the variation of energy deposited by the particle in the scintillator.

$$L \propto \Delta E \tag{2.28}$$

However, a scintillator response is more complex and furthermore it depends on the particle and ionization density and particle linear energy transfer (LET). In particular, heavy particles (e.g. alpha particles) show a deviation from the proportional relationship at lower energies with respect to, for instance, electrons [42]. The response of organic scintillators can be described relating the fluorescence per unit length ($dL/dx$) with the energy lost by the charged particle per unit length ($dE/dx$). The semi-empirical model used is the Birks' formula [43]:

$$\frac{dL}{dx} = \frac{S\frac{dE}{dx}}{1 + kB\frac{dE}{dx}} \tag{2.29}$$

where $S$ is the scintillator efficiency, $B$ and $k$ are proportionality constants that depend on experimental data fit. Assuming a scenario in which the density of the excited molecules is directly proportional to the ionization density and assuming the approxi-

mation of negligible quenching[6] (k≈0), the light produced is proportional to the energy lost, as per:

$$\frac{dL}{dx} = S\frac{dE}{dx}. \tag{2.30}$$

### 2.3.4 Photomultipliers

A photomultiplier is a vacuum tube that generates an electric signal in response to visible electromagnetic radiation. It is capable of detecting radiation intensity extremely low, up to the single photon. It is composed of two parts: a phototube, sensitive to electromagnetic radiation in the visible region and an electronic multiplier which act as multi-stage amplifier. The photosensitive area and the electronic multiplier are located

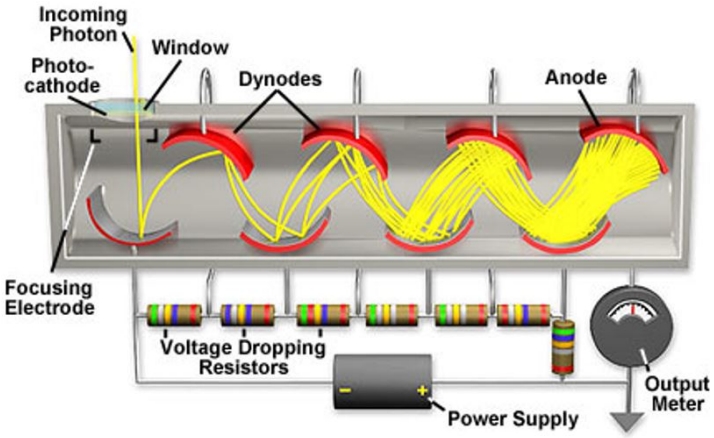


Figure 2.11: Schematic illustration of a photomultiplier tube. Image from the web [44].

inside a vacuum glass tube (or quartz tube). The photosensitive area is called photocathode and constitutes the primary electron emitter. This is generally formed by a photoemitter material, deposited in the form of a thin film on an optically-transparent glass window, which constitutes the entrance to the phototube. Electrons are emitted from the surface exposed to the vacuum tube. If the photons of the electromagnetic radiation incident on the photocathode have suitable energy, it emits a number of photoelectrons proportional to the light intensity ,due to the voltage applied between photocathode and anode. A suitable electric circuit creates increasing voltage differences between anode and photocathode, by means of a series of intermediate electrodes, called dynodes. The first photon-generated electron is accelerated towards the first dynode where it transfers its energy to the electrons of the material. The electrons that acquire an energy greater than the extraction energy, are emitted by the dynode (secondary emission) and, in turn, are accelerated towards the next dynode. This process is repeated in cascade, exponentially increasing the number of electrons until the final dynode (anode). Here the amplified signal is collected, constituting therefore an electric signal.

[6]Quenching is the phenomenon by which the fluorescence is self-absorbed, damped or degraded.

## 2.4 Pulse Shape Discrimination

Signals produced in organic scintillators from different particles are electronic waveforms that, after being acquired and stored, are discriminated by mathematical algorithms. This process is called Pulse Shape Discrimination (PSD). In the context of this thesis, these PSD algorithms are applied particularly to the separation of neutrons and $\gamma$ rays. This section aims to give a brief introduction of the most important PSD techniques used nowadays.

The detection of neutrons is often associated with by the detection of a considerable number of $\gamma$ rays. They come directly from neutron production processes or either as a consequence of interactions with surrounding materials or from the environmental background. To select only the neutron component of the detected radiation, it is necessary to use techniques to discriminate, event by event, the acquired signals.

The two most important and widespread algorithm groups are the Charge Comparison Method (CCM) and Pulse Gradient Analysis (PGA); another important, less used method, however historically significant, are the Zero Crossing Method (ZCO), Neural Networks and Wavelet transforms.

### 2.4.1 Charge comparison method

The Charge Comparison (CC) method [45] is based on the integration of the charge collected from the detector over the time (figure 2.12). The charge deposited by the

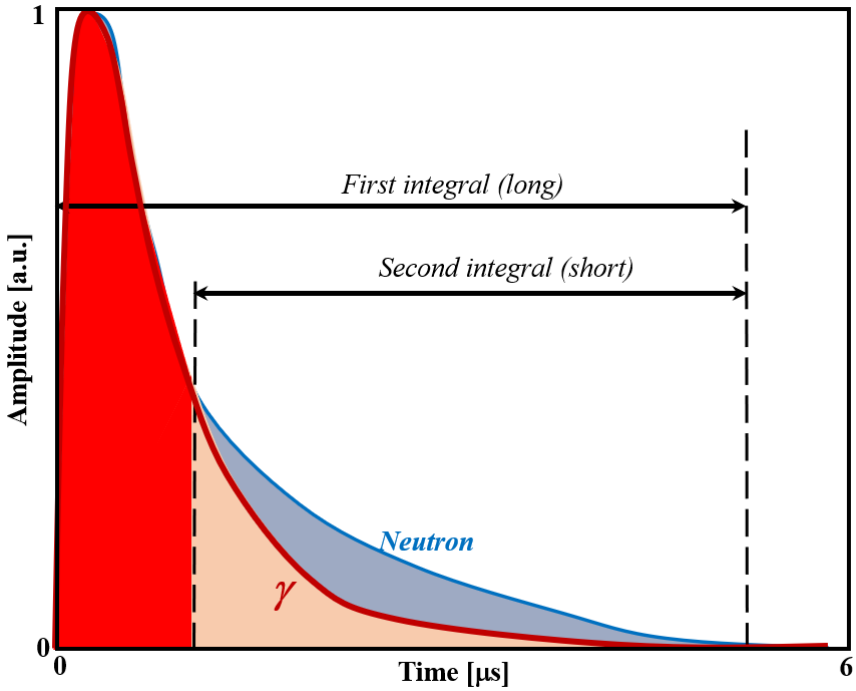


Figure 2.12: A schematic, qualitative illustration of the different signal shapes produced by a neutron and a $\gamma$ ray in a generic detector. The two interval of integration over the time are also shown.

radiation into the detector, produces a signal, which is integrated over two different time

intervals: the first is known as long integral, the second is known as short integral. The former, refers to the area of the whole pulse, whilst the latter considers only part of the signal tail. The first extreme of the long integral, is the starting point of the signal while the final extreme is the end of the signal itself. The short integral has the same endpoint as the long integral, however, its starting point is variable and can be adjusted in such a way as to set the best discrimination parameter. This value depends on the detector used and its electronics. As the impulse decays more slowly for neutrons, the short integral will be greater for the same long integral in comparison with that of the gamma, thus producing a different short/long ratio for neutrons and gammas.

### 2.4.2 Pulse gradient analysis

Pulse Gradient Analysis (PGA) [46] focuses on the comparison between the amplitude of the peak of a certain signal and the amplitude of the same signal acquired after a certain time scored from the peak itself. The former, is known as Peak Amplitude, while the latter is known as Discrimination Amplitude. The time interval that regulates this amplitude selection depends on the characteristics of the detector. The original signal is generally filtered before performing the operations mentioned to minimize the influence of electronic noise on the signal quality. A pulse induced by a neutron has a greater

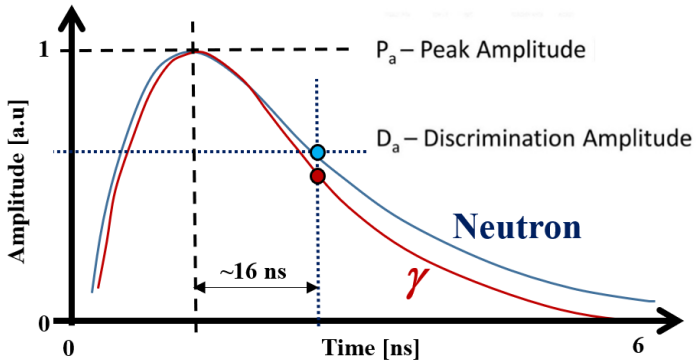


Figure 2.13: A schematic, qualitative illustration of two different signals produced by a neutron and a $\gamma$ ray. The different Discrimination Amplitude, key parameter in the discrimination of these two particles, is highlighted.

discrimination amplitude than the peak amplitude, compared to a range, due to a decay rate lower than the slow component of the signal.

Compared to other PSD methods, PGA algorithms are fast, require very little calculation capacity, so they are particularly suitable for *real-time* analysis and in a scenario when the user has to deal with a complex apparatus equipped with many detectors. The parameters of the algorithms can be optimized to obtain the best discrimination according to the type of light emission of the scintillator and the response of the photodetector used.

# Chapter 3

# Neutron imaging

## 3.1 Generalities

Neutron imaging is a huge field which comprises several different techniques that use neutrons to obtain internal images of objects or to probe samples in order to study specific features. Examples of neutron imaging methods are neutron radiography, neutron tomography, neutron phase imaging, small angle neutron scattering, thermal neutron holography and neutron-based magnetic resonance imaging[1]. In this particular chapter, neutron imaging refers to neutron radiography and tomography only, since these are the techniques used in the research presented in this thesis.

Neutron radiography (NR) and tomography (NT) are well-established, non-destructive testing techniques used to evaluate the properties of the materials, components and systems without causing damage to samples under scrutiny. NT and NR are based on the same principles of the well-known X-ray imaging (X-ray CT). The difference between neutron imaging and X-ray imaging lies in the fact that neutron and photons interact differently with matter, thus providing different informations about the objects under investigation.

Depending on their energy, photons interact by means of photoelectric effect, Compton scattering and pair production, and the intensity of this interaction depends on the atomic number Z of the interacting element. On the other hand, when neutrons interact, they may undergo a variety of nuclear processes depending on their cross section, which in turn depends on their energy (figure 3.1). Among these processes, the most important are the elastic scattering, inelastic scattering, radiative neutron capture, induced fission and several nuclear reactions, such as (n,p), (n,d), (n,$\alpha$), etc. For some elements, moreover, the total interaction cross section is relatively high for low-Z elements (in particular hydrogen-rich compounds, helium, boron and lithium) and, as a matter of fact, the neutron tomography can be complementary to the X-ray or $\gamma$-ray tomography achieved when imaging same elements.

[1] See, for instance, [47], for an overview of neutron imaging methods.

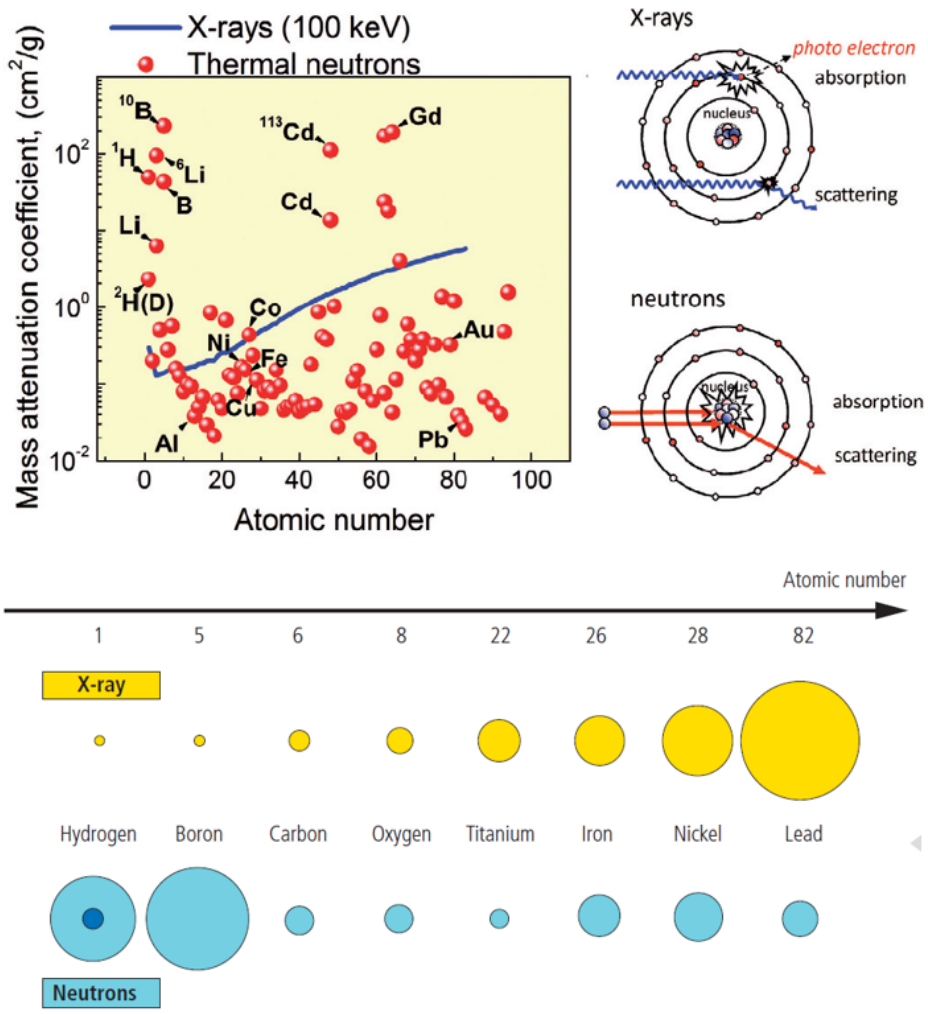


Figure 3.1: Top: Mass attenuation coefficients of thermal neutrons (0.025 eV energy) and X-rays (100 keV energy) against atomic number. Bottom: Qualitative comparison of X-ray and thermal neutron interaction cross sections for some elements. Images from [2, 48]

## 3.2 Fundamentals of radiography and tomography

The history of neutron radiography dates back to 1935, only three years after the discovery of the neutron. Kallmann and Kuhn [49] generated the first images using neutrons. Nowadays, neutron radiography is a well-established non-destructive method (NDT), thanks to the progress made in neutron detection, detector electronics, signal analysis and data processing methods. Yet, neutron imaging is still relatively far from its application on a large industrial scale. The main problem is due to neutron sources, which are relatively difficult to be produced on a large scale, or require special safety/regulatory procedures to be used.

### Sources, moderation and collimation

Neutron sources are of three types: accelerators, radioisotopes and nuclear reactors. Accelerators produce neutrons between $10^7$ and $10^{10}$ n/cm$^2$/s. Neutron generators fall into this category, and sometimes they can also produce $10^{11}$ n/s isotropically. Radioactive sources have lower fluency, approximately in the range of $10^5$-$10^9$ n/cm$^2$/s. On the one hand, they have the drawback of not having an on/off mechanism; however, on the other hand they have the advantage of being portable and being relatively simple to use. Nuclear reactors are the sources that provide the highest fluxes, in the order of $10^{10}$ - $10^{15}$ n/cm$^2$/s.

The majority of the aforementioned source, emit fast neutrons, therefore in the energy spectrum region that goes from about 1 MeV (fission neutrons) to up 14 MeV (neutron generators exploiting D-T reaction). Radiographs and tomographs are usually performed using thermal or epithermal neutrons, (0.025 eV - 10 keV). Consequently, the neutrons produced by these sources must be moderated. It is known that the most effective moderators are water, graphite, paraffin, polyethylene, etc. These slow down neutrons without great losses thereof, during the moderation process[2]. A schematic picture of a typical radiography or tomography system is given in figure 3.2.

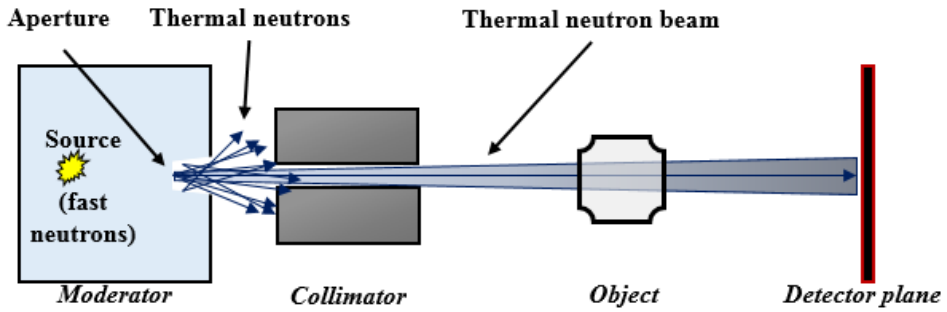


Figure 3.2: Schematic of a typical neutron imaging system. The detector plane is usually a scintillator screen, in the case of thermal neutron tomography.

Thermal and epithermal neutrons must be collimated in a beam that allow an object to be scanned. Since neutrons do not have an electric charge, they cannot be focused as electrons or protons or charged particles are. The best way to collimate them is simply to produce an aperture in the moderator and shielding, so as to direct the neutrons towards the collimator, which will have a certain design able to produce the desired beam-geometry. The collimator has to be be made with a high neutron capture cross section material, for example boron, gadolinium, or cadmium. Reflectors such as tungsten and lead can also be used.

The most common beam geometries are the cone beam, fan beam, and parallel beam, shown in figure 3.3 [50]. Geometries such as the parallel beam or the cone beam, have the advantage of producing radiographic images with a single exposure, while the fan

[2]One of the novelties of the research work presented in the results part is that no moderator is used, and only fast-neutron tomography is performed.

beam requires the scan of the object in such a way as to produce many projections, that, properly implemented in a reconstruction code, produce the radiographic or tomographic image. Fan beams are generally used in tomography rather than radiography.

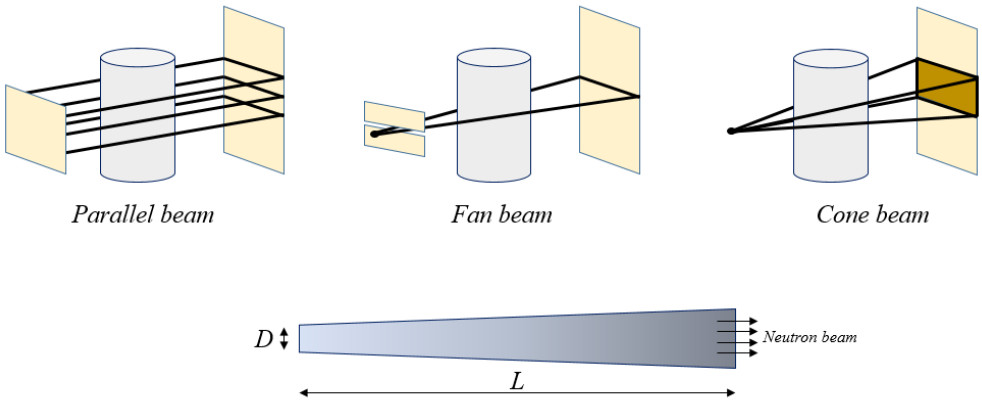


Figure 3.3: On top: illustration of the three possible geometry beam configurations: parallel beam, fan beam and cone beam. On Bottom: illustration of the beam divergence inside a collimator. L is the collimator length and D is the diameter or collimator aperture where the source is located (collimator gap).

The spatial resolution, assuming an ideal detector of infinite resolution and 100% efficiency, is fixed by the L/D ratio, which gives also an idea of the divergence of the beam. L is the collimator tube length and D is the source diameter or the collimator gap (Figure 3.3, bottom). The L/D ratio must be the highest achievable by the system. The ratio $\phi = L/D$ gives a quantitative indication on the divergence of a beam and is a fundamental parameter in radiography and tomography. The higher the L/D ratio, the smaller the horizontal and vertical divergence will be. A well collimated beam is synonymous with low divergence and this means high spatial resolution. In [50], it has been shown that values of L/D>70 produce acceptable radiographs. Currently, L/D values of several hundred to a thousand are available [51].

### Detectors

The choice of the detector depends on whether the tomography is carried out with fast neutrons or thermal/cold neutrons. The way to detect neutrons of different energies depends on the interaction probability, which is higher for low energy neutrons. This is the main reason why the majority of approaches in scientific literature exploit thermal, epithermal and cold neutrons, rather than fast neutrons. Generally speaking, all detectors for low energy neutrons use elements such as $^{6}$Li, $^{10}$B, and $^{nat}$Gd/$^{157}$Gd as converters for scintillation screens [52].

Most studies investigate the use of scintillation screens and charged-coupled devices (CCDs). In particular, scintillator screens in conjunction with CCDs or even with flat amorphous silicon detectors, have been widely used because of their shorter exposure times and faster read-out. CCDs provide a good signal-to-noise ratio, thus improving

the image quality. However, CCD chips suffer radiation damage if placed under the neutron beam, so they have to be placed in such a way as that the light coming from the scintillator screen is deflected by a mirror towards them, at usually $90^o$ out of the neutron beam [51, 53–55].

A different scenario arises when fast neutrons are to be detected. When the neutron energy range is in the MeV spectrum region, the absorption cross section drops, therefore detectors relying on converters are unsuitable for neutron detection, because of the low efficiency. Fast neutrons are relatively difficult to be detected, however they tend to be scattered by light isotopes. Organic scintillators are good candidates because of their sensitivity to fast neutrons. In particular, organic-liquid scintillators are sensitive to fast neutrons because they exploit the elastic scattering with hydrogen. Their main advantage is that they can be used in presence of mixed radiation fields, thus ensuring that pulse shape discrimination (PSD) techniques can be applied to discriminate pulses generated by different incident particles.

In the last decade, great improvements have been made in the research of new organic scintillation detectors; for instance, liquids with a high flashpoint and low toxicity, such as EJ-309 [56]. These, coupled with the advent of fast electronics for real-time PSD [16, 17], have made this technology suitable for use in industrial environments [56, 57].

As a matter of fact, the potential to perform combined acquisition of both neutron and $\gamma$ ray events, which has not been explored extensively yet, emerges because organic scintillators detect both.

## 3.3 Neutron tomography/radiography: *state-of-the-art*

Neutron radiography and neutron tomography have been investigated for over seven decades [51]. During the last forty years, thanks to important improvements in image reconstruction algorithms, the advent of calculators and computers, as well as improvements in neutron detection and digital data treatment, neutron tomography has been consolidated as a non-destructive testing (NDT) technique. The vast majority of neutron NDTs are carried out making use of neutron imaging facilities across the world. They are almost all located in close proximity of nuclear reactors, particle accelerators and spallation neutron sources [58]. This is mainly due to the requirement of having high neutron flux in order to achieve a good quality image and acceptable spatial resolution [59]. The flux densities at the sample position available nowadays range from $10^6$ $cm^{-2}$ $s^{-1}$ to about $10^9$ $cm^{-2}$ $s^{-1}$ in modern instruments [51]. Because of the complexity to access these facilities, the feasibility of performing neutron tomography is mainly restricted to scientific and research purposes. Several studies have been focused on the development of mobile and transportable systems for neutron radiography and/or tomography [11, 12, 60]. All these works make use of neutron generators as the radiation source. The use of compact neutron generators has the advantage of offering an on/off switching mechanism for the emitted neutrons. However, the use of such devices still limits the portability of the tomography system as a consequence of their weight and sometimes of their high neutron flux generated, which requires particular health and

safety regulations. In the last ten years huge progress has been made to make neutron generators smaller and portable. The portability of the system is therefore mainly determined by the radiation source. Portable neutron sources, which are also relatively inexpensive, are restricted to isotopic radiation sources such as, for instance, californium-252, americium-241/beryllium and few others americium-related sources. The disadvantages are that they might have relatively low neutron fluxes, they do not have any on/off switching mechanism and they have to be properly shielded. With this regards, the design, construction and commissioning of a portable system for fast neutron tomography, using $^{252}$Cf as a source, is presented in [31]. This particular research is strictly related and set the basis of this Ph.D. work. This particular system is based on the use of real-time pulse-shape discrimination in 7 organic liquid scintillation detectors. The $^{252}$Cf source used has a neutron emission rate of $1.5{\cdot}10^7$ per second into $4\pi$ and the exposure time of the system is approximately 2h. The applications of neutron tomography range from archaeology, geology and chemistry, to material science, engineering, nuclear energy, homeland security and contraband detection. The following sub-paragraphs present some examples of the most remarkable research that can be found in literature, showing the current *state-of-the-art* of neutron radiography and tomography in several fields.

### 3.3.1 Material science and engineering

Neutron imaging is mostly applied for material science purposes [48] and for the engineering industry. Neutron tomography is usually used to identify the presence of corrosion or defects in metal components, measures of hydrogen concentration, liquid flow visualization in pipes, imaging of fuel cells, waste packages, reinforcing internal structures and so on.

Most research works, as already stated, use thermal neutrons or even ultracold neutrons, because of their high capture cross section in some isotopes such as $^6$Li and $^{10}$B, used in neutron converters. Pioneering work is lead by Paul Sherrer Institute [2], in Zürich, at the neutron imaging facility of the spallation source SINQ [61]. Figure 3.4 shows three different steps of a ultracold, real-time radiography of a coffee machine. The plastic components of the machine, the coffee and the water, being materials with a high hydrogen component, absorb or deflect neutrons, resulting in a high attenuation index and therefore in a high image contrast. On the contrary, the metal components of the machine, mainly aluminium or steel, are relatively "transparent" to neutrons.

In [62], neutron tomography is used to estimate the hydrogen concentration in metal castings, in order to measure the degradation of some metal alloy properties, such as the loss of ductility. In this work, a scintillator screen and a CCD camera is used as detector whereas a 2MW research reactor is used as a source of thermal neutrons. Internal corrosion of in-service turbine blades is measured with NT in [63]. Once again, a 2MW research reactor is exploited to generate a thermal neutrons flux. Defects in aircraft parts have been explored with neutron imaging in [64–66] and internal fluid flows have been imaged in [67, 68]. [30] explores heterogeneities in concrete, such as reinforcement

structures, measuring the variation of transmitted fast-neutron flux. [69] was one of the first, about two decades ago, to investigate neutron radiography to image the water gradient in fuel cells. In [70] advancements and the potential of neutron imaging for fuel cells are discussed. Finally, a recent, interesting work [71], carried out at the NECTAR facility [3] in Germany, presents also the potential to image a package of low radioactive waste.

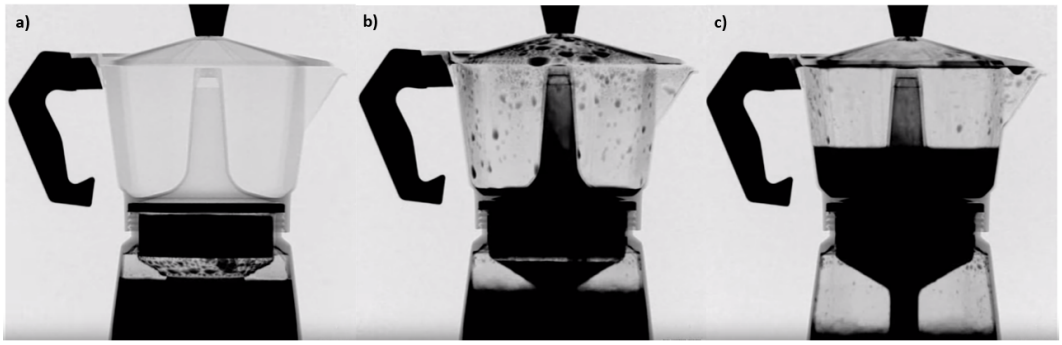


Figure 3.4: Three stages of a real-time, ultracold neutron tomography of a coffee machine, Paul Sherrer Institute [2, 72].

### 3.3.2 Palaeontology, archaeology and cultural heritage

Neutron imaging is also widely used for the characterization of archaeological samples. For instance, [73] describes the use of neutrons and X-rays to visualize archaeological objects in blocks of soil and [74] to characterize archaeological glasses. [75] describes studies of the inner morphology of a bimetallic Chinese sword of the 1st century BCE; [76] uses nCT to look into the tooth structure of a pelycosaurs (one of the most primitive mammals). [77] uses neutron tomographic analysis to ascertain the truthfulness of coins from Ancient Greece. In this regards, it has to be highlighted the remarkable research done by the ANSTO/DINGO [4] facilities in Australia, which are making neutron imaging a key analytical tool as a non-invasive approach in fields such as cultural heritage, archaeology and conservation science [78, 79].

### 3.3.3 Geology

Since neutrons interact mainly with low atomic number materials, in particular hydrogenous compounds, they are exploited in geology mainly to highlight the presence of water or hydrocarbons in rocks [80–83]. Neutron tomographs are often compared and studied with X-ray CTs. In particular, in [84], borehole rock samples are investigated. This work shows how thermal-neutron tomography can be inappropriate when imaging high density or thick samples (Figure 3.5). However, in a scenario in which the sample has relatively low density, thermal neutrons remain the preferred way to probe these materials. For instance, [85] shows an interesting comparison on how thermal neutrons can clearly highlight the presence of water in sand and limestones, in contrast to what arise using X-rays. The use of thermal neutrons is widely spread, whilst, as it happens

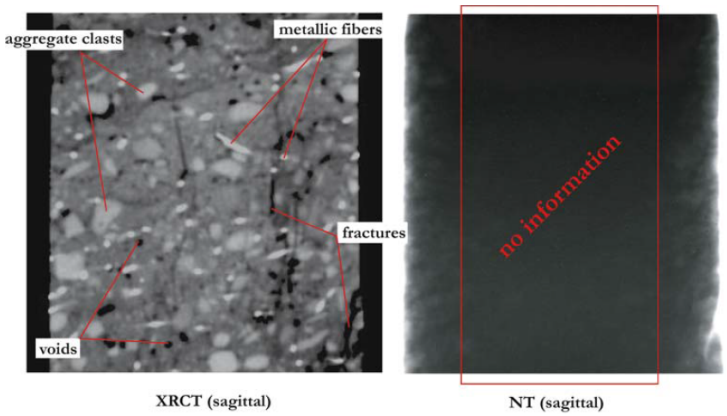


Figure 3.5: On the left: X-Ray CT of a fractured rock sample. On the right: thermal neutron CT of the same rock sample. n-CT is poorly resolved due to inadequate sample dimensions: neutron do not penetrate the sample do to the presence of hydrate species within the rock matrix. Image from [84].

in many other fields, fast neutrons are not intensively studied, yet. With this regard, one of the main objective of the Ph.D. research presented in this thesis is based on the use of fast neutrons, which can deeply penetrate high density materials.

### 3.3.4 Chemistry and biology

Carbon, hydrogen and oxygen are the most abundant elements in organic materials, and therefore in biological tissues. Since low-Z elements scatter neutrons more than any other nuclei, hydrogen, in particular, is the principal factor of neutron contrast in biological materials. Current probes in medical imaging comprise X-ray tomography and radiography, ultrasound, positron emission tomography (PET), magnetic resonance imaging (MRI) and so on. They all have specific functions, different from each other that make them unique and highlight different characteristics, such as blood flow, metabolic functions, bones, etc. Nowadays, thermal neutron imaging has reached similar spatial resolution and it is competitive with these techniques since, in many cases, it is able to visualize different elemental and isotopic contrasts [47].

Thermal neutron imaging is widely spread to better understand the distribution of ions in lithium-polymers batteries [86–89], thanks to the high absorption cross section of $^{6}$Li. In this regards, a chapter of this thesis is dedicated to the research work carried out at Lancaster University, using fast neutrons to image a lithium ion battery of a laptop. Furthermore, neutrons are useful and have been used recently to image crystal growth and crystallographic structures and metal alloys [90–92].

### 3.3.5 Homeland security, contraband detection and nuclear safeguards

A considerable amount of research is reported in the scientific literature, presenting neutron-based techniques for security applications [7,93,94], detection of explosives [95–97], nuclear fuel and reactor-related materials [98–102] as well as special nuclear materials

(SNM[3]) [103–107].

However, none of these techniques are used routinely for safety and security inspection, despite their extensive development. The main reason is that, at the moment, several challenges still limit a large-scale industrial application of these techniques. For instance, the number of false-positive threats is still too high with respect to the number of checks, limiting thus the normal operational time of the inspections. Borders, airports and ports are, nowadays, the locations that raise major concerns because of the incredible amount of goods that pass through them every day. The possibility of placing a neutron inspection system is limited by the possibility to locate a neutron source in proximity of these locations. This means that either a small accelerator or a neutron generator (DD or DT) has to be placed in these environments. Therefore problems such as device size, weight, its general complexity, costs, as well as the inspection time above all, arise and have to be solved.

## 3.4 Combining neutrons and $\gamma$ rays

Neutron radiation can be used as complimentary and/or supplement tool to $\gamma$-ray computer tomography. Exploiting the different interactions of photons and neutrons in matter and combining them in a sort of cross-check it would be possible to discriminate between different materials, that would be hard to distinguish otherwise using only $\gamma$-ray tomography or only neutron-tomography. Photon-based tomographs are unlikely to discriminate between elements of similar density and underperforming when imaging low-Z materials. Neutron-based techniques, instead, are more likely to highlight low-Z materials, porous materials, and substances with high neutron reaction cross-sections, as it can be seen in figure 3.6. The union of these different features can lead to a better understanding providing both density and composition information of the object investigated. In [109] Monte-Carlo simulations have been carried out to examine the feasibility of a combined neutron-photon CT of a model container. In this particular research work, neutrons of different energies, coming from a neutron generator (2.5 MeV from the D-D reaction and 14 MeV from the D-T reaction) and $\gamma$ ray sources, such as 1 MeV, 6 MeV and 9 MeV, have been simulated with the aim to verify the application of this technology for security inspection. In a real scenario, this would imply the use of two different radiation sources for both neutrons and $\gamma$ rays. Moreover, the detectors simulated are an ideal array that retain all neutrons and gammas crossing the detector surface.

In [95, 111], a feasibility study conducted by the Missouri University of Science and Technology has developed a combined neutron - X-ray radiography system for explosive detection and homeland security applications, with focus on concealed material detection. The work [8] is remarkable, a fast-neutron and $\gamma$-ray interrogation system has been built for air cargo containers, thanks to a collaboration between the International Atomic Energy Agency (IAEA) and the Commonwealth Scientific and Industrial Re-

[3]SNM are radioactive materials, fissile materials, and other materials associated with nuclear weapons.

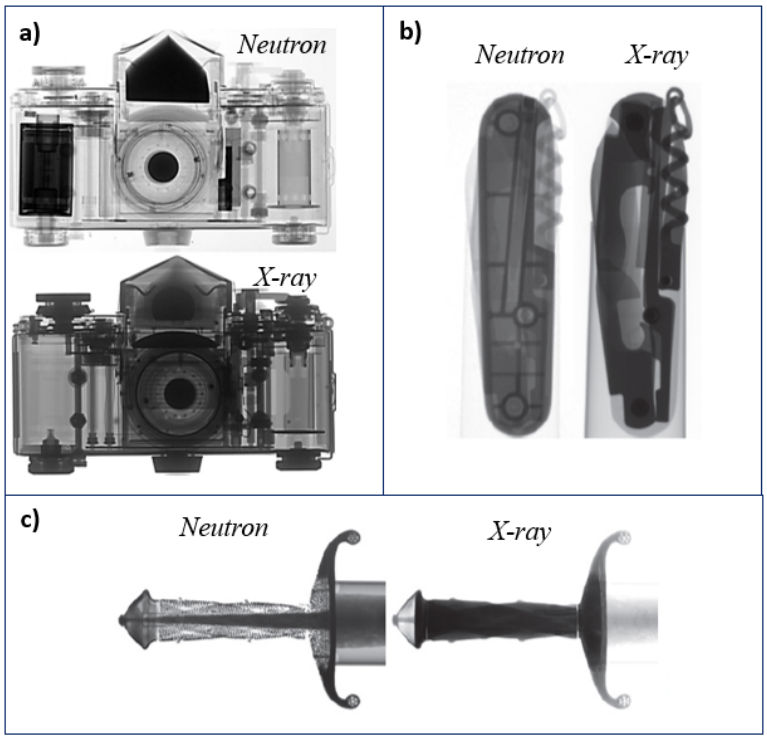


Figure 3.6: Comparisons of thermal neutron radiography and X-Ray radiography of a) a camera, b) a Swiss knife and c) a sword. These images, taken from [2], are some results extracted from the pioneering work (see also [108,110]) in thermal and ultracold neutron tomography carried out at the Paul Scherrer Institute.

search Organisation (CSIRO). The trials of this system were successfully conducted for the Australian Government at Brisbane airport and showed that high resolution image for both X-ray and fast neutrons can be obtained. This system is based on a dual energy X-ray source of 2.4 GBq $^{60}$Co (3 and 6 MeV) and a DD neutron generator, with a neutron yield of $2\times10^{10}$n/s.

Several other research works investigated the potential of combined neutron-photon imaging [93,112–115], with application mostly for homeland security, but also to image lithium-batteries in order to understand their degradation and performances [116].

However, none of the aforementioned works consider the use of the same radiation source to produce an acceptable flux of both neutrons and $\gamma$ rays, on the hypothesis that they can be detected simultaneously at the same time, by the same detector system.

## 3.5 Focus on: image reconstruction

Tomography techniques are now fundamental for medical diagnostics and, more generally, for a wide range of non-destructive testing. Image reconstruction starting from the data acquired from the instrumentation has been a mathematical problem for several decades.

The reconstruction process consists on the identification of the spatial distribution of a quantity in a plane-section. This is implemented starting from the measure of pro-

jections, namely the integrals of the distribution function along straight lines of different directions, and acquired by rotating and translating the section under examination. The generation of projections is described mathematically by the Radon Transform while the inverse problem, i.e. the tomographic reconstruction, can be solved via two different approaches: analytically, via filtered back projection algorithms (FBP) or algebraically, via algebraical image reconstruction algorithms (ART). To obtain sufficiently detailed reconstructed images is a problem present in all diagnostic imaging methods. This depends on the imaging systems, that have intrinsic resolution limits linked to the physics of the processes involved and to the detection system. These problems are mainly due to the low signal-to-noise ratio, detector efficiency and size. Therefore, a mathematical model able to elaborate correctly the acquisition of experimental data and its insertion within the reconstruction algorithms, is a crucial point.

Conventionally, a projection data representation of the object under examination is the sinogram: a two-dimensional image in which the position of the detector is represented in one axis, against the angular positions of the detector in the second axis. Given a sinogram $s$, the problem is ascribable to identify the distribution of $f$ in the section of interest.

In Computed Tomography (CT), the rotation (scan) of the entire radiation source and detectors around the axis of an object (or the rotation of the sample under examination around its axis, depending on the frame of reference), records a set of projections resulting from the radiation passing through the same direction in different sections. The irradiated section of the object is treated as a function, called the density distribution function, that has to be found by methods of reconstruction. Reconstruction methods can be divided into two categories: analytical and iterative, as shown in the scheme of figure 3.7, each of them with its own advantages and drawbacks. In this particular

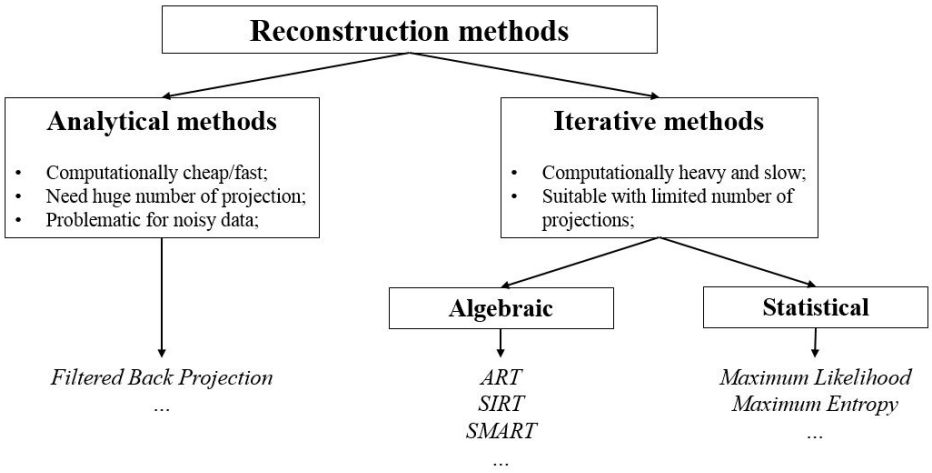


Figure 3.7: Schematic classification of the different groups of image reconstruction algorithms.

section, filtered back projection and algebraic reconstruction, will be described. The former, is probably the most common and used method in image reconstruction (particularly in the medical field) and indeed it is as historically important as mathematically

elegant; the latter instead, is rather "effective" and it adapts easily to different geometries. Iterative methods are the type of algorithms used in the research presented in this thesis, the motivations for this particular choice are given in the next sections and chapters.

### 3.5.1 Filtered back projection

Let us consider a section of an object with unknown density distribution $\mu(x, y)$. By definition, a projection of a two-dimensional function is a set of line integrals. The Radon Transform (RT) is the mathematical tool used to perform a series of line integrals through $\mu(x, y)$. Therefore, RT can be applied to compute projections of the density distribution $\mu(x, y)$, along a specified direction, as per:

$$p(\xi, \phi) = \int \mu(x, y)\delta(xcos\phi + ysin\phi - \xi)dxdy \tag{3.1}$$

where $p(\xi, \phi)$ is the Radon Transform of $\mu(x, y)$. $\delta$ is the Dirac Delta function, $\xi$ is the offset and $\phi$ is the rotation angle, as defined in figure 3.8. The function $p(\xi, \phi)$

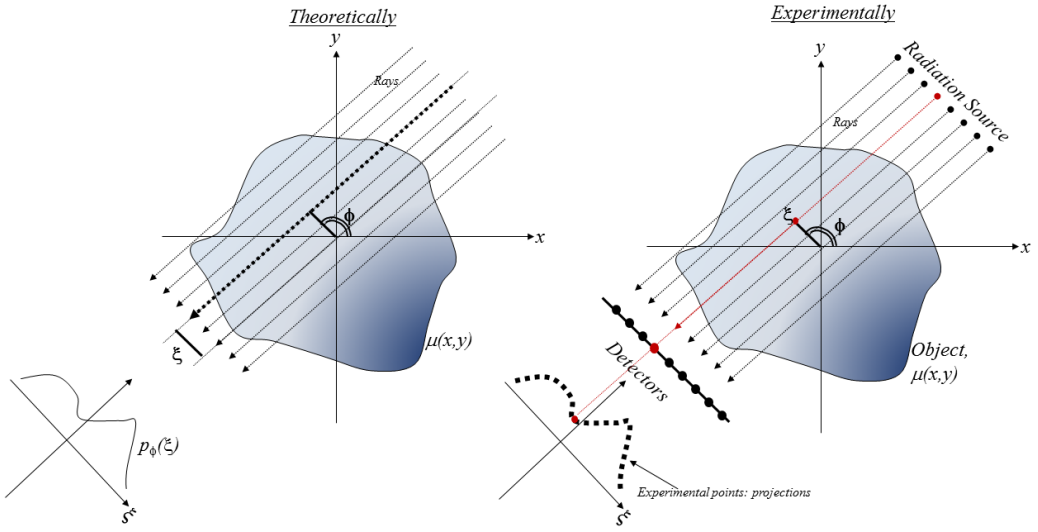


Figure 3.8: Schematics of the radon transform of a generic object with cross section depending on the unknown attenuation $\mu(x, y)$. The Radon transform in this picture represent the calculation along a line, at a fixed angle $\phi$ and a distance $\xi$ from the origin. On the left, the mathematical fundation are pictured, whereas on the right, a theoretical transposition in a experimental scenario, is shown.

is called *sinogram* and the goal of tomographic reconstruction is to find $\mu(x, y)$, given knowledge of $p(\xi, \phi)$. Figure 3.8 shows also an analogy between theory and experiment: in fact, experimentally, the projections are the set of detector readings per position and rotation angle of the system source-detectors (or sample position, depending on the frame of reference used). For instance, taking into account as radiation source neutrons or photons (X-/$\gamma$ rays), the interaction probability of such radiation in matter is identified by the linear attenuation coefficient of the material ($\mu$), which is, considering

a section, a dual-dimensional function, and can be identified as the density distribution $\mu(x, y)$. As seen in chapter 1, the intensity of the radiation suffers an exponential decay described by the attenuation law (also known as Beer-Lambert law).

$$I(x, y) = I_0 \cdot exp\left(-\int_{path} \mu(x, y) \cdot ds\right) \tag{3.2}$$

Simply, in the one-dimensional case, it becomes:

$$I = I_0 e^{-\mu x} \Leftrightarrow \mu x = ln\frac{I_0}{I} \tag{3.3}$$

$I_0$ is the initial intensity of the radiation, whereas $I$ is the final, $x$ is the distance travelled by neutrons or $\gamma$ rays. The logarithmic ratio $ln(I_0/I)$ is known as one-dimensional projection of the body in the direction of the incident radiation.

Known the sinogram $p(\xi, \phi)$, the task of measuring $\mu(x, y)$ can be achieved applying the so-called back-projection operator to the sinogram. It propagates the measured sinogram into the image space along the projection paths. Mathematically:

$$\mu_{BP}(x, y) = \int_0^{\pi} p(\xi, \phi) d\phi = \int_0^{\pi} p(xcos\phi + ysin\phi, \phi) d\phi \tag{3.4}$$

The image reconstruction is then reduced to the solution of integral 3.4, which is a numerical process performed with the help of a computer. A huge amount of algorithms are available in literature, all based on the fact that applying the Fourier transform of the projections $p(\xi, \phi)$, the space frequency distribution of function $\mu(x, y)$ is obtained. Within the computer algorithms used, frequency filters are also applied, in order to clean the image from the noise and achieve a good image contrast. A general, illustrated scheme of the FBP algorithm is shown in figure 3.9, using as an example the famous Shepp-Logan phantom.

### 3.5.2 Algebraic reconstruction techniques

Algebraic Reconstruction Techniques (ART) were introduced by Gordon, Bender and Herman in 1970 [118]. They solved the problem of 3-dimensional reconstruction applied to electron microscopy and radiology. The problem, analogous to the aforementioned FBP, consists of finding the density distribution function by discretising the irradiated sample section, into a matrix of unknowns. The elements of such a matrix correspond to the pixels of the image. Therefore, they represent a discretization of the density distribution function $\mu(x, y)$ (Figure 3.10). In this representation, a ray corresponds to a band that mostly coincides with the width of one pixel. The solution of the reconstruction algorithm assigns to each unknown, therefore to each pixel, a numerical value, which corresponds approximately, to the density function distribution in that particular region of space, delimited by the pixel. The more matrix elements are present, the better spatial resolution can be achieved, however, the more projections are needed to solve the unknowns.

Figure 3.10 illustrates the principles of ARTs. The large square area is a two-

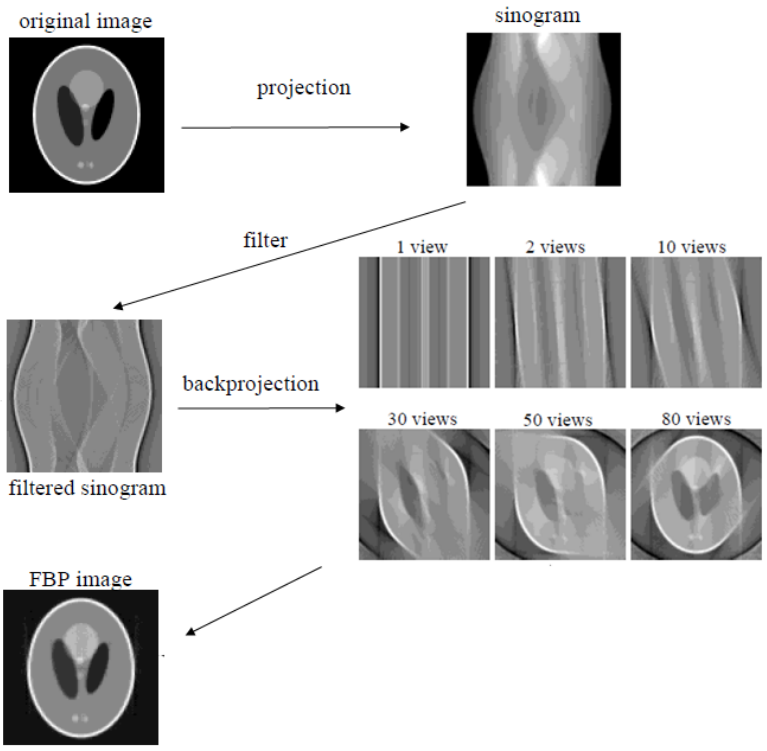


Figure 3.9: Scheme of the Filtered Back-Projection algorithm applied to the Shepp-Logan phantom. Image extrapolated from [117].

dimensional matrix of dimension $M \times M$ pixels and $M \times M = N$ elements. A generic, parallel radiation ray $R_j$ traverses the object (shaded area) of density function $\mu(x, y)$ through the area $A$, and it generates the measurement or the projection $p_j$ at the detector. The total set of unknown pixels $N$ can be expressed as a vector column $\mu$. Such a vector describes the pixel values of the section of the scanned sample. The shaded parts of the square elements of the matrix constitute the region of the image subtended by the j$^{th}$ parallel ray. Defining

$$w_{ji} = \begin{cases} 1 \text{ if the centre of the i}^{th} \text{ square lies in the j}^{th} \text{ ray;} \\ 0 \text{ otherwise.} \end{cases}$$

and generalizing to all the rays (projections), the so-called *projection matrix* $\mathbf{W}$ "can be built". Each ray $j$ = *1,...L* with $L$ = total number of projection, generates a row of *i=1,...,N* elements, creating in this way its elements $w_{ji}$. The matrix $\mathbf{W}$ is a linear operator that describes how the vector $\mathbf{p}$, containing the projection data, depends on the unknown image pixels:

$$\sum_{i=1}^{N} W_{ji} \cdot \mu_i = p_j \tag{3.5}$$

which written in vectorial form becomes:

$$\mathbf{W}\boldsymbol{\mu} = \mathbf{p} \tag{3.6}$$

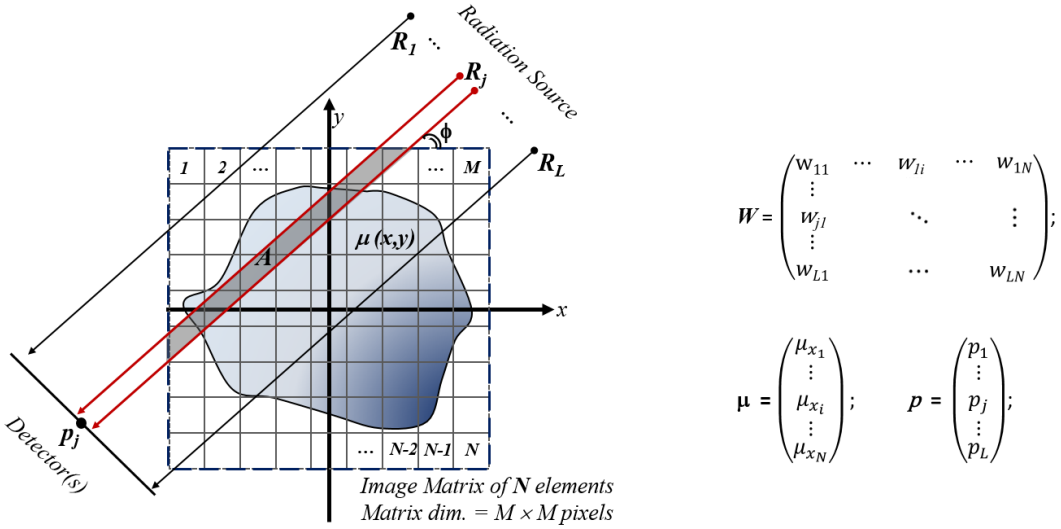


Figure 3.10: Discretization of the irradiated section.

The multiplication of $\mathbf{W}$ with the vector $\mu$ is called *forward projection* (FP) whereas the multiplication of $\mathbf{W}^T$ with the vector $\mathbf{p}$ is called *back-projection* (BP). The values of $\mathbf{W}$ must be specified accurately, and depends on the geometry of the scanning system [119]. An image can be reproduced inverting the matrix operator $\mathbf{W}$, applying it to the projection data, as per

$$\boldsymbol{\mu} = \mathbf{W}^{-1}\mathbf{p}. \tag{3.7}$$

$\mathbf{W}$ is strongly sparse, due to the geometry of projections,and its size can be enormous. For instance, with the hypothesis of reconstructing the section of an object with a texture of 128 × 128 pixels, the number of columns of W would be 16384. With the hypothesis of scanning the object with 1 degree step in 360 degrees, and with the assumption of having, say, 10 detectors, the number of projection data would be 3600 (360 view × 10 det.), therefore $\mathbf{W}$ would become a 16384 × 3600 matrix, which is clearly non-invertible. An algebraical reconstruction algorithm aims to solve equation 3.7 via iterative techniques which are based on different steps: creation of the initial image, calculation of the corrections, patches and application of the convergence test. The most used algebraic algorithms are the Simultaneous algebraic Reconstruction technique (SIRT, [120]), the Multiplicative Algebraic Reconstruction Technique (MART) and the Simultaneous Multiplicative Algebraic Reconstruction Technique (SMART). They only differ with each other on the way corrections are applied.

An example of the basic ART is given in below:

$$\boldsymbol{\mu}'_{k+1} = \boldsymbol{\mu}'_k + \lambda \cdot \mathbf{W}^T \cdot \frac{\mathbf{p} - \boldsymbol{\mu}'_k \mathbf{W}}{\sum_{i=1}^{N} w_{ji}^2} \tag{3.8}$$

where $\lambda$ is a relaxation parameter (usually between 0 and 2), and $k$ the interaction step of the algorithm. The algorithm begins (first interaction) with an initial image array with N elements, arbitrary random or zero. It ends when a fixed ($\Delta\mu \leq 0.01\%$) convergence criterion is met.

# Chapter 4

# Monte Carlo methods: principles and applications

The term Monte Carlo (MC) method can be used to define any numerical technique that uses random number generators to solve a certain problem. MC methods have been known for a very long time. The first use of random numbers, for the resolution of integrals, dates back to 1777, when the theoretical foundation were laid by Georges-Louis Leclerc, count of Buffon, a French mathematician who reported in his book "Essai d'aritmetique morale" [121] its experiment on the use of random number simulation to estimate the value of $\pi$. By dropping a needle of length $L$ a huge number of times over a horizontal plane, on which a bundle of parallel lines had been drawn distant from each other $d$ (with d>L), it was possible to calculate the probability $P$ that the needle intersects one of the lines. Leclerc showed that this probability is $P = L\pi/2d$.

After about 150 years, in the early 1930's, Fermi developed a "statistical sampling" system to predict the results of its experiments on neutron scattering and absorption [122]. These processes are stochastic by nature, therefore it is perfectly legitimate to match a hypothetical sample constructed with random numbers, to the real sample. Ten years later, Ulam and Von Neumann, studied and extended Fermi's idea, while working on the Manhattan project to study the dynamics of nuclear explosions [123]. They have the merit of having independently rediscovered the MC method and, furthermore, they also have the merit of having shown its possibilities, potentials and physical applications.

Initially, the interest was more academic than practical since there were no computers and analogue devices built for this purpose were extremely slow. The advent of computers gave the decisive impulse to the use of MC techniques in large scale: it no longer represented only a mathematical curiosity but was an indispensable tool for scientific research. Computers are, in fact, able to perform long, complex calculations and, especially, are able to easily generate random numbers, which is the key point to implement a MC technique.

Nowadays, applications range the most varied fields of research, from nuclear physics to chemistry, from statistical and quantum mechanics to finance and economics.

## 4.1 Main principles

Imagine a problem in which a certain parameter $F$ of a defined ensemble (i.e. a real number, an array or a variable) has to be estimated . The Monte Carlo method is a technique that reproduces a sample of this ensemble with the purpose to extract from it a statistical estimate of $F$.

In the context of the research presented in this thesis, Monte Carlo methods are the ideal tools to reproduce a statistical process theoretically, such as the interaction of radiation and particles in matter. The probabilities of each event that the radiation can face in a physical system are simulated sequentially. The distributions governing these events are statistically sampled in order to describe the total process [124].. This consists of tracking each particle generated from a user-defined radiation source from its creation to its death, due to some physical process (e.g. absorption, escape, etc.). Each type of process has its own probability distribution which is randomly sampled using mainly transport data to calculate and visualize the particle's life evolution, at each step. The statistical sampling process is based on the selection of random numbers [124].

The use of the MC method depends on the modelling of the physical system studied. For example, the heat transfer equation described in Boltzmann transport law requires the use of MC as a numerical integrator, while the transport of a radiation beam through matter requires the use of the MC as a stochastic simulator. This particular instance can be taken to divide MC techniques into two categories:

1. **Numerical integration**: particularly useful in the case of multi-dimensional spaces. Let us consider as a simple example the calculus of an area of a figure of irregular shape. Suppose we have a square of side 1 with an irregularly shaped object inside it (figure 4.1). By generating random numbers uniformly distributed

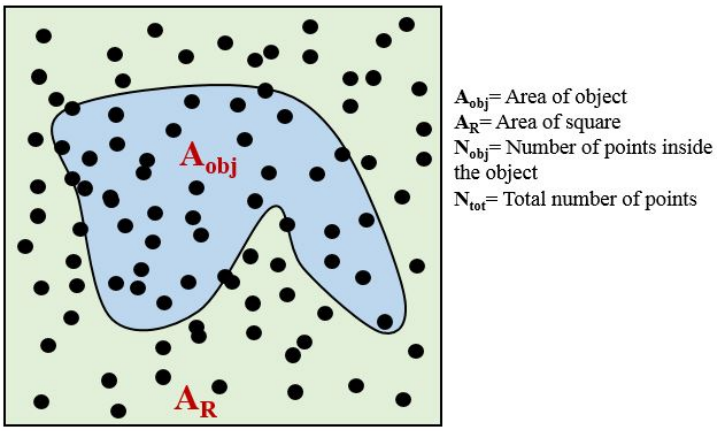


Figure 4.1: Illustration of the most common application of Monte Carlo method: the numerical integration. In this picture, a bidimensional (x-y) integration to calculate the Area of an irregular shape, is shown.

in the interval [0,1] and extracting pair of values (x,y), both uniformly distributed in the interval [0,1], it is legitimate to interpret (x,y) as the coordinates of a random point located inside the square. The Monte Carlo consist of generating $n$

points ($x_1$, $y_1$),..., ($x_n$, $y_n$) of this type and counting which are inside the object and which ones are outside. Thus, the area of the irregular shaped object inside the square will be given simply by:

$$A_{obj} = A_R \times \frac{N_{obj}}{N_{tot}} \tag{4.1}$$

The result of the MC is random, however it gradually tends to the theoretical result by increasing the number of points (events or histories) $n$ generated. It will be shown that the error estimation of a Monte Carlo simulation goes according to $1/\sqrt{n}$.

2. **Simulation of physical reality**: in this case, the MC attempts to reproduce in detail the physical process under examination. For instance, let us examine a neutron entering into a slab of some fissionable material, as shown in figure 4.2. Depending on the physics governing the material defined and the probability of the processes involved, the Monte Carlo selects randomly whether a certain process may occur or not. In this particular case, the neutron firstly scatters (event 1) and generates a photon, which is subsequently absorbed (event 7). The scattered neutron is diverted with a certain angle, selected randomly according the physical scattering distribution. Such a neutron undergoes fission (event 2), producing two more neutrons, which are respectively absorbed (event 3) and leaked (event 4). In addition, the fission produces a photon that firstly scatters (event 5) and then escapes the slab of material without any other interaction (event 6). All these events generated by an initial neutron are known as "history". More histories increases the statistics, improving the knowledge of the neutrons and photon distribution of the process described. Particles can also be tracked one-

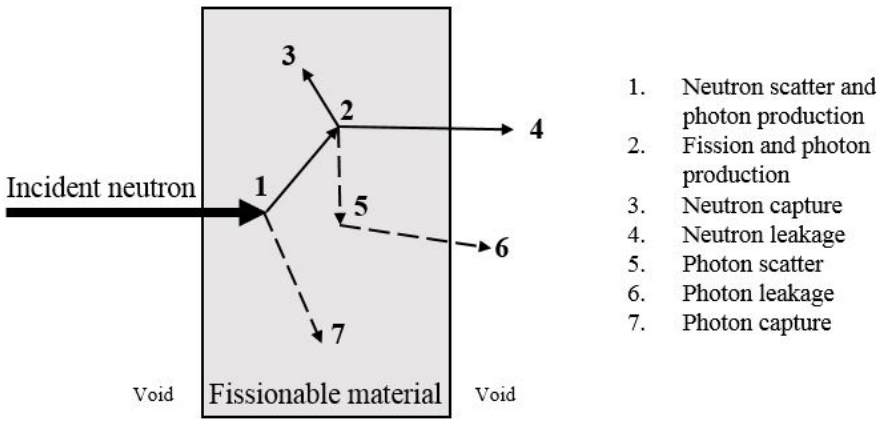


Figure 4.2: An illustrative example of a possible neutron history inside a fissionable material. Figure from [124].

by-one and step-by-step. After a reasonable statistics are achieved, the correct information can therefore be estimated. Quantities such as surface current, surface flux, volume flux, particle and fission heating, energy or charge deposition, can be

tallied along with their respective uncertainties.

### 4.1.1 Monte Carlo integration, estimators and errors

Thanks to calculators, the existence of generators of random or pseudo-random numbers allows the use of stochastic techniques for the integration of functions. For instance, let us consider a certain quantity $I$ that has to be determined with the following integral:

$$I = \int_a^b h(x)dx \tag{4.2}$$

where *h(x)* is a function of real variable, defined in the domain $[a, b]$. Defining the function *g(x)* as per

$$g(x) = \begin{cases} \frac{1}{b-a} \text{ if } a \leq x \leq b; \\ 0 \text{ elsewhere;} \end{cases} \tag{4.3}$$

integral 4.2 can then be expressed as

$$I = (b-a)\int_a^b h(x)g(x)dx. \tag{4.4}$$

Function $g(x)$ represents a uniform probability distribution in the interval $[a, b]$. This integral represents, by analogy with the statistics theory, the expected value of *h(x)*, with $x$ random variable distributed according to *g(x)*. This technique requires that $a$ and $b$ are finite. However, it can be shown[1] that, through appropriate change of variables, it is valid also for infinite integration intervals, as follow:

$$E_g[h(x)] = \int_X h(x)g(x)dx \tag{4.5}$$

where $E_g[h(x)]$ denotes the expected value. Making use of the law of large numbers[2] it is legitimate to use as estimator of the expected value $E_g[h(x)]$ of *h(x)*, the quantity:

$$\bar{H} = \frac{1}{n}\sum_{i=0}^{n} h(x_i) \tag{4.6}$$

As $n$ increases, $\bar{H}$ converges to $E_g[h(x)]$.

This method allows also to integrate some functions that have discontinuity points and singularities. However, this method is efficient only for functions that do not vary much across the integration interval. Since the integration interval is sampled uniformly, the risk of not exploring some intervals with the proper level of detail, arises. For instance, this may happen when the integrating function assumes very large/low values, which obviously make a great/small contribution to the integral. In these cases, other Monte Carlo techniques, not treated within this thesis, are required. In the case that the function is not particularly complex, this technique gives quite reliable results, and

[1] This demonstration goes beyond the scope of this work.

[2] The law of large numbers states that as the number of trials of a random process increases, the percentage difference between the expected and the average of the results obtained, tends to zero.

it can be indeed generalized to multiple domains.

Since the estimator shown in equation 4.6 tends to $E_g[h(x)]$ in the limit $n \to \infty$, the probability distribution of $\bar{H}$, according to the Central Limit Theorem[3], tends to a Gaussian of average $\mu = E_g[h(x)]$ and variance $\sigma^2/n$, where

$$\sigma^2 = \int_{-\infty}^{+\infty} [h(x) - \mu] g(x) dx \tag{4.7}$$

is the variance of *h(x)*. The Monte Carlo method, therefore, gives an estimation of $\mu$ equal to

$$\bar{H}_n \pm \frac{\sigma}{\sqrt{n}} \tag{4.8}$$

where the range of variability corresponds to a confidence interval of one standard deviation ($1\sigma$), i.e., for $n$ relatively high, $\bar{H}_n$ has a probability of 68.26% of being in the range $[\mu - \sigma/\sqrt{n}\ ;\ \mu + \sigma/\sqrt{n}]$

The value of $\sigma$ is not usually known, but it can be evaluated from the Monte Carlo itself through the estimator

$$S_n^2 = \frac{1}{n}\sum_{i=0}^{n} h^2(x_i) - [\frac{1}{n}\sum_{i=0}^{n} h(x_i)]^2 \tag{4.9}$$

The quantity $S_n/\sqrt{n}$ is known as the *statistical error*. The procedure of evaluating expectation values and integrals described in this particular section, is called *Analog Monte Carlo*. Such a method has the drawback that the statistical error decreases slowly, as $1/\sqrt{n}$ when $n$ increases. To halve the statistical error means to quadruple the sample size. The solution to this issue are the so called *variance reduction techniques*: they reduce the variance without altering the expected value. Variance reduction techniques are based on a statistical method known as *Importance Sampling*, which consists of using a "more appropriate" distribution to generate the random variable. When these techniques are exploited the Monte Carlo becomes *Non-Analog*.

## 4.2 Monte Carlo methods in Physics and Engineering

Monte Carlo techniques are mainly used to simulate physical processes that generate a certain type of signal. For instance, to simulate neutron interactions inside a detector or with a certain type of material, to simulate physical processes that may "mimic" a signal, as the amount of light produced by neutrons and/or $\gamma$ rays in an organic scintillation detectors; to estimate the response of the detector to a certain type of radiation; to predict the outcome and feasibility of measurements and experiments and finally, to evaluate signal and background.

In physics and some engineering fields, the MC method is used in two steps:

1. **Simulation of the physical process**. This occurs with algorithms (called Event

[3]The sum or the average of a great number of random variables independent with each other tends to a normal distribution.

Generators) that generate events with specific characteristics and with a certain physics. They can be:

- Parametric: fast response, they are not built considering all the physics of the process, but simply considering data from other experiments.
- Complete: the physics of the process is defined: energy, dimensions, directions and sense of the particles to be generated, etc

2. **Detector simulation**. Three points are crucial in the simulation of the detector:

- Geometry: the geometry of the detector must be defined as much precisely as possible;
- Hits simulation: consists in the simulation of the response of the detector; as well as the definition of the boundary conditions, i.e. the definition of the sensitive part of the detector.
- Digitization: definition of resolutions, efficiencies etc.

The use of MC is fundamental to discover the sensitivity of an experiment a priori, and, for instance, to understand if it is worth building it and asking for funding.

The best codes on the market in terms of completeness and reliability are GEANT4 [125] and MCNP [126]. GEANT, a simulation tool kit developed by CERN, is mostly used for high energy, nuclear and accelerator physics, medical and space science. MCNP is treated with more detail in the next section.

In this thesis, MCNP is the tool chosen to perform Monte Carlo simulation. The main reason is that MCNP was developed particularly for neutron and photon transport, and their physics processes and interactions are described with particular level of detail.

## 4.3 Monte Carlo N-Particle: MCNP

MCNP is a general-purpose simulation code developed by Los Alamos National Laboratory [127], in particular for neutron, photon, electron, or combined neutron/photon/electron transport [128, 129]. Its applications are mainly for radiation protection and dosimetry, shielding evaluations, radiography, medical physics, detector design, nuclear physics, with a particular focus on fission and fusion physics, decontamination and decommissioning.

MCNP is based on a user-defined input file which contains all the specifications and information about the problem to be studied. The input code contains information such as system geometry; materials with their respective cross section evaluations; location, geometry and energy spectrum of neutron and/or photon and/or electron source; the type of tallies, namely the quantity that the user wants to study, number of histories to be generated and possible variance reduction techniques.

Neutron energies as well as cross sections and nuclear data for the vast majority of elements range from $10^{-11}$ MeV to 20 MeV, whilst photon energies range from 1 keV to 1 GeV. The nuclear and atomic data libraries are sourced primary from the Evaluated

Nuclear Data File [130] (ENDF) and the Evaluated Nuclear Data Library (ENDL). Nuclear data tables considered by MCNP comprise neutron and photon interactions, neutron-induced photons, neutron dosimetry, neutron activation and thermal particle scattering [128, 129]. The neutron interaction tables available apply to approximately 100 isotopes, whereas photon interaction tables are present from hydrogen (Z=1) to plutonium (Z=94).

### 4.3.1 Input file: an example

Figure 4.3 shows the structure of a general MCNP input file. The file is constituted by three parts: cell cards, surface cards and data cards. The title line begins the file and blank lines separate the three sections with each other. Cell, surface and data cards are lines of code limited to 80 characters. The system geometry is specified within cell and surface cards whilst radiation source, physics, materials, histories and tallies have to be defined within the data cards. Comments code are defined by the dollar symbol ($) or with the letter "C" in the first character of the line. The example of figure 4.3 describes

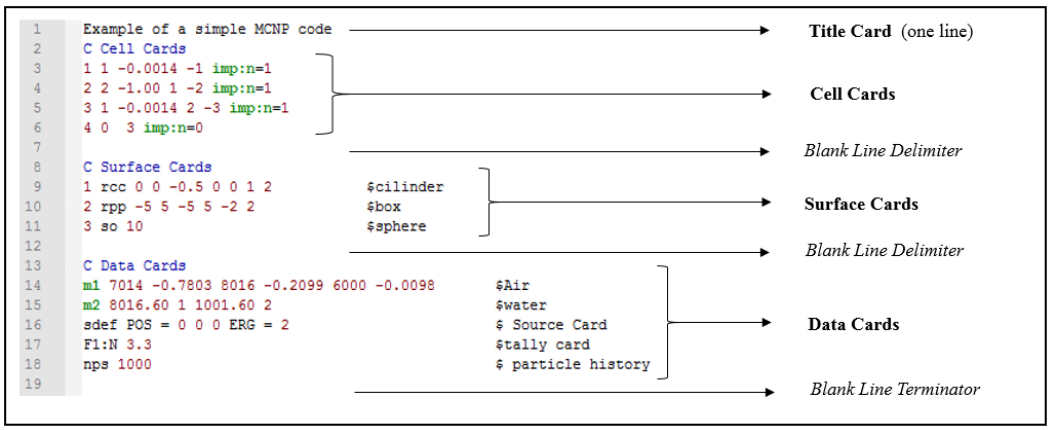


Figure 4.3: An illustration of the MCNP input file general structure.

a neutron source placed within an air cylinder in turn inside a water box. The water box is located in a sphere (world) filled with air (only nitrogen and oxygen are reproduced, other elements are considered negligible). Figure 4.4a shows the X-Z cross section of such geometry, plotted with the MCNP viual editor (VisEd). Herein is also shown an example on how the simulation evolves qualitatively, in terms of neutron-induced interactions. Figure 4.4b shows the collisions created by 100 neutrons generated. The collisions are mainly located in the water volume, which is perfectly reasonable due to the presence of hydrogen and oxygen that increase the probability for neutron scattering. Figure 4.4c instead, qualitatively and quantitatively gives an indication of all neutron scores over surface 3 (the sphere), as requested by the code.

### 4.3.2 Geometry specification: cell and surface cards

The cell and surface cards are strictly related with each other and together define the system geometry. Surface cards are inputs that, via user-defined shapes and volumes,

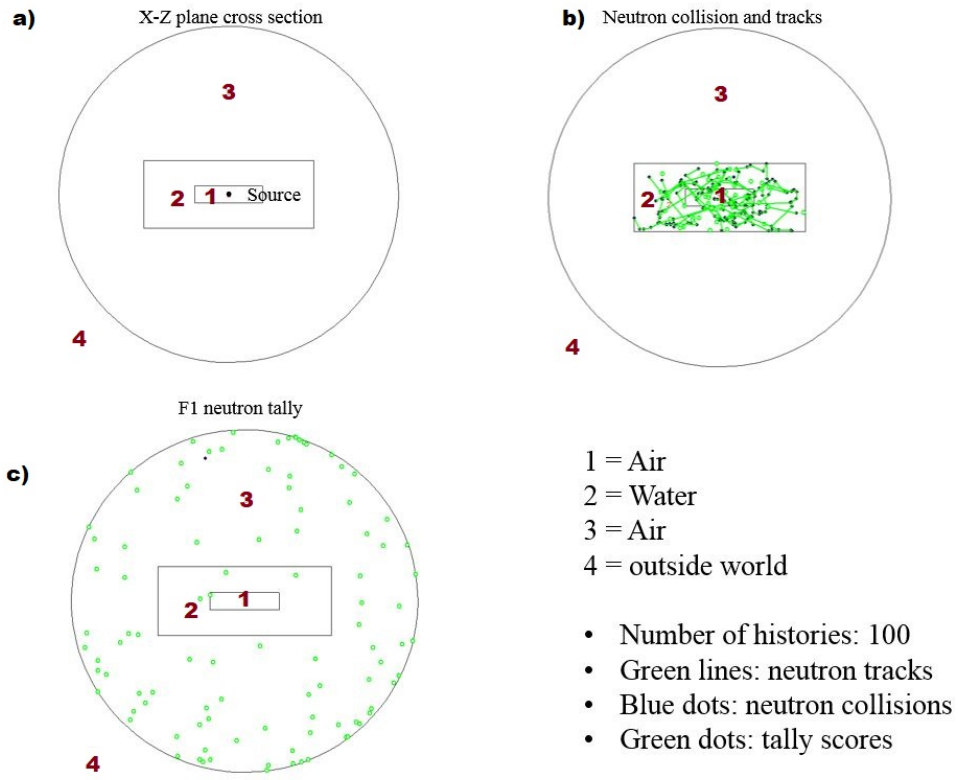


Figure 4.4: Three different ways of qualitative displaying geometry and output of an MCNP6 simulation. On top-left the geometry of the code described in figure 4.3 is shown; on bottom-left the tally scores across the surface of the sphere are pictured, wherease on top-right only neutron tracks and collisions are plotted.

serve to build the cells.

Cell card inputs are built including the list of surfaces bounding the cell itself. The cell number must be the first character that define and fix that particular cell; subsequently, cell material number and its density follow. Density can be expressed in terms of $10^{-24}$atoms/cm$^3$ (positive entries) or g/cm$^3$ (negative entries). Finally, following the geometry description, cell parameters, such as the "cell importance", can be defined. For example, taking into account the code presented in figure 4.3, the line

1 1 -0.0014 -1 IMP:N=1

means that cell 1 is made of material 1 (air), with density 0.0014 g/cm$^3$ inside the cylinder defined by surface 1. The sign '-'in front of the density value means that the units are g/cm$^3$, whereas the sign in front of surface number means that the material is confined "inside" the specified surface.

With regards to surface cards, as per cell cards, the first entry is the number which marks the surface itself. After this, an alphabetic code sequence, followed by a number that serves to define the surface equation, are requested. For instance, considering once again the example of figure 4.3, the line

1 RCC 0 0 -0.5 0 0 1 2

means that surface 1 is a cylinder (rcc) with base of coordinates XYZ of 0,0,-0.5 (cm), height vector with dimensions XYZ of 0,0,1 (cm) and radius 2 cm.

### 4.3.3 Data cards

Source, materials and tallies are the most important data cards. A wide variety of sources can be reproduced. By default, if not specified otherwise, the code generates neutrons.

#### Sources

The example of figure 4.3, indicates an isotropic, point neutron source of energy 2 MeV, located in the point of coordinates XYZ: 0,0,0, as per:

$$\text{SDEF POS} = 0\ 0\ 0\ \text{ERG} = 2.$$

MCNP allows the user to define the dimension and the shape of the sources, as well as its energy spectrum. The user can define energy range and probability distributions, or make use of some built-in functions such as Watt, Gaussian and Maxwellian distributions. In Appendix A an extract of the MCNP codes are presented for the americium-beryllium (AmBe) and californium-252 ($^{252}$Cf) neutron-gamma sources used in the research works presented in this thesis. Concerning the AmBe source, both neutrons and gamma probability distribution are user defined and the respective probabilities have been taken from the literature. Regarding the ($^{252}$Cf) neutron-gamma source reproduced, a Watt fission spectrum has been used, due to the fact that this distribution best reproduce the typical spontaneous fission neutron spectrum; whereas for gammas a user-defined probability distribution, taken from the literature and typical of californium-252, was used.

#### Material cards

Material cards have to be defined in order to specify elements or compounds that will be used in cell cards. The MCNP syntax is composed by two mandatory sections: material number and the elemental (or isotopic) composition. As an option, the user can specify the use of a particular cross section for each isotope defined. Isotopes and materials can be defined using atomic abundance or their mass fraction. The materials described in example of figure 4.3, are water and air. The air, which is defined with "m1" is reproduced using the mass fraction of oxygen and nitrogen, whereas water is described by means of the atomic abundance of oxygen and hydrogen. Mass fractions are identified using the 'minus' in front of the fraction itself.

#### Tallies

Tally cards are inputs that allow the user to "measure" quantities such as particle current, particle flux, and energy deposition. Tallies units are normalized per number of histories generated. Generally speaking, a quantity $C$, depending on the energy fluence

$\phi(E)$ and probability distribution *f(E)*, in accordance with equation 4.10 below, can be tallied.

$$C = \int \phi(E) f(E) dE \tag{4.10}$$

*f(E)* usually is represented by one or more cross section libraries or a user-defined response function. The only data card required to specify the tally within the MCNP code is known as the "F" card, followed by an integer $< 999$. The last digit of such integer can be only from 1 to 8 and defines the tally type. A summary of type, description and units of the tallies is briefly introduced in table 4.1.

| **Symbol** | **Description** | **Units** |
|---|---|---|
| F1 | Current integrated over a surface | particles |
| F2 | Flux averaged over a surface | particles/cm2 |
| F4 | Flux averaged over a cell | particles/cm2 |
| F5 | Flux at a point or ring detector | particles/cm2 |
| F6 | Energy deposition averaged over a cell | MeV/g |
| F7 | Fission energy deposition averaged over a cell | MeV/g |
| F8 | Energy distribution of pulses created in a detector | pulses |

Table 4.1: The 8 types of tallies used in MCNP. Table from [124]

! 

For instance, the F1 tally explained in the example aforementioned (F1:N 3) means that all neutrons passing through surface number 3 are scored.

Cards such as energy, time, meshing, dose, etc, are optional and can be added after the F card is specified.

MCNP6, is the Monte Carlo tool chosen to perform the simulations carried out in this research and presented in the second part of this thesis. Each experiment was preceded by a period of simulation and design, in which the sensitivity and performance of the experimental system was predicted. Given the complexity of some experiments, the simulation of the system response with appropriate models, if fundamental for an estimation of both signals and background events. Monte Carlo simulations are fundamentals even after the experiment has been performed, as the simulation hypothesis can be compared with data analysis. The comparison between real data and simulations is an important step to analyse and interpret the results of an experiment.

# Part II

# RESULTS

# Chapter 1

# Fast-neutron/$\gamma$-ray computed tomography: a Monte Carlo study

M. Licata and M.J. Joyce. *"**Concealed nuclear material identification via combined fast-neutron/$\gamma$-ray computed tomography (FNGCT): a Monte Carlo study**"*. Journal of Instrumentation, Volume 13, February 9, 2018.

**Abstract**. The potential of a combined and simultaneous fast-neutron/*gamma*-ray computed tomography technique using Monte Carlo simulations is described. This technique is applied on the basis of a hypothetical tomography system comprising an isotopic radiation source (americium-beryllium) and a number (13) of organic scintillation detectors for the production and detection of both fast neutrons and *gamma* rays, respectively. Via a combination of $\gamma$-ray and fast neutron tomography the potential is demonstrated to discern nuclear materials, such as compounds comprising plutonium and uranium, from substances that are used widely for neutron moderation and shielding. This discrimination is achieved on the basis of the difference in the attenuation characteristics of these substances. Discrimination of a variety of nuclear material compounds from shielding/moderating substances (the latter comprising lead or polyethylene for example) is shown to be challenging when using either $\gamma$-ray or neutron tomography in isolation of one another. Much-improved contrast is obtained for a combination of these tomographic modalities. This method has potential applications for *in-situ*, non-destructive assessments in nuclear security, safeguards, waste management and related requirements in the nuclear industry.

## 1.1 Introduction

Computed Tomography (CT) is a well-known, non-destructive technique that is used to investigate the internal characteristics of materials. X-rays or $\gamma$ rays have often been used as the form of radiation, particularly for medical purposes, whilst neutrons have also been used extensively, predominantly for materials characterisation [51]. Neutrons and photons interact differently in matter, thus providing sources of information related to

the structure of materials under investigation that can be complementary. Depending on their energy, photons interact by means of the photoelectric effect, Compton scattering and pair production. The probability of each interaction also depends on the atomic number Z of the element in which the photons are interacting. On the other hand, when neutrons interact, they may undertake a variety of nuclear processes, including elastic scattering, inelastic scattering and radiative neutron capture, induced fission and several other types of nuclear reactions, such as (n, p), (n, d), (n, $\alpha$), etc. For some elements moreover, the interaction cross section, especially for elastic scattering and absorption, is relatively high for low-Z elements. Due to these differences, neutron and $\gamma$-ray tomographies often yield different results when imaging the same objects because two different materials with attenuation coefficients that are similar for photons may have contrasting coefficients for neutrons, and vice versa. For instance, photon-based tomographies are unlikely to discriminate between different materials of similar density or atomic number (Z) and underperform when imaging low-Z materials; neutron-based techniques, on the other hand, are more suited to highlighting structural contrast in low-Z, porous materials and substances that have high reaction cross sections for neutron scattering and absorption [85].

Simultaneous and combined neutron-$\gamma$ imaging is a relatively unexplored technique. Some works have investigated the potential of the combined neutron-photon imaging technique when used for non-destructive tests [95, 111, 115, 131–135]. In particular, Monte-Carlo simulations have been carried out in [109] in order to examine the feasibility of a combined neutron-photon CT of a model container. The simultaneous n-$\gamma$ technique is often applied making use of two different imaging facilities for both neutron and $\gamma$/X-rays as well as separate detector systems for each types of radiation. Research reactors, spallation facilities or neutron generators are often used as neutron sources, and the limited transportability of these facilities can constrain the potential of a tomography system for large-scale industrial applications and/or *ex-situ* assessments. Moreover, the majority of neutron techniques involve the use of thermal neutrons. These are relatively easy to detect and can yield high resolution images but have the drawback of having poor penetration capabilities when the requirement is to probe high density materials [84]. The use of fast neutrons can be preferable in such applications.

The purpose of this study is to demonstrate the potential of a simultaneous neutron-$\gamma$ CT technique that is able to achieve a reasonable image resolution and an acceptable level of contrast of materials relevant to scenarios in which nuclear materials might be concealed, using an isotopic radiation source. The identification of special nuclear materials is often based on the detection of the radiation they emit, either passively or following stimulus by an external source of radiation. Due to this fact, it is anticipated that were they to be smuggled they would be concealed by significant quantities of shielding materials, in order to prevent their interception, particularly because the emissions from natural decay processes are relatively weak. *In-situ*, non-destructive, real-time assessment methods to overcome the challenges posed by such scenarios are therefore needed, particularly where the requirement to investigate suspicious objects is

widespread, such as at territorial borders, transport hubs and shipping terminals.

The CT system presented in this work has been designed and simulated in such a way as to allow a combined neutron-$\gamma$ scan with a single source of fast neutrons and rays. The system is based on the same concept of the fast-neutron tomography system reported in [31], which was based on the use of a real-time pulse-shape discrimination (PSD) technique [16] in 7 organic liquid scintillation detectors. In this prior report, fast neutron tomography was demonstrated to discern voids, corners and inhomogeneity in concrete samples and the potential to apply this system for fast neutron assay was discussed. The PSD technique makes both experimental fast-neutron and $\gamma$-ray data available but only neutron data were used in the subsequent off-line data analysis.

## 1.2 Methods and procedures

Four features fix the geometry of a computed tomography system: the source-to-object distance,the source-to-detector distance, the area to be imaged and the solid angle covered by the detectors. In this particular study, a 20 MBq americium-beryllium (AmBe) source has been simulated. This source emits a mixed radiation field comprising both fast neutrons (from thermal energies to 10 MeV) and $\gamma$ rays of 4.4 MeV. Californium-252 is also a candidate that might be used as a source, emitting neutrons and$\gamma$ rays as a result of spontaneous fission. The radiation produced by AmBe is collimated into a fan beam directed towards the phantoms to be scanned. The fan beam geometry allows a volume to be reconstructed as a stack of different single slices consistent with the type of configuration that is in widespread use in CT scanning machines. The use of this particular beam arrangement requires the phantom to be moved in order to obtain a range of projections with which to optimise image resolution. Parallel beam and cone beam arrangements are also widespread in tomography and radiography applications. Cone beams, in particular, produce a radiographic image with only one projection and are particularly suitable when pixelated detectors such as charge coupled devices (CCDs) are used. The fan beam geometry has been selected in this study as it is considered that which is most compatible with the type and arrangement of the detectors that have been used in the related prior art [31] and that have been selected for the simulation. Since one of the main purposes of this research is to exploit the same detection system for fast neutrons and $\gamma$ rays, the choice of detectors is restricted to organic scintillation materials that, in a possible experimental scenario, would be read out with real-time pulse-shape discrimination systems [16], discriminating and recording neutrons and $\gamma$ rays simultaneously. The constraints associated with their physical dimensions, sensitive volume and shape limits the possibility of using parallel and cone beams. Also, in the context of a there being a small sample under scrutiny (i.e. relative to the size and mass of the detector system), it is easier to manipulate the position of the sample than it is to move the detector system. Depending on the specific application in mind, the converse might be the case; for example, where the requirement is to assess the integrity of a fixed object such as a freight container or transport vessel.

Schematic diagrams of the plan, elevation and perspective of the computed tomogra-

phy system are presented in figure 1.1. The whole system and a generic laboratory space in which it is anticipated that it might be required to function have been simulated with MCNP6 [124].

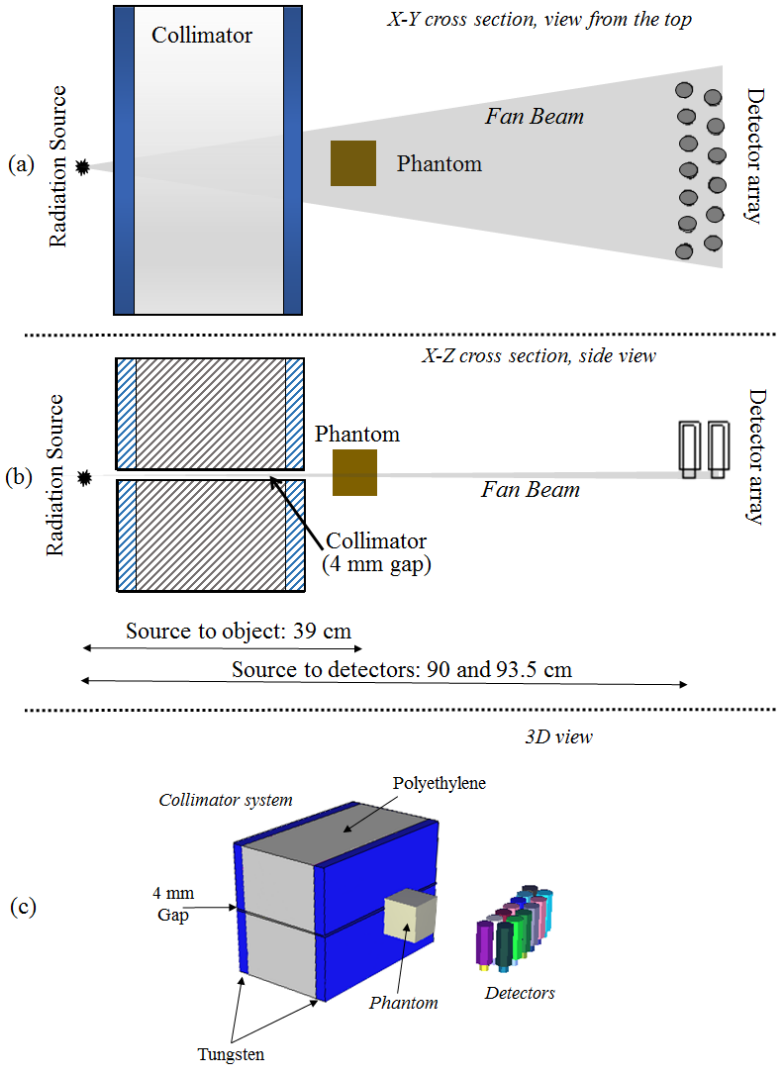


Figure 1.1: System design details: (a) plan view(x-y) of the system is shown, (b) side elevation is represented, corresponding to the x-z cross section and (c) an image of the system shown in perspective

.

### 1.2.1 Collimator

The collimator is designed to produce fan beams of both the neutrons and rays emitted by the AmBe source and therefore it comprises: two polyethylene blocks of thickness 24 cm and four tungsten blocks of 3-cm thickness, separated by a 4-mm gap. Lead might also be used in place of tungsten, potentially reducing the cost of the system in the event that this is a requirement. The total length of the collimator is 30 cm. The first tungsten layer is included to attenuate the rays, followed by high-density polyethylene to attenuate the neutrons. A second tungsten layer, located after the polyethylene

block is included to shield any residual $\gamma$ radiation arising for example due to scatter in the environment, background or as a result of neutron capture on the hydrogen present in the polyethylene. The 4-mm gap between this arrangement of materials with complementary attenuation properties yields the desired, mixed-field fan beam.

A fundamental requirement in tomography when designing the collimator is the L/D ratio: this is the ratio of the source-to-object-distance (L) to the source diameter (D) In this particular case, D corresponds to the 4-mm collimator gap [136]. The objects analysed in the simulations have been located at 39 cm from the source; hence L/D = 97.5. The L/D ratio provides a quantitative indication of the beam divergence and infers the quality of a projection. The correspondence of different L/D ratios on the tomographic reconstruction is described in [137].

### 1.2.2 Detectors

The detectors have to be positioned as close as possible to the object [138] if detection sensitivity is to be optimised. However, the area to be imaged is constrained by the dimensions of the object itself, as well as by the dimensions of the detectors. For example, if the detectors are located too close to the object, the area subtended by some of them at the position of the object will be beyond the imaging area (this is illustrated in figures 1.2a and 1.2b). On the other hand, if the detectors are placed too far from the sample, whilst all of them then benefit from having a clear line-of-sight of the imaging area, the radiation flux subtended at them by the source would be too weak for most practical purposes. The effect of the latter is to increase the required imaging time, potentially rendering the system unsuitable for time-constrained applications. Therefore, a suitable compromise between number of detectors (the larger the number the better) and sample-detector distance (the smaller the better) must be struck.

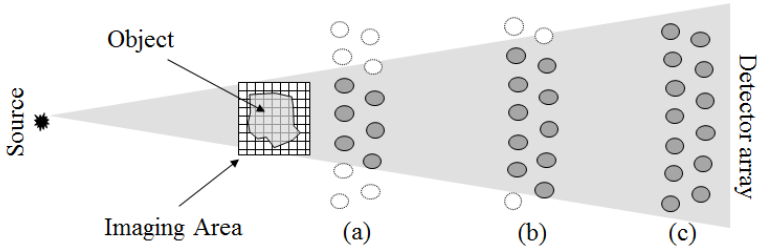


Figure 1.2: A plan view of the imaging area viewed by the detectors. In (a) and (b) the detectors in white do not have line-of-sight of the object in terms of the trajectory of the fan beam. In (c) all the detectors, depicted in grey, have line-of-sight of the object and the total area to be imaged.

The choice adopted for this research comprised a twin array of thirteen organic liquid scintillation detectors, with seven and six located at 90 cm and at 93.5 cm from the source, respectively (as depicted in figures 1.1a, 1.1b and 1.1c). This specific arrangement has been selected in order to remove the gap in the imaging area that arises between each pair of detectors in the scenario where a single row is used. Gaps between detectors

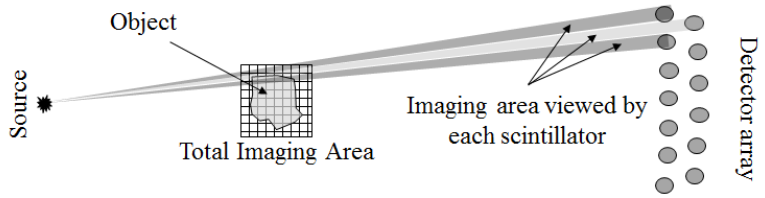


Figure 1.3: A schematic diagram of the plan view of the tomography set-up depicting the solid angle subtended by three detectors in the twin-row detector arrangement.

produce ring artefacts after the image reconstruction and limit the extent of the final spatial resolution. This can be reduced by placing the detectors as close to one another as possible but even in this case there is a gap in between their sensitive volumes of neighbouring detectors, due to the size of the scintillator cover and its photomultiplier. The double-row array configuration is more suitable to ensure that the total imaging area covered under the view of the detectors is a *quasi*-continuous space (as depicted in figure 1.3). It is also anticipated that cross-talk between detectors will be a less significant effect for the twin-row arrangement relative to a single row of closely-packed detectors.

The detectors simulated in this research were of type VS-0653-2 (Scionix, Netherlands [139]) containing the EJ-301 liquid scintillant (Eljen Technologies, U.S.); alternatives such as EJ-309 or the plastic EJ-299 are feasible. The detectors are placed vertically, as shown in figure 1.1b, equidistant from the source with each row forming an arc such that the balance of the radiation flux at each detector is maintained, as per the inverse-square dependence with distance.

### 1.2.3 Modus operandi

The interaction probability of $\gamma$ rays and neutrons is parameterised by the linear attenuation coefficient of the material ($\mu$). The intensity of the radiation exhibits an exponential dependence with material thickness described by the Beer-Lambert law, as per,

$$I = I_0 e^{-\mu_x x}; x \equiv y; \tag{1.1}$$

where $I_0$ is the initial intensity of the radiation, whereas $I$ is the final intensity and $x$ is the distance travelled by the radiation. The logarithmic ratio $log_e(I_0/I)$ is called the one-dimensional projection of the body in the direction of incidence of the radiation quantum. Scanning the object with a series of rotations and translations, the attenuation coefficient can be treated as function $\mu(x, y)$ representing the radiating section of the object (figure 1.4). This particular function has to be determined by a reconstruction algorithm.

Under the condition that the imaging area is the same for both components of the mixed field, two different attenuation indices for neutrons $\mu_n$ and $\gamma$ rays $\mu_\gamma$ can be extracted for a fixed position of the object.

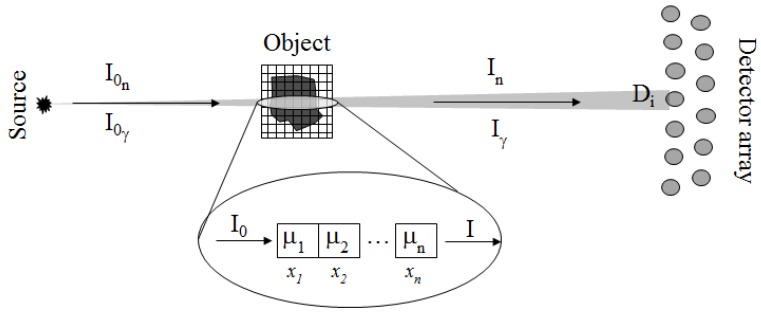


Figure 1.4: A schematic representation of bulk radiation attenuation de-convolved into its constituent attenuation coefficients.

In this research, the tomography arrangement has been simulated with MCNP6, recording both neutrons and $\gamma$ rays interacting with the detectors after placing the phantom in 624 different positions obtained by its incremental translation and rotation: 26 translations have been made and for each one of these the phantom has been rotated in the horizontal plane through successive 15° steps, 24 rotations per translation. Moreover, an ideal laboratory room, i.e. neglecting background radioactivity and assuming homogeneous material composition, has been reproduced and the residual scatter induced by the simulated AmBe source in the room measured by the detectors. The initial flux intensities, $I_{0_n}$ and $I_{0_\gamma}$, have been determined by measuring the flux at the detector without any object and the intensity of the neutron and $\gamma$ flux ($I_n$ and $I_\gamma$) at the detectors has been determined for each projection.

The background (denoted *bkg*) has also been evaluated by simulating a laboratory room in which the tomography system would be located. The level of the background then has been subtracted from both intensities. The attenuation coefficient has then been determined for each projection for both neutrons and $\gamma$ rays, according to equations 1.2 and 1.3, as per,

$$\mu_n = log\frac{I_{0_n} - bkg}{I_n - bkg} \tag{1.2}$$

$$\mu_n = log\frac{I_{0_\gamma} - bkg}{I_\gamma - bkg} \tag{1.3}$$

Since 13 detectors have been used, the total number of projections is 8112 (624x13). This number is far greater than the minimum number of projection ($N_{proj}$) necessary to yield a satisfactory degree of sampling of the object, defined by the Nyquist-Shannon theorem [138] in equation 1.4 :

$$N_{proj} = \pi O_{pix} \tag{1.4}$$

where $O_{pix}$ is the number of pixels defined in the horizontal dimension of the total imaging area. As is shown in the next section, an algebraic image reconstruction algorithm has been used, therefore a larger number of projections improves the solution for the unknown image pixels. In this specific study, after a detailed analysis considering both sampling time and computer processing time, $O_{pix}$ is 128 pixels and the imag-

ing area 13x13 cm. This means that the dimension of each single pixel corresponds approximately to 1 mm.

### 1.2.4 Phantom tested

In general, the phantoms studied in this research comprise small cylinders of compounds containing uranium or plutonium placed in a variety of arrangements with lead and polyethylene, designed to conceal their presence from view primarily in terms of the radiation they emit and that might otherwise enable them to be detected. The cylinders are 5-mm thick and have a diameter of 2.5 cm (plutonium) and 3 cm (uranium). Hypothetically, the plutonium compounds have been concealed inside a lead box of dimension 6 cm, located in turn inside a 10-cm polyethylene box (as depicted in figure 1.5a) in order to shield the emission of both neutrons and $\gamma$ rays in view of the likelihood of neutron emission from spontaneous fission (SF) of constituent quantities of $^{240}$Pu. Similarly, uranium compounds have been hidden inside a 7-cm lead cuboid (figure 1.5b), in order to shield the residual $\gamma$-ray emission from the decay of $^{238}$U etc. The small amount of SF in $^{238}$U and the related neutron yield was neglected for the purposes of these measurements. Tables 1.1 and 1.2 summarise the materials used for the 6 different samples and configurations, in detail.

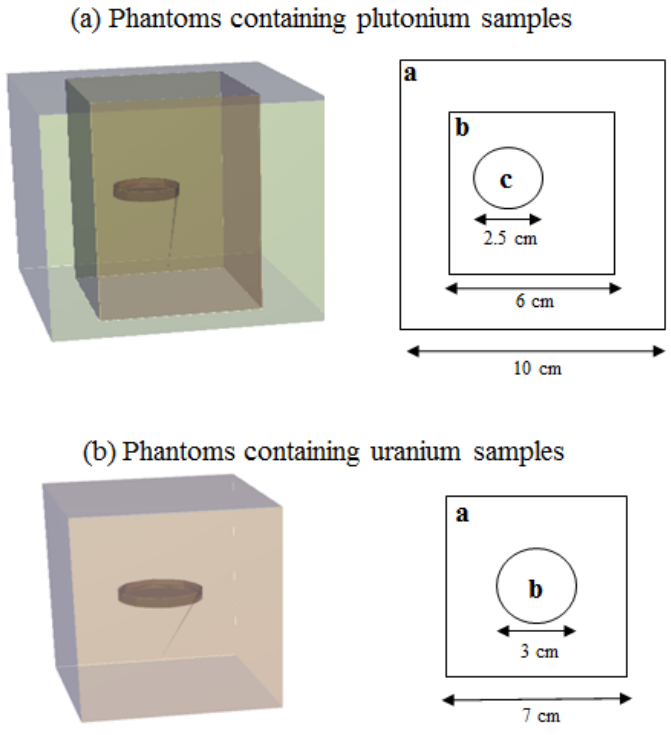


Figure 1.5: Schematic pictures of the objects simulated in this research: (a) the configuration used to conceal the plutonium samples, whilst in (b) the lead box used to conceal uranium samples is depicted.

| Sample name | Material A | Material B | Material C |
|---|---|---|---|
| Pu1 | HDPE | Lead | Plutonium metal |
| Pu2 | Lead | HDPE | Plutonium metal |
| Pu3 | HDPE | Lead | Plutonium oxide |

Table 1.1: Description of the phantoms containing plutonium-based samples.

| Sample name | Material A | Material B |
|---|---|---|
| U1 | Lead | High-Enriched Uranium (HEU) |
| U2 | Lead | $U_3O_8$ |
| U3 | Lead | $UC_2$ |

Table 1.2: Description of the phantoms containing uranium-based samples.

## 1.3 Results

### 1.3.1 Qualitative observations

The CT results are presented in figures 1.6 and 1.7 in terms of attenuation index as a function of dimension in x and y. For each sample the results of its fast-neutron tomography, $\gamma$-ray tomography and the combination of neutron and $\gamma$-ray tomography are shown.

The image reconstruction algorithm used to reproduce the neutron and the $\gamma$-ray tomography is the Simultaneous Multiplicative Algebraic Reconstruction Technique (SMART). The next section describes the motivation for this particular choice. In order to simulate combined neutron/$\gamma$-ray tomography, it is necessary to reconstruct the $\gamma$-ray and neutron images separately and then to normalize them to the maximum value of the attenuation coefficient in each case. This is a crucial process since both the neutron and $\gamma$-ray tomography data originate from a mixed radiation source, with each radiation type having a different intensity and energy spectrum. Once they are normalized, the combined neutron/$\gamma$-ray tomography ($\mathbf{Q}_{n\gamma}$) can be obtained according to equation 1.5,

$$\mathbf{Q}_{n\gamma} = (\frac{1}{2} - \alpha)\mathbf{Q}_n + (\frac{1}{2} + \alpha)\mathbf{Q}_\gamma \tag{1.5}$$

where $\mathbf{Q}_n$ and $\mathbf{Q}_\gamma$ are the neutron and $\gamma$-ray images, respectively, and $\alpha$ is a scalar parameter associated with the contrast of the image and with the condition that -1/2< $\alpha$ <1/2. Thus, for $\alpha = 1/2$, $\mathbf{Q}_{n\gamma} = \mathbf{Q}_\gamma$ or if $\alpha =$ - 1/2, $\mathbf{Q}_{n\gamma} = \mathbf{Q}_n$. The results presented here are for the specific case $\alpha$= 0, and the combined tomography is simply the average of the neutron and $\gamma$-ray images. However, this depends on the materials that are imaged. The $\alpha$ parameter can be varied to highlight features either from the neutron image or from the $\gamma$-ray alternative. A similar technique can be applied using the data fusion methodology reported in [140].

Concerning the data for the plutonium samples (as shown in figure 1.6), the polyethylene and the lead boxes have similar attenuation indices when using the neutron CT only, even when the polyethylene and the lead box are swapped with each other (configurations

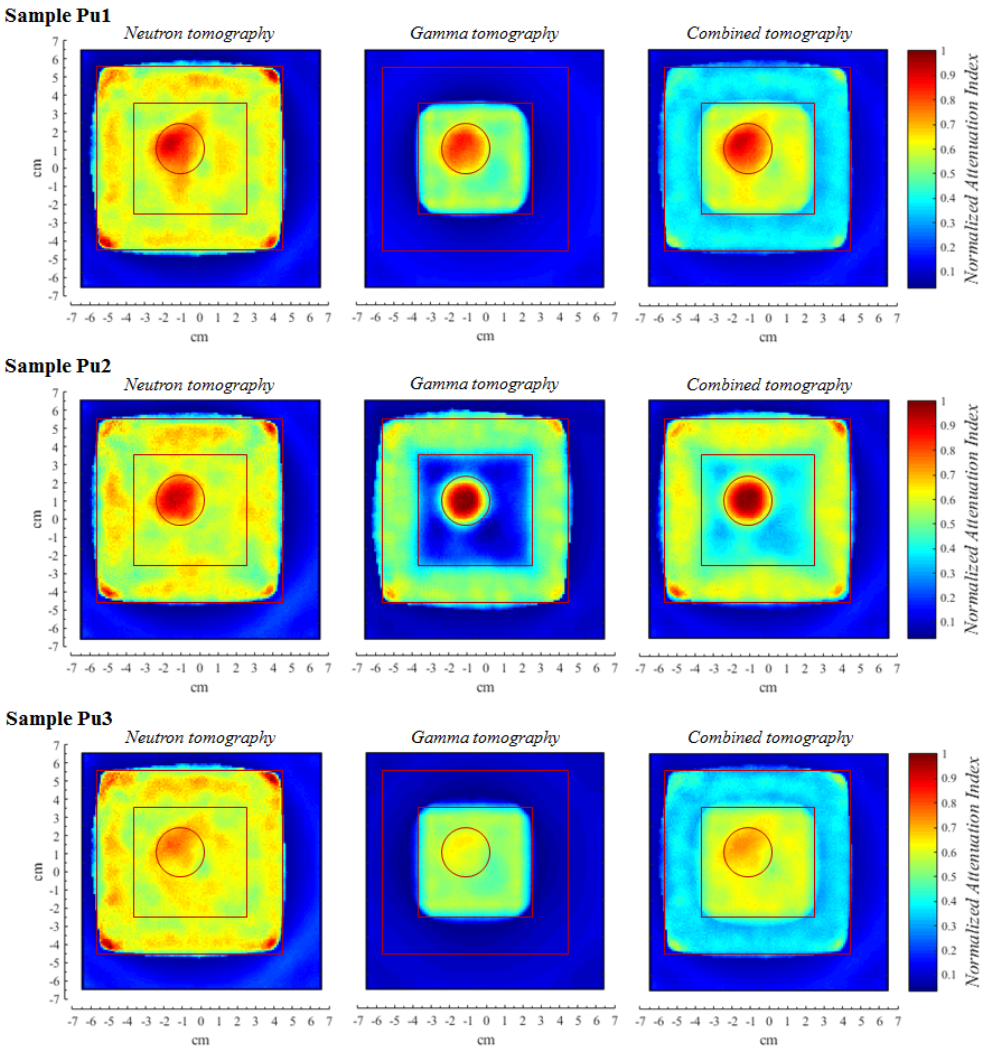


Figure 1.6: Tomographic results corresponding to the normalized attenuation index as a function of x and y, obtained for plutonium-based samples concealed in polyethylene and lead. See table 1.1 for a summary of the different materials used in each of the three cases.

Pu1 against Pu2). In contrast, the $\gamma$-ray CT highlights the lead box and the plutonium metal cylinder (sample Pu1 and Pu2) but, conversely, it does not show evidence of the polyethylene box (sample Pu1, Pu2 and Pu3), which appears instead as a void of similar attenuation index to that of the air. Moreover, the $\gamma$-ray CT does not discern lead from plutonium oxide (sample Pu3). Combining the two tomographies, the polyethylene box and the inner lead cuboid with plutonium metal and plutonium oxide are all clearly discernible (samples Pu1, Pu2 and Pu3).

Regarding the uranium-based samples (figure 1.7), the neutron CT does not discriminate uranium trioxide from lead (sample U2), and neither does the $\gamma$-ray CT discriminate between uranium carbide and lead (sample U3). When the combined neutron/$\gamma$-ray CT is applied, all the three uranium samples (U1, U2 and U3) are clearly discernible.

For the purposes of these simulations the samples (both plutonium and uranium) have deliberately not been located in the centre of the rotation imaging area because

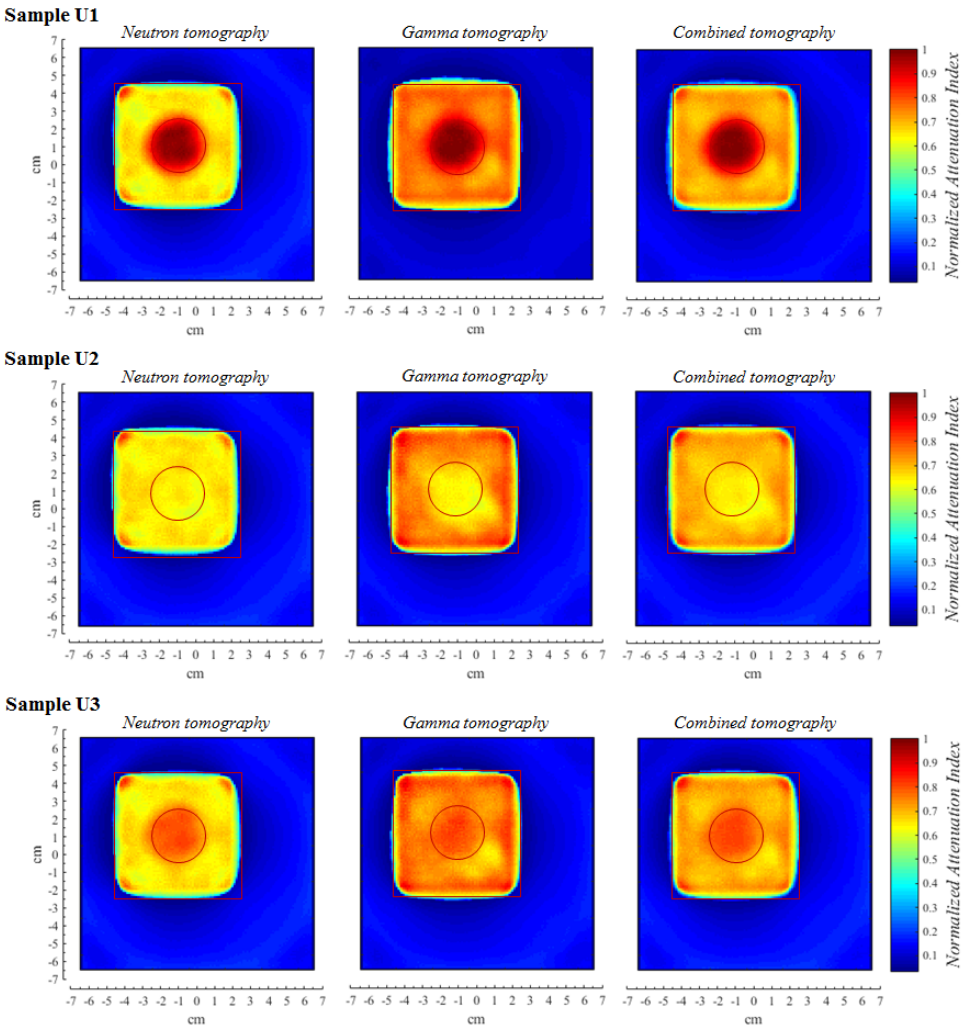


Figure 1.7: Tomographic results corresponding to the normalized attenuation index as a function of x and y, obtained for uranium-based samples concealed in a lead box. See table 1.2 for a summary of the different materials used in each of the three cases.

when the shape is a cylinder or a sphere, ring artefacts may appear as a result of the reconstruction process. Finally, in the prospect of a real experiment, with a source activity in the order of a few MBq, the estimated time needed for the entire tomography experiment is estimated to be of the order of three to four hours, depending on the choice of the sampling duration.

### 1.3.2 Spatial resolution

Spatial resolution has been calculated by measuring the attenuation index profile along a fixed projection. The variation of the attenuation index of a given material from another has been fitted with a distribution function of a Fermi-Dirac form on an entirely empirical basis, as per,

$$f(x) = \frac{A}{1 + e^{[(x-B)/C]}} \tag{1.6}$$

where A, B and C are constants that depend on the profile being fitted. This particular function has been chosen in order to base the spatial resolution on the 10-90% edge response technique.

In figure 1.8, the results of sample Pu1, namely plutonium metal, are shown. The images on the left refer to neutron-CT (1.8a), $\gamma$-CT (1.8b), and neutron/$\gamma$-ray CT (1.8c), which are also presented in 3D for clarity.

The plots on the right, by contrast, show both the attenuation coefficient profile and the respective Fermi-Dirac type fit. The attenuation profile has been extracted along the red, dashed, horizontal line highlighted on the left side and passing through the centre of plutonium cylinder. This line, which extends from one border to the other, covers 128 pixels along the x dimension. For each sample, the minimum and maximum spatial resolution was measured using the 10-90% edge response method. For instance, in the case study of the Pu1 sample, the best resolution obtained was 3 mm, and this has been achieved with the combined neutron/$\gamma$-ray CT. The uncertainty of the resolution measurements presented is 1 mm, since, as mentioned in the previous section, 1mm corresponds approximately to the dimension of 1 pixel. The spatial resolution results concerning the other samples are shown in table 1.3. In five cases out of six, neutron/$\gamma$-ray CT shows a better degree of resolution, with the exception of the U1 sample (namely highly-enriched uranium) for which a better resolution with neutron-CT alone is achieved.

| **Sample** | **neutron-CT** | | **$\gamma$-CT** | | **neutron/$\gamma$-CT** | |
|---|---|---|---|---|---|---|
| | *min* | *max* | *min* | *max* | *min* | *max* |
| Pu1 | 6 | n.a | 4 | 7 | 3 | 5 |
| Pu2 | 4 | n.a | 6 | 8 | 3 | 5 |
| Pu3 | 5 | n.a | 6 | 9 | 4 | 6 |
| U1 | 4 | 4 | 5 | 8 | 5 | 7 |
| U2 | n.a | n.a. | 5 | 5 | 4 | 4 |
| U3 | 4 | 4 | 7 | 8 | 4 | 5 |

Table 1.3: Spatial resolution estimation using the 10-90% edge response method. Values are presented in millimetres. Each value has an uncertainty of $\pm 1$ mm.

It has to be highlighted that spatial resolution varies depending on the materials being analysed, due to this fact, the interaction with some materials by neutrons is better than it is with $\gamma$ rays and *vice versa*, thus yielding different levels of contrast, which in turn means better or worse spatial resolution. For instance, in the case of sample U2 ($U_3O_8$) and with respect to neutron-CT, the minimum spatial resolution cannot be determined because the attenuation coefficient profile does not allow discrimination between uranium trioxide and lead. The same applies to the neutron-CT analyses of Pu1, Pu2 and Pu3, which do not distinguish polyethylene from lead. On the other hand, it is indeed possible to estimate a minimum resolution exploiting the discrimination of plutonium from either polyethylene or lead.

Shapes, borders and position of the samples are instead recognized with a precision of 2 mm. Using the combined neutron/$\gamma$-ray CT, all the samples of uranium and plutonium

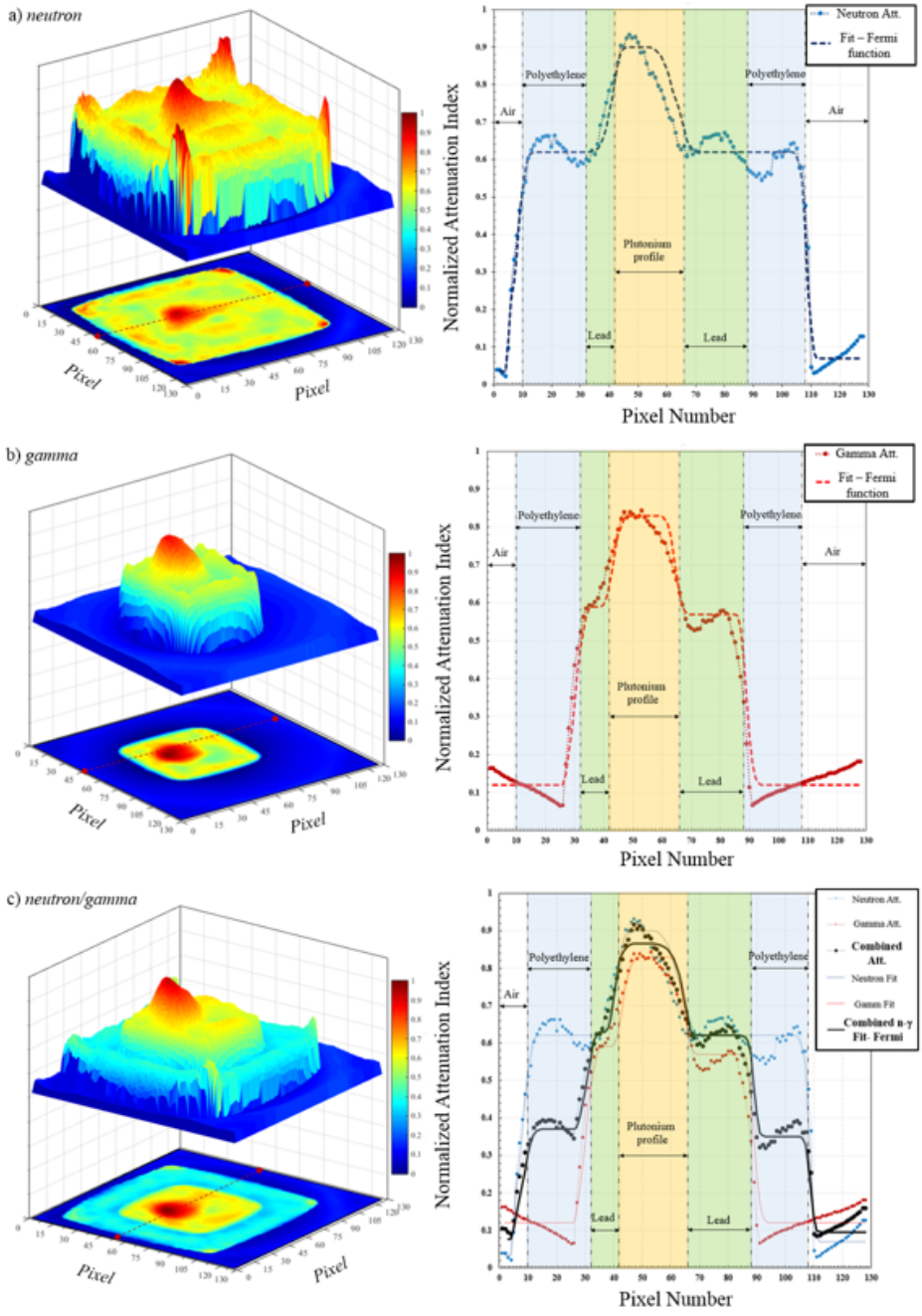


Figure 1.8: On the left: tomographic results corresponding to the normalized attenuation index as a function of x and y, concerning the sample Pu1 (plutonium metal). On the right: the attenuation index profile as a function of the pixel number along the red dotted line traced within the tomographic result on the left.

are identified inside the shielding materials that they are concealed by, with a spatial resolution that ranges from a minimum of 3mm (sample Pu1 and Pu2) to a maximum of 7mm (sample U1).

## 1.4 On the choice of the image reconstruction approach

Image reconstruction from projections is a problem that has been studied extensively over several decades. A significant number of works have treated the two most-known groups of reconstruction algorithms in detail, namely the filtered back projection approach (FBP) and the algebraic reconstruction method (Gordon, [141]). The former requires a large number of projection data taken over a large number of angles [142,143]. In some cases, it is not possible to acquire the amount of data necessary, often due to time constraints, costs and the wide variety of experimental issues that can constrain acquisition flexibility. When geometries dealing with limited data (i.e. data coming from an incomplete set of projections) are used, algebraic reconstruction techniques (ART) tend to show the best results compared to the most common FBP techniques [142,144].

The system geometry and the number of projections acquired in this work fall within the category of reconstruction with limited data. Since ART results depend strongly on the geometry of the system, three different algebraic reconstruction algorithms have been compared and applied to the geometry used in this particular research. Four test-phantoms have been used to test ART (Gordon), SIRT (simultaneous iterative reconstruction technique, Gilbert [120]) and SMART, adapted specifically to the simulated system. The algebraic method most suited to the particular system geometry used in this work is yet to be determined.

Other algebraic algorithms, such as Maximum Entropy and Minimum Energy have not been taken into account since this goes beyond the focus of this study at this stage. Two of the four phantoms have been selected deliberately to be the same as presented in [142] and described mathematically in equations 1.7 and 1.8,

$$Cosine(x,y) = 0.25\{1 - cos[2\pi(x+0.5)^{4/5}]\} \times \{1 - cos[2\pi(y+0.5)^{2/3}]\} \tag{1.7}$$

for $|x,y|$ <0.5,

$$CosGauss = 1.09\{0.3Cosine(x,y) + Gauss_1(x,y) + Gauss_2(x,y)\} \tag{1.8}$$

where $Gauss_1$ is,

$$Gauss_1(x,y) = 0.8e^{-[9(x-0.2)]^2-[6(y-0.1)]^2} \tag{1.9}$$

and $Gauss_2$ is,

$$Gauss_2(x,y) = e^{-[8(x-0.2)]^2-[30(y+0.35)]^2} \tag{1.10}$$

The other two test objects of relevance are the Shepp-Logan phantom and spikes made of three square peaks with other small peaks distributed randomly across the image, configured in order to reproduce noise over the image. The noise level in the first

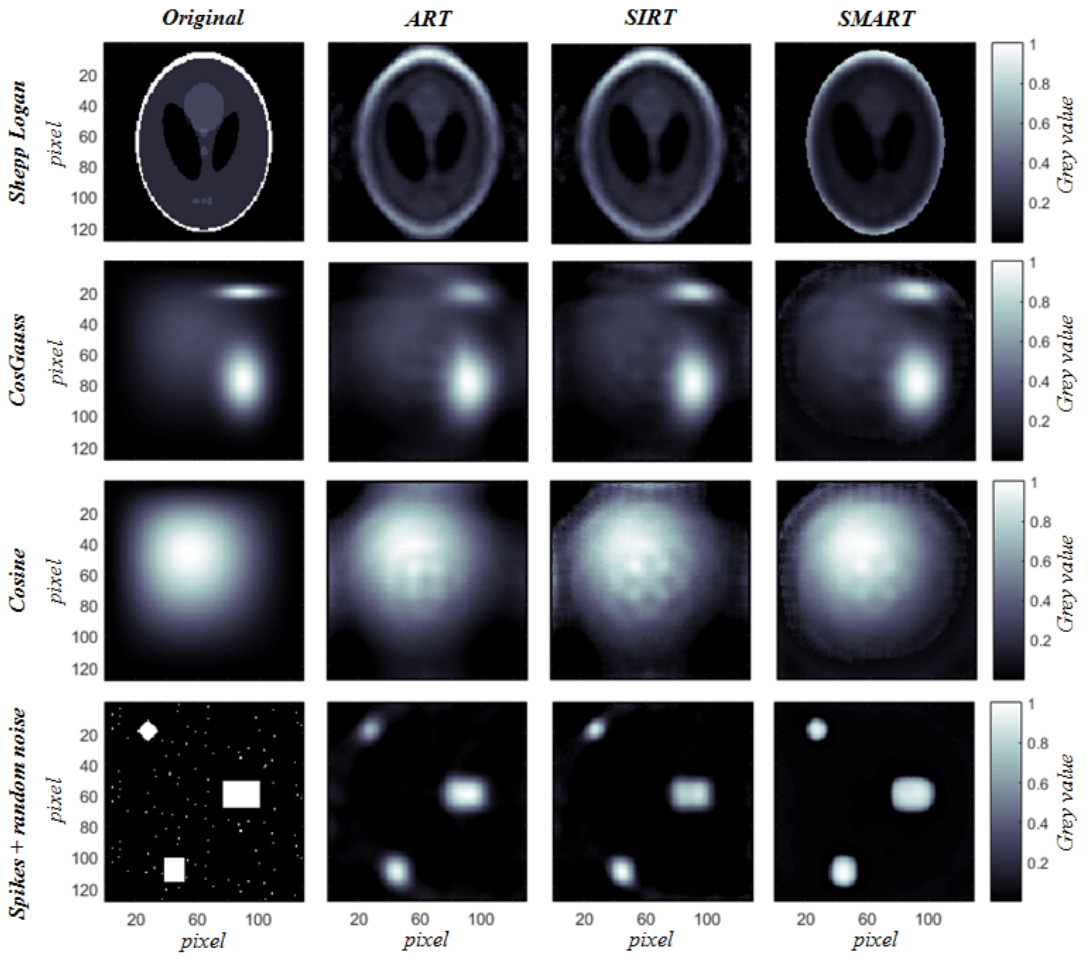


Figure 1.9: A comparison of the results of three different algebraic image reconstruction algorithms applied to four different test-phantoms.

three phantoms instead is kept to zero.

The original phantoms and the results are shown in figure 1.9. The imaging area has been discretized in 128x128 pixels and projection data have been generated calculating the integral of each projected ray analytically. As in the case of the aforementioned MCNP simulations, phantoms have been translated in 26 steps, and for each step have been rotated in turn by 15deg each time, obtaining in this way 24 angles over a 360deg total angle of view. In this way there are 624 projections for each of the 13 viewing angles corresponding to the 13 detectors.

In order to understand which algebraic algorithm is more suited to this particular configuration the Root Mean Square (RMS) error between the original and the reconstructed phantom has been calculated. The error, shown in table 1.4 for each algorithm, is defined as:

$$RMS = \sqrt{\frac{\sum_{i=1}^{N}[S(i) - S'(i)]^2}{\sum_{i=1}^{N} S(i)}} \tag{1.11}$$

where *S(i)* is the pixel value of the original phantom and *S'(i)* is the reconstructed pixel value; N is the total number of pixels in the image.

| Phantom | RMS | | |
|---|---|---|---|
| | ART | SIRT | SMART |
| Shepp-Logan | 0.44 | 0.44 | 0.37 |
| CosGauss | 0.18 | 0.15 | 0.17 |
| Cosine | 0.19 | 0.19 | 0.18 |
| Spikes and random noise | 0.59 | 0.57 | 0.53 |

Table 1.4: RMS for each of the algorithms tested.

In three cases out of four the SMART algorithm shows better performance than SIRT and ART. This is the reason why it has been chosen to analyse the Monte Carlo simulation data in this research and shows promise for the analysis of the data from future experimental measurements.

## 1.5 Conclusion

This study contributes to the development of neutron/$\gamma$ based inspection technologies. The vast majority of the existing neutron non-destructive techniques exploit the production of either prompt or delayed neutrons and $\gamma$ rays for the inspection/recognition of special nuclear materials (SNM) [103]. However, these techniques are often applied to the identification of other hazardous materials such as explosives and contraband (especially illegal drugs) rather than to recognize substances of significance in a nuclear context [97].

The current *state-of-the-art* denotes that combined neutron- and $\gamma$-ray tomography is always undertaken using two different facilities for neutron-CT and $\gamma$-CT, therefore comprising separate radiation sources, instrumentation, detectors and image reprocessing techniques. A major advantage of the approach and technique described in this research is that it can provide quick and reliable information about objects under investigation, using the same radiation source and instrumentation, with a significantly-reduced requirement for off-line analysis yielding data in a few minutes and carried out subsequent to the estimated three-to-four hours measurement time. In particular, this technique has been applied intentionally in a nuclear framework since the majority of neutron- and $\gamma$-radiography/tomography techniques in this environment are often focused on the investigation of nuclear fuels [145]. Only a few papers report tomography as a way for the identification of concealed nuclear materials [13, 104, 105]. In addition, on the one hand several works use radioactive sources such as $^{60}$Co or $^{137}$Cs to carry out $\gamma$-CT, whilst on the other, only [31] and [13] exploit an isotopic neutron radiation source such as $^{252}$Cf to perform fast-neutron CT. Conversely, $^{252}$Cf is used mostly to undertake thermalized neutron analysis (TNA). It has also to be highlighted that few if any reports focus on the use of an AmBe source for fast-neutron tomography, as done in this study. The technique presented in this paper could be investigated further and improved using a neutron generator as a source, exploiting relatively recent developments in terms of the portability of these systems [146, 147]. A neutron generator would provide a higher-

energy, monochromatic neutron flux and therefore potentially a reduction in terms of sampling time.

This research also indicates that materials used in the nuclear industry are discernible from materials that might be used for shielding purposes to conceal these substances. The simulated system in this work is compatible with use in an ordinary laboratory room and has potential for application for security inspection purposes or, from a more general perspective, for non-destructive assessments for which $\gamma$-ray or neutron tomography methods in isolation of one another are not able to provide information with which to discern the composition of the objects under scrutiny. The system can recognize the position and the physical size of the sample to a 2-mm level of precision and an uncertainty of $\pm 1$ mm; the minimum spatial resolution achieved identifying the different samples tested has been of $(3 \pm 1)$ mm. Finally, a comparison and a quantitative result on the choice of using the simultaneous multiplicative algebraic reconstruction technique rather than one another, has been provided.

## 1.6 Acknowledgments

The authors acknowledge the support of the U.K. Engineering and Physical Sciences Research Council (EPSRC), the Lloyd's Register Foundation, the Next Generation Nuclear (NGN) - Centre for Doctoral Training and Lancaster University. M.J. Joyce acknowledges the support of the Royal Society via a Royal Society Wolfson Research Merit Award.

# Chapter 2

# The potential of imaging low-Z materials via fast-neutron/$\gamma$-ray radiography

M. Licata, M.J. Joyce, I. Tsitsimpelis, D. Clark, B.A. Shippen. *"**The potential of real-time, fast neutron and $\gamma$ radiography for the characterization of low-mass, solid-phase media**"*. Nuclear Instruments and Methods in Physics Research Section A: Accelerators, Spectrometers, Detectors and Associated Equipment. In presss. Available online 18 December 2018. https://doi.org/10.1016/j.nima.2018.12.021.

M. Licata and M.J. Joyce. ***Simultaneous Real-Time Fast-Neutron/$\gamma$Ray Tomography and Radiography.*** Published in: 2018 IEEE Nuclear Science Symposium and Medical Imaging Conference Proceedings (NSS/MIC). 10-17 Nov. 2018. Sydney, Australia. DOI: 10.1109/NSSMIC.2018.8824443

## 2.1 Abstract

Most techniques that are used for transmission imaging with ionising radiation use X-rays, which have the advantage of providing quick, high-resolution images with a relatively small dose of radiation. However, they also have the disadvantage that their penetrating power can be limited in some forms of matter. This can make the discrimination of materials with a low atomic number particularly challenging. Of specific interest in this regard is the need to screen a diversity of man-made items that are heterogeneous and with the tendency to have many interfaces between components that can comprise a diversity of low-mass elements and compounds. These items usually have a compact geometry and a high density of components, which can make them less easy to be imaged quickly and effectively with X-rays. This limit of current screening technology necessitates further stages of examination reducing the ease with which this is done for manufacturing and quality assurance applications. The results presented in this paper demonstrate that, either via fast-neutron radiography or tomography, the

potential exists to discern a variety of low-A compounds from one another. Via Monte Carlo simulations, it will be shown that fast-neutron radiography undertaken with a portable, isotopic radiation source (californium-252), absorption and scattering by the doped polymeric materials yields a degree of distinction from other substances. Considering these results, the state-of-the-art of the technique leading to the realization of a combined, real-time fast-neutron and $\gamma$-ray radiography system will also be presented, as well as the first experimental results.

## 2.2 Introduction

Non-destructive tests (NDT) and inspection techniques have been studied extensively in the last few decades. Radiography and tomography are two of the most used techniques, often drawing on the knowledge developed for medical applications. The majority of such assessments is done with X-rays, thanks to the availability, relatively low cost, practicality and feasibility of this modality, and also due to the widespread availability of X-ray machines. The use of neutrons, albeit less common, has also been studied extensively as a radiation source applied to NDTs [51]; however, due to the less widespread availability of neutron imaging facilities, the use of neutrons is less prominent. Neutrons are attenuated exponentially, as a result of their interaction with matter, but interact differently to photons (by definition) and thus the results of imaging techniques based on them also differs: neutrons tend to highlight features in low-mass and low-density elements and compounds, whereas X-rays have a tendency to depict features associated with relatively high atomic number.

However, X-rays have the drawback that their penetrating power is relatively limited by the materials comprising some compounds and manufactured items, and the discrimination of materials with either similar or a low atomic number, can be challenging. In addition, whilst X-ray screening machines provide high-resolution images, the detection of some hazardous materials remains problematic; for instance, laptop computers and large electronic devices cannot be left inside passenger bags during screening because this can complicate the ease with which they are screened by X-rays [148, 149], due to their compact construction and density. Such devices are of particular interest because of their potential to be used to conceal contraband or, worse, to hide hazardous materials. In this regard, the family of lithium-ion polymer materials (LiPo) [150–152] are of particular interest because of their widespread use in batteries of such electronic devices. Their elemental composition is similar to a number of hazardous organic materials yielding a similar effective atomic number ($Z_{eff}$) and density, which can render their discrimination with X-rays particularly difficult. Neutron radiography and tomography are valid methods to image materials with a high content of hydrogen, carbon, nitrogen, oxygen, and lithium; as shown in [153], thermal neutron imaging methods have been used for the investigation of fuel cells, batteries, hydrogen storage systems and nuclear fuel. Moreover, in [154] both fast neutrons and high-energy X-rays are exploited for the interrogation of air cargo containers, because of their high penetration capabilities.

This paper will present both a Monte Carlo study and experimental results demon-

strating the potential of fast neutrons as a probing radiation to image low-atomic number materials and hazardous compounds. Using Monte Carlo simulations (MCNP6 [126]) to reproduce a tomography system that exploits a californium-252 ($^{252}$Cf) radiation source, it will be shown that a reasonable level of different image contrast between LiPo and a number of candidate hazardous materials is achievable. In particular, the aim of this research is to perform a combined n-$\gamma$ radiography of a laptop battery, in order to show the potential of this particular imaging technique to highlight the presence of LiPo in some laptop batteries. By exploiting the $\gamma$ rays emitted by the spontaneous fission of $^{252}$Cf, additional absorption information about the screened items is obtained. The Monte Carlo simulation results have been taken as a basis on which to develop a simultaneous, real-time fast-neutron/$\gamma$-ray radiography technique. The novelty of this research lies in the use of a single radiation source and detection system for the production and detection of both fast neutrons and $\gamma$ rays, respectively. Moreover, the radioactive source used is relatively low-dose and the system has the potential for deployment for industrial *in-situ* assessments. The *state of the art* of such a project will also be described and the experimental results, namely a fast neutron radiography of a laptop lithium-ion battery, are presented.

## 2.3 Monte Carlo Simulations

Lithium-ion polymers have similar densities with some materials synthesised for use as explosives and with some liquids that can be combined to make hazardous materials. In order to compare the different attenuation indices of these materials under fast neutron and $\gamma$-ray radiation, the tomography system presented in [155] has been used. This computed tomography system is based on a $^{252}$Cf radioactive source and 13 liquid organic scintillation detectors. The choice of $^{252}$Cf has been made because its spontaneous fission produces both fast neutrons and $\gamma$ rays. Therefore, in an experimental scenario, by coupling the detectors to a real-time pulse shape discrimination system (PSD), as done in [31], it is possible to obtain both fast neutron and $\gamma$-ray scans of the sample being analysed, simultaneously.

The tomographic assessment has been simulated by detecting and recording both neutrons and $\gamma$ rays interacting with the detectors after placing the samples in a variety of different positions. Six, 2-cm diameter cylinders of water, water peroxide, acetone, a nitramide-based explosive compound (RDX), trinitrotoluene (TNT) and nitrocellulose (NC) have been scanned together with a 2-cm cylinder diameter of LiPo, as shown in Fig. 2.1. The results of the Monte Carlo simulations are presented in Fig. 2. Concerning the neutron tomography, the image contrast in LiPo is clearly greater than explosives such as TNT, RDX, and NC, whereas the tomography response under $\gamma$ irradiation indicates the potential to be slightly misleading; consider, in particular, the comparison of LiPo with TNT and NC. Interesting results are also the differences in attenuation in water, hydrogen peroxide and acetone for fast neutrons as compared to that of $\gamma$ rays. The two tomographies can also be combined with each other, providing potentially more qualitative information regarding the objects analysed. These results have been taken

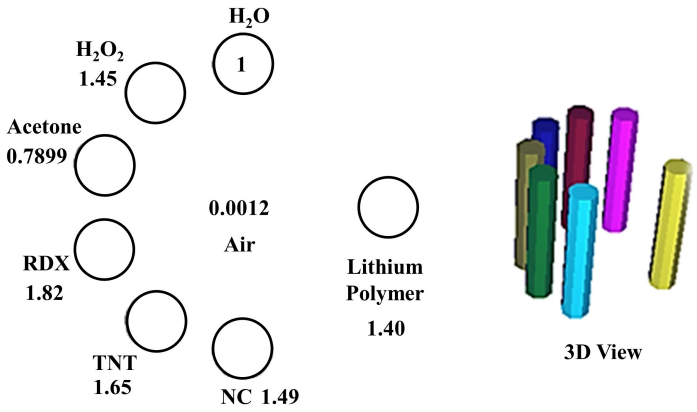


Figure 2.1: A schematic plan view of the phantom arrangement explored in this research (left) and a view in perspective (right); 2-cm diameter cylinders of materials of which the density in g/cm$^3$ is written in bold.

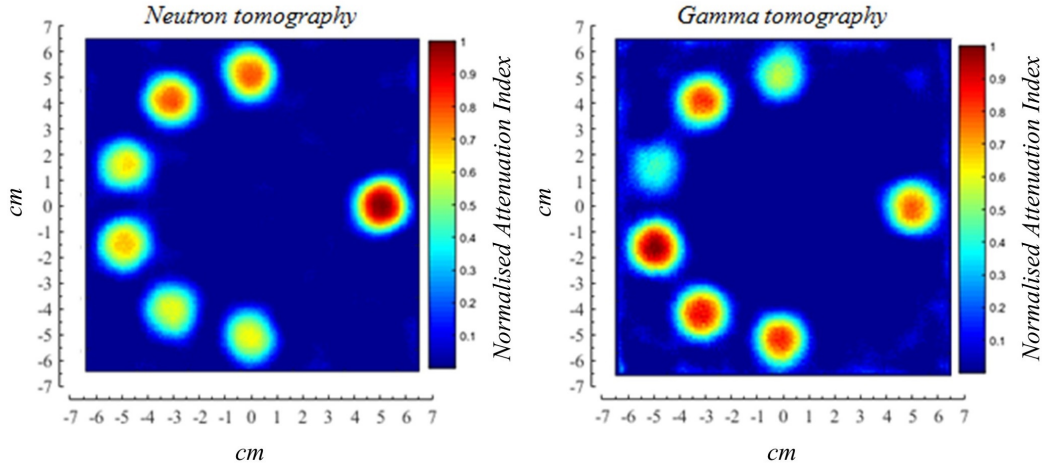


Figure 2.2: Neutron tomography (left) and $\gamma$-ray tomography (right) of the samples and materials described in Fig. 2.1. The image reconstruction algorithm used is the Simultaneous Iterative Reconstruction Technique (SIRT), as explained in [155].

as a basis to develop a real-time, combined (when needed), fast-neutron, $\gamma$-ray imaging technique.

## 2.4 Experimental procedure

Experimentally, a system has been reproduced in order to perform fast neutron radiographs of a laptop, with the aim in this context to highlight the lithium-ion polymer of its battery. The choice of radiography has been made, as opposed to tomography, because a radiograph is quicker to produce relative to a tomograph. Therefore, radiographs are advantageous where measurements are constrained in time and space. The experimental set-up used is shown schematically in Fig. 2.3. The system consists of a $^{252}$Cf

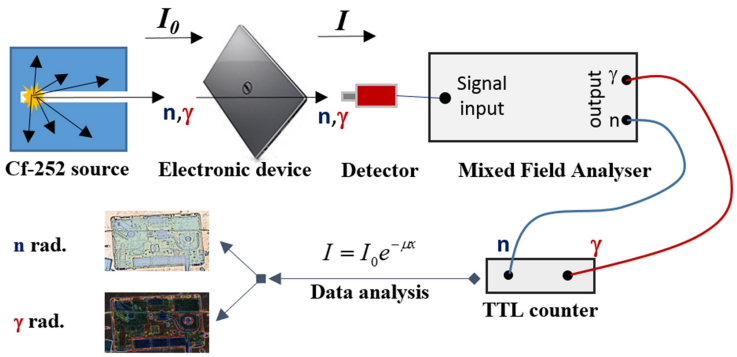


Figure 2.3: Schematics of the experimental setup used.

radiation source of 15 MBq: $^{252}$Cf decays via 96.914% $\alpha$ decay and 3.086% spontaneous fission (SF), the latter yielding an average neutron multiplicity of 3.76 and an average neutron energy of approximately 2 MeV. Neutrons and $\gamma$ rays used in this context are often collimated, for example with polyethylene and lead, to form a pencil-like beam (typical diameter 1 cm). However, in this research, only fast neutron data are presented as the collimator was made solely of polyethylene to focus on the neutron-component of the source of radiation. The radiation field is directed towards the sample under scrutiny (a laptop in this case), which can be scanned in a variety of different positions. Only the portion of the laptop around the battery has been scanned in this research[1]. The laptop was placed perpendicular with respect to the beam direction and scanned horizontally and vertically in 138 different positions (23 along the horizontal axis and 6 along the vertical axis). For each position, the beam intensity after its interaction with the sample has been measured. This is done with an organic liquid scintillator detector (scintillant EJ-301, detector type VS-0653-2 (Scionix [139], liquid scintillant Eljen Technologies, U.S. [156]) connected to a mixed-field analyser (MFA, Hybrid Instruments [157], Fig. 2.4). The discrimination between the detected neutrons and $\gamma$ rays is performed with these real-time pulse-shape discrimination systems [17, 31]. PSD is performed with the pulse gradient analysis algorithm, exploiting the differences in long and short pulse shapes that arise for neutrons and $\gamma$ rays in these scintillation media. Neutrons and $\gamma$ rays are thus discriminated in real time and recorded. The analyser emits each detection event in the form of a 50 ns transistor-transistor logic (TTL) pulse for each event processed from a given detector.

The number of neutron and $\gamma$ ray events in a fixed sampling time and in a fixed sample position has been recorded with a PC running an algebraic image reconstruction algorithm.

The interaction probability of $\gamma$ rays and neutrons can be quantified by the linear attenuation coefficient of the material ($\mu$). Concerning photons, $\mu_\gamma$ depends on the relative probability of photoelectric effect, Compton scattering, and pair production for a given energy distribution of the specific source of photons (X-rays and $\gamma$rays). On the

[1] A description of the scanning system, the developed Graphical User Interface and control system can be found in the Appendix of this thesis.


Figure 2.4: Picture of a single channel Mixed Field Analyzer MFAx1.3.

other hand, the neutron $\mu_n$ depends on the elastic, inelastic and absorption interaction cross-sections. The intensity of the radiation follows the Beer-Lambert law (Eq. 2.1), exhibiting an exponential dependence with the thickness of the material:

$$I = I_0 e^{-\mu x} \tag{2.1}$$

The background induced by the californium source into the laboratory room ($bkg$) has been evaluated and subtracted to the detector readings before and after the sample ($I_{0_n}$ and $I_n$ for the case of neutrons, respectively). This has been measured by closing the pencil-like beam and measuring the neutron radiation produced by the source in the laboratory room. The neutron and $\gamma$-ray attenuation coefficients are thus given by Eq. 2.2 and 2.3:

$$\mu_n = log \frac{I_{0_n} - bkg}{I_n - bkg} \tag{2.2}$$

$$\mu_n = log \frac{I_{0_\gamma} - bkg}{I_\gamma - bkg} \tag{2.3}$$

Data analysis can be done either real-time or off-line, to yield the desired fast-neutron and $\gamma$ radiographs.

## 2.5 Results

A fast neutron radiograph of a HP-Pavilion dv6 laptop computer is shown in Fig. 2.5. The battery location is delineated by the black dotted line overlaid on the radiograph. Qualitatively, the neutron absorption level in the vicinity of the battery is clearly higher than it is for the rest of the laptop. Moreover, a portion of the battery exhibits a level of attenuation that is higher than for the rest of the battery zone. This might concur with where the lithium is located in the cells of the battery structure. The attenuation index has been measured with the Beer-Lambert law and this is shown in Fig. 2.6. The attenuation index was calculated along four different image profiles. Profile

1 indicates the presence of low-Z material in the battery, with respect to the other laptop components within a reasonable level of uncertainty. The minimum and maximum value of the attenuation index of a single experimental point, which constitute one error bar, has been calculated taking into account the standard deviation of the detector counts corresponding to the square root of the detector readings.

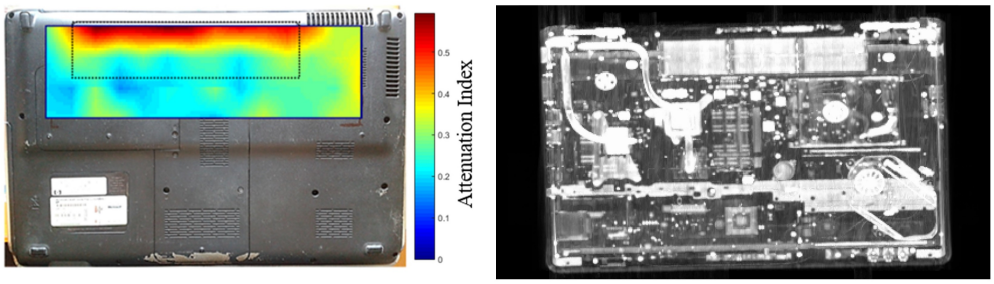


Figure 2.5: A fast neutron radiography of a laptop portion (left), where a high level of contrast infers high levels of absorption and the dotted line indicates where the lithium-ion battery is located in the laptop structure. An X-ray radiograph of the laptop taken at the Henry Moseley X-Ray Imaging facility in Manchester, UK. The image reconstruction algorithm used is the Algebraic Reconstruction Technique (ART).

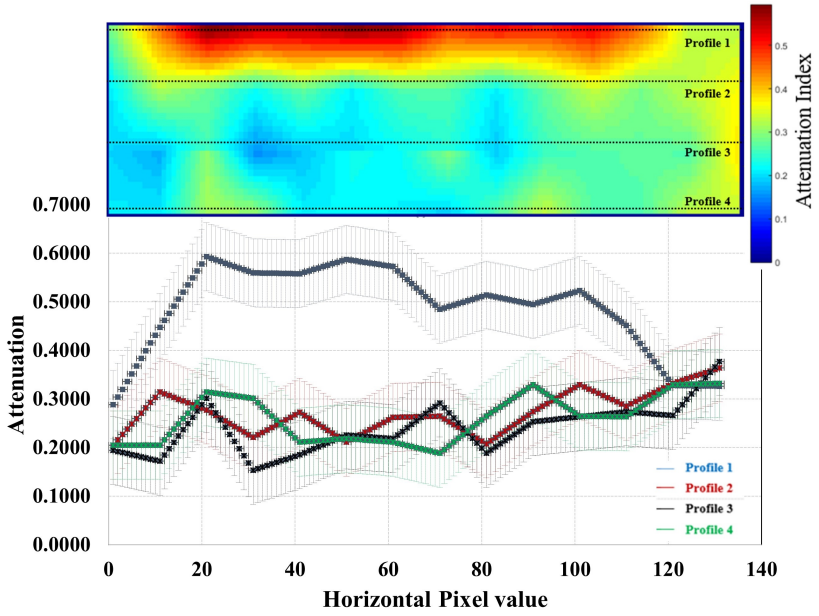


Figure 2.6: The attenuation index profile and its uncertainty across four different image profiles (bottom) and the location of the profiles indicated as per the diagram (top).

For comparison purposes, an x-ray radiograph of the laptop has been carried out using a Rapiscan RTT110 machine, which is of the same prototype of the systems used widely in airport security checks. This scan was taken at Henry Moseley X-ray imaging facility of the University of Manchester, UK, and is shown in Fig 2.5b. The battery can be seen clearly inside the laptop to the upper left of this image. The level of image

contrast, however, is different from that of the fast neutron radiograph, in which only half of the battery has higher contrast than the rest of the battery. Such a result opens several areas for future consideration.

A second experiment was carried out subsequently, focusing only on the laptop battery, who was extracted from the laptop and scanned alone, with the same system set-up. The results regarding the fast-neutron, $\gamma$-ray and combined n-$\gamma$ radiography are shown in figure 2.7a. The neutron radiography results show a different level of absorption in

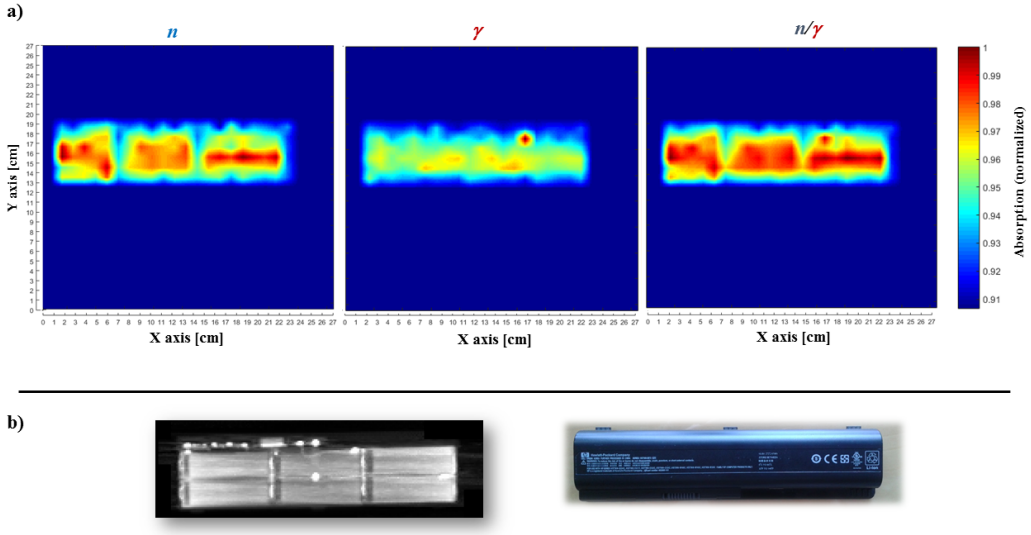


Figure 2.7: a) from left to right respectively: fast neutron, $\gamma$-ray and combined neutron-$\gamma$ radiograph of a lithium ion battery. b) the X-ray scan of the battery alone (left) and a picture of the same HP-Pavilion dv6 laptop battery.

three specific regions of the battery, in contrast to the results of the $\gamma$ radiography, which instead suggest a more uniform attenuation index across the battery. A possible reason for this is that the energy of the $\gamma$ rays produced by the californium does not produce a high level of image contrast, except for a spike on the right side of the battery. The low attenuation is consistent with the relatively high energy of the $^{252}$Cf $\gamma$ rays (around 1 MeV); therefore, the majority of them pass through the battery media; the spike in contrast can be interpreted as a metallic junction inside the battery. On the other hand, the neutron radiography suggests the presence of three battery cells, within which the attenuation index is in turn distributed non-uniformly. The combined neutron-$\gamma$ radiography data set has been obtained merging the neutron and the $\gamma$ radiograph. This shows both the metallic spike and the battery cells. However, in this particular case, it does not allow discrimination between the metallic spike and the cell polymer. In order to understand its inner structure, the battery alone was also scanned with the Rapiscan RT110 machine of the Henry Moseley X-ray imaging facility. The image of the battery, extracted from the entire laptop, shown in figure 2.5 appears to have three cells only, that are clearly visible on the top side of the laptop, however, the image contrast appears uniformly distributed. Undertaking a more accurate and detailed radiography

of the battery only (see figure 2.7b.), the cells depicted are instead six in number. Still, the image grey-level is relatively constant across the cells, except the battery metallic junctions, which appear as white spikes.

X-ray radiography machines do not provide material identification, but they rely only on particular fingerprints, unique of some materials and, qualitatively, compounds of comparable density are imaged with the same contrast-level. This fact stimulates the investigation to the use of explosive simulants in place of the battery. Most explosives have similar densities and effective atomic numbers to LiPo; therefore, X-rays do not provide discrimination, unlike neutrons, as shown by the Monte Carlo simulations described in the previous section.

In addition, the design and the composition of the battery has to be determined in order to identify the exact composition of the battery compound; this would be a "cross check" in order to understand where the lithium is located so this can be used to better understand the experimental results and as a proof of concept. The X-ray machine used to scan the laptop, as well as the machines used in most airports, do not provide material identification and therefore compounds with a similar density appear with the same level of image contrast. This opens up the use of some explosive simulants and organic hazardous materials in place of the battery, in order to understand whether they can be discerned from the Li-ion polymer under neutron radiography, as demonstrated by the aforementioned Monte Carlo simulations. Finally, since lithium ions move into the battery, the concentration of these is subject to change in the battery itself; therefore the potential to discern the level of battery charge/discharge under neutron irradiation should be investigated more in detail, as well as the combined, simultaneous, real-time fast neutron and $\gamma$ imaging technique presented in this work. The combination of these two imaging techniques has the potential to provide more absorption information of the objects under investigation and to allow material identification.

## 2.6 Conclusion

The potential of the development of a real-time fast neutron and $\gamma$-ray imaging system suitable for characterization of low-mass, solid-phase media, has been presented in this paper. The novelty of this research is that it highlights the potential for a method to discern low-Z materials in laptops and electronic devices that are potentially confused by established methods of image-based screening in security applications. This imaging method has the potential to be coupled with the already-existing advanced cabin baggage screening systems, improving their detection performance and possibly reducing the reaction time of the screener. Moreover this method shows its potential to provide quick and reliable information when high levels of image sensitivity are required and would also be suitable particularly for manufacturing and product quality assurance applications. The possibility to discern charge-state of a given, electronic battery configuration is also presented. This fast-neutron/ $\gamma$ ray radiography or tomography (when needed) technique can be applied in several different engineering fields, when high levels of security or quick non-intrusive inspections are required.

Future research will investigate the potential to discern charge-state of a given, electronic battery configuration, as well as investigating different levels of charging. In addition, further research is needed to elucidate the system geometry, for instance, spatial resolution and the system response to different materials can be improved increasing the number of detectors coupled with the use of different beam geometries (i.e., fan and/or cone beam).

## 2.7 Acknowledgments

The authors acknowledge the support of the UK Research and Innovation (UKRI), the Lloyd's Register Foundation, the Next Generation Nuclear (NGN) Centre for Doctoral Training, Lancaster University. The authors would like also to acknowledge Dr. Tristan Lowe, Dr. Julia Behnsen and the Henry Moseley X-Ray Imaging facility. M. J. J. acknowledges the award of a Wolfson Research Merit Award by the Royal Society.

# Chapter 3

# Backscatter, fast-neutron/$\gamma$-ray tomography

M. Licata, M. D. Aspinall, M. Bandala, F. Cave, S. Conway, D. Gerta, M. J. Joyce, H. M. O. Parker. **"*Depicting corrosion-born defects in pipelines with combined neutron / $\gamma$ ray backscatter: a biomimetic approach*"**. Scientific Reports 10, 1486 (2020). https://www.nature.com/articles/s41598-020-58122-3.

## 3.1 Abstract

The identification of corrosion, cracks and defects in pipelines used for transporting oil and gas can reduce the possibility of leaks, and consequently, it can limit the extent of an environmental disaster, public hazard and the associated financial impact of such events. Typically, corrosion in oil pipelines is measured with non-destructive ultrasonic or electromagnetic techniques, on the basis that corrosion and defects are often manifest as a change of thickness in the steel from which pipelines are made; however, such approaches are not practical for underground pipelines and their deployment can be complicated for the case of pipelines covered by insulation. In this paper, we present an innovative, non-destructive testing technique, which exploits the backscatter of a combination of fast-neutron and $\gamma$ radiation from steel samples of a variety of thicknesses consistent with changes that might arise due to corrosion of a pipe wall. Our research demonstrates the potential to measure and characterise different steel thicknesses by detecting both the elastic, fast-neutron backscatter, and the Compton-scattered $\gamma$ radiation, simultaneously. Further, we demonstrate that the presence of insulation yields a consistent and separable influence on the experimental, wall-thickness measurements. The data from experimental measurements are supported by a comprehensive Monte Carlo computer simulation study.

## 3.2 Introduction

The processes by which mechanical and electromagnetic waves are reflected by materials, are phenomena exploited by a variety of animal species for orientation, to procure food and for a great diversity of other purposes. A biomimetic relationship exists in this regard between the natural world and technological human achievements, exemplified on the one hand by the reliance of some species of mammals (predominantly bats) on ultrasound, with which to hunt, avoid predators and even to classify different types of plants [159–163], and on the other by sonar [164]. The latter is central to a wide variety of non-destructive, industrial assessment techniques and a related international industry, such as the measurement of distance, density, porosity and imaging. Similar analogies exist for the case of reflected electromagnetic waves, e.g., sight, radar [165] etc.

Amongst the first observations of the scattering of particles are those of Rutherford in his famous gold foil experiments (1908-1913). At the atomic scale, the reflections of waves and particles approach one another phenomenologically, and offer one of the founding scientific observations supporting wave-particle duality. In this regard, neutron scattering and its applications are perhaps amongst the most remarkable and tangible exemplars of quantum-mechanics. As to whether a scattering process is elastic or inelastic is inferred by the corresponding isotopic cross section, calculated on the basis of neutrons affording properties of complex plane waves. Below the MeV range in energy, the radiation wavelength is much greater than the range of the strong nuclear force (of the order of femtometres) that is responsible for scattering from a single nucleus. This renders neutron scattering, according to the first-order Born approximation, isotropic. Similarly, the same approximation, is applied in radar [166, 167].

Scattered radiation is exploited in several non-destructive assessments. Electron backscatter is the principle of the scanning electron microscope [168], muon scattering tomography has been tested for nuclear reactor core imaging [169], monitoring volcanic activity [170] and the detection of chambers in pyramids [171]. X-ray backscatter radiography (BCT) has numerous applications in safety and security inspection, particularly for the detection of dangerous materials and border inspections [172], biomedical science [173], engineering and industry, such as the oil and gas sector and aerospace [174–176]. The advantage of backscatter radiography and tomography is that they allow the investigation of items that cannot be scanned with the most widely-used axial computerized tomography (CT), due to either the large size of the item and inability for it to be moved, or because the transmission image data is not interpreted easily. Elastic neutron scattering is usually used to assess water content, porosity and hydrogen fraction in rocks [177, 178], and to identify the presence and assess the level of water, gas, wax, paraffin and/or defects in pipelines [179–183]. Elastic scattering cross sections and the loss of energy after a single scattering event are fundamental to many non-destructive, fast-neutron backscatter techniques. In comparison with X- and $\gamma$ ray, fast neutrons penetrate deeper into high-Z matter, due to their lack of charge, and thus high-density materials can be investigated. X- and $\gamma$-ray backscatter is the result of the Compton effect; its probability depends on the electron density of the material. On the one hand,

this makes X- and $\gamma$ rays particularly suitable for the investigation of heavy metals, but, on the other, limits the extent to which they can be used to probe relatively thick material samples, because high-Z media attenuate them significantly.

In this research, the backscatter of fast neutrons and $\gamma$ rays is used to identify different carbon-steel thicknesses. Our approach is to exploit and possibly combine two different imaging techniques, performed real-time, simultaneously with a single source-detection system. Defects in steels, as well as corrosion and rust, produce a variation of the mean density and of the thickness of the steel comprising the pipe wall; therefore the backscattered neutron and $\gamma$-ray flux induced by a radiation beam changes.

Pipelines are subject to several types of corrosion. It can be internal or external. The former is mainly due to galvanic corrosion, microbiological reasons, stray currents and selective seam weld corrosion, and is often exacerbated by the presence of crude oil, hydrogen sulphide, carbon dioxide, various natural gases, vapours and water [184, 185]; the latter is caused by a pipeline carrying a corrosive commodity, low-pH aqueous media and erosion. The quantification of corrosion-born defects is particularly important for industries that rely on many thousands of kilometres of pipelines for transporting resources and also to inform estimates of resources required to replace compromised pipeline parts. Statistical results show that, in the U.S., the U.K and Europe from 2010 to 2015, 24% of failures in gas pipelines and 25% in oil pipelines, were due to corrosion. Failures in pipelines can cause economic losses, environmental pollution, injuries and casualties. Failure frequencies of oil pipelines range from 0.4 to 0.6 times/kkm/yr in the U.S. whilst gas pipelines failure ranges from 0.04 to 0.14 times/kkm/yr [186]. The primary form of corrosion is pitting, and numerous mathematical and numerical models have been studied to predict the specific corrosion rate of this [187–189]. The evolution of corrosion pitting over time is considered constant, universally, with a linear damage-velocity rate. Corrosion depth depends on the time $t$ according to $\alpha t^{\beta}$, with $\alpha$ and $\beta$ constants that depend on the system, the pipeline environment and type of corrosion [190]. These constants are evaluated from in-field measurements and come from fits to corresponding data. These measurements to yield such data, as well as the experimental estimation of corrosion rates, are usually carried out with periodical in-line inspections

Most in-line inspections are carried out by means of Pipelines Inspection Gauges (PIGs) based on ultrasound [191–193]. However, ultrasound requires a coupling medium, such as oil, and therefore these inspections are mainly applied to liquid lines and not for gas pipelines. Our approach is, to some extent, complimentary to the ultrasound technology, since it probes the pipeline from outside, and demonstrates potential to be able to measure different steel thicknesses in the presence of insulation (i.e., pipelines covered by layers of concrete and polyethylene). We present a radiography/tomography system in which a mixed radiation field (comprising neutron and $\gamma$), produced by a californium source ($^{252}$Cf), is collimated with a combination of lead and polyethylene to produce a pencil-like beam of probing radiation (it is anticipated that a portable neutron generator could be used in place of an isotopic source if necessary). Finally, this is directed toward the steel under consideration. The induced fast-neutron and $\gamma$-

ray backscattered flux has been measured with four organic liquid scintillation detectors with the collimator described above, to constitute a prototype connected to a mixed-field analyser (MFA), providing real-time, digital, pulse-shape discrimination (PSD) [16], to yield transistor-transistor logic (TTL) signals that are retained and recorded with a digital counter. A mechanical rig enables the source-collimator arrangement to raster across a sample to afford scans of each steel sample under inspection. This system, as described, enables combined, simultaneous, fast neutron and $\gamma$ ray backscatter imaging.

A variety of steel thicknesses have been investigated with the influence of insulation replicated by placing a layer of concrete and high density polyethylene (both of 1-cm thickness) above the steel. The novelty of combining different imaging modalities leads to improved discrimination of contrasting material thicknesses, particularly when layers of concrete are used to replicate insulation of this type covering a pipe. The contrasting properties of neutrons and $\gamma$ rays, allows a fine depiction of pits in pipelines, from both a qualitative and a quantitative point of view. By analogy with the natural world, the collimated beam of neutrons and $\gamma$ rays can be compared to the chirp generated from bats, which is a superposition of different ultrasound wavelengths, read simultaneously after their interaction with the surroundings, by the same ear-detector. Furthermore, the sensitivity modulation of the sensory system to their own self-vocalised, ultrasonic pulses in some bat species [194], which is understood to enable the return to be better isolated, constitutes an evolutionary feature comparable to the collimator in our system. This, albeit infinitely more crudely, blinds the scintillation detectors from the direct, un-scattered component that would otherwise perturb the sensitivity of the system to the backscattered component. Similarly, some nocturnal moths have evolved wings that absorb ultrasound, suppressing the echo that the bat receives and rendering the moths invisible to these predators [195, 196]. It appears likely that the nature of the backscattered return provides the bat with a significant amount of information as to the type and extent of material around them, as to whether it is solid, diffuse, moving, stationary, etc.

## 3.3 Results

### 3.3.1 Detection system and neutron-$\gamma$ collimator

The neutron and $\gamma$-ray flux backscattered from a variety of different steel slabs were measured with a system designed for this purpose comprising: a mechanical rig, collimator and an array of small, organic scintillation detectors (Scionix, Netherlands) which were connected to a multiple-channel, mixed-field analyzer (Hybrid Instruments Ltd) and to a bespoke embedded control system. Measurements were carried out at the low-scatter neutron facility at the National Physical Laboratory (NPL), in Teddington, London, UK. The rig-source-collimator-detector system consists of an aluminum frame in which two stepper motors have been configured to afford the system two degrees of freedom (in the X-Y plane, Fig. 3.1a, 3.1b). The collimator is designed to constrain the neutron and $\gamma$ radiation generated by the $^{252}$Cf to a defined area of interest of the steel

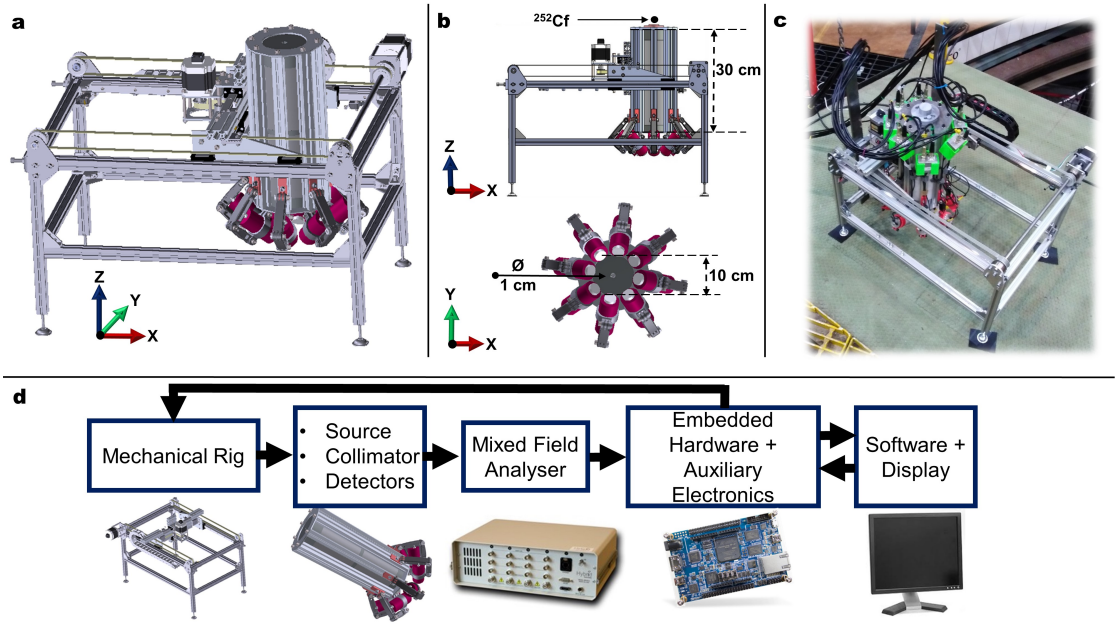


Figure 3.1: **System assembly**. (a) A 3-dimension CAD design of mechanical rig, collimator and detectors, designed, assembled and demonstrated in this research. (b) The elevation (top) and plan (bottom) CAD views of the system, with a focus on the collimator-detector combination. The collimator is made of layers of lead and polyethylene, height: 30 cm, external diameter: 10 cm and internal diameter of the pinhole: 1 cm. The radiation source is placed above the collimator, concentrically with the pinhole. (c) A photograph of the system built, deployed and used at the low-scatter facility of the National Physical Laboratory. (d) A sequential schematic of the experimental set-up: the mechanical rig, controlled remotely by software running on a laptop, drives the system comprising the source, collimator and detectors. The detectors are connected to a multiple-channel, mixed-field analyser, which digitises the detected events, separates the neutron and $\gamma$ ray signals and sends a corresponding transistor-transistor logic signal for each event to an embedded digital counter that is linked by Ethernet to a computer. The entire system is coordinated and controlled by a graphical user interface.

sample, comprising cylinders of high-density polyethylene (HDPE) and lead (Pb).

Organic liquid scintillation detectors of type EJ-301 [197] are secured in a fixed angle of orientation with adjustable arms. Up to eight detectors can be used in the geometrical configuration shown in Fig.3.1. However, it has been found that four detectors enable the total geometric efficiency to be optimised, i.e., maximising the area of the hemisphere subtended by the detectors. The position of the radiation-sensitive liquid-volume in the detectors has been configured to be in a region of the space below the collimator sheltered from the radiation flux that streams from the 1-cm diameter, collimator pinhole (Fig.3.1b and 3.2a). With this particular approach, the detectors are isolated from the incident flux but, at the same time, they are positioned sympathetically with the trajectory of the backscattered flux generated at the focus of the radiation beam collimated by the pinhole. The beam-and-detector focus-area is the point where the radiation beam reaches the surface of a given sample, and it is located approximately 10 cm after the collimator aperture (Fig. 3.2a).

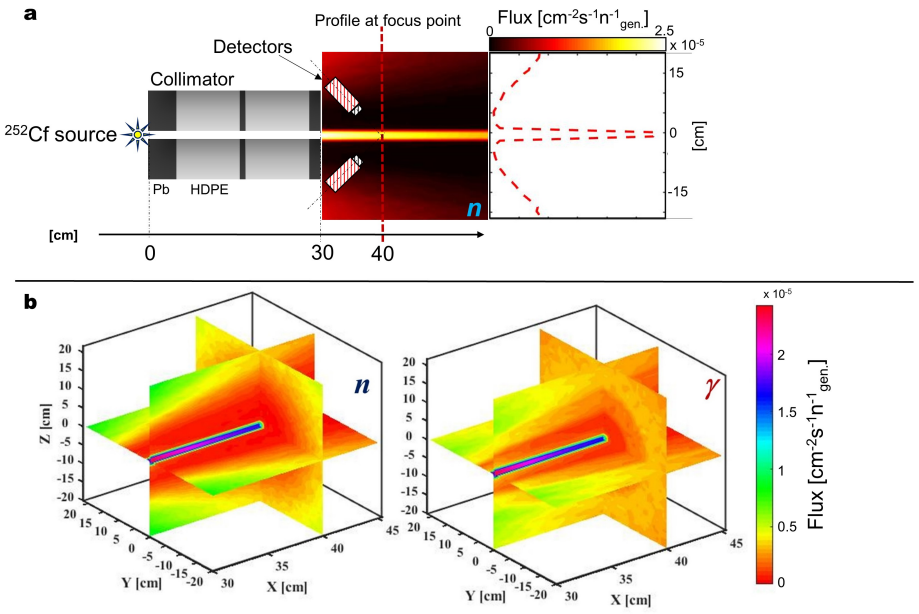


Figure 3.2: **Collimator modelling**. (a) A schematic representation in elevation of the source-collimator-detector arrangement (from left to right) combined to demonstrate the relative, quantitative significance of the fast neutron flux throughout. The colour heatmap depicts the neutron flux leaving the collimator, whereas the plot on the right presents a quantitative measure of the same flux along the dotted red line passing through the detector focus point. (b) An MCNP6, 3-dimensional quantitative illustration of both fast neutron (left) and $\gamma$ ray flux after the collimator aperture, demonstrating the relatively small component of the direct field impinging on the detectors, consistent with the fundamental concept explored in this research.

An extensive Monte Carlo computer simulation study was performed in order to identify the best collimator geometry and detector position. MCNP6 [128, 129] (Monte Carlo N-Particle transport code), developed in Los Alamos National Laboratory [127], is the tool used to model the experiment and compute the simulations. The results are presented in Figs. 3.2a and 3.2b. Neutron and $\gamma$-ray flux are shown in 3-dimensions for the X-Z, X-Y and Y-Z planes. In particular, the plots show the flux beyond the collimator aperture, with the Y-Z plane modelled at X = 40 cm, i.e., approximating to the radiation focus at the sample. Detectors are located at circa 5 cm from the beam, in the position of minimum flux.

### 3.3.2 Calibration

The EJ-301 detectors were calibrated prior to the backscatter measurements by setting the high-voltage of the photomultiplier of each detector, to yield a balanced response across all four units, and the pulse-shape discrimination parameters were adjusted via the MFA to optimise the discrimination between neutrons and $\gamma$ rays. Using a 17 MBq $^{137}$Cs source, the voltage of the scintillator photomultiplier was adjusted to align the caesium Compton edges (at ~478 keV) to the same ADC channel (Fig. 3.3, left, inner plot on the top). The use of the $^{137}$Cs source ensures a response to $\gamma$ rays of a single energy

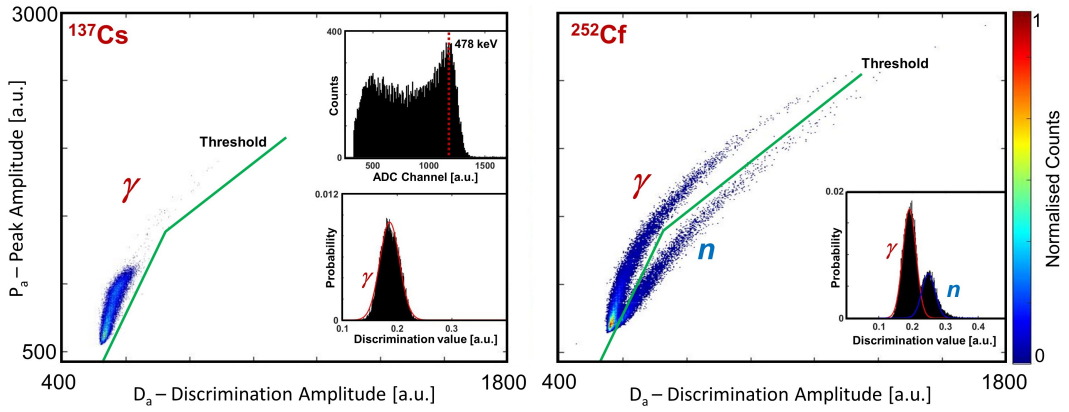


Figure 3.3: **Pulse shape discrimination**. **Left**: A scatter plot (peak amplitude versus discrimination amplitude) of the $\gamma$ radiation generated by $^{137}$Cs with an EJ-301 detector in this research. The peak and discrimination amplitudes are respectively the maximum signal amplitude and the signal magnitude measured after a fixed discrimination-time. The top-inner plot is the Compton spectrum when an EJ-301 is exposed to $\gamma$ rays from $^{137}$Cs, whereas the bottom-inner histogram is the discrimination value of the $\gamma$-event produced with $^{137}$Cs. **Right**: A scatter plot obtained with an EJ-301 scintillation detector exposed to $^{252}$Cf in this research. The upper plume corresponds to the $\gamma$ component of the mixed field produced by $^{252}$Cf, whereas the lower plume corresponds to the neutron component. The inner histogram (lower-right) shows the discrimination values for n-$\gamma$events produced by $^{252}$Cf. Signals have been normalised and their baseline removed. The discrimination data have been fitted (red lines) with Gaussians.

(662 keV), thus making possible to set the discrimination threshold on each individual scintillator, using only the $\gamma$ plume (Fig. 3.3, scatter plot on the left). Pulse-shape discrimination is performed by the MFA via a pulse gradient analysis algorithm [46]. The discrimination value (i.e., the ratio between discrimination amplitude and signal peak amplitude) of each $\gamma$ event generated by the aforementioned caesium source was also calculated. The results (Fig. 3.3 left, inner plot on the bottom) show the presence of a single peak, consistent with only $\gamma$ radiation being present for the case of the $^{137}$Cs source. Subsequently, $^{252}$Cf was used in order to verify the n-$\gamma$ response of the scintillators and to verify the PSD threshold settings. Two separate plumes were observed (Fig. 3.3, scatter plot on the right) consistent with an appropriate PSD setting; two peaks are also observed when the discrimination value of the mixed neutron/$\gamma$ field events is plotted as a histogram.

### 3.3.3 Neutron-$\gamma$ backscatter

When a narrow, collimated radiation field hits a material, part of its radiation is transmitted, part is absorbed and part is backscattered (Fig. 3.4a). The flux of backscattered radiation, as a function of the material thickness, is related closely to the linear attenuation law,

$$\Phi_{tr}(x) = \Phi_0 e^{-\mu x} \tag{3.1}$$

where $\Phi_{tr}$ is the transmitted component for a thickness $x$, of the initial flux $\Phi_0$, $\mu$ is the linear attenuation coefficient for a field comprised by $\gamma$ rays, whilst it corresponds to the total macroscopic cross section ($\Sigma_{tot}$ in radiation fields constituted by neutrons [36]. The backscattered flux can be expressed as,

$$\Phi_{sc} = \Phi_0 - \Phi_{abs} - \Phi_{tr} \tag{3.2}$$

where $\Phi_{abs}$ is the absorbed component of the radiation flux, for a thickness $x$. Thus, the scattered flux is given by,

$$\Phi_{sc} = \Phi_0(1 - e^{-\Sigma_{tot}x}) - \Phi_{abs}. \tag{3.3}$$

If the radiation encounters a combination of different materials (see example depicted in Fig. 3.4b), whilst the physical principle is the same, the mathematical model becomes more sophisticated because both scattered and absorbed components derive from the superposition of effects from each of the different compounds. Figure 3.4c presents the measured, experimental backscattered neutron flux as a function of the steel thickness measured in this research; the backscattered neutron flux was assumed to be isotropic but this is not the case for $\gamma$ rays, since Compton scattering is not isotropic. These experimental data are compared with the mathematical model presented in equation 3.3. Experimental results are presented with both $\pm 1\sigma$ and $\pm 3\sigma$ standard deviation and demonstrate consistency with the model given in equation 3.3.

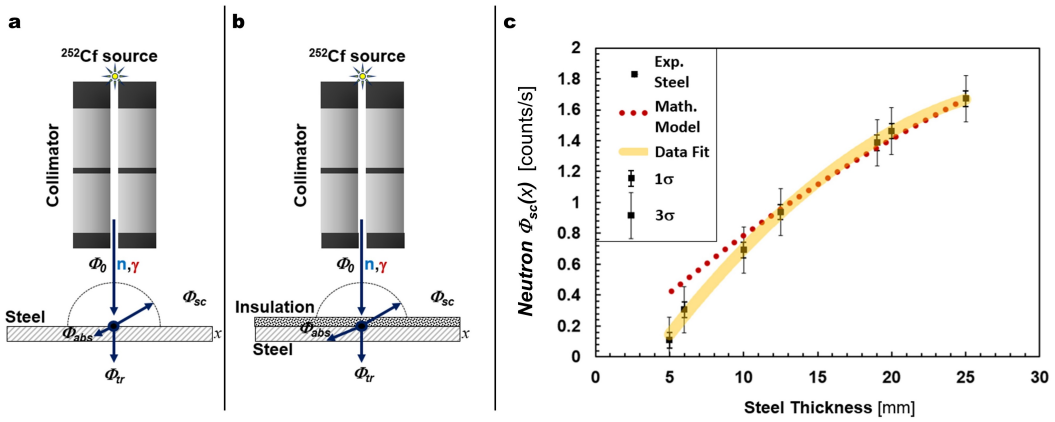


Figure 3.4: **Mathematical relationship**. (a, b) Schematic illustrations of the mathematical model developed in this research for steel and a combination of steel and insulation. (c) Backscattered neutron flux versus thickness of bare steel. The yellow band represents a second-order polynomial fit to the data, of $\pm 1\sigma$ spread. The theoretical model is represented by the red dotted line. $\Sigma_{tot}$ has been estimated using the tabulated neutron cross sections from ENDF/B-VII.1 of the National Nuclear Data Center [39].

The flux of backscattered neutron and $\gamma$ rays are presented in Fig. 3.5a, as a function of the steel thickness in the presence of a 1-cm thick layer of high-density polyethylene and 1-cm thick layer of concrete to illustrate the effect of insulation on the technique. The reflected neutrons and $\gamma$ rays were measured over a period of 20 minutes for each individual sample of steel, for a total of 1 hour per slab given the three cases as fol-

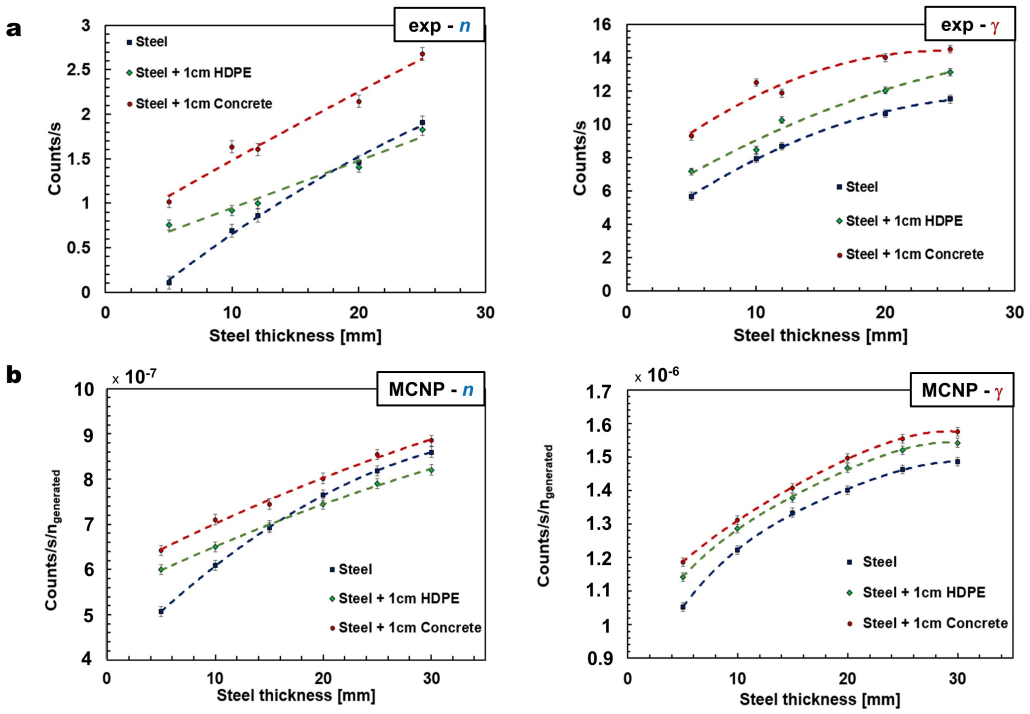


Figure 3.5: **Experimental and simulation results**. (a) Experimental results for neutron (left) and $\gamma$-ray (right) backscatter in terms of counts per second versus steel thickness, for bare steel (dark blue symbols), steel with 1-cm thickness polyethylene insulation (green symbols) and steel with 1-cm thick concrete as insulation (red symbols). (b) Results of Monte Carlo simulations performed with MCNP6; neutron (left) and $\gamma$-ray (right) backscatter in terms of normalised counts per second, per neutron generated in the Monte Carlo simulation, versus steel thickness, for bare steel (dark blue symbols), steel with 1-cm thickness polyethylene as insulation (green symbols) and steel with 1-cm thickness concrete as insulation (red symbols).

lows: bare steel; steel and polyethylene; and steel and concrete. The results from these measurements are compared qualitatively with the corresponding results from MCNP6 simulations (Fig. 3.5b) obtained prior to the experiment. In this case, uncertainties are presented as $\pm 1\sigma$ and the fit to the data is a second-order polynomial function.

The possibility of $\gamma$ rays arising from inelastic neutron reactions exists but this is anticipated to be small for the energy of the neutrons from $^{252}$Cf and therefore this has not been accounted for in this research. If sources with harder neutron spectra are considered for this application, such as AmBe or D-T generators, then this influence would need to be quantified.

### 3.3.4 Combined Neutron-$\gamma$ backscattered tomography: a case study

For the case of neutron and $\gamma$-ray backscatter from a sample comprising steel and concrete (included by way of insulation), a relevant scenario is that of a steel pipeline of 25-mm wall thickness, insulated with concrete and which is to be scanned to identify regions of corrosion. Using the experimental data of Fig. 3.5a (red dotted curves) of such a 25-mm pipeline, an exemplar pipe tomography study has been conceived and is

presented in Fig. 3.6. Two different regions of different thicknesses have been inserted

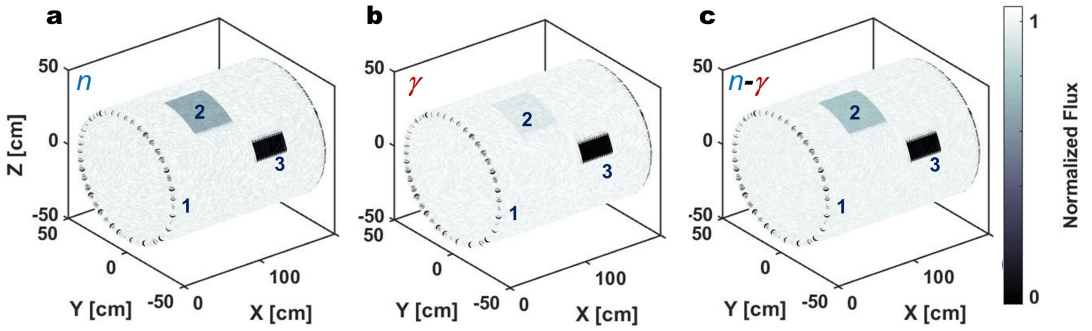


Figure 3.6: **Neutron-$\gamma$ imaging**. Fast neutron (a), $\gamma$ ray (b) and combined n-$\gamma$ (c) backscatter tomography of a 25-mm thick pipeline of 40 cm radius. The different regions of pipe wall thickness are identified as per: region 1 denotes the unadulterated 25-mm thick region of pipe, 2 and 3 indicate the 20-mm and 5-mm thick regions included to illustrate contrasting degrees of corrosion severity, respectively. The backscattered flux has been normalised and plotted using greyscale, as is used by convention in tomography studies.

deliberately, and positioned randomly in the pipeline wall to emulate regions of corrosion. The first region is 5 mm thick and the second region 20 mm (Fig. 3.6a, denoted by numbers 2 and 3). The experimental backscattered flux from each of these features has been reproduced and imaged, together with the backscattered flux of the original 25-mm thick pipe. Figs. 3.6a, 3.6b and 3.6c show the fast neutron backscatter tomography (FN-BCT), the $\gamma$-BCT and the combined n-$\gamma$ BCT, respectively, for this case. The 5- and 20-mm regions, that render the steel respectively 20- and 5-mm thick, are clearly discernible using fast neutrons, whereas the 5-mm pit-area is not easily-discernible scanning the pipe with $\gamma$ rays in isolation. Combining the two different imaging modalities, it is still possible to identify the two areas of reduced thickness. However, this scenario can arise in reverse, that is, depending on which materials are scanned, the neutron tomography data that results might mislead, in contrast to the $\gamma$-ray case, as explained in previous work for transmission tomography [31, 155].

### 3.3.5 System Sensitivity

The minimum time necessary to discern between different thicknesses of steel with and without insulation, can be correlated with the sensitivity of the system. Hypothetically, when the number of accumulated counts from the detectors is plotted as a function of time, backscattered counts arising from contrasting wall thicknesses will have similarly-contrasting gradients or count rates. In this particular circumstance, after a given observation time $t$ has elapsed, the error ($\sigma$) on the counted number of events (N) is the square root ($\sigma = \sqrt{N}$), assuming Poisson statistics. Equation 3.4 describes the minimum time needed to differentiate two different thicknesses of the same material,

within a sensitivity of $n_\sigma$= 1, 2, 3... standard deviations,

$$t \geq \left( \frac{n_\sigma[\sqrt{tg\alpha} + \sqrt{tg\beta}]}{tg\beta - tg\alpha} \right)^2 \equiv \left( \frac{n_\sigma[\sqrt{N_1} + \sqrt{N_2}]}{N_2 - N_1} \right)^2 \tag{3.4}$$

where $N_1$ and $N_2$ are the counts, at a given time $t$, of the two thicknesses. An illustrative example with respect to this sensitivity formulism is given in Fig. 3.7a. Here,

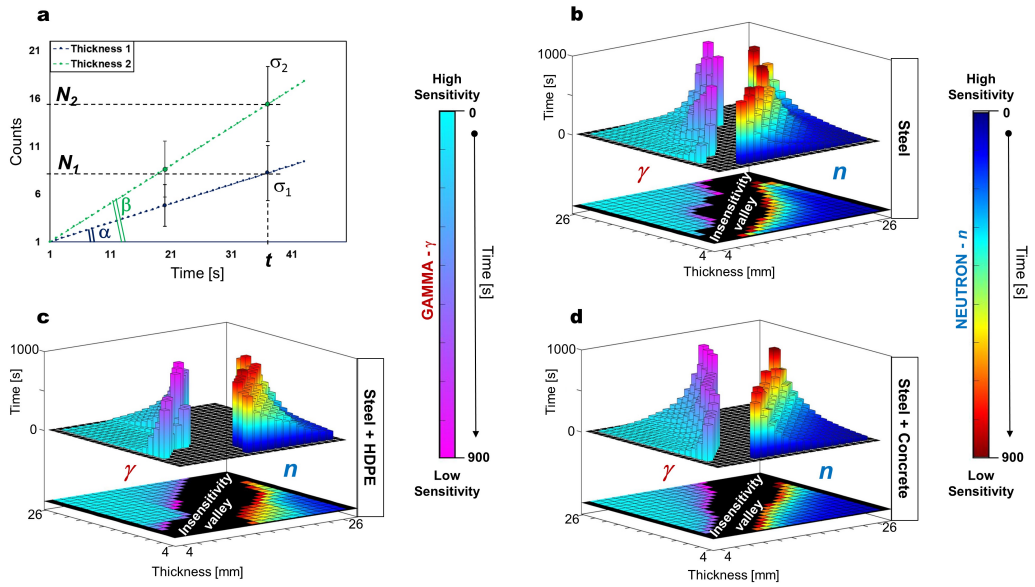


Figure 3.7: **Sensitivity matrix**. (a) Qualitative and quantitative example of the minimum time needed to separate two different backscattering counting rates with different standard deviations. (b, c, d) System sensitivity matrices for $\gamma$ rays (colour map light blue-to-magenta type) and neutrons (colour map blue-to-red) regarding steel (b), steel and polyethylene (c) and steel and concrete (d). The colour scale levels in the matrices, coupled with the height of the histograms, indicate quantitatively and qualitatively the time. Times above 900 seconds are cut and plotted in black (depicted by the valleys between the neutron and $\gamma$ ray histograms).

equation 3.4 has been used to construct a sensitivity matrix for neutrons and $\gamma$ rays, for the system tested with bare steel (Fig. 3.7b), steel with polyethylene (Fig. 3.7c) and steel with concrete (Fig. 3.7d). The left side of the matrices in Figs 3.7b, 3.7c, 3.7d corresponds to $\gamma$ rays and the right to neutrons. Two different colour maps for $\gamma$ rays and neutrons have been used to separate the sensitivity of each, and a 900-second cut-off on the minimum measurement time necessary to distinguish two thicknesses has been set deliberately, on the basis of what is anticipated to be an acceptable limit in the field. Generally speaking, times lower than this value allow the discrimination of difference in thicknesses from 5 mm and upwards. For the identification of possible pits of less than 5 mm depth, the measurement time required increases exponentially, at which point this technique starts to become impractical. The sensitivity matrix presented here has been calculated with the experimental data presented in Fig. 3.5a, using a $^{252}$Cf source with an emission rate of $8.7\times10^6$ neutrons/second into $4\pi$. The sensitivity can be improved and thus the experimental exposure time reduced using a source of higher activity. Al-

ternatively, shielding the detectors in order to reduce false-negative scattering events due to background and cross-talk between detectors could also improve the sensitivity.

## 3.4 Discussion

The results presented in this paper demonstrate that it is possible to discern different thicknesses of steel slab with a combination of fast neutron and $\gamma$-ray backscattering. Our research was carried out using organic liquid scintillators, although a diversity of organic scintillators exists which could be similarly applied; for example stilbene might constitute a valid alternative to the EJ-301 used in this research if a liquid scintillant is not desirable in the application field. Organic scintillators, coupled with the real-time PSD system used in this research, are particularly suitable because their detection efficiency falls sharply for energies below $\sim$1 MeV for neutrons and below 200 keV for $\gamma$ rays. The elastic scattering cross sections for neutrons in the range 1-10 MeV, are of the same order of magnitude for the majority of elements (between 1 barn and 10 barns). However, since the neutron energy loss after an elastic collision is far greater for low-atomic number materials, incident fast neutrons can fall below the detection energy threshold of the scintillator detectors when scattered. This fact, for example, explains the difference in slope in the responses for steel and steel-polyethylene for neutrons in Figs. 5a and 5b, since HDPE is rich in hydrogen relative to concrete, and thus moderates neutrons more effectively. For small thicknesses (i.e. $\leq$ 15 mm), the polyethylene-induced backscattering is higher than that measured with bare steel. As the steel thickness is increased, the number of elastic neutron collisions also increases; therefore, before reaching the detector, the backscattered neutrons pass through an extra thickness of polyethylene, accruing a higher probability of falling below the energy threshold for detection, and thus reducing the proportion of the backscattered component that is detected. Conversely, this does not occur for $\gamma$ rays because Compton scattering depends on the atomic number of the material, which is relatively low for polyethylene compared to that of steel, and consequently, the gradient of the $\gamma$-ray backscatter count dependence with thickness is similar for all three sample arrangements. Our results are consistent with what is predicted on a qualitative basis by the MCNP6 simulations for both neutrons and $\gamma$ rays. The mathematical relationship elaborated for neutrons overlaps the neutron experimental data for the case of bare-steel, in the range 6-25 mm, when results are presented within $\pm 3\sigma$ from the mean. The novelty of this research lies, *in primis*, in the demonstration of a non-destructive imaging alternative to the widespread modality of X-ray computed tomography. Moreover, this technique comprises the parallel application of both neutrons and $\gamma$ rays, leading to three different final illustrations of a given sampler (i.e., n-, $\gamma$- and n-$\gamma$-BCT). Read together, these yield a more comprehensive and faster representation of the inner structure of steel and possibly, other materials. Our research highlights and confirms the potential of combining different imaging modalities. Not only does this technique have applications in an engineering context, but it may also have potential in wider materials science applications such as for quality assessments of metals and materials, and also in a wide range of different scenarios, ranging from the medical field

(as proposed by [198]) to safety and security inspections, and particularly where in situ examinations are required. This research not only highlights the benefit of combining the effects of contrasting reflection phenomena for technological requirements, such as non-intrusive corrosion assessment; it also illustrates the significant potential that can accrue from our primitive mimicry of sensing modalities that have evolved for analogous requirements in the natural world.

## 3.5 Methods

### 3.5.1 The mechanical rig

The rig frame is made from an assembly of 20×20 mm aluminium extrusions, it has dimensions 600×400×340 mm (L×W×H). The collimator sits within the aluminium frame and is mounted to four guide rails, two in both the X- and Y-axis, respectively. This gives the collimator the freedom of movement in the X-Y plane, actuated using a stepper motor and pulley system. A symmetrical array of detectors are mounted to a cylindrical assembly using Go-Pro arms. The assembly is made from eight aluminium extrusions around 360deg with aluminium plates top and bottom; the cylindrical components of the collimator itself sit flush within the extrusion assembly. The entire assembly has a height of 311 mm and a diameter of 140 mm. On the top plate of the assembly, a bespoke 3D-printed component is mounted to house the isotopic source directly above the collimator void. The rig is controlled using an Arduino microcontroller board which interfaces with the user's device via USB. All electronic components on the rig are controlled by the Arduino which receives commands from the user. The user specifies coordinates relating to a position in the X-Y plane, the Arduino then handles the calculation necessary to get to the desired position. Limit switches at the end of each axis are used to calibrate the positioning of the collimator assembly as well as a fail-safe to prevent it from driving off the rails.

### 3.5.2 Control system and counter

The acquisition system consists of a printed circuit board (PCB) that contains an Intel Cyclone V FPGA / ARM Processor system. A set of sixteen 32-bit transistor-transistor-logic (TTL) compatible counters were configured on the FPGA. The system uses a 50 MHz clock signal and Phase-locked Loop (PLL) logic allowing pulses of less than 1 $\mu$s width to be detected. The 4-channel MFA produces TTL signals from separate output ports dependent on whether a neutron or a $\gamma$ ray has been detected. The 4 $\gamma$-ray outputs and the 4 neutron outputs from the MFA were connected up to the aforementioned 16-channel counter (thus up to 8 detectors can be used: 8 channels for neutron detection and 8 channels for $\gamma$ ray detection). The Cyclone V ARM Processor system runs an embedded version of Linux capable of interfacing to the described logic in the FPGA part of the integrated circuit. A bespoke program developed in C++ was written to monitor the status of the 16-channel counter in real time. This monitor program utilised the TCP/IP Protocol to send data to a PC at a specified frequency.

The counters can be set to either count-rate mode or cumulative mode for calibration and measurement operations, respectively. A bespoke program was written in C♯ for a PC, with an accompanying Graphical User Interface (GUI). This program has the ability to configure the aforementioned counter modes via the TCP/IP Protocol. This application also creates files to log all the information received from the FPGA board. Additionally, the application controls the actuators of the mechanical rig through the pre-configured serial port.

### 3.5.3 The National Physical Laboratory low-scatter neutron metrology facility

It is located at the National Physical Laboratory in Teddington, London, UK. The room is 23 m long, 17 m wide and 18 m high. Walls are shielded by approximately 1 m of concrete [199]. The measurements in this research were carried out on a ground-elevated mobile platform, known as the pit-circle, roughly 6 m high. This particular platform can be accessed via a low-density, mobile, walkway.

### 3.5.4 Radiation sources

A $^{252}$Cf source with an emission rate of $8.727\times10^6$ neutrons/second ($\pm$ 0.6% at $1\sigma$) and an approximate activity of 76 MBq, has been used for this research. The source anisotropy factor in the position with which the source was used, is 1.022. The source is encapsulated in a 1 cm diameter cylinder of stainless steel. The $\gamma$ source used for the detector calibration was $^{137}$Cs, with an activity of 17 MBq.

### 3.5.5 Detectors stability, flux evaluations and background level

The whole experimental set up was assembled approximately 20 hours prior to the start of the experimental measurements. Detectors, mixed field analyzer, electronics, embedded hardware and control software were turned on and their functioning monitored and verified. The stability of the detectors, with and without neutron and $\gamma$ irradiation, was also demonstrated both in the laboratory at Lancaster University and at the National Physical Laboratory. Within 48 hours, during the preliminary tests carried out at Lancaster University, the counting rate of the detectors were observed to be constant over elapsed time. The baseline level of neutron and $\gamma$-ray background at the low scatter facility was measured, as well as the background level induced by the $^{252}$Cf source in the room. Albeit being a low-scatter facility, a low-level of background is present due to the interaction of the radiation with air, room walls, laboratory and experimental components. This background was subtracted from the readings of the detectors when performing the data analysis. Finally, the mixed radiation flux from the collimator ($\Phi_0$, see eq. 3.3) was evaluated carefully for each individual detector. This value has been 10 times higher than the value of the background induced by the californium source and measured by the detectors when placed in the position hidden by the collimator (see, for instance, Fig 3.1b and 3.2a), confirming experimentally the validity of the simulations

and collimator function.

### 3.5.6 MCNP6 simulation

The final design of the collimator is the result of a detailed MCNP6 simulation study that has been performed in order to optimise the system geometry, materials and system characteristics. The collimator is a cylinder of 10-cm diameter and 30-cm length. It has a 1-cm diameter pinhole which allows the passage of the mixed field radiation produced by the aforementioned radiation source. Three layers of lead (respectively of 3 cm, 1 cm and 2 cm) and two layers of high-density polyethylene (12 cm thickness each) shield the detectors from the radiation emitted by the source. The experiment carried out has been modelled as accurately as possible with MCNP6 simulations. Six steel thicknesses (from 5 mm to 30 mm) of a pipeline have been reproduced in this way. Neutrons and $\gamma$ rays for scattered events from the pipeline wall have been tallied simulating the EJ-301 detectors and its liquid scintillant. The collimator and $^{252}$Cf source have also been modelled in the experiment-simulation. The steel (0.3% carbon component), concrete (Hanford type, dry) and polyethylene model details are listed in the Radiation Portal Monitor Project, Compendium of Material Composition Data for Radiation Transport Modelling [200].

## 3.6 Acknowledgements

The authors would like to thank the National Physical Laboratory for the use of the low scatter facility, in particular N. Roberts and G. Taylor for the help during the experimental campaign and for providing us the radiation sources. The authors wish to acknowledge: Lancaster University, the Engineering and Physical Sciences Research Council (EPRSC), the Next Generation Nuclear Centre for Doctoral Training (NGN-CDT) and the Lloyd's Register Foundation (both supporting the Ph.D. studentship of M.L.) and Innovate UK, for supporting this project. M. B. acknowledge the UK Engineering and Physical Sciences Research Council (EPSRC), supported by the grant EP/R02572X/1 (National Centre for Nuclear Robotics).

## 3.7 Authors contributions

F.C. managed the supporting project on behalf of Hybrid Instruments Ltd., contributed to technical discussions and to the paper. M.J.J. conceived the original premise for the research, the life sciences analogy adopted in the paper, contributed to the paper and supervised the related PhD studies of M.L. M.L. primary author of the paper, proposed the back scattering technique, collimator design, led the analysis, conceived the concept for the sensitivity formulism, performed MCNP simulations. H.P. proposed the back scattering technique, performed MCNP simulations and preliminary experimental tests/measurements. M.A. supervised D.G. and S.C, performed the experimental measurements, contributed to technical and design discussions and to the paper. M.B.

performed the experimental measurements, developed the counter system, control software and system electronics, cooperated to the conceptualization of the rig design. S.C. performed the experimental measurements, designed the mechanical rig, and collaborated to the development of the counter system, control software and system electronics. D.G. performed the experimental measurements, designed the mechanical rig, and cooperated to the development of the counter system, control software and system electronics. N.R. and G.T cooperated, assisted and advised during the experimental campaign at the National Physical Laboratory. All authors contributed to the preparation of the manuscript.

# Chapter 4

# Fast Neutron Activation Analysis: simulations and measurements at IPN Orsay

The objective of the work presented in this chapter is to demonstrate the utility and the potential of combining fast neutron activation analysis with fast neutron tomography. This work presents a Monte Carlo simulation study based on the experiments carried out at the ALTO facility [201, 202] of the Institute of Nuclear Physics d'Orsay (IPN Orsay - Paris, France). In addition, preliminary experimental evidence of such measurements is also presented, pending a complete data analysis, currently in progress.

## 4.1 Introduction

Most neutron-induced reactions are followed by the emission of secondary particles, in particular $\gamma$ rays, protons and electrons. These reactions therefore have the consequence of activating some materials, namely, the nucleus becomes radioactive. In the vast majority of cases there is some $\gamma$-ray emission, which can be immediate (prompt $\gamma$ rays) or with long half-life (delayed $\gamma$ rays).

The spectroscopic analysis of neutron-induced $\gamma$ rays is the subject of the work presented in this chapter. In particular, $\gamma$ rays produced by the inelastic scattering of neutrons on metals are studied. This type of analysis is called, within the scientific literature, neutron activation analysis (NAA) and involves different types of neutron-induced reactions. The most common type of NAA is that with thermal neutrons (TNAA). For instance, when a sample is irradiated with a thermal neutron beam and viewed by a high resolution $\gamma$ spectrometer, it would be possible a qualitative and quantitative analysis of the neutron-capturing elements present in the sample. The most common example is hydrogen, which captures a neutron to become deuterium, which in turn emits a 2.223 MeV $\gamma$ ray. The research presented here, however, deals with fast neutron activation analysis (FNAA), i.e. the analysis of $\gamma$ rays generated by the interaction of fast neutrons with the sample under examination. The capture cross section, for fast neutrons, is very

low, and they interact mainly by means of elastic or inelastic scattering. This produces high energy $\gamma$ rays due to the excitation of the nuclei in the irradiated material.

In the literature a considerable number of works about neutron activation analysis [203], can be found, in particular related to nuclear physics [204–206], archaeometry [207], chemistry [208–210], neurology [211], geophysics [212] and numerous other fields. As previously stated, most of the works deal with thermal neutrons, however, fast neutron activation analysis, sometimes called neutron stimulated $\gamma$ emission, plays an important role, as well. Furthermore, the latter has been also investigated, in an attractive study, in order to verify the feasibility of FNAA to perform neutron stimulated emission computed tomography [213].

Two factors have developed enormously over the past 20 years, allowing NAA to evolve. The first is the increasing availability of neutron generators, even portable, although they are still quite expensive. They allow research that previously were only allowed in some laboratories, making FNAA an interesting research field, with possible numerous applications. The second factor is the development of large, high-resolution $\gamma$-ray detectors, that have made possible more precise measurements.

Broadly speaking, the principles of FNAA are the same of TNAA, with the difference that instead of detecting the $\gamma$ rays produced by neutron capture, the detection of $\gamma$ rays signatures produced by nuclear excitation induced by neutrons in certain isotopes, is exploited.

FNAA allows quantitative measurements when analysing the intensity of the signatures detected. For instance, in [214], FNAA has been applied for the detection of explosives and narcotics. Their structure, mainly composed by carbon, nitrogen and oxygen (C-N-O), produces peaks of fixed energy, with different C/O, N/O and C/N ratios. Inelastic carbon scattering, for example $^{12}$C(n,n')C, releases a signature at 4438 keV, while oxygen $^{16}$O(n,n')$^{16}$O has a transition at 6128 keV and one more intense $\gamma$ ray at 7115 keV, whilst nitrogen, $^{14}$N(n,n')$^{14}$N at 5104 keV. To excite nuclear levels of this energy, neutrons of greater energy than the energy transition level are needed. Within the cited research, 14 MeV neutrons, produced by a portable neutron generator that exploits the DT reaction, are used.

Many metals, have slightly lower energy nuclear levels [215, 216] than CNO-based molecules, of the order of a few hundred of keV and up to 1-1.5 MeV. For these, neutrons of 14 MeV are not always necessary and neutrons of lower energy, of the order of 2-2.5 MeV, as demonstrated in this research work, may be sufficient.

In the research presented here, a neutron beam of about 2 MeV is directed towards samples of different metals. Relatively high-energy $\gamma$ rays are produced by the interaction of the beam with the metals and are detected by germanium spectrometers located above the samples and out of the beam direction path. A plastic scintillation detector, based on 8×8 photomultipliers measures the intensity of the beam after its interaction with the metals. These samples are continuously translated and rotated and, for each position, it is possible to measure the beam attenuation and determine the energy of the $\gamma$ rays generated. The novelty of this research lies in the fact of combining FNT with FNAA,

in order to obtain qualitative and quantitative information on the samples investigated. The fact that metals emit $\gamma$ rays of fixed energy in response to neutron exposure, allows material identification, and to identify the spatial distribution of isotopes, within the material. Spatial information is given by the FNT, while the identification of the isotope itself would be provided by the FNAA. Another innovation lies in the fact of applying an image reconstruction technique to the FNAA with the aim of reconstructing the spatial distribution of a certain element within the material. In particular, in this study, an iron-56 block and a copper-63 cylinder are exploited as case studies to prove the concept of the paired FNT-FNAA. This work shall be understood as proof of concept and aims to highlight the potential of the technique. It should also be stressed that such research study does not pretend to be a rigorous, detailed-quantitative work, but rather a qualitative work, which aims to present the potential of an imaging technique still in the process of being matter of research.

## 4.2 The IPN ALTO facility

ALTO stands for "Linear Accelerator and Tandem at Orsay". The facility (figure 4.1) is powered by two accelerators: a 15 MV Tandem and a 50 MeV linear accelerator (e-Linac), both dedicated to the production of radioactive beams. The main lines of research concern astrophysics and basic nuclear physics.


Figure 4.1: A schematic image of the ALTO facility of the Institute of Nuclear Physics d'Orsay. Image from [202].

The Tandem is a an electrostatic based accelerator. Ions are produced negative charged with an ion source, and subsequently pre-accelerated and injected into a low-energy acceleration tube and directed towards the positive high voltage terminal. Here, the ions pass through an electron stripper made of a carbon foil and loose the electrons and therefore their negative charge, acquiring a positive one. Thus, they are accelerated again through an high energy accelerator tube. The ALTO Tandem can supply beams of 75 different isotopes, from hydrogen (proton beams) to gold (Au). These beams are

usually represented by 20% of light ions, such as protons and helium, and 60% of heavy ions, from lithium to iodine and the remaining 20% of $C_nH_m$ ion clusters.

The LINAC, (LINear ACcelerator, figure 4.2) accelerates charged particles or ions to high energies, by injecting them into a linear beam line made of a series of oscillating electric potentials. The ALTO e-Linac (e stand for electrons) beam line is focused by 2 dipole magnets and 6 quadrupoles. The beam, composed by electrons, is directed towards a target located in a bunker. Such a target consists of 150 uranium carbide ($^{238}UC_x$) discs of 14 mm in diameter and 1 mm in thickness. Using a 50 MeV electron beam with a current intensity of 10 $\mu$A, approximately $10^{11}$ fissions/s are generated. The facility can send radioactive beams up to 5 different experimental areas. The fission fragments emitted by the interaction of the beam are ionized and transported onto a system that contains a mass separator. Rare beams as well as neutron beams of different energies can thus be produced and exploited.

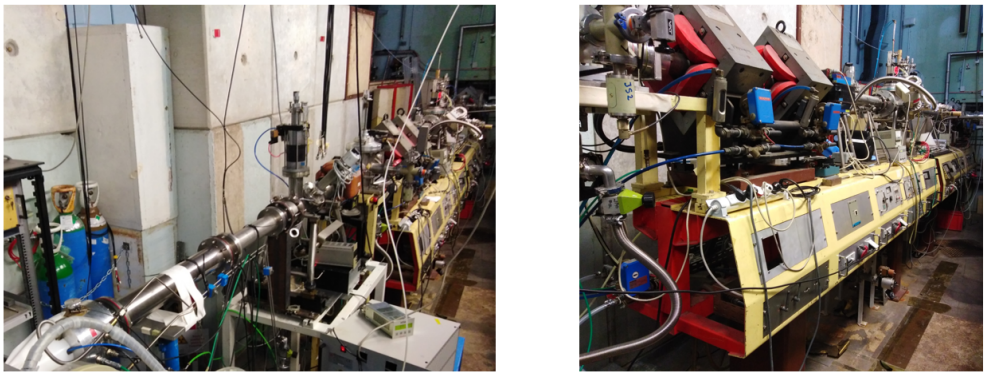

Figure 4.2: A picture of the Linac at IPN Orsay. On the left: final part of the beam line. On the right: main part, with two quadrupoles that can be spotted on the top.

## 4.3 Experimental set up

The measurements were carried out irradiating several metallic objects with a neutron beam of energy *circa* 2 MeV, produced by the Linac with the reaction

$$p + {}^7Li \rightarrow n + {}^7Be$$

bombarding with protons a lithium target. The neutron beam produced has been properly collimated with a 15 cm thick paraffin cylinder, with an internal pinhole of 1 cm diameter, in order to produce a cone beam with a relatively small divergence. The paraffin collimator was placed at the end of the beam line. The neutrons generated, after interacting with the objects under investigation, hit a plastic scintillator consisting of 8×8 photomultipliers.

Two High-Purity Germanium (HPGe) detectors were placed above the neutron beam path, and above the scanning plane (see schematics in figure 4.3). These spectrometers must detect only the high energy $\gamma$ rays produced by the samples, due to the inelastic scattering reaction of fast neutrons with the metals. Due to this purpose, the germanium spectrometers are further shielded from the beam and from possible interactions

with scattered neutrons as well as from $\gamma$ rays induced by secondary reactions, in the laboratory room. Furthermore, the shielding is needed both to avoid radiation damage of the detectors, as HPGe are easily damaged by neutrons, and to reduce the background level due to unwanted $\gamma$ rays. Lead was the material chosen for the shielding, which is both an excellent material for stopping $\gamma$ rays and a good neutron reflector.

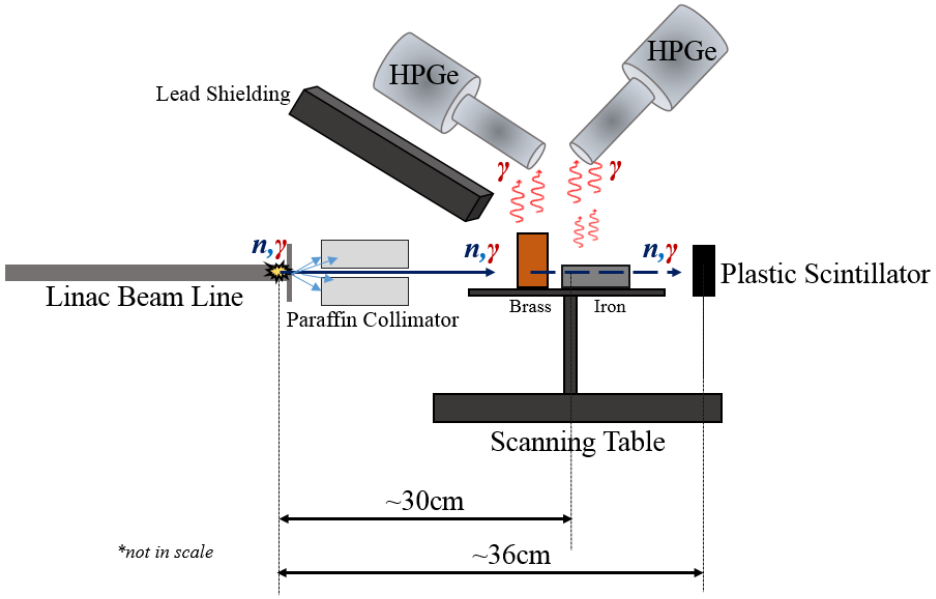


Figure 4.3: Schematics, not in scale, of the experimental setup (side view).

The source-to-object distance, i.e. from the source to the centre of rotation plane, was approximately 30.5 cm while the source-to-detector distance circa 36.5 cm. The scans were performed by continuously translating and rotating the samples, which were fixed onto the rotating table plane. This turntable was connected to the data acquisition system (DAQ), as well as the detectors, in such a way as to be able to trace the position of the rotating table as well as the number of events detected for a given sample position.

The plastic scintillators were calibrated prior to the experiment, with a weak, small-dose of californium-252 whilst the germanium detectors were calibrated with different sources, including europium-152 and cobalt-60, to have a calibration in energy up to about 2 MeV. Scintillation detectors reveal both the $\gamma$ rays present in the beam, the background $\gamma$ rays, the $\gamma$ rays produced by beam interactions with irradiated materials, and finally, most importantly, they detect fast neutrons after their interaction with the materials. The signals, generated by $\gamma$ rays and fast neutrons, are recorded and processed offline, by means of pulse shape discrimination (PSD) algorithms.

Several objects were examined in 4 different experiments: in the first two experiments, objects of known metals such as a block of iron measuring 3×5×13 cm and a brass cylinder of 5 cm diameter were irradiated. This experimental set up is shown in figure 4.4. In the second measure the complexity was increased, adding other metals. Experiments 1 and 2 ran for three hours each. In the third and fourth experiments, objects of unknown composition and shape were placed in two different black boxes and

hermetically sealed. These measurements lasted 12 hours each.

At the present stage of writing this thesis, the data analysis of these experiments is still ongoing[1]. However, some preliminary results and some results of a Monte Carlo simulation study are presented in the next section.

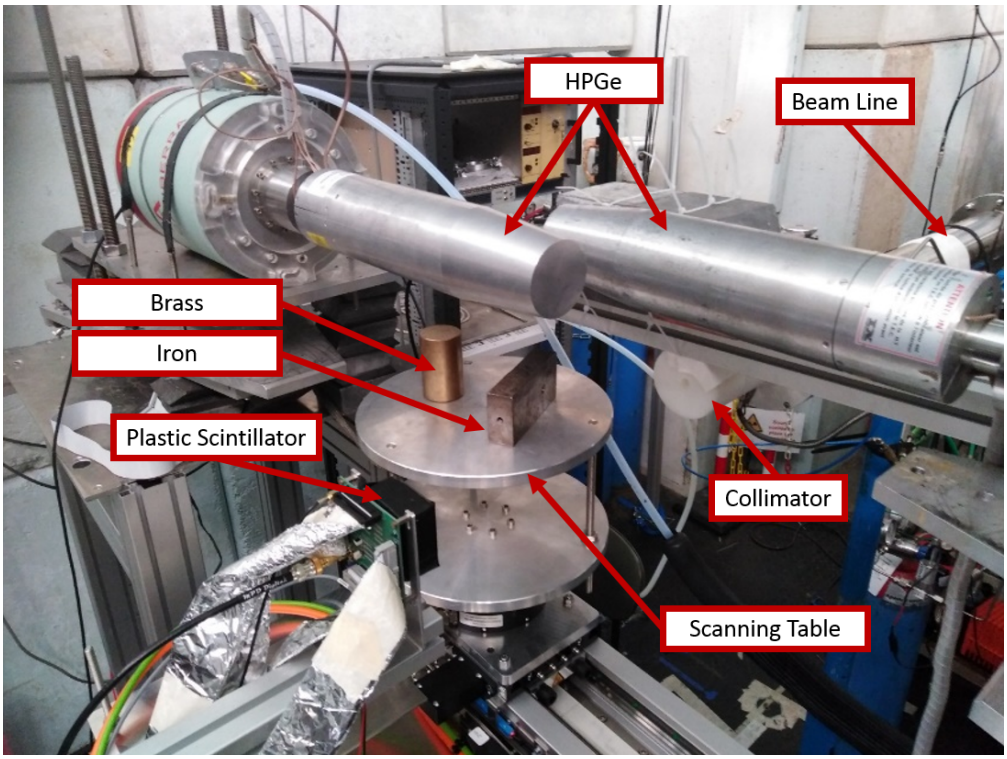


Figure 4.4: A picture of the experimental setup. The plastic scintillator is from the University of York, whereas the HPGe is from IPN Orsay.

## 4.4 Simulations, preliminary studies and first experimental evidences

A Monte Carlo study was carried out with the MCNP6 simulation tool, already addressed during this thesis. A similar measurement to that done at IPN Orsay, albeit with several approximations and differences below described, was reproduced in MCNP6, focusing on the behaviour of some metal isotopes under neutron irradiation. The metals under investigation are $^{56}$Fe and $^{63}$Cu. This choice lies in the fact that $^{56}$Fe and $^{63}$Cu have the first level of nuclear excitation respectively at 847 keV and 962 keV. Other isotopes of these metals have energy levels either much lower, or above a certain threshold for which the 2 MeV neutrons do not have sufficient energy to excite their nuclear levels.

This study was approached with the same principles of the study presented in chapter 1 of the results part. The present work has been an opportunity to test the image reconstruction code developed and described in the aforementioned chapter, applied to a different framework. It has to be emphasized that this study was conducted not

[1]The data analysis is being carried out by other researchers of the University of York and IPN Orsay, whilst the Monte Carlo simulations were carried out at Lancaster University, by the author of this thesis.

with the aim of modelling the experiment carried out at the ALTO facility in detail, but with the aim of investigating and studying its foundations and implications, with the possibility of extending it to new lines of research. For this reason, instead of using a *quasi*-monochromatic 2 MeV neutron source as it was used in the experiment, a californium-252 source was modelled in the simulation. Californium-252 has an average neutron energy of about 2 MeV and moreover it produces $\gamma$ rays, as already discussed in the previous chapters. This fact opens up the possibility of testing 3 different imaging modalities: two modalities, fast-neutron and $\gamma$-ray tomography obtained with the plastic scintillator, give spatial information of the objects under examination; while the third modality, obtained from germanium spectrometers by selecting only fixed $\gamma$-ray energy lines, gives information about the materials.

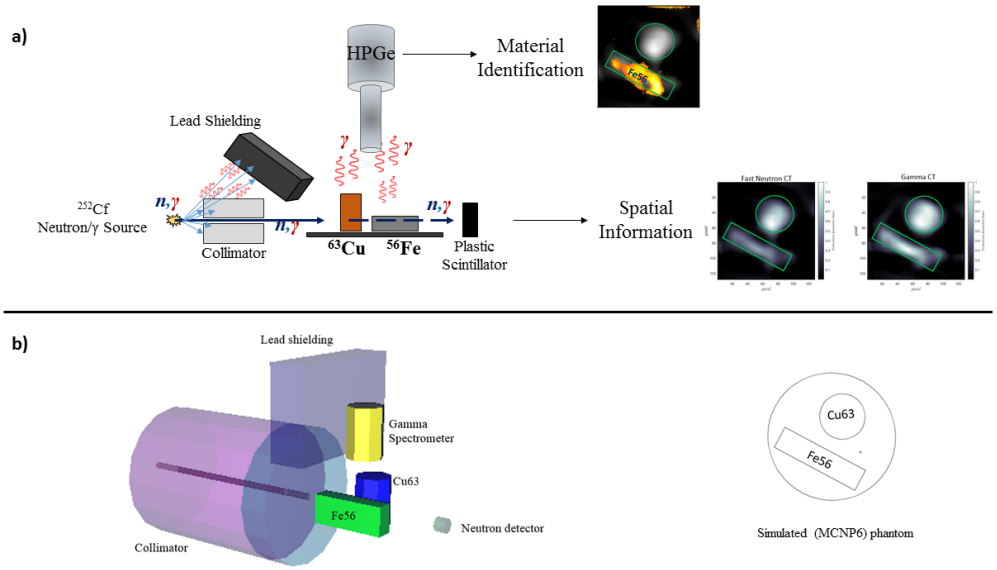


Figure 4.5: Illustration of the foundations for the three-modality tomography and schematics used within the MCNP6 simulations. On the bottom left, a 3D view of the MCNP6 simulation is shown, while on the bottom right a section (view from the top of the samples analysed can be visualised.

The simulation was then setup with the same schemes as the simulations presented in chapter 1. The difference lies in the source-to-object and source-to-detector distance for which those used in the experiment were reproduced. In addition, a plastic scintillator was also modelled as well as a germanium detector, shielded with lead, and placed above the beam line and the scanning plane. Finally, a cone beam was produced using as a collimator layers of high density polyethylene and lead, in order to properly collimate both neutrons and $\gamma$ rays.

The beam has been directed towards the objects: a block of $^{56}$Fe of dimension 10×4×2.5 cm and a cylinder of $^{63}$Cu of diameter 5 cm and 7 cm of height. These have been scanned in 3660 projections[2]: 61 translations × 60 rotations (6° step over 360° ). Every sample position corresponds to a projection and to a different simulation.

[2]3660 projections correspond to 3660 different sample position and therefore simulations, for a total running time of approximately 10 days

100 million neutrons were generated per simulation.

Each simulation scored three different features: the total neutron fluence at the plastic scintillator, the total $\gamma$ ray fluency at the plastic scintillator and $\gamma$ ray spectrum measured with the germanium detector. The physics of the detectors was not modelled, therefore all the neutrons and $\gamma$ rays passing through the detector were scored, considering thus an efficiency of 100%. This approximation was mainly due to time reasons: a computer simulation considering all variables and parameters would have required an amount of resources not available at the stage when the simulations were carried out. However, it has to be highlighted that the purpose of these simulations is to give an idea purely qualitative, without pretending (yet) to have accurate, quantitative results.

Making use of the projection data and the simulation results, the neutron tomograph was generated, in order to analyse the spatial information of the objects being studied. Subsequently, with the $\gamma$ data spectra (one spectrum per projection were created by the simulation), the $\gamma$ counts of the 847 keV peak ($^{56}$Fe), ware selected per projection and the $\gamma$ image was thus generated. This process was repeated selecting the 962 keV peak of $^{63}$Cu.

The algebraic reconstruction algorithm used was SIRT, reported in the appendix, since the number of projections was relatively small (see chapter 1 for a detailed explanation). A different approach, such as the filtered back projection (FBP), could be used for the analysis of the experimental data, as the experiment was conducted with a continuous and repeated scan, which allows for a very large number of projections. However, the FBP can only be applied to resolve the spatial information given by neutron tomography, but not that given by the germanium spectrometer. This is purely due to mathematical and geometry reasons. SIRT, on the other hand, is an algorithm that can be easily adapted also to reconstruct the image that would be obtained using the information of the germanium spectra, as it was done for the analysis of the simulation results, presented here.

Figure 4.6 shows the neutron tomography results, the $\gamma$-ray tomography and the combined fast-neutron $\gamma$-ray CT. It has to be highlighted that the $\gamma$ rays exploited to obtain such imaging are those produced by the $^{252}$Cf source, and not those induced by fast neutrons.

The results are quite similar to each other, with a slight prevalence of contrast in the $\gamma$ ray tomography, mainly due to the relatively high-atomic number of iron and copper, that, instead, attenuate fast neutrons much less producing therefore less image contrast. As already stated, the neutron and $\gamma$ tomography in this study aim to give a merely qualitative information of the material structure and its spatial distribution.

Particularly important and interesting are the results presented in Figure 4.7. These concern the image generated by the selection of fixed energy peaks in the germanium detector spectra. In particular, the peak of the first nuclear level of iron-56, at 847 keV, and the first level of copper-63, at 962 keV, were selected. The data were processed using the SIRT image reconstruction code.

Regarding $^{56}$Fe, its presence can be clearly identified within the image. The presence

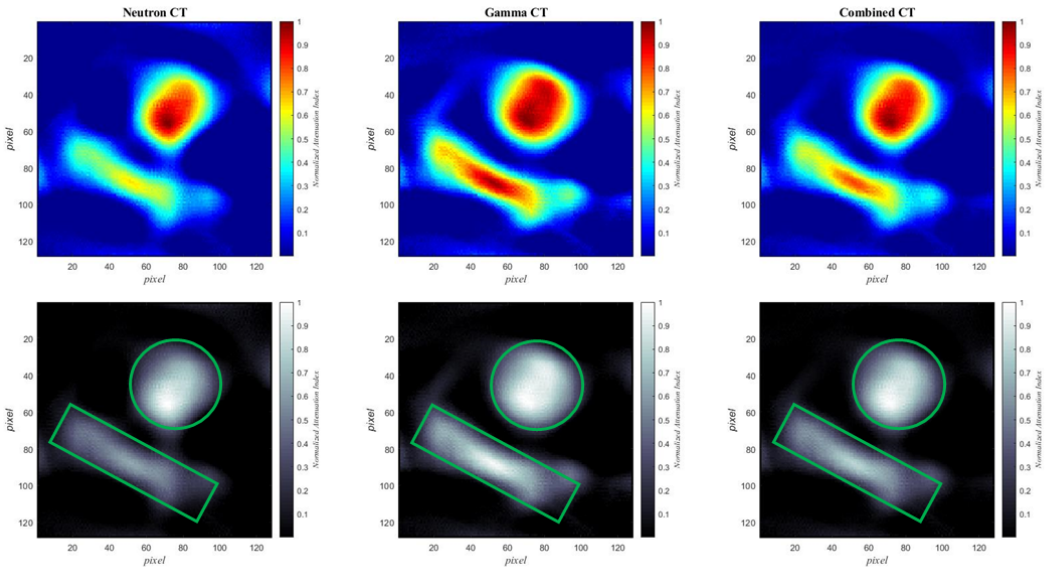


Figure 4.6: On top: Monte Carlo simulations of: fast-neutron, $\gamma$ ray and combined fast-neutron/$\gamma$-ray tomography of the iron block and copper cylinder. The colour scale used aims to highlight differences in contrast. On bottom: same picture plotted with the conventionally used grey-level colour scale.

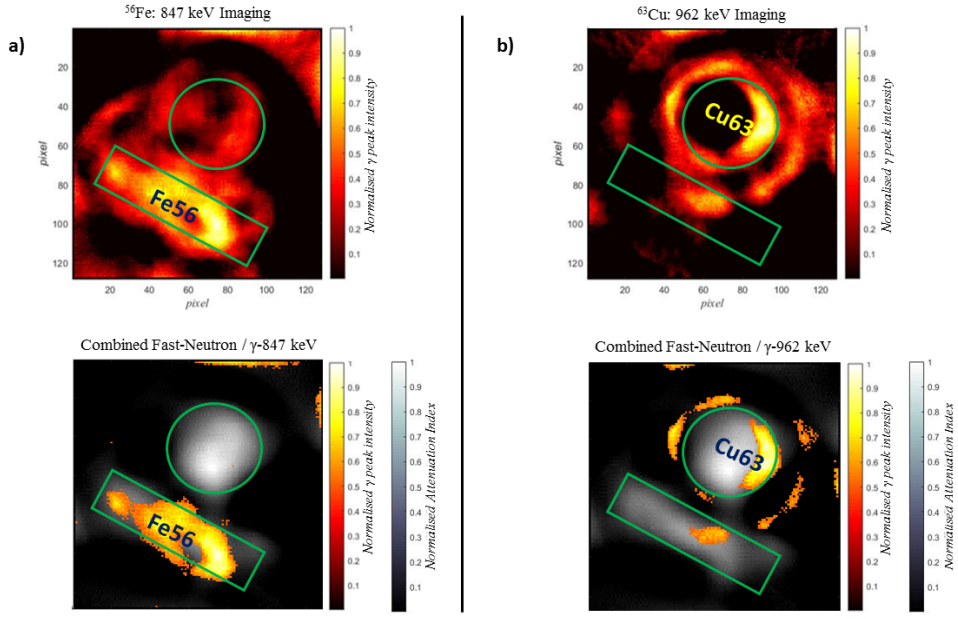


Figure 4.7: a) on the left: Monte Carlo simulations $\gamma$ imaging of the iron block (top) and the same image superimposed to the neutron tomograph (bottom), obtained increasing the threshold level of the iron peak intensity. b) on the right: Monte Carlo simulations $\gamma$ imaging of the copper cylinder (top) and the same imaging superimposed to the neutron tomograph (bottom), obtained increasing the threshold level of the copper peak intensity.

of noise and artefacts can also be noticed. This is mainly due to the reconstruction code, which has still room for improvement. By raising the threshold level of the iron

peak intensity, the image on the bottom is obtained, superimposing the $\gamma$ image with the fast-neutron tomograph. In this case, by raising the threshold, the noise disappears and only the iron remains. Copper is not present for the fact that only the 847 keV $\gamma$ rays, emitted only by iron and not by copper, have been selected.

Concerning copper, by selecting only its 962 keV $\gamma$ rays, the cylindrical shape of the sample cylinder is clearly denoted. Artefacts and noise are still present, as it occurred with iron; whilst in the bottom image (figure 4.7b), carried out by raising the peak intensity threshold and superimposing it with the neutron tomograph, the cylindrical shape of $^{63}$Cu is best seen. A fundamental aspect emerges from the data analysis on the copper sample: the centre of the cylinder appears as if it were empty. This fact is very interesting because it does not occur with the iron sample. The most rational reason is the fact that the copper sample, unlike the iron one, is much thicker, in fact it has a diameter of 5 cm, and the fast neutrons used, of average energy 2 MeV, have just enough energy to excite only the external regions of the cylinder. After their interaction, they lose energy which will no longer be such as to excite even the internal structure. For cases like this, higher energy neutrons, such as 14 MeV produced by neutron generators, are recommended.

Although the experimental data are not yet fully available for the analysis, some preliminary experimental evidence of clear detection of the 847 keV peak of $^{56}$Fe, emerged during the experiment itself. Some $\gamma$ spectra were obtained from germanium detectors. In particular, the iron block was placed in a fixed position for which it was directly irradiated by the beam. The peak of the excitation level was clearly observed, as shown in figure 4.8. Oppositely, when the sample was out of the neutron beam, due to the scan translation movement, and therefore not being irradiated, this peak was not present, clearly indicating that it was generated by the sample *solo* irradiation. This is indeed an experimental indication of fundamental importance, pending the results of the complete data analysis, which is currently ongoing.

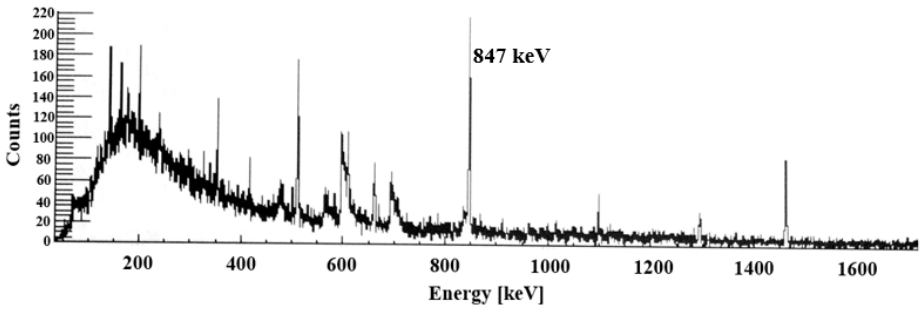


Figure 4.8: Germanium detector spectrum obtained irradiating an iron block. The peak at 847 keV of $^{56}$Fe most probable nuclear transition is clearly visible. Iron is composed by 91.75% of $^{56}$Fe and the rest is 5.85% $^{54}$Fe and 2.12% $^{57}$Fe.

## 4.5 Conclusion

Currently, the data analysis of the measurements described in this work is ongoing. Preliminary results and first experimental evidences seem to be promising. The work presented in this chapter, whilst still being at its embryonic stage, is intended to show the potential of an innovative experimental technique that combines the advantages conferred by fast neutron tomography and neutron activation analysis, with the option to also combine a third technique, $\gamma$-ray tomography.

The experiments were conducted at the ALTO facility of the Institute of Nuclear Physics of Orsay, using the neutron beam produced by the interaction of a proton beam in a lithium target. The energy of neutrons produced was about 2 MeV, sufficient to excite the first nuclear transition levels of some metals, as shown in the previous section. Looking ahead it would also be interesting to explore this technique using neutrons of higher energies, as well. For instance, neutrons of 14 MeV, which would allow to have a much greater penetrating power. In fact, as shown by the analysis of the copper cylinder, for thick samples, relatively low energy neutrons are just enough to excite the outer layers of the sample. A use of 14 MeV neutrons, is more likely to induce a higher $\gamma$ ray yield. Furthermore, a greater range of elements of the periodic table can be analysed, for example samples of geological and biological materials, mainly composed by elements such like carbon, nitrogen, oxygen silicon, phosphor and sulphur.

Comparing the technique presented here, with an analogy to the medical field, this would be comparable to combined Positron Emission Tomography and Computed Axial Tomography (PET-CT): the CT provides spatial information of a body/object section scanned, while the PET gives the spatial distribution of a certain material inside the body/object itself. Similarly, in this work, fast neutron tomography provides the internal structure information of the metals analyzed, whilst the $\gamma$ emission stimulated by neutrons themselves, allows to identify certain isotopes thanks to their particular signatures emitted.

The technique presented has many potential applications. Several scenarios would open up, for instance, from the identification of particular metal isotopes within materials, Above all, the analysis of bulk materials and quality control of different minerals as well as the determination of their ore composition, would be one of the main applications.

# Chapter 5

# Conclusions

## 5.1 Discussion

The technological and scientific progress of recent years led to the development of 3D imaging methods, the increasing use of a wider variety of neutron energies and real-time analysis. Furthermore, with the advent of portable neutron sources, neutron imaging is being used increasingly independent of dedicated neutron facilities where, until recently, its use has relied upon. This has made it possible to apply neutron imaging in areas for which it was not previously possible [217], such as the search of drugs and explosives concealed in luggage and cargo containers, as well as weapons and special nuclear materials. The outcomes of these applications depend on the neutron source properties and on the detection system. It is the demand of new research in these areas that has led to the development of digital, real-time imaging and new modern image processing tools.

Within this framework, the research presented in this thesis has addressed several topics of fundamental importance today, with the aim to contribute at the current *state of the art* of fast-neutron/$\gamma$-ray-based inspection technologies.

The Monte Carlo simulation study presented in the results, chapter 1, has shown the potential of fast-neutron/$\gamma$-ray combination applied for the identification of concealed actinide-based compounds. Current radiography systems have important limitations in identifying special nuclear materials, especially when small quantities of these are concealed or placed inside dense objects [218]. SNM are usually detected by radiation portal monitors that detect $\gamma$ radiation passively, or by X-ray scans generated irradiating objects with $\gamma$ sources such as $^{60}$Co, $^{137}$Cs or a linear accelerator. The probability of SNM identification decreases as the size of the threat object becomes smaller, therefore it is relatively difficult for current radiography systems to detect a small piece of SNM. Better results are obtained by performing different scans of the same object with $\gamma$ rays of different energies, such as 6 and 9 MeV [219]. Dual-energy, monoenergetic, gamma radiography allows different opacity levels to be correlated and to best distinguish high Z materials from each other [220]. Some detection systems use fast neutron detectors for the identification of SNM. In fact, special nuclear materials and/or actinide-based substances, may emit neutrons, due to induced fission when they are inspected actively

with an external neutron source, or naturally, due to the spontaneous fission of plutonium or uranium-238 in related compounds. However, neutrons can also be shielded, or moderated, using materials rich in hydrogen content, that consequently would mask the presence of SNM [221]. Neutron-based, non-intrusive inspection approaches [97] include fast neutron activation analysis (FNAA) and pulsed fast neutron analysis (PFNA), which use fast neutrons as a probing radiation with the subsequent detection of $\gamma$ rays produced by neutron inelastic scatter; associated particle imaging (API) [29, 147], that usually exploits 14 MeV neutron to actively investigate samples; and thermal neutron analysis (TNA), which is based on the detection of neutron-capture $\gamma$ rays. Neutron scatter cameras [222–224] and the use of coded aperture imaging methods are also an innovative neutron imaging techniques, which often allow the deployment of relatively portable imaging systems [225] . All these methods are used to track down SNM and/or illicit materials such as drugs and explosives by detecting particular $\gamma$-ray fingerprints or neutron spectra. Only a few researches report the use of these methods in combination to other different imaging techniques, as well as only a few report the use of fast neutron tomography or radiography, or the combinations of fast-neutrons and $\gamma$ rays, for the identification of SNM [107, 226–228].

The study presented in the first results chapter of this thesis is focused on the identification of actinide-containing materials in shielded arrangements, with a single source of $\gamma$ rays and fast neutrons (americium-beryllium), under the hypothesis that radiation quanta are detected by a scintillation array connected to a digital real-time pulse shape discrimination system (mixed field analyser). This study has demonstrated the possibility to distinguish SNM such as plutonium and uranium compounds from materials used for their shielding (lead and polyethylene), and, albeit in qualitative terms, with a spatial resolution of a few millimetres. Combined n-$\gamma$ tomography has been able to identify 2.5 cm diameter tablets of plutonium metal and plutonium oxide, shielded with an arrangement of several centimetres of high-density polyethylene (HDPE) and lead. The discrimination of both actinides, Pb and HDPE was not possible prior to this research, for example by using fast neutron tomography or $\gamma$ rays in isolation. Similar outcomes were obtained simulating 3 cm tablets of highly enriched uranium (HEU), uranium carbide and uranium trioxide, concealed in a lead box of 7 cm. In this scenario, combined neutron-$\gamma$ tomography aids the identification of HEU and $UC_2$ whilst $U_3O_8$ appears to be best distinguishable using $\gamma$ ray tomography alone. In this research, a parallel study concerning the development of an image reconstruction algorithm was also conducted, based on the well-known ART, suitable for the simulated tomography system. This study turned out to be also useful for the experimental measurements carried out subsequently in this work.

Most non-intrusive inspections are also suitable for the identification of explosives and illicit materials. These inspections play a key and crucial role particularly at airports and borders. In this case, X-ray scanning is often the only technique used, however, neutron based inspections are being studied and deployed [8]. In this regard, the research presented in the second chapter of the results part, sought to understand, via Monte

Carlo simulations, how combined fast-neutron and $\gamma$-ray imaging responds when interrogating samples containing a lithium polymer, some explosives, and some low density substances. Experimentally, the fast-neutron, $\gamma$-ray, and combined n-$\gamma$ radiography of a lithium ion battery were compared to that obtained by X-rays performed using the same scan machine used in many UK airports.

The technological advancements of X-ray computed tomography made possible to investigate the internal structure of batteries and their performance in great detail [229–231]. In recent years, the use of neutron imaging for battery applications has also increased, particularly for the investigation of lithium polymer-related batteries. The reason for this growing interest is the presence of lithium-6, an isotope well-known for its high neutron capture cross section. The potential of neutron imaging for lithium cell scans is presented in [232–234], whilst [235] and [236] have shown the use of X-rays and neutron CT as complementary techniques. In [116], instead, an interesting 4D imaging study of neutron and X-ray tomography was presented recently, in which the mechanical degradation processes and the lithium diffusion is shown in its temporal evolution, and demonstrates the potential of combination of X-rays and (thermal) neutrons as a complementary source of information. These studies used neutron spallation sources, or research reactors, as well as different detection systems for X-rays and thermal neutrons.

To the author's knowledge, fast neutrons have not been used to investigate lithium ion batteries prior to this research, although neutron imaging is a valid method to image materials with a high content of hydrogen, carbon, nitrogen, oxygen, and lithium; as shown in [153]. The experimental research presented in chapter 2 has explored the use of fast neutrons and $\gamma$ rays, produced by the 75 MBq californium-252 source at Lancaster University and detected by a digital, real-time pulse shape discrimination system (as per the hypothesis of the previous simulation studies), to investigate the battery of a commercial laptop. The study demonstrated the potential of fast neutron tomography to highlight the cells of the lithium battery, in contrast to that obtained by using $\gamma$ rays in isolation, that did not provide a great deal of information about the cells. Both fast-neutron and combined n-$\gamma$ tomography, furthermore, were compared to an X-ray CT performed at the Henry Moseley Manchester facility in Manchester, using a CT Rapiscan machine used for the security checks in airports. The Monte Carlo simulations that integrated this study wanted to show the potential use of fast neutron imaging for the depiction of a common lithium polymer against some hazardous materials with similar density, in contrast to what happens using only $\gamma$ imaging, which does not allow discrimination. With fast neutron tomography in isolation, a lithium polymer was clearly discernible from explosive such as NC, TNT and RDX, as well as from acetone, water peroxide and water. These materials can be inspected with fast neutrons thanks to the differences in energy loss following elastic scattering. Explosives have molecules of C, N, O, while in different ratios, polymers have C, H, O, to which lithium is added. This produces a greater neutron energy loss for lithium polymers which will cause a greater number of neutrons to drop below the detection threshold, giving a result similar to that obtained with the absorption of thermal neutrons. Liquid scintillators, whose detection

threshold is about 0.5 MeV [237], are then particularly suitable as detection system for fast neutron tomography. After a few scatters with these sample, neutrons fall below the detection threshold, therefore not being revealed, and this makes lithium polymers look as if they were "opaque" materials to neutrons, when they are imaged.

Another alternative and innovative non-intrusive imaging technique is backscatter imaging, as described in chapter 3. Several studies describe the use of X-ray backscatter [173] imaging in different fields, for example to reveal dense materials, such as SNM [172, 238], or in the oil & gas sector [179] and in the aerospace [174, 175]. Neutron backscatter is also used, in particular for geological and geophysical studies, such as the study of the water content on some types of rocks, porosity assessments of rocks and their fraction in hydrogen [177, 178, 239]. In addition, it has been used to inspect pipelines to measure the presence and/or the level of liquids and to seek for defects. Furthermore, fast-neutron, elastic scatter, using a DT neutron generator, was applied using associated particle imaging techniques to obtain material-specific information of HDPE, steel, tungsten, lead and depleted uranium [240].

In light of this scientific literature, combined gamma and neutron backscatter has been explored, according to the same experimental principles described in previous research, once again with the use of a single source (californium-252) and a detection system connected to the real time pulse shape discrimination system. Slabs of a single material (steel) of different thicknesses have been investigated. It has been shown that the backscattered flux varies according to the thickness of the steel, and this produces a measurable effect, both with $\gamma$ rays and fast neutrons, for thicknesses ranging from 5 mm to 25 mm. This result is important because, if applied to non-intrusive oil and gas pipeline measurements, it may allow measure different grades of corrosion and defects to be discerned, since both corrosion and defects cause variations in the thickness of the steel.

Pipelines are often covered with insulating layers, such as polyethylene and concrete. Whilst in the case of bare steel, neutrons and $\gamma$ rays provide similar results, and thus not necessarily requiring their combination, interesting results have been obtained in this work by measuring the flux backscattered by the same steel thicknesses, with 1 cm of high density polyethylene and 1 cm of concrete above them. In this case, the combination of $\gamma$ rays and neutrons is often fundamental, for example, if a 5 mm pit difference in a pipeline with a wall thickness of 25 mm, insulated with concrete, needs to be assessed.

By means of the use of digital real-time pulse shape discrimination systems, this research also wanted to provide an alternative and complementary method to other inspection techniques. In particular, ultrasound technology, which is widely used thanks to its speed and precision, is performed inserting inspection systems inside the pipeline; however, this requires a medium as the ultrasound scan has does not have a great penetrating power (limited to a few cm), thus not being able to identify possible irregularities in the external pipeline region and in the insulating layer. The technique presented in this thesis, whilst relatively slow to reveal differences in thickness (from a few seconds

up to a couple of minutes), it is compatible with inspection of the material from the outside, without reliance on there being a medium present. This technique may also be applied in fields where non-intrusive assessments in order to verify the integrity of relatively large structures are required.

Finally, the last research presented in this thesis integrates the experimental methods discussed above, with a third technique, namely the fast neutron activation analysis. FNAA is widely addressed in the scientific literature [203–205] and it is applied for different purposes [206, 208, 212, 214]. However, these studies only allow to recognize the presence of a given element or isotope, not letting its spatial distribution being analysed. This weakness was overcome with the research described in chapter 4, by combining fast neutron tomography and high precision spectroscopy of $\gamma$ rays generated by fast neutron irradiation. The research is based on Monte Carlo simulations and has shown the potential to identify metal isotopes, such as iron-56 and cooper-63, by selecting fixed, high energy $\gamma$ rays produced by activating the samples with fast neutrons of relatively low energy (2 MeV). The data analysis of the experiments carried out at IPN Orsay, can provide experimental evidence of the hypothesis explored in such research .

## 5.2 Recommendations for future study

The research presented this thesis aims to be a starting point to provide new ideas for future research.

As future research, it would be interesting to reproduce the tomography system as well as the same shielded actinides arrangements described in the Monte Carlo study presented in chapter 1 of the results section. During the course of the PhD this turned out to be challenging, due to restricted access to special nuclear materials samples and the potential time needed to the authorization to proceed for their use, travel to achieve access overseas etc.

Another potential future research avenue can be appreciated from consideration of the experimental measurements of chapter 2. In this regard, it would be interesting to verify the results obtained from the simulations, experimentally, investigating the differences between conventional explosives and lithium polymer. In this case, explosive simulants could be used if required due to access restrictions, arguably more easily than for SNMs. In addition, to replace the laptop battery with the same explosive stimulants, repeating both the fast neutron radiography and the X-ray radiography, would be explored, in order to compare the results with those presented here. Finally, related to this, a destructive test of the battery could provide more information about its internal structure.

As far as the detector topic is concerned, the experimental measurements too date in this specific research study have always been carried out with liquid scintillators EJ-301, which provide excellent pulse shape discrimination (PSD), usually slightly better than EJ-309. Furthermore, their size, being smaller than EJ-309 detectors available for use in this study, provides better spatial resolution, when imaging as part of a scintillator array. However, the EJ-301 scintillant has a low flashpoint, making them problematic to be used in certain environments, difficult to transport etc. A valid alternative could be provided

by stilbene crystals. These, although more expensive than the EJ-301, are excellent scintillators, usually even smaller than EJ-301s (due to limitations on their growth) and provide similar or better performance in terms of PSD. Hence, it would be exploring the use of these detectors in place of the EJ-301s. Still concerning detectors and pulse shape discrimination, it would be worth exploring and implementing digital pulse shape discrimination algorithms applied to lithium-loaded plastic or liquid scintillators, so as to be able to also detect both fast and thermal neutrons, in addition to $\gamma$ rays, making thus possible three simultaneous detection functions, with widespread application potential, especially in nuclear safeguards and homeland security.

Strictly related to detectors is the study of the neutron cross-talk. In the presence of detector arrays, in which the detectors are close to each other, neutrons scattering from the sensitive volume of a detector to one another can produce false-positive events, in the sense that post-scattering they are no longer characteristic of the sample being characterised. The cross-talk neutron rate that one detector induces on the others should therefore be measured and simulated. This is particularly relevant for large volume detectors, such as the EJ-309 devices in use at Lancaster as part of the ADRIANA facility, whilst it was neglected in this research, since the smaller EJ-301 variants were used; however, a correct estimation of the cross-talk may improve the spatial resolution and materials discrimination, given that this is widely considered not to be trivial.

Finally, the experimental measurements of this thesis have been carried out using californium-252 sources, assuming an isotropic neutron and gamma emission dependence. This was an approximation, it being known that the californium emission in this case is slightly anisotropic due mainly to the influence of the water bath in which it is contained. Therefore, such anisotropies should be evaluated and corrections applied to the detected flux, as a function of detector distance and position with respect to the source.

## 5.3 Final remarks

The use of neutrons for non-destructive tests goes back for more than 50 years, when the first neutron sources were available. Since then, there has been a continuous development and a succession of improvements and discoveries, including new techniques, starting from the common radiography, passing through computed tomography, up to the development of the most advanced techniques of refractometry, interferometry, and small angle neutron scattering.

Although neutron imaging and neutron non-destructive testing techniques are undoubtedly a technology with several advantages, it is difficult to attract investments and funds due to difficulties and costs necessary, for instance, to build a neutron facility from scratch, or to buy a neutron generator, or even to have an area suitable for the measures. To have an idea, currently, there are around 450 operational nuclear reactors worldwide, and 72 of these can be used to perform neutron imaging, 8 are under construction, and 14 are planned. It is plausible that, due to the relative age of the reactors, the future number of these facilities will tend to decrease instead of increase. Considering nuclear spallation sources, definitely not a huge number worldwide, one more factor to consider

are shutdown periods of time due to maintenance. Nowadays, all these problems are an obstacle to the research & development and they contribute to not making neutron imaging a competitive technology on the market. This scenario is obviously placed side by side by the advantages of the X-ray technology, that, despite being different and complementary, is ahead and more widespread in an industrial context.

It is therefore needed to focus on the potential strength of neutron imaging and on the ease of allowing researchers and industrial partners to access neutron imaging facilities. Furthermore, it is crucial to provide multiple image techniques in a single measure to reduce costs, times and provide detailed and precise measurements, a fundamental need today. In fact, techniques such as, for example in the medical field, dual ray X-ray radiography, combined positron emission tomography - computed axial tomography, or even the single-photon emission computed tomography together with computed axial tomography, have been developed. Also, thanks to recent developments in the technological field and in the detection of neutrons and $\gamma$ rays, are being studied experimental methods to combine thermal neutrons and fast neutrons, which is the analogous of the dual x-ray radiography, however with neutrons of different energy.

Within this context is based the research work presented in this thesis. The aim was to demonstrate advantages and applications of different imaging techniques, using neutrons *in primis*, and, secondly, turning into an advantage the fact that neutrons are always followed by $\gamma$ rays when produced in the sources. These $\gamma$ rays are usually considered source of noise and of background in most experiments, however, thanks to the possibility provided by real-time pulse shape discrimination systems, developed at Lancaster University in previous research, it was possible to exploit these $\gamma$ rays, by developing thus a simultaneous, radiographic and tomographic neutron-gamma imaging technique.

# Part III

# APPENDIXES

# Appendix A

# MCNP6

## A.1 Californium source

SDEF PAR=D1 ERG=FPAR=D2 POS=0.0001 0.0001 0.0001
si1 L n p
sp1 1 1
ds2 S 3 4
si3
sp3 -3 1.025 2.926
si4 A 0.085 0.09 0.1 0.11 0.12 0.13 0.14 0.15 0.16 0.17 0.18 0.19 0.2 0.21 &
0.22 0.23 0.24 0.25 0.26 0.27 0.28 0.29 0.3 0.35 0.4 0.45 0.5 0.55 0.6 &
0.65 0.70 0.75 0.80 0.85 0.90 0.95 1.0 1.05 1.1 1.15 1.2 1.25 1.3 1.35 &
1.4 1.45 1.5 1.55 1.6 1.65 1.7 1.75 1.8 1.85 1.9 1.95 2 2.05 2.1 2.15 &
2.2 2.25 2.3 2.35 2.4 2.45 2.5 2.55 2.6 2.65 2.7 2.75 2.8 2.85 2.9 2.95 &
3 3.05 3.1 3.15 3.2 3.25 3.3 3.35 3.4 3.45 3.5 3.55 3.6 3.65 3.7 3.75 &
3.8 3.85 3.9 3.95 4 4.05 4.1 4.15 4.2 4.25 4.3 4.35 4.4 4.45 4.5 4.55 &
4.6 4.65 4.7 4.75 4.8 4.85 4.9 4.95 5 5.05 5.1 5.15 5.2 5.25 5.3 5.35 &
5.4 5.45 5.5 5.55 5.6 5.65 5.7 5.75 5.8 5.85 5.9 5.95 6 6.05 6.1 6.15 &
6.2 6.25 6.3 6.35 6.4 6.45 6.5 6.55 6.6 6.65 6.7 6.75 6.8 6.85 6.9 6.95 &
7 7.05 7.1 7.15 7.2 7.25 7.3 7.35 7.4 7.45 7.5 7.55 7.6 7.65 7.7 7.75 &
7.8 7.85 7.9 7.95 8 8.05
sp4 0.0 0.000182468 0.000556455 0.000942761 0.001341689 0.001753553 0.00217867
0.002617366 0.003069975 0.003536836 0.004018297 0.004514714 0.005026448 &
0.005553871 0.006097362 0.006657308 0.007234104 0.007828155 0.008439874 &
0.009069682 0.009718011 0.010385300 0.011099912 0.009894086 0.008819253 &
0.007861184 0.007007193 0.006245974 0.005567450 0.004962637 0.004423526 &
0.003942982 0.003514640 0.003132831 0.002792500 0.002489140 0.002218735 &
0.002081267 0.001969888 0.001864470 0.001764693 0.001670256 0.001580872 &
0.001496272 0.001416199 0.001340412 0.001268680 0.001200787 0.001136527 &
0.001075706 0.001018139 0.000963654 0.000912084 0.000863274 0.000817076 &
0.000773350 0.000731965 0.000692794 0.000655719 0.000620628 0.000587415 &
0.000555980 0.000526227 0.000498066 0.000471412 0.000446184 0.000422307 &

0.000399707 0.000378317 0.000358071 0.000338909 0.000320772 0.000303606 &
0.000287359 0.000271981 0.000257426 0.000243650 0.000230611 0.000218270 &
0.000206589 0.000195534 0.000185070 0.000175166 0.000165792 0.000156919 &
0.000148522 0.000140574 0.000133051 0.000125931 0.000119192 0.000112813 &
0.000106776 0.000101062 0.000095653 0.000090535 0.000085690 0.000081104 &
0.000076764 0.000072656 0.000068768 0.000065087 0.000061604 0.000058308 &
0.000055187 0.000052234 0.000049439 0.000046793 0.000044289 0.000041919 &
0.000039675 0.000037552 0.000035543 0.000033641 0.000031840 0.000030136 &
0.000028524 0.000026997 0.000025552 0.000024185 0.000022891 0.000021657 &
0.000020506 0.000019409 0.000018370 0.000017387 0.000016457 0.000015576 &
0.000014742 0.000013954 0.000013207 0.000012500 0.000011831 0.000011198 &
0.000010599 0.000010032 0.000009495 0.000008987 0.000008506 0.000008050 &
0.000007620 0.000007212 0.000006826 0.000006461 0.000006115 0.000005788 &
0.000005478 0.000005185 0.000004907 0.000004645 0.000004396 0.000004161 &
0.000003938 0.000003727 0.000003528 0.000003339 0.000003161 0.000002991 &
0.000002831 0.000002680 0.000002536 0.000002401 0.000002272 0.000002151 &
0.000002035 0.000001927 0.000001823 0.000001726 0.000001634 0.000001546 &
0.000001463 0.000001385 0.000001311 0.000001241 0.000001174 0.000001112 &
0.000001052 0.000000996 0.000000942

## A.2 Americium-Beryllium neutron-gamma source

SDEF PAR=D1 ERG=FPAR=D2 POS=0.0001 0.0001 0.0001
si1 L n p
sp1 1 1
ds2 S 3 4
si3 H 4.14E-07 0.11 0.33 0.54 0.75 0.97 1.18 1.4 1.61 1.82 2.04 &
2.25 2.47 2.68 2.9 3.11 3.32 3.54 3.75 3.97 4.18 4.39 4.61 4.82 &
5.04 5.25 5.47 5.68 5.89 6.11 6.32 6.54 6.75 6.96 7.18 7.39 7.61 &
7.82 8.03 8.25 8.46 8.68 8.89 9.11 9.32 9.53 9.75 9.96 10.18 10.39 &
10.6 10.82 11.03
sp3 D 0 0.0144 0.0334 0.0313 0.0281 0.025 0.0214 0.0198 0.0175 0.0192 &
0.0222 0.0215 0.0225 0.0228 0.0295 0.0356 0.0368 0.0346 0.0307 0.0300 &
0.0269 0.0286 0.0318 0.0307 0.0333 0.0304 0.0274 0.0233 0.0206 0.0181 &
0.0177 0.0204 0.0183 0.0163 0.0168 0.0168 0.0188 0.0184 0.0169 0.0143 &
0.0097 0.0065 0.0043 0.0037 0.0038 0.0051 0.0062 0.0055 0.0047 0.0037 &
0.0028 0.0015 0.0004
si4 A 4.34 4.390 4.440 4.490 4.54
sp4 0.000 0.125 0.750 0.125 0.000

## A.3 MCNP6: example of code

Input file

```
C CELL CARDS
C ———————————————————— COLLIMATOR
1 5 -19.300 -1 imp:n=1 imp:p=1
2 5 -19.300 -2 imp:n=1 imp:p=1
3 10 -0.955 -3 imp:n=1 imp:p=1
4 10 -0.955 -4 imp:n=1 imp:p=1
5 5 -19.300 -5 imp:n=1 imp:p=1
6 5 -19.300 -6 imp:n=1 imp:p=1
7 4 -11.350 -7 imp:n=0 imp:p=0
10 7 -1.000 -10 imp:n=0 imp:p=0
11 7 -1.000 -11 imp:n=0 imp:p=0
C
C
C
C ———————————————————— SAMPLE
12 9 -2.550 -12 122 imp:n=1 imp:p=1
140 10 -0.955 -130 #141 #142 imp:n=1 imp:p=1
141 14 -14.000 -131 imp:n=1 imp:p=1
142 4 -11.350 -132 #141 imp:n=1 imp:p=1
C
C ———————————————————— DETECTORS
C ———————————————— S4d
16 2 -0.8745 -16 imp:n=1 imp:p=1
17 3 -2.6989 16 -17 imp:n=1 imp:p=1
18 1 -0.0012 -18 imp:n=1 imp:p=1
19 3 -2.6989 18 -19 imp:n=1 imp:p=1
C ———————————————— S3d
26 LIKE 16 BUT trcl=20
27 LIKE 17 BUT trcl=20
28 LIKE 18 BUT trcl=20
29 LIKE 19 BUT trcl=20
C ———————————————— S2d
36 LIKE 16 BUT *trcl=30
37 LIKE 17 BUT *trcl=30
38 LIKE 18 BUT *trcl=30
39 LIKE 19 BUT *trcl=30
C ———————————————— S1d
46 LIKE 16 BUT *trcl=40
47 LIKE 17 BUT *trcl=40
48 LIKE 18 BUT *trcl=40
```

```
49 LIKE 19 BUT *trcl=40
C ------------------------------ S5d
56 LIKE 16 BUT *trcl=50
57 LIKE 17 BUT *trcl=50
58 LIKE 18 BUT *trcl=50
59 LIKE 19 BUT *trcl=50
C ------------------------------ S6d
66 LIKE 16 BUT *trcl=60
67 LIKE 17 BUT *trcl=60
68 LIKE 18 BUT *trcl=60
69 LIKE 19 BUT *trcl=60
C ------------------------------ S7d
76 LIKE 16 BUT *trcl=70
77 LIKE 17 BUT *trcl=70
78 LIKE 18 BUT *trcl=70
79 LIKE 19 BUT *trcl=70
C
C
C ------------------------------ S1p
261 LIKE 16 BUT trcl=21
271 LIKE 17 BUT trcl=21
281 LIKE 18 BUT trcl=21
291 LIKE 19 BUT trcl=21
C ------------------------------ S2p
361 LIKE 16 BUT *trcl=32
371 LIKE 17 BUT *trcl=32
381 LIKE 18 BUT *trcl=32
391 LIKE 19 BUT *trcl=32
C ------------------------------ S3p
461 LIKE 16 BUT *trcl=43
471 LIKE 17 BUT *trcl=43
481 LIKE 18 BUT *trcl=43
491 LIKE 19 BUT *trcl=43
C ------------------------------ S4p
561 LIKE 16 BUT *trcl=54
571 LIKE 17 BUT *trcl=54
581 LIKE 18 BUT *trcl=54
591 LIKE 19 BUT *trcl=54
C ------------------------------ S5p
661 LIKE 16 BUT *trcl=65
671 LIKE 17 BUT *trcl=65
681 LIKE 18 BUT *trcl=65
```

```
691 LIKE 19 BUT *trcl=65
C ——————————————————— S6p
761 LIKE 16 BUT *trcl=76
771 LIKE 17 BUT *trcl=76
781 LIKE 18 BUT *trcl=76
791 LIKE 19 BUT *trcl=76
C
C
C
C
C ——————————————————————————— ROOM
980 1 -0.0012 -990 #2 #3 #4 #5 #6 #7 #10 #11 &
#12 #16 #17 #18 #19 &
#26 #27 #28 #29 &
#36 #37 #38 #39 &
#46 #47 #48 #49 &
#56 #57 #58 #59 &
#66 #67 #68 #69 &
#76 #77 #78 #79 &
#140 #141 #142 &
#261 #271 #281 #291 &
#361 #371 #381 #391 &
#461 #471 #481 #491 &
#561 #571 #581 #591 &
#661 #671 #681 #691 &
#761 #771 #781 #791 &
#1 imp:n=1 imp:p=1
990 6 -2.18 990 -100 imp:n=0 imp:p=0
100 0 100 imp:n=0 imp:p=0
C
C

C SURFACE CARDS
C ——————————————————————————— COLLIMATOR
1 RPP 0.0 3.0 -25.0 25.0 -18.15 -0.2
2 RPP 0.0 3.0 -25.0 25.0 0.2 18.2
3 RPP 3.0 27.0 -25.0 25.0 -18.15 -0.2
4 RPP 3.0 27.0 -25.0 25.0 0.2 18.2
5 RPP 27.0 30.0 -25.0 25.0 -18.15 -0.2
6 RPP 27.0 30.0 -25.0 25.0 0.2 18.2
9 RPP 0.00 30.0 10.0 25.0 -0.15 0.15
10 RPP -32.5 -2.5 -25.0 25.0 -18.15 18.15
```

```
11 RPP -32.5 27 -25.0 25.0 -50 -20
7 RPP 27 30 -25.0 25.0 -50 -20
C
C
C
C ———————————————————————— T. and SAMPLE
12 RPP 34 56 -30.5 30.5 -64 -17
122 RPP 34.5 55.5 -30 31 -63.5 -17.5
C
130 1 RPP -5.5 4.5 -4.5 5.5 -5 5
131 1 RCC -1 1 -4 0 0 8 1.25
132 1 RPP -3.5 2.5 -2.5 3.5 -4.5 4.5
C
138 1 RPP -6.5 6.5 -6.5 6.5 -5 5
C
C ———————————————————————— DETECTOR
16 10 RCC 0 0 0 0 0 1.5 0.95
17 11 RCC 0 0 0 0 0 1.60 1.0
18 12 RCC 0 0 0 0 0 7.4 0.95
19 13 RCC 0 0 0 0 0 8.0 1.7
C ———————————————————————— ROOM
990 RPP -180 280 -280 280 -64 220
100 RPP -200 300 -300 300 -100 240
C
C

C DATA CARDS
C ———————— materials
C
m1 7014 -0.7803 8016 -0.2099 6000 -0.0098
m2 1001 -0.077418 6000 -0.922582
m3 13027 1.000000
m4 82208 1.000000
m5 74000.21c 1.000000
m7 1001 -0.111894
8016 -0.888106
m9 8016 -0.486722
12000 -0.036182
13027 -0.132313
14000 -0.280461
20000 -0.064322
m10 1001 0.666662
```

```
6000 0.333338
m14 8016 -0.062713 $--PuO--$
94238 -0.000469
94239 -0.876363
94240 -0.056237
94241 -0.003749
94242 -0.000469
m16 8016 -0.152037 $--U3O8--$
92234 -0.000226
92235 -0.025439
92236 -0.000117
92238 -0.822181
m17 6000 -0.091692 $--UC2--$
92234 -0.000243
92235 -0.027249
92236 -0.000125
92238 -0.880691
m30 92234 -0.009800 $--HEU--$
92235 -0.931550
92236 -0.004500
92238 -0.054150
C
C ———————— physics
C
mode n p
phys:n
phys:p
C
C
C ———————————————————————— SOURCE AmBe
C
C — as per previous section
C
C
C
C ———————— coordinate transformation
C
C Sample transformation for tomography
*TR1 39 0 0 0 90 90 90 0 90 90 90 0 1
C
C Detector positions
*TR10 90.00 0 -0.75 0 -90 90 90 0 90 90 90 0 1
```

```
*TR11 90.00 0 -0.8 0 -90 90 90 0 90 90 90 0 1
*TR12 90.00 0 0.8 0 -90 90 90 0 90 90 90 0 1
*TR13 90.00 0 0.8 0 -90 90 90 0 90 90 90 0 1
C
*TR20 0 0 0 2.23 -87.77 90.00 92.23 2.23 90.00 90.00 90.00 0.00 1
*TR30 0 0 0 4.46 -85.54 90.00 94.46 4.46 90.00 90.00 90.00 0.00 1
*TR40 0 0 0 6.68 -83.32 90.00 96.68 6.68 90.00 90.00 90.00 0.00 1
*TR50 0 0 0 -2.23 -92.23 90.00 87.77 -2.23 90.00 90.00 90.00 0.00 1
*TR60 0 0 0 -4.46 -94.46 90.00 85.54 -4.46 90.00 90.00 90.00 0.00 1
*TR70 0 0 0 -6.68 -96.68 90.00 83.32 -6.68 90.00 90.00 90.00 0.00 1
C
*TR21 3.5 0 0 5.97 -84.03 90.00 95.97 5.97 90.00 90.00 90.00 0.00 1
*TR32 3.5 0 0 3.58 -86.42 90.00 93.58 3.69 90.00 90.00 90.00 0.00 1
*TR43 3.5 0 0 1.19 -88.81 90.00 91.19 1.19 90.00 90.00 90.00 0.00 1
*TR54 3.5 0 0 -1.19 -91.19 90.00 88.81 -1.19 90.00 90.00 90.00 0.00 1
*TR65 3.5 0 0 -3.58 -93.58 90.00 86.42 -3.58 90.00 90.00 90.00 0.00 1
*TR76 3.5 0 0 -5.97 -95.97 90.00 84.03 -5.97 90.00 90.00 90.00 0.00 1
C
C ———————— Tallies
C
C neutrons
F11:n 47017.1
F21:n 37017.1
F31:n 27017.1
F41:n 17.1
F51:n 57017.1
F61:n 67017.1
F71:n 77017.1
F111:n 271017.1
F121:n 371017.1
F131:n 471017.1
F141:n 571017.1
F151:n 671017.1
F161:n 771017.1
C photons
F811:p 47017.1
F821:p 37017.1
F831:p 27017.1
F841:p 17.1
F851:p 57017.1
F861:p 67017.1
F871:p 77017.1
```

```
F911:p 271017.1
F921:p 371017.1
F931:p 471017.1
F941:p 571017.1
F951:p 671017.1
F961:p 771017.1
C neutrons
E11 1 9i 12
E21 1 9i 12
E31 1 9i 12
E41 1 9i 12
E51 1 9i 12
E61 1 9i 12
E71 1 9i 12
E111 1 9i 12
E121 1 9i 12
E131 1 9i 12
E141 1 9i 12
E151 1 9i 12
E161 1 9i 12
C photons
E811 0.1 9i 8
E821 0.1 9i 8
E831 0.1 9i 8
E841 0.1 9i 8
E851 0.1 9i 8
E861 0.1 9i 8
E871 0.1 9i 8
E911 0.1 9i 8
E921 0.1 9i 8
E931 0.1 9i 8
E941 0.1 9i 8
E951 0.1 9i 8
E961 0.1 9i 8
C ———————— print
print
C ———————— particle gun
nps 20000000
```

# Appendix B

# Scanning control system

## B.1 Brief description of the scanning and control system

The scanning system used in several measurements described in this thesis is composed of a mobile table (turntable) that allows the movement of the sample to be analysed and a TTL signal counter, synchronized with each other by a graphical user interface (GUI) written in Visual C#.

The mobile table was developed during a research project prior to this [31] doctorate, while the TTL counter is an improvement on the one used in this same [31] project. The GUI control system was instead completely written and developed during the doctoral research carried out at Lancaster University.

The turntable allows the phantom being investigated to be rotated and translated both horizontally and vertically. In this way it is possible to store data in different contrasting positions (projections), being able to provide cross sectional images of the samples. Three stepper motors are responsible of the rotational, horizontal and vertical

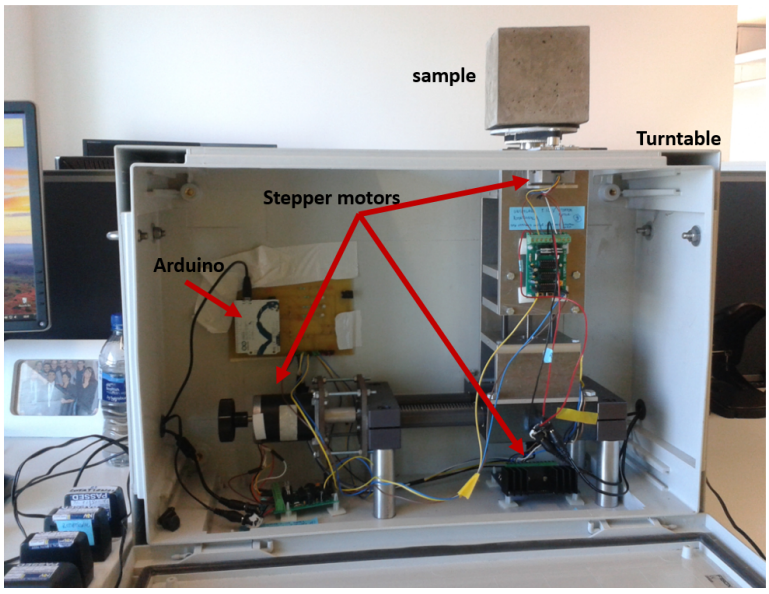


Figure B.1: Picture of the Turntable.

movement. The motors are controlled by three drive circuit boards (Quasar Electronics).

An Arduino Leonardo micro-controller is used to provide the control signals to the motor drive boards. The Arduino has its own programming software and was chosen, prior to this research project, thanks to its flexibility, ease of use and adequate number of input/output pins.

The turntable provides 100 mm of horizontal translations, 110 mm of vertical translation and 360° of rotation. Table B.1 shows the minimum and maximum displacement that each movement parameter can achieve and the total number of steps over the full displacement length.

Table B.1: Displacement values for Vertical, Horizontal and Rotational movements

| | Vertical | Horizontal | Rotational |
|---|---|---|---|
| Min. displacement | 0.0075mm | 0.02mm | 0.27° |
| Max. displacement | 110mm | 100mm | 360° |
| Number of steps | 14666.7 | 5000 | 1333.4 |

The position of the sample that has to be scanned, must be synchronised with the image data coming from the TTL counter, therefore a control system is needed. Such control system should meet several requirements:

- Arrange the sample in the desired position, communicating with the Arduino driving the turntable motors.
- Command the counter to start and then stop counting after a desired measurement time has been reached.
- Receive data from the counter.
- Combine phantom position and counter readings.
- Output data ready for reconstruction.

It was chosen Visual C# as a language for the implementation of the control system. This choice is due to its relative simplicity in building graphical interfaces and making executable applications. Visual C# is an object oriented programming language, with a huge amount of libraries allowing integration with external data acquisition systems, throw protocols such as USB, Ethernet and PCI. C# is also suitable for being interfaced with Arduino systems, via serial communication protocols.

Microsoft Visual Studio 2015® is the open source integrated development environment (IDE) used to develop the graphical user interface (GUI) and its control system. Once the GUI was created and built by the software, an executable Windows application is created. This application runs in any computer with Windows Operating System and with no need of having installed Microsoft Visual Studio.

The code consists of about 1200 C# lines and the final executable application is shown in figure B.6. The Graphical User Interface can be divided into two sections: the

first part controls the motors and the second controls the counter system. Both sections are synchronised with each other in order to achieve the requirements aforementioned.

The system communicates with and Arduino controlling the motors and with a Teensy board controlling the counter, both via USB protocol, that is used as serial communication protocol. The Teensy board is also programmable with the Arduino code. As a first step for driving the turntable motors, the serial port in which the Arduino is linked, has to be selected and opened (Fig. B.2). After that, it is possible to

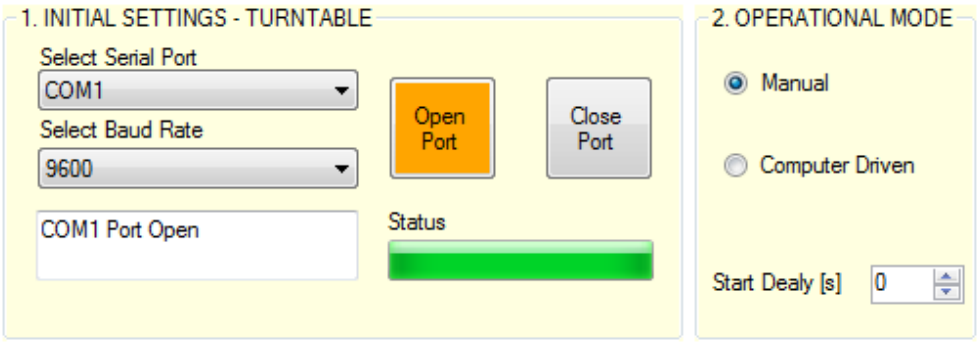


Figure B.2: Initial settings of the GUI. Section of image B.6.

choose between two operational modes: "manual" and "computer driven". The former allows the sample to be set in a single, fixed desired position, while the latter is the mode usually used to perform the entire scan, from a user-defined initial sample position to its final.

The "manual" operational mode (Fig. B.3) can be useful to test the system, the motors and the counter in their first configurations. Once the position is set by the user,

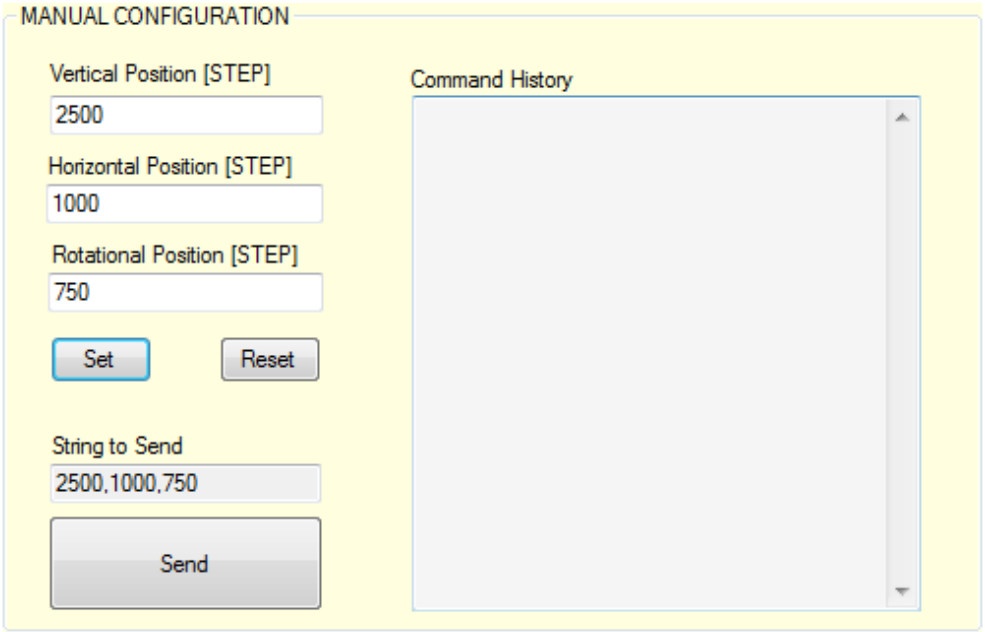


Figure B.3: Manual operational mode of the GUI. Section of image B.6.

this has to be sent to the Arduino. The instructions are an array of character bytes.

The array read by the Arduino is in the form of: "ZZZZ,YYYY,$\theta\theta\theta\theta$". Z, Y and $\theta$ are respectively the desired sample position with respect to the z-axis, the y-axis and the rotation around the z-axis, all expressed in terms of number of motor steps.

The "computer driven" operational mode (figure B.4) allows to set the initial, the final position and the discrete size increments for the three required phantom translations. Moreover, the user can define the sampling time during which the counter records the TTL signals coming from the radiation detected by the scintillators and discriminated by the multichannel analyzer. Once the button "start" is pressed, the motors arrange

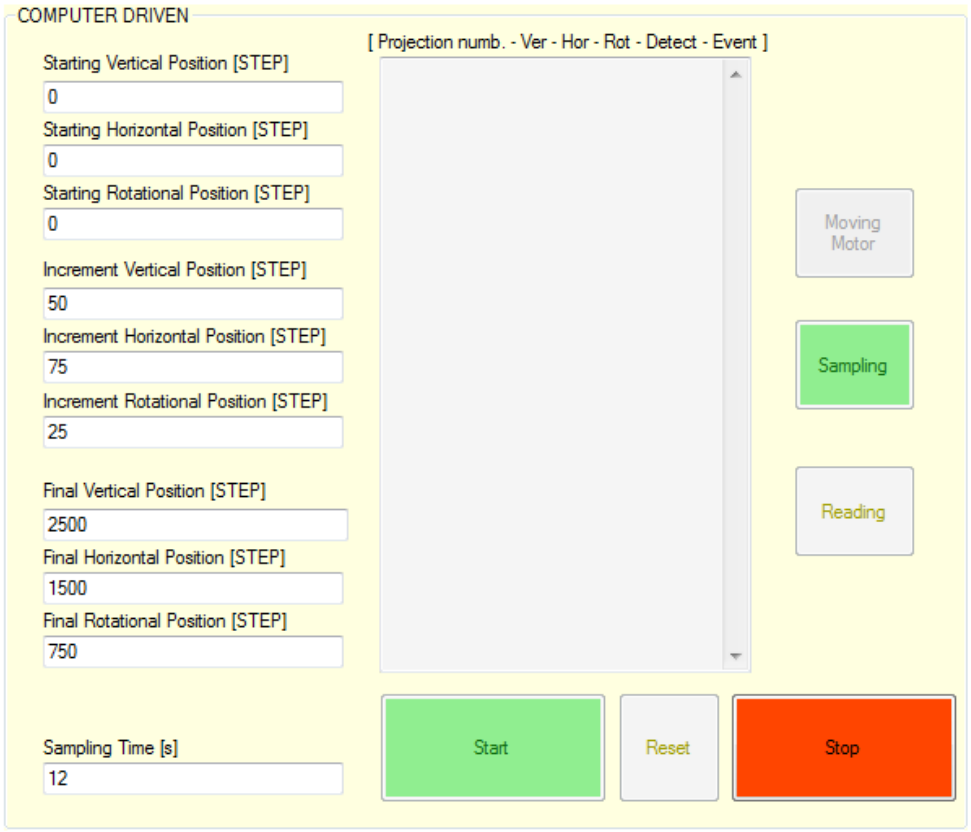


Figure B.4: Computer driven operation mode of the GUI. Section of image B.6.

the sample in the initial position, and once it is fixed, the counter begin to count for the pre-defined sampling time. After that, the counter stops and records the sample current position and the number of events measured. Successively the stepper motors fix the sample in the next position, and subsequently this step, the counter starts again. This process is repeated recursively until the final position is reached.

As soon as the scanning process is finished, a text file is generated and saved by the application. Such file contains for each projection of the sample, the number of neutrons and/or $\gamma$ rays detected by each detector. This file will be processed by the proper algorithm reconstruction code.

One section of the graphical user interface is dedicated to the detection and counter system (Fig. B.5). The Arduino-Teensy board controlling the counter system is different to the one controlling the stepper motors, therefore a different serial-USB port has to be

selected and opened. The user can set the number of detector used during an experiment and the type of radiation that wants to retain. The counter system can be used also

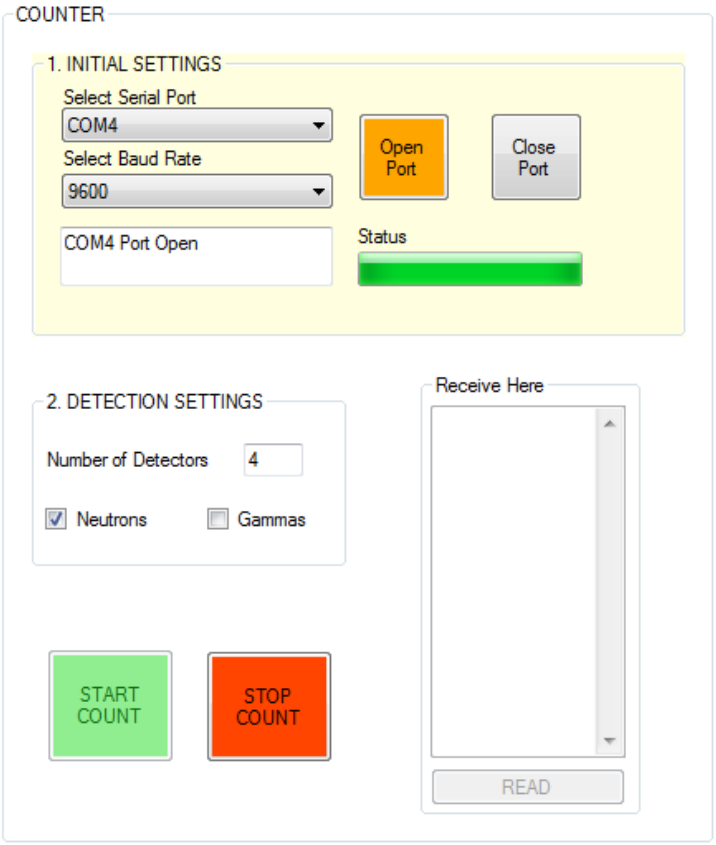


Figure B.5: Counter system section of the GUI.

independently to the turntable control system. This can be done when the "manual mode" is selected. Once the "computer driven" mode is selected, instead, the counter is automatically synchronized with the turntable control system; in other words, the two Arduinos are synchronized with each others.

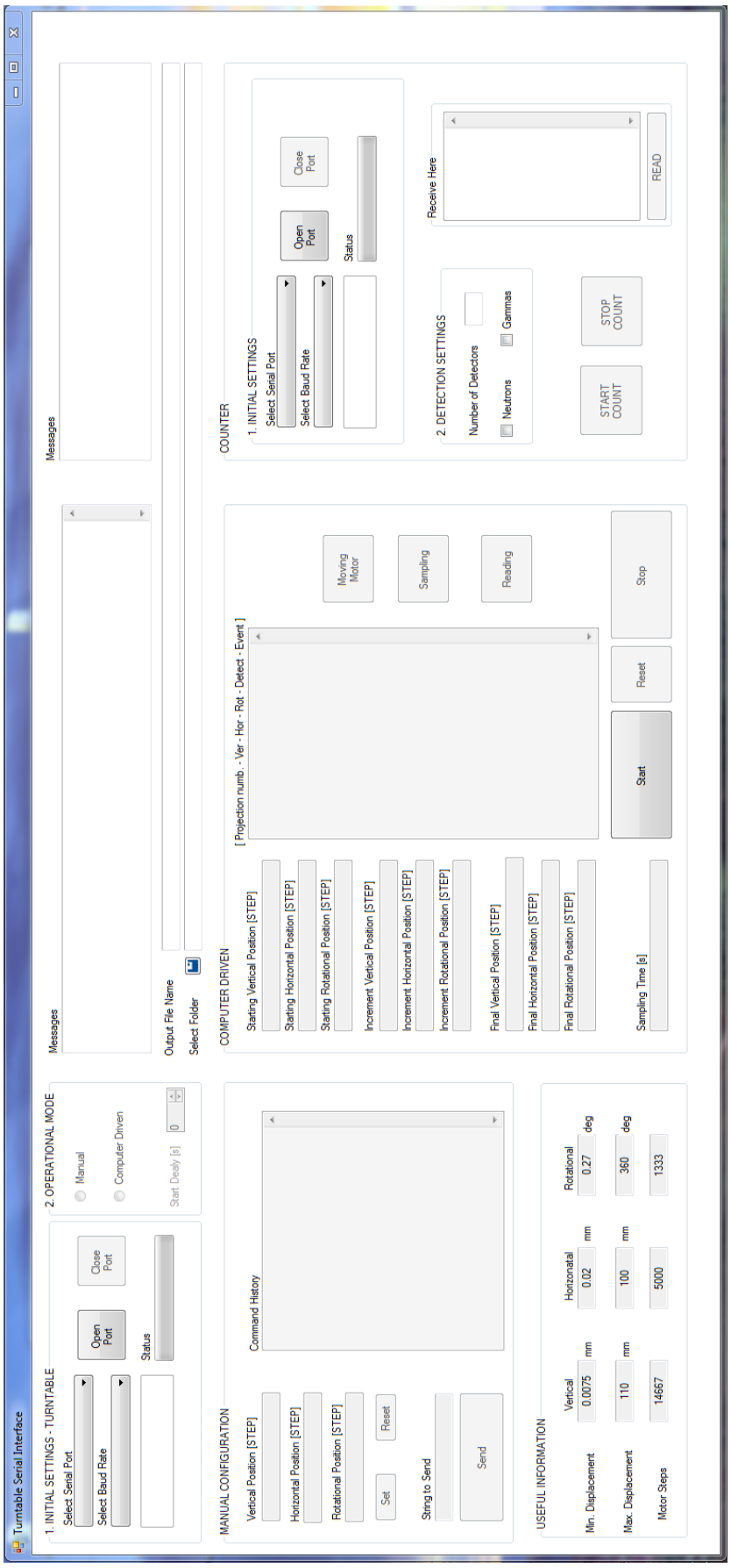


Figure B.6: Tomography Control System Graphical User Interface.

## B.2 Counter boards Design

The signal produced by the analyzer is 50 ns TTL (Transistor-Transistor Logic) pulse, and once processed, is sent to an external counter system. Such a device works with a maximum frequency of 20 MHz and was designed such that 32 Counting channels were available. This means that it can count the neutron events up to 32 scintillators detectors or both the neutron and $\gamma$ events generated by 16 scintillators. Another important feature is that the device has been designed as a 32-bit counter, in order to allow long-duration assessments with their possible large amounts of neutron/$\gamma$ counts. Thee counter is controlled by a Teensy 3.1/3.2 chip (figure B.7). The Teensy is smaller than Arduino, it has more pins and is faster, and the advantage is that it supports the Arduino language code, therefore it is easily programmable. In the same Teensy control board, an Adafruit Multiplexer allows to connect up to 8 different 16-channel counter, for a potential of 128 Channels. The designed configuration consists of 2×16-channel counters (figure B.8). Each counter is made of 2×4 four-channel boards connected in series with each other and in turn connected to a control board mounting the Teensy board. The boards were designed with the software of PCB design Eagle.

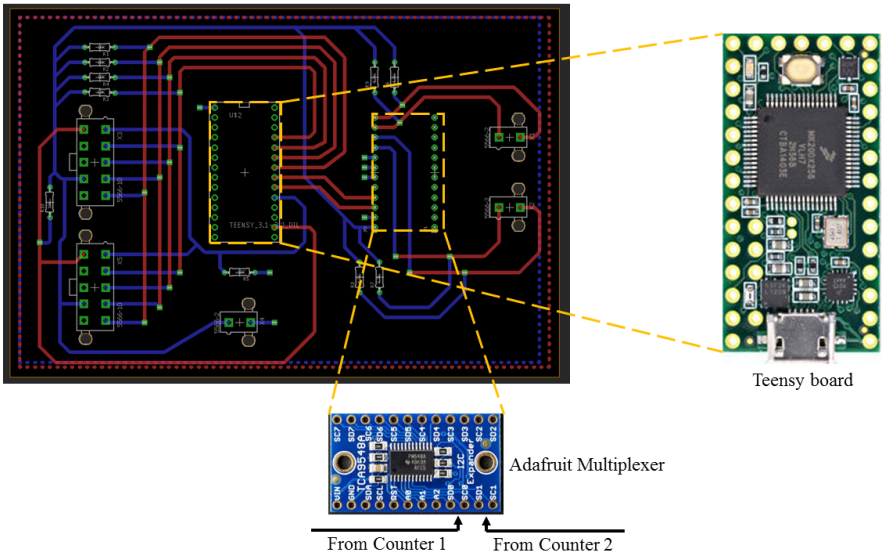


Figure B.7: Eagle design and schematics of the Teensy control board.

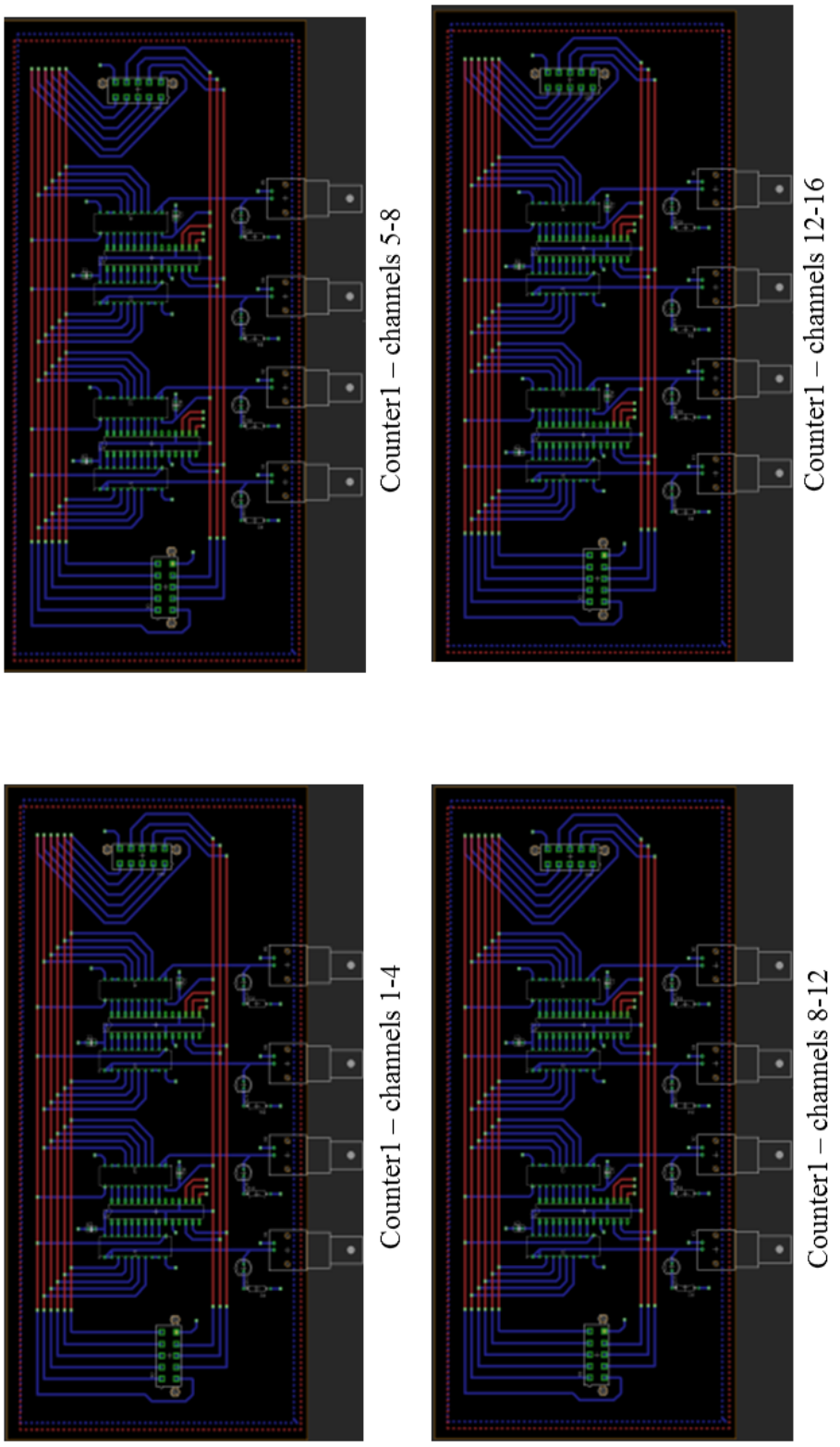


Figure B.8: Eagle design and schematics of boards constituting a 16-channel counter.

# Appendix C

# Codes and script

## C.1 Projection matrix generator: C++ code

```
#include "stdafx.h"
#include <iomanip>
#include <ios>
#include <iosfwd>
#include <iostream>
#include <istream>
#include <ostream>
#include <sstream>
#include <streambuf>
#include <cstring>
#include <string>
#include <cstdlib>
#include <cmath>
#include <ctime>
#include <time.h>
#include <cfloat>
#include <string>
#include <algorithm>
#include <vector>
#include <iterator>
#include <limits>
#include <windows.h>
#include <fstream>

using namespace std;
ofstream OUTPUT;


//************************************************
// DEFINE PARAMETERS AND CONSTANTS
#define PI 3.14159265358979323846

//mm -- must be the centre of the matrix of the area you want to scan
#define DISTANCE_SOURCE_TO_OBJECT 390
#define DISTANCE_SOURCE_TO_DETECTOR 1300              //mm
```

```
#define NUMBER_OF_DETECTORS 1
#define DETECTOR_WIDTH 28.5                                    //mm
#define GAP_BETWEEN_DETECTORS 0                                //mm
#define OFFSET_BETWEEN_DETECTORS 0                             //degree!!!

#define MATRIX_DIMENSION_MM 100                                //mm
#define MATRIX_DIMENSION_PIX 128                               //square pixel matrix

#define THETA_START 0                                          //degree
#define Y_START -30                                            //mm
#define THETA_INCREMENT 15                                     //degree
#define Y_INCREMENT 5                                          //mm
#define MAX_ROTATION 360                                       //degree
#define MAX_TRANSLATION 100                                    //mm

// IF ROTATION IS COUNTERCLOCKWISE --> CLOCK_SENSE = 1
// IF ROTATION IS CLOCKWISE --> CLOCK_SENSE = 2
#define CLOCK_SENSE 2

//*************************************************
//*************************************************

// function declarations
void SetGeometry();
void SetTomographyParameters();
void SetDetectorGeometry();
void SetProjectionMatrix();
void Reset_Matrix_Detector_View();
void ProjectonMatrix_OpenFile(int d);
void ProjectonMatrix_FillFile(string value);
void ProjectonMatrix_CloseFile();

//variables and arrays declarations
int MatrixDimension_pix;
double Distance_Source_to_Object, Distance_Source_to_Detector,
       Detector_Width, Gap_between_Detectors,
       Source_Position_x, Source_Position_y;

double MatrixDimension_mm, Pix_dimension,
       X_Matrix_Centre, Y_Matrix_Centre, x_pix, y_pix,
       newY_Matrix_Centre, Theta_Increment, Y_Increment,
       Max_Rotation, Max_Translation;

double M_a[NUMBER_OF_DETECTORS], M_b[NUMBER_OF_DETECTORS],
       X_a[NUMBER_OF_DETECTORS], X_b[NUMBER_OF_DETECTORS],
       Y_a[NUMBER_OF_DETECTORS], Y_b[NUMBER_OF_DETECTORS];

double Gamma_a[NUMBER_OF_DETECTORS], Gamma_b[NUMBER_OF_DETECTORS];

unsigned long
 Detector_View[NUMBER_OF_DETECTORS][MATRIX_DIMENSION_PIX][MATRIX_DIMENSION_PIX];
```

```
//*************************************************
//************************************************* MAIN CODE
int main()
{
cout << "   TOMOGRAPHY RECONSTRUCTION VISUAL C++ CODE   " << endl;
cout << "    Mauro Licata -- m.licata@lancaster.ac.uk " << endl;
cout << "    mauro.licata88@gmail.com " << endl;
cout << endl << endl << endl;

time_t s = time(0);

SetGeometry();
SetTomographyParameters();
SetDetectorGeometry();
SetProjectionMatrix();

time_t e = time(0);

cout << " Execution Time: " << e - s  << " seconds" << endl;

return 0;
}


//*************************************************
//************************************************* FUNCTIONS DEFINITION
//set Geometry variables and paramenters
void SetGeometry()
{
Source_Position_x = 0;
Source_Position_y = 0;
Distance_Source_to_Object = DISTANCE_SOURCE_TO_OBJECT;
Distance_Source_to_Detector = DISTANCE_SOURCE_TO_DETECTOR;
Detector_Width = DETECTOR_WIDTH;
Gap_between_Detectors = GAP_BETWEEN_DETECTORS;
Offset = OFFSET_BETWEEN_DETECTORS;

cout << " Source Position X [mm]: " << Source_Position_x << endl;
cout << " Source Position Y [mm]: " << Source_Position_x << endl << endl;
cout << " Distance Source to Object [mm]: "<<Distance_Source_to_Object<<endl;
cout << " Distance Source to Detector [mm]: "<<Distance_Source_to_Detector<<endl;
cout << " Detector_Width [mm]: " << Detector_Width << endl;
cout << " Gap between Detectors [mm]: " << Gap_between_Detectors << endl;
cout << " Offset between Detectors [degree]: " << Offset << endl;

}


// set tomography parameters
void SetTomographyParameters()
```

```
{
//define square area to be scanned and its matrix dimension
MatrixDimension_mm = MATRIX_DIMENSION_MM;
MatrixDimension_pix = MATRIX_DIMENSION_PIX;
Pix_dimension = MatrixDimension_mm / MatrixDimension_pix;

//Initial Matrix (and sample) position.
//Centre of the Matrix taken into account
X_Matrix_Centre = Distance_Source_to_Object;
Y_Matrix_Centre = Y_START;

//define steps for translation and rotations -- projection generation
//it depends on how you performed your experimets
Theta_Start = THETA_START;                              //degree
Y_Start = Y_START;                                     //mm
Theta_Increment = THETA_INCREMENT;
Y_Increment = Y_INCREMENT;
Max_Rotation = MAX_ROTATION;
Max_Translation = MAX_TRANSLATION;

cout << "TOMOGRAPHY_PARAMETERS" << endl;
cout << " Matrix Dimension [mm]: " << MatrixDimension_mm << endl;
cout << " Matrix Dimension [pixel]: " << MatrixDimension_pix << " x "
         << MatrixDimension_pix << endl;
cout << " Matrix resolution: 1 Pixel = " << Pix_dimension << " mm " << endl;
cout << " Matrix centre coordinates (at the initial position): " << endl;
cout << "      X: " << X_Matrix_Centre << " mm " << endl;
cout << "      Y: " << Y_Start << " mm " << endl << endl;
cout << " Initial Position: " << Y_Start << " mm " << endl;
cout << " Y Increment: " << Y_Increment << " mm " << endl;
cout << " Final Position: " << Max_Translation << " mm " << endl << endl;
cout << " Initial angle of rotation: " << Theta_Start << " deg " << endl;
cout << " Angle Increment: " << Theta_Increment << " deg " << endl;
cout << " Max Rotation: " << Max_Rotation << " deg " << endl << endl;
cout << " NUMBER OF PROJECTIONS per Detector: "
         <<(((Max_Translation - Y_Start)/Y_Increment)+ 1)*
         ((Max_Rotation - Theta_Start) / Theta_Increment) << endl;
cout << " TOTAL NUMBER OF PROJECTIONS: "
         << (((Max_Translation - Y_Start) / Y_Increment) + 1)*
         ((Max_Rotation-Theta_Start)/Theta_Increment)*NUMBER_OF_DETECTORS
         <<endl;
}


// set Detector Geometry
//calculation of the deector angular cofficient
// with respect to the source (origin of axis)
void SetDetectorGeometry()
{

//if the number of detector is even.
if (NUMBER_OF_DETECTORS % 2 == 0) {
```

```
        //central detector included!
        int Number_of_Detectors_counterclockwise = NUMBER_OF_DETECTORS / 2;
        int Number_of_Detectors_clockwise = NUMBER_OF_DETECTORS / 2;
        double Beta = atan((Detector_Width/2)/Distance_Source_to_Detector);
        double Angle_between_Det=2*atan((Gap_between_Detectors / 2)/
                Distance_Source_to_Detector) + (Offset / 180 * PI);
        double Distance_Source_to_Detector_Edge = Distance_Source_to_Detector /
                 cos((Detector_Width / 2) / Distance_Source_to_Detector);
        double GammaaMAX = (Number_of_Detectors_counterclockwise - 0.5) *
                Angle_between_Det+2*Number_of_Detectors_counterclockwise*Beta;
        double GammabMAX = (Number_of_Detectors_counterclockwise - 0.5) *
                Angle_between_Det+2*(Number_of_Detectors_counterclockwise-1)*Beta;

        cout << "␣DETECTOR␣GEOMETRY" << endl;
        cout << "␣Total␣Number␣of␣Detectors:␣"
             << NUMBER_OF_DETECTORS << endl;
        cout << "␣Number␣of␣Detectors␣counterclockwise:␣"
             << Number_of_Detectors_counterclockwise << endl;
        cout << "␣Number␣of␣Detectors␣clockwise:␣"
             << Number_of_Detectors_clockwise << endl;
        cout << "␣Maximum␣Angle␣Aperture␣(Detector␣edge␣A):␣"
             << GammaaMAX * 180 / PI << "␣degree" << endl;
        cout << "␣Maximum␣Angle␣Aperture␣(Detector␣edge␣B):␣"
             << GammabMAX * 180 / PI << "␣degree" << endl << endl;

        cout << "␣Angle␣viewed␣from␣each␣Detector:␣"
             << 2 * Beta * 180 / PI << "␣␣" << endl;
        cout << "␣Angle␣between␣each␣Detector:␣"
             << Angle_between_Det * 180 / PI << endl << endl;
        cout << "␣Detector␣" << "␣Angle␣" << "␣␣␣␣␣␣"
             << "␣X␣" << "␣␣␣␣␣␣␣␣" << "␣Y␣"
             << "␣coeff␣A" << "␣coeff␣B" << endl;

        for (int i = 0; i < Number_of_Detectors_counterclockwise; i++) {

                Gamma_a[i] = GammaaMAX - i * 2 * Beta - i*Angle_between_Det;
                Gamma_b[i] = GammabMAX - i * 2 * Beta - i*Angle_between_Det;
                X_a[i] = Distance_Source_to_Detector_Edge * cos(Gamma_a[i]);
                X_b[i] = Distance_Source_to_Detector_Edge * cos(Gamma_b[i]);
                Y_a[i] = Distance_Source_to_Detector_Edge * sin(Gamma_a[i]);
                Y_b[i] = Distance_Source_to_Detector_Edge * sin(Gamma_b[i]);
                M_a[i] = Y_a[i] / X_a[i];
                M_b[i] = Y_b[i] / X_b[i];

                cout << setprecision(3) << fixed
                << "␣␣␣␣␣" << i + 1
                << "␣␣␣␣␣" << (Gamma_a[i] + Gamma_b[i])*(180 / PI) / 2
                << "␣␣␣␣␣" << (X_a[i] + X_b[i]) / 2
                << "␣␣␣␣␣" << (Y_a[i] + Y_b[i]) / 2
                << "␣␣␣␣␣" << M_a[i]
                << "␣␣␣␣␣" << M_b[i] << endl;
        }
```

```
        //detectors coordinates and their angular coefficents
        //--- CLOCKWISE
        for (int i = Number_of_Detectors_clockwise;
             i < NUMBER_OF_DETECTORS;
             i++) {

                Gamma_a[i] =
                Gamma_aMAX - i * 2 * Beta - i*Angle_between_Det;
                Gamma_b[i] =
                Gamma_bMAX - i * 2 * Beta - i*Angle_between_Det;
                X_a[i] =
                Distance_Source_to_Detector_Edge * cos(Gamma_a[i]);
                X_b[i] =
                Distance_Source_to_Detector_Edge * cos(Gamma_b[i]);
                Y_a[i] =
                Distance_Source_to_Detector_Edge * sin(Gamma_a[i]);
                Y_b[i] =
                Distance_Source_to_Detector_Edge * sin(Gamma_b[i]);
                M_a[i] = Y_a[i] / X_a[i];
                M_b[i] = Y_b[i] / X_b[i];

                cout << setprecision(3) << fixed
                << "      " << i + 1
                << "      " << (Gamma_a[i] + Gamma_b[i])*(180 / PI) / 2
                << "      " << (X_a[i] + X_b[i]) / 2
                << "      " << (Y_a[i] + Y_b[i]) / 2
                << "      " << M_a[i]
                << "      " << M_b[i] << endl;
        }
}

// if the number of detector is odd.
else {
        //central detector included!
        int Number_of_Detectors_counterclockwise =
        NUMBER_OF_DETECTORS / 2 + 1;
        int Number_of_Detectors_clockwise = NUMBER_OF_DETECTORS / 2;
        double Beta = atan((Detector_Width / 2) / Distance_Source_to_Detector);
        double Angle_between_Det =
        2 * atan((Gap_between_Detectors / 2) / Distance_Source_to_Detector)
        + (Offset / 180 * PI);
        double Distance_Source_to_Detector_Edge = Distance_Source_to_Detector
        /cos((Detector_Width / 2) / Distance_Source_to_Detector);
        double Gamma_aMAX = (2 * Number_of_Detectors_counterclockwise - 1)
        *Beta+(Number_of_Detectors_counterclockwise - 1)*Angle_between_Det;
        double Gamma_bMAX = (2 * Number_of_Detectors_counterclockwise - 3)
        *Beta   +(Number_of_Detectors_counterclockwise - 1)*Angle_between_Det;

        cout << " DETECTOR GEOMETRY" << endl;
        cout << " Total Number of Detectors: "
             << NUMBER_OF_DETECTORS << endl;
```

```
        cout << "␣Number␣of␣Detectors␣counterclockwise:␣"
             << Number_of_Detectors_counterclockwise << endl;
        cout << "␣Number␣of␣Detectors␣clockwise:␣"
             << Number_of_Detectors_clockwise << endl;
        cout << "␣Maximum␣Angle␣Aperture␣(Detector␣edge␣A):␣"
             << GammaaMAX * 180 / PI << "␣degree" << endl;
        cout << "␣Maximum␣Angle␣Aperture␣(Detector␣edge␣B):␣"
             << GammabMAX * 180 / PI << "␣degree" << endl << endl;

        cout << "␣Angle␣viewed␣from␣each␣Detector:␣"
             << 2 * Beta * 180 / PI << "␣␣" << endl;
        cout << "␣Angle␣between␣each␣Detector:␣"
             << Angle_between_Det * 180 / PI << endl << endl;
        cout << "␣Detector␣" << "␣Angle␣" << "␣␣␣␣␣␣"
             << "␣X␣" << "␣␣␣" << "␣Y␣" << "␣coeff␣A" << "␣coeff␣B" << endl;

        //detectors coordinates and their angular coefficents
        //--- COUNTER CLOCKWISE
        for (int i = 0; i < Number_of_Detectors_counterclockwise; i++) {

          Gamma_a[i] = GammaaMAX - i * 2 * Beta - i*Angle_between_Det;
          Gamma_b[i] = GammabMAX - i * 2 * Beta - i*Angle_between_Det;
          X_a[i] = Distance_Source_to_Detector_Edge * cos(Gamma_a[i]);
          X_b[i] = Distance_Source_to_Detector_Edge * cos(Gamma_b[i]);
          Y_a[i] = Distance_Source_to_Detector_Edge * sin(Gamma_a[i]);
          Y_b[i] = Distance_Source_to_Detector_Edge * sin(Gamma_b[i]);
          M_a[i] = Y_a[i] / X_a[i];
          M_b[i] = Y_b[i] / X_b[i];

          cout << setprecision(3) << fixed
            << "␣␣␣␣␣" << i + 1
               << "␣␣␣␣␣" << (Gamma_a[i] + Gamma_b[i])*(180 / PI) / 2
               << "␣␣␣␣␣" << (X_a[i] + X_b[i]) / 2
               << "␣␣␣␣␣" << (Y_a[i] + Y_b[i]) / 2
               << "␣␣␣␣␣" << M_a[i]
               << "␣␣␣␣␣" << M_b[i] << endl;
        }


        //detectors coordinates and their angular coefficents
        //--- CLOCKWISE
        for (int i = Number_of_Detectors_clockwise + 1;
             i < NUMBER_OF_DETECTORS;
             i++) {

          Gamma_a[i] = GammaaMAX - i * 2 * Beta - i*Angle_between_Det;
          Gamma_b[i] = GammabMAX - i * 2 * Beta - i*Angle_between_Det;
          X_a[i] = Distance_Source_to_Detector_Edge * cos(Gamma_a[i]);
          X_b[i] = Distance_Source_to_Detector_Edge * cos(Gamma_b[i]);
          Y_a[i] = Distance_Source_to_Detector_Edge * sin(Gamma_a[i]);
          Y_b[i] = Distance_Source_to_Detector_Edge * sin(Gamma_b[i]);
          M_a[i] = Y_a[i] / X_a[i];
```

```
            M_b[i] = Y_b[i] / X_b[i];


            cout << setprecision(3) << fixed
                 << "     " << i + 1
                 << "     " << (Gamma_a[i] + Gamma_b[i])*(180 / PI) / 2
                 << "     " << (X_a[i] + X_b[i]) / 2
                 << "     " << (Y_a[i] + Y_b[i]) / 2
                 << "     " << M_a[i]
                 << "     " << M_b[i] << endl;
        }
}
cout << "  " << endl;
}


// calculate the projection matrix and the detector view
// most important function of the code
void SetProjectionMatrix()
{
/*
This particular section of the code is available from the author
on reasonable request. mauro.licata88@gmail.com
*/

}


void ProjectonMatrix_OpenFile(int d)
{
        string name = "Projection_Matrix_DET_";
        string det = std::to_string(d + 1);
        string format = ".dat";
        string FILENAME = name + det + format;
        OUTPUT.open(FILENAME.c_str(), std::ios::app);
}


void ProjectonMatrix_FillFile(double value)
{
OUTPUT << setprecision(3) << fixed << value << " ";
}
void ProjectonMatrix_FillFile_string(string value)
{
OUTPUT << value;
}
void ProjectonMatrix_CloseFile()
{
OUTPUT.close();
}
```

```
double Weight_Calc(double x_pix, double y_pix, double theta, int detector)
{

double inside = 0.0;
double outside = 0.0;
double x_pix_min = x_pix - Pix_dimension / 2;
double x_pix_max = x_pix + Pix_dimension / 2;
double y_pix_min = y_pix - Pix_dimension / 2;
double y_pix_max = y_pix + Pix_dimension / 2;

// only used once to initialise (seed) engine
std::random_device rd;

// random-number engine used (Mersenne-Twister in this case)
std::mt19937 rngX(rd());
std::mt19937 rngY(rd());

// guaranteed unbiased
std::uniform_int_distribution<int> uniX(x_pix_min, x_pix_max);
std::uniform_int_distribution<int> uniY(y_pix_min, y_pix_max);

for (int i = 0; i < 10000; i++) {

        auto random_X = uniX(rngX);
        auto random_Y = uniY(rngY);

        double random_x_pix_RotoTransl =
        random_X*cos(theta*PI / 180) - random_Y*sin(theta*PI / 180)
        + X_Matrix_Centre;
        double random_y_pix_RotoTransl =
        random_X*sin(theta*PI / 180) + random_Y*cos(theta*PI / 180)
        + newY_Matrix_Centre;

        double random_PixCoef =
        random_y_pix_RotoTransl / random_x_pix_RotoTransl;

        if ((M_a[detector] >= random_PixCoef) &&
            (random_PixCoef >= M_b[detector])) {
                inside = inside + 1;
                }
        else {
                outside = outside + 1;
                }
}

weight = inside / (inside + outside);
return weight;
}
```

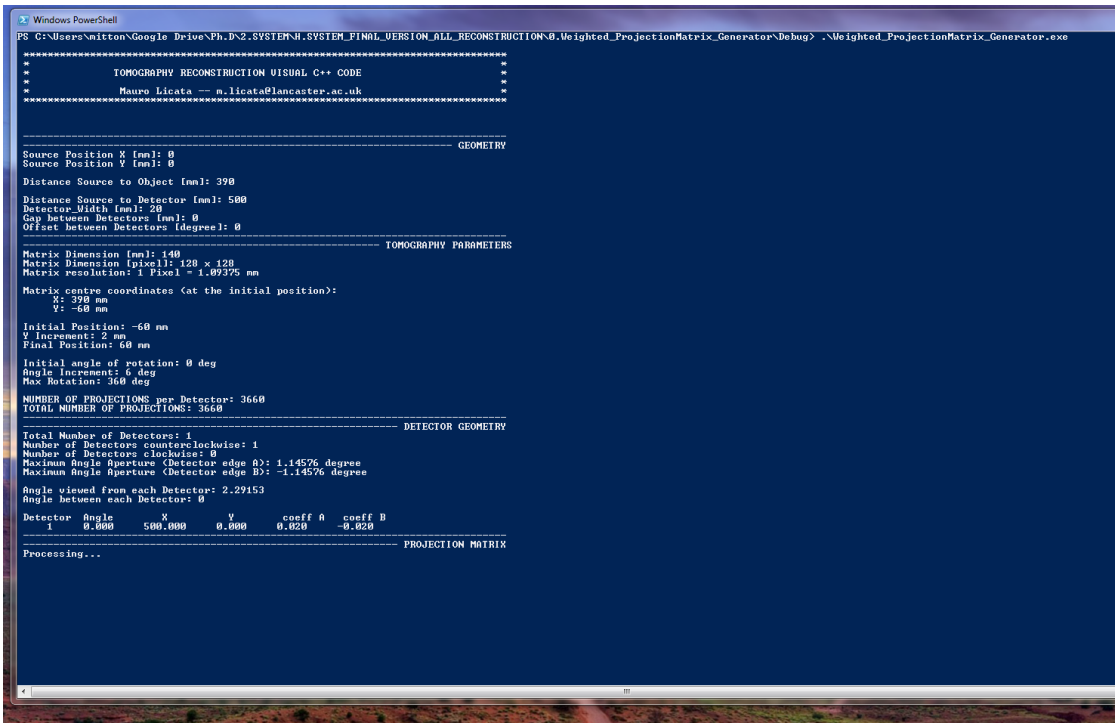


Figure C.1: A screenshot of the image reconstruction program.

## C.2 Image reconstruction: Matlab script

```
%%%%%%%%%%%%%%%%%%%%%%%%%%%%%%%%%%%%%%%%%%%%%%%%%%%%%%%%%%%%%%%%%%%%%%%%%%%%%%%%
%%%%%%%%%%%%%%%%%%%%%%%%%%%%%%%%%%%%%%%%%%%%%%%%%%%%%%%%%%%%%%%%%%%%%%%%%%%%%%%%
RECONSTRUCTION CODE --- SIRT
%%%%%%%%%%%%%%%%%%%%%%%%%%%%%%%%%%%%%%%%%%%%%%%%%%%%%%%%%%%%%%%%%%%%%%%%%%%%%%%%
%%%%%%%%%%%%%%%%%%%%%%%%%%%%%%%%%%%%%%%%%%%%%%%%%%%%%%%%%%%%%%%%%%%%%%%%%%%%%%%%
%%
%% m.licata@lancaster.it
%% algoritm implemented by the author with the help of the
%% astra toolbox
%W. V. Aarle, W. J. Palenstijn, J. D. Beenhouwer,
%T. Altantzis, S. Bals, K. J. Batenburg, J. Sijbers.
%The ASTRA Toolbox: A platform for advanced algorithm
%development in electron tomography.
%Ultramicroscopy 157 (2015) 35-47.
%%%%%%%%%%%%%%%%%%%%%%%%%%%%%%%%%%%%%%%%%%%%%%%%%%%%%%%%%%%%%%%%%%%%%%%%%%%%%%%%
%%%%%%%%%%%%%%%%%%%%%%%%%%%%%%%%%%%%%%%%%%%%%%%%%%%%%%%%%%%%%%%%%%%%%%%%%%%%%%%%
%%
DIM = 128;
% number of proj. per detector
//(say 744 = 31 translations x 24 rotation positions)
NUMBER_OF_PROJECTION=744;
% number of proj. times nummber of detectors
TOTAL_NUMBER_OF_PROJECTION = 9672;
%number of iterations
kiter = 51;
%%
```

```
%%
%%IMPORT PROJECTION MATRIX from the output generated by the c++ code
%% Initialize variables.
delimiter = ' ';
% configuration with 13 detectors
DETECTOR1 = 'Projection_Matrix_DET_1.dat';
.
.
.
DETECTOR13 = 'Projection_Matrix_DET_13.dat';
formatSpec = '%f%f%f%f%f%f%f%f.....% f%f%f%f%f%f%[^\n\r]';
fileID_DETECTOR1 = fopen(DETECTOR1,'r');
.
.
.
fileID_DETECTOR13 = fopen(DETECTOR13,'r');
dataArray_DETECTOR1 = textscan(fileID_DETECTOR1, formatSpec,
'Delimiter', delimiter, 'MultipleDelimsAsOne', true,
'EmptyValue' ,NaN, 'ReturnOnError', false);
.
.
.
dataArray_DETECTOR13 = textscan(fileID_DETECTOR13, formatSpec,
'Delimiter', delimiter, 'MultipleDelimsAsOne', true,
'EmptyValue' ,NaN, 'ReturnOnError', false);
%%
fclose(fileID_DETECTOR1);
.
.
.
fclose(fileID_DETECTOR13);
%% Create output variable
ProjectionMatrixDET1 = [dataArray_DETECTOR1{1:end-1}];
.
.
.
ProjectionMatrixDET13 = [dataArray_DETECTOR13{1:end-1}];
%%
W1 = ProjectionMatrixDET1;
.
.
.
W13 = ProjectionMatrixDET13;
W = vertcat(W1, W2, W3, W4, W5, W6, W7, W8, W9, W10, W11, W12, W13);
%%
%%
%% Clear temporary variables
clear vars  delimiter formatSpec ans;
clearvars DETECTOR1 fileID_DETECTOR1
dataArray_DETECTOR1 ProjectionMatrixDET1;
.
.
```

```
.
clearvars DETECTOR13 fileID_DETECTOR13
dataArray_DETECTOR13 ProjectionMatrixDET13;
%%
%%


%%
%%
%%- IMPORT ATTENUATION INDEX DATA
%% Initialize variables.
delimiter = '␣';
%%
DATA_DETECTOR1 = 'DET_1_DATA_NEUTRON.txt';
.
.
.
DATA_DETECTOR13 ='DET_13_DATA_NEUTRON.txt';
%%
formatSpec = '%*s%*s%*s%f%[^\n\r]';
formatSpecATTENUATION_INDEX = '%f%[^\n\r]';
%%
fileID_DATA_DETECTOR1 = fopen(DATA_DETECTOR1,'r');
.
.
.
fileID_DATA_DETECTOR13 = fopen(DATA_DETECTOR13,'r');
%%
dataArray_DATA_DETECTOR1 = textscan(fileID_DATA_DETECTOR1, formatSpec,
'Delimiter', delimiter, 'MultipleDelimsAsOne', true,
'ReturnOnError', false);
.
.
.
dataArray_DATA_DETECTOR13 = textscan(fileID_DATA_DETECTOR13, formatSpec,
'Delimiter', delimiter, 'MultipleDelimsAsOne', true,
'ReturnOnError', false);
%%
fclose(fileID_DATA_DETECTOR1);
.
.
.
fclose(fileID_DATA_DETECTOR13);
%%
%%
ATT_INDEX_DETECTOR1 = dataArray_DATA_DETECTOR1{:, 1};
.
.
.
ATT_INDEX_DETECTOR13 = dataArray_DATA_DETECTOR13{:, 1};
%%
%%
p1 = ATT_INDEX_DETECTOR1;
```

```
.
.
.
p13 = ATT_INDEX_DETECTOR13;
p = vertcat(p1, p2, p3, p4, p5, p6, p7, p8, p9, p10, p11, p12, p13);
%%
%% Clear temporary variables
clearvars delimiter formatSpec ans;
clearvars fileID_DATA_DETECTOR1  DATA_DETECTOR1 dataArray_DATA_DETECTOR1
ATT_INDEX_DETECTOR1;
.
.
.
clearvars fileID_DATA_DETECTOR13  DATA_DETECTOR13 dataArray_DATA_DETECTOR13
ATT_INDEX_DETECTOR13;
%%
%%
%%%%%%%%%%%%%%%%%%%%  SIRT algorithm
%%
W_t = transpose(W);
W1_t = transpose(W1);
.
.
.
W13_t = transpose(W13);
%%
R  = W * ones(DIM*DIM,1); R(R==0)=Inf; R(R<1.e-4)=Inf;
R1 = W1 * ones(DIM*DIM,1); R1(R1==0)=Inf; R1(R1<1.e-4)=Inf;
.
.
.
R13 = W13 * ones(DIM*DIM,1); R13(R13==0)=Inf; R13(R13<1.e-4)=Inf;
%%
C = W_t * ones(TOTAL_NUMBER_OF_PROJECTION, 1); C(C==0)=Inf; C(C<1.e-4)=Inf;
C1 = W1_t * ones(NUMBER_OF_PROJECTION, 1); C1(C1==0)=Inf; C1(C1<1.e-4)=Inf;
.
.
.
C13 = W13_t * ones(NUMBER_OF_PROJECTION, 1); C13(C13==0)=Inf; C13(C13<1.e-4)=Inf;
%%
v = zeros(DIM*DIM, 1);
v1 = zeros(DIM*DIM, 1);
.
.
.
v13 = zeros(DIM*DIM, 1);
%%
for k = 1:kiter
                r = (p(:) - W*v) ./ R;
                r1 = (p1(:) - W1*v1) ./ R1;
                .
                .
```

```
                .
                r13 = (p13(:) - W13*v13) ./ R13;
                %%
                v = v + (W_t*r) ./ C;
                v1 = v1 + (W1_t*r1) ./ C1;
                .
                .
                .
                v13 = v13 + (W13_t*r13) ./ C13;
                %%
                v(v<0)=0;
                v1(v1<0)=0;
                .
                .
                .
                v13(v13<0)=0;

end
%%
totalimage = vec2mat(v,DIM);
image1 = vec2mat(v1,DIM);
.
.
.
image13 = vec2mat(v13,DIM);
%%
colormap jet;
axis square;
subplot(2,7,1);
imagesc(image1);
.
.
.
axis square;
subplot(2,7,13);
imagesc(image13);
title('DET13');

axis square;
subplot(2,7,14);
imagesc(totalimage);
title('TOTAL');
axis square;
%%
save totalimage_NEUTRON_AmBe.dat totalimage -ASCII
% ------------------------------------------------------------
```

## C.3 Arduino Counter Code

```
//================================================//
// 05/04/2018 IT/ML Pulse counter verfication test  //
// Data collection from I2C port0 of multiplexer    //
// Serial monitor interface. ML to update for .exe  //
//================================================//
//
//
//=======================================//
//              Initialisation           //
//=======================================//

/* For I2C communication */
#include "Wire.h"
/* For bus scanning */
extern "C" {
#include "utility/twi.h"
}

/* Multiplexer address */
#define TCAADDR 0x70
/* ch12 stores channel 1 and 2 bytes */
int ch12[2][4];
int ch34[2][4];
int ch56[2][4];
int ch78[2][4];
int ch910[2][4];
int ch1112[2][4];
int ch1314[2][4];
int ch1516[2][4];
int j;
int h;
int f;
int b;
int t;
int mpx;
int ch[16];

/* Counter pins to Teensy's I0 pins, see SN74LV8154 datasheet, page 3*/
const int AL=20;
const int AU=21;
const int BL=22;
const int BU=23;
const int CCLR = 14;
const int RCLK = 17;

/* Port selection global function */
void tcaselect(uint8_t i) {
if (i > 7) return;
Wire.beginTransmission(TCAADDR);
```

```
Wire.write(1 << i);
Wire.endTransmission();
}

/* Get GPIOA or GPIOB data (channel 1 or 2 individual byte, e.g. GAL) */
char writeaddress[2]={0x13, 0x12};
//char address[4]={0x20, 0x24, 0x20, 0x24};

/* Combos to get all individual bytes for each channel */
const int combos[4][4]={{LOW, HIGH, HIGH, HIGH},
{HIGH, LOW, HIGH, HIGH},
{HIGH, HIGH, LOW, HIGH},
{HIGH, HIGH, HIGH, LOW}};


//=========================================//
//                  Setup                  //
//=========================================//
void setup()
{
pinMode(AL, OUTPUT);
pinMode(AU, OUTPUT);
pinMode(BL, OUTPUT);
pinMode(BU, OUTPUT);
pinMode(CCLR, OUTPUT);
pinMode(RCLK, OUTPUT);
Wire.begin();
Serial.begin(9600);

}


//=========================================//
//                 Main loop               //
//=========================================//
void loop()
{
readcounters();
}



//=========================================//
//                Pulse counter            //
//=========================================//

void readcounters(){

while (Serial.available() == 0);
/* Wait for user input; number in minutes */
int val = Serial.parseInt();
/* one second interval loop */
```

```
for (j=1; j<=val ; j++) {

digitalWrite(CCLR, HIGH);
delay(1000);
/* Activate RCLK to update counter */
digitalWrite(RCLK, HIGH);
digitalWrite(RCLK, LOW);

Serial.print(j);

/* multiplexer address selection */
for (mpx=0; mpx<=1 ; mpx++) {

tcaselect(mpx);

/* For each individual combo */
for (f=0; f<4; f++){
digitalWrite(AL, combos[f][0]);
digitalWrite(AU, combos[f][1]);
digitalWrite(BL, combos[f][2]);
digitalWrite(BU, combos[f][3]);

/* For each GPIO (A and B) of mcp23017 1 ********************** 000*/
for (b=0; b<2; b++){
Wire.beginTransmission(0x20);
Wire.write(writeaddress[b]);
Wire.endTransmission();
Wire.requestFrom(0x20,1);
ch12[b][f]=Wire.read();
}
/* For each GPIO (A and B) of mcp23017 2 ********************** 001*/
for (b=0; b<2; b++){
Wire.beginTransmission(0x24);
Wire.write(writeaddress[b]);
Wire.endTransmission();
Wire.requestFrom(0x24,1);
ch34[b][f]=Wire.read();
}
/* For each GPIO (A and B) of mcp23017 3 ********************** 010*/
for (b=0; b<2; b++){
Wire.beginTransmission(0x22);
Wire.write(writeaddress[b]);
Wire.endTransmission();
Wire.requestFrom(0x22,1);
ch56[b][f]=Wire.read();
}
/* For each GPIO (A and B) of mcp23017 4 ********************** 110*/
for (b=0; b<2; b++){
Wire.beginTransmission(0x26);
Wire.write(writeaddress[b]);
```

```
Wire.endTransmission();
Wire.requestFrom(0x26,1);
ch78[b][f]=Wire.read();
}
/* For each GPIO (A and B) of mcp23017 5 ******************** 001*/
for (b=0; b<2; b++){
Wire.beginTransmission(0x21);
Wire.write(writeaddress[b]);
Wire.endTransmission();
Wire.requestFrom(0x21,1);
ch910[b][f]=Wire.read();
}
/* For each GPIO (A and B) of mcp23017 6 ******************** 101*/
for (b=0; b<2; b++){
Wire.beginTransmission(0x25);
Wire.write(writeaddress[b]);
Wire.endTransmission();
Wire.requestFrom(0x25,1);
ch1112[b][f]=Wire.read();
}
/* For each GPIO (A and B) of mcp23017 7 ******************** 011*/
for (b=0; b<2; b++){
Wire.beginTransmission(0x23);
Wire.write(writeaddress[b]);
Wire.endTransmission();
Wire.requestFrom(0x23,1);
ch1314[b][f]=Wire.read();
}
/* For each GPIO (A and B) of mcp23017 8 ******************** 111*/
for (b=0; b<2; b++){
Wire.beginTransmission(0x27);
Wire.write(writeaddress[b]);
Wire.endTransmission();
Wire.requestFrom(0x27,1);
ch1516[b][f]=Wire.read();
}
}

/* After each read, store to ch array */
ch[0]=(ch12[0][0]+ch12[0][1]*255+ch12[0][2]*65025+ch12[0][3]*16581375);
ch[1]=(ch12[1][0]+ch12[1][1]*255+ch12[1][2]*65025+ch12[1][3]*16581375);
ch[2]=(ch34[0][0]+ch34[0][1]*255+ch34[0][2]*65025+ch34[0][3]*16581375);
ch[3]=(ch34[1][0]+ch34[1][1]*255+ch34[1][2]*65025+ch34[1][3]*16581375);
ch[4]=(ch56[0][0]+ch56[0][1]*255+ch56[0][2]*65025+ch56[0][3]*16581375);
ch[5]=(ch56[1][0]+ch56[1][1]*255+ch56[1][2]*65025+ch56[1][3]*16581375);
ch[6]=(ch78[0][0]+ch78[0][1]*255+ch78[0][2]*65025+ch78[0][3]*16581375);
ch[7]=(ch78[1][0]+ch78[1][1]*255+ch78[1][2]*65025+ch78[1][3]*16581375);
ch[8]=(ch910[0][0]+ch910[0][1]*255+ch910[0][2]*65025+ch910[0][3]*16581375);
ch[9]=(ch910[1][0]+ch910[1][1]*255+ch910[1][2]*65025+ch910[1][3]*16581375);
ch[10]=(ch1112[0][0]+ch1112[0][1]*255+ch1112[0][2]*65025+ch1112[0][3]*16581375);
ch[11]=(ch1112[1][0]+ch1112[1][1]*255+ch1112[1][2]*65025+ch1112[1][3]*16581375);
ch[12]=(ch1314[0][0]+ch1314[0][1]*255+ch1314[0][2]*65025+ch1314[0][3]*16581375);
```

```
ch[13]=(ch1314[1][0]+ch1314[1][1]*255+ch1314[1][2]*65025+ch1314[1][3]*16581375);
ch[14]=(ch1516[0][0]+ch1516[0][1]*255+ch1516[0][2]*65025+ch1516[0][3]*16581375);
ch[15]=(ch1516[1][0]+ch1516[1][1]*255+ch1516[1][2]*65025+ch1516[1][3]*16581375);

/* print readings */
for (int h=0; h<16; h++){
Serial.print('␣');
Serial.print(ch[h]);
Serial.print('␣');
}

}

Serial.println('␣');

// digitalWrite(CCLR, LOW);  //if you want to reset the counters each second
}

digitalWrite(CCLR, LOW);  // reset counters at the end

}
```

# Bibliography


[1] J. Chadwick. *Possible existence of a Neutron.* Nature 129, 312 (1932).

[2] Paul Sherrer Institut. *Neutron imaging at the spallation source SINQ Information for potential users and customers* .

[3] T. Bucherl et al. *NECTAR-A fission neutron radiography and tomography facility.* Nuclear Instruments and Methods in Physics Research Section A. Volume 651, Issue 1, 21 September 2011, Pages 86-89.

[4] ANSTO. https://www.ansto.gov.au/.

[5] ISIS Neutron and Muon Source: https://www.isis.stfc.ac.uk/Pages/home.aspx

[6] Instute Laue Langevin, Neutrons for Society. https://www.ill.eu/

[7] Eberhardt J.E. et nal. *Fast neutron radiography scanner for the detection of contraband in air cargo containers.* Applied Radiation ad Isotopes Volume 63, Issue 2, August 2005, Pages 179-188

[8] B. D. Sowerby et al. *Fast neutron and gamma ray interrogation of air cargo containers* . IAEA CRP on Neutron Based Techniques for the Detection of Illicit Materials and Explosives, Johannesburg, 16-20 November 2009.

[9] J. Rynes et al. *Gamma-ray and neutron radiography as part of a pulsed fast neutron analysis inspection system.* Nuclear Instruments and Methods in Physics Research A 422 (1999) 895-899.

[10] Z. D. Whetstone and K. J. Kearfott. *A review of conventional explosives detection using active neutron interrogation* . J Radioanal Nucl Chem (2014) 301:629-639

[11] J. G. Fantidis et al. *Fast and thermal neutron radiographies based on a compact neutron generator.* Journal of Theoretical and Applied Physics 2012, 6:20.

[12] J.G. Fantidis, G. E. Nicolaou and N. F. Tsagas. *Optimization study of a transportable neutron radiography unit based on a compact neutron generator.* Nuclear Instruments and Methods in Physics Research A 618 (2010) 331-335.

[13] P.A. Hausladen et al. *Portable fast-neutron radiography with the nuclear materials identification system for fissile material transfers.* Nucl. Instrum. Meth. B 261 (2007) 387.

[14] R . Adams et al. *A novel fast neutron tomography system based on a plastic scintillator array and a compact D-D neutron generator.* Applied Radiation and Isotopes 107(2016)1-7.

[15] N. Zaitseva et al. *Plastic scintillators with efficient neutron gamma pulse shape discrimination.* Nuclear Instruments and Methods in Physics Research A668(2012)88-93.

[16] M.J. Joyce, M.D. Aspinall, F.D. Cave, K. Georgopoulos and Z. Jarrah. *The design, build and test of a digital analyzer for mixed radiation fields.* IEEE. Trans. Nucl. Sci. 57, 2625-2630 (2010). https://doi.org/10.1109/ANIMMA.2009.5503698.

[17] M. J. Joyce et al. *A 16-Channel Real-Time Digital Processor for Pulse-Shape Discrimination in Multiplicity Assay.* IEEE Transactions on Nuclear Science NS-59 (4) (2012) 1245.

[18] K.A.A. Gamage, M.J.Joyce, N.P.Hawkes. *A comparison of four different digital algorithms for pulse-shape discrimination in fast scintillators.* Nuclear Instruments and Methods in Physics Research A642 (2011)78-83.

[19] K.A.A. Gamage, M.J.Joyce, J.C.Adams. *Combined digital imaging of mixed-field radioactivity with a single detector* . Nuclear Instruments and Methods in Physics Research A635 (2011) 74-77.

[20] J. Beaumont et al. *Imaging of fast neutrons and gamma rays from 252Cf in a heavily shielded environment.* Nuclear Instruments and Methods in Physics Research A 847 (2017) 77-85.

[21] J. Beaumont, M. Mellor and M. Joyce. *Real-time, Fast-neutron Spectroscopy for Source Identification in Mixed-field Imaging Applications.* 2012 IEEE Nuclear Science Symposium and Medical Imaging Conference Record (NSS/MIC).

[22] J. Beaumont et al. *High-intensity power-resolved radiation imaging of an operational nuclear reactor.* Nature Communications, 6:8592, DOI: 10.1038/ncomms9592.

[23] https://www.llnl.gov/

[24] L.F. Nakae et al. *Recent Developments In Fast Neutron Detection And Multiplicity Counting With Verification With Liquid Scintillator.* International Workshop on Fast Neutron Detectors and Applications. Ein Gedi, Israel. November 6, 2011 through November 11, 2011.

[25] G. F. Chapline et al. *Monitoring Spent or Reprocessed Nuclear Fuel Using Fast Neutrons.* Fusion Science and Technology, 61:1T, 150-154, DOI: 10.13182/FST12-A13412 https://doi.org/10.13182/FST12-A13412

[26] P. Kerr and V. Mozin. *Stilbene Scintillator Detector Array and Data-Acquisition System for Active Interrogation.* Tecnical Report. LLNL-TR-757673.

[27] Leslie F. Nakae. *Fast Neutron and Gamma Ray Detection and Multiplicity Counting with LLNL Scintillator Array.* 2017 International Conference on Applications of Nuclear Techniques (CRETE 17). Rethymno, Crete, Greece, June 11-17, 2017. LLNL PRES 732980.

[28] B. Canion et al. *Point Kinetics Framework for Characterizing Prompt Neutron and Photon Signatures from Tagged Neutron Interrogation.* IEEE Transactions on Nuclear Science. Volume 64 , Issue: 7 , July 2017.

[29] Phil Kerr et al. *Active detection of small quantities of shielded highly-enriched uranium using low-dose 60-kev neutron interrogation.* Nucl. Instrum. Meth. B. Volume 261, Issues 1-2, August 2007, Pages 347-350

[30] K. Mitton, A. Jones and M.J. Joyce. *Digital fast neutron radiography of steel reinforcing bar in concrete* . Journal of Instrumentation, 9 C12045. Doi:10.1088/1748-0221/9/12/C12045.

[31] M.J. Joyce et al. *Fast neutron tomography with real-time pulse-shape discrimination in organic scintillation detectors.* Nucl. Instrum. Meth. A 834 (2016) 36-45.

[32] K.S. Krane. *Introductory Nuclear Physics.* Jonh Wiley and sons, 444-456.

[33] H. Kluge and K. Weise. *The neutron energy spectrum of a 241Am-Be(alpha,n) source and resulting mean fluence to dose equivalent conversion factors.* Radiation Protection Dosimetry 2 (1982) 85-93.

[34] R.C Martin et al. *Production, distribution and applications of californium-252 neutron sources.* Applied Radiation and Isotopes, Volume 53, Issues 4-5, 2000, Pages 785-792, https://doi.org/10.1016/S0969-8043(00)00214-1.

[35] W. W. T. Crane et al. *Average Number of Neutrons Emitted During the Spontaneous Fission of Cf252.* Phys. Rev. 97, 242. Published 1 January 1955; Erratum Phys. Rev. 97, 1727 (1955)

[36] G. F. Knoll. *Radiation Detection and Measurements.* 4th Edition. John Wiley and Sons. 2010.

[37] E. Hjalmar et al. *Energy Spectrum of Neutrons from Spontaneous Fission of Californium-252.* Phys. Rev. 100, 1542. Published 1 December 1955

[38] L. Green et al. *The Californium-252 Fission Neutron Spectrum from 0.5 to 13 MeV.* Pages 257-272 Published online: 13 May 2017. https://doi.org/10.13182/NSE73-A28979

[39] National Nuclear Data Center https://www.nndc.bnl.gov/.

[40] W.R.Leo *Techniques for nuclear and particle physics experiments.* Springer-Verlag Berlin Heidelberg Gmb. pp 149-163.

[41] Online source. Data from XCOM database: https://www.nist.gov/pml/xcom-photon-cross-sections-database

[42] R.L.Craun, D. L.Smith. Nucl. Instr. and Meth. 80, 239 (1970).

[43] J. G. BirK. Proc. Phys. Soc. A64, 874 (1951);

[44] Online source: https://micro.magnet.fsu.edu/primer/digitalimaging/concepts/photomultipliers.ht

[45] D. Wolski et al. *Comparison of n-$\gamma$ discrimination by zero-crossing and digital charge comparison methods.* Nuclear Instruments and Methods in Physics Research A 360 (1995) 584-592

[46] D'Mellow, B. et al. *Digital discrimination of neutrons and $\gamma$-rays in liquid scintillators using pulse gradient analysis.* Nuclear Instruments and Methods in Physics Research. Section A. Vol. 578, no. 1, pp. 191-197. https://doi.org/10.1016/j.nima.2007.04.174.

[47] Ian S. Anderson, Robert L. McGreevy, and Hassina Z. Bilheux. *Neutron Imaging and Applications: A Reference for the Imaging Community.* ISBN 9780387786926, 2009.

[48] N. Kardjilov et al. *Neutron imaging in materials science.* Materials Today. Number 6, Volume 14, June 2011.

[49] H. Kallmann. *Neutron Radiography.* Research; a journal of science and its applications. 1(6), pp. 254-260

[50] B. Schillinger, E.Lehmann, P. Vontobel. *3D neutron computed tomography: requirements and applications.* Physica B 276-278 (2000) 59-62.

[51] Strobl M., Manke I., Kardjilov N., Hilger A., Dawson M., Banhart J. *Advances in neutron radiography and tomography.* J. Physics D. 42 (2009) 243001.

[52] Banhart J. *Advanced Tomographic Methods in Materials Research and Engineering.* 2008, Oxford University Press.

[53] Lehmann E. and Vontobel P. *The use of amorphous silicon flat panels as detector in neutron imaging* . 2004 Appl.Radiat. Isot. 61 567.

[54] Estermann M. et al. *The performance of an amorphous silicon flat panel for neutron imaging at the PSI NEUTRA facility.* 2005 Nucl. Instrum. Methods A 542 253.

[55] Pleinert H., Lehmann E. and Korner S. *Design of a new CCD-camera neutron radiography detector.* 1997 Nucl. Instrum Methods A 399 382

[56] A. Tomanin et al. *Characterization of a cubic EJ-309 liquid scintillator detector.* Nuclear Instruments and Methods in Physics Research A 756 (2014) 45-54.

[57] L. Stevanato et al. *Neutron detection in a high gamma-ray background with EJ-301 and EJ-309 liquid scintillators.* Nuclear Instruments and Methods in Physics Research A 690 (2012) 96-101.

[58] Lehmann E. H. *Facilities for neutron radiography in Europe: performance, applications and future use.* Proc.15th World Conf. on Non-destructive Testing (Rome, Italy, October 2000).

[59] M. Kureta and H. Iikura. *Development of an ultra high speed scanning neutron tomography system for high-quality and four-dimensional visualizations.* Nuclear Instruments and Methods in Physics Research A 605 (2009) 81-84.

[60] P. Andersson et al. *Design and initial 1D radiography tests of the FANTOM mobile fast-neutron radiography and tomography system.* Nuclear Instruments and Methods in Physics Research A 756 (2014) 82-93.

[61] *Neutron imaging at the spallation source SINQ. Information for potential users and customers.* (Leaflet) Paul Sherrer Institute.

[62] M.R. Gibbons, W.J.Richards, K.Shields. *Optimization of neutron tomography for rapid hydrogen concentration inspection of metal castings.* Nucl.Instrum. Methods Phys.Res. 424(1) (1999)53-57.

[63] C.M. Sim, S.H.Oh, T.J.Kim, Y.S.Lee, Y.K.Kim, S.S.Kwak, Y.H.Hwang. *Detecting internal hot corrosion of in-service turbine blades using neutron tomography with Gd tagging.* J.Nondestruct.Eval.33(4)(2014)493-503

[64] Edenborough, N.B. *Neutron imaging to detect residual core in investment cast turbine air foils.* ASTM, STP 586, 152-157 (1976)

[65] Brenizer, J.S. et al. *The use of contrast agents to enhance crack detection via neutron imaging.* NDT&E Int. 32, 37-42 (1999)

[66] Dance, W.E., et al. *Demonstration of mobile accelerator neutron imaging for in situ detection of moisture and corrosion in aircraft structures.* AIAA Aircraft Design, Systems and Technology Meeting, Oct. 17-19 1983 Fort Worth (1983)

[67] Lindsay, J., et al. *Internal flow measurement of the SSME fuel preburner injector element using real time neutron imaging.* AIAA/SAE/ASME/ASEE 26th Joint Propulsion Conference, July 16-18, Orlando, (AIAA-90-2293) (1990)

[68] Hatakenaka, R., et al. *Visualization of internal fluid behavior in a miniature loop heat pipe using neutron imaging.* 41st International Conference on Environmental System, 17-21 July Portland, Oregon (AIAA 2011-5140) (2011)

[69] Bellows, R.J. et al. *Neutron imaging technique for in situ measurement of water transport gradients within Nafion in polymer electrolyte fuel cells.* Journal of the Electrochemical Society, Volume 146, Issue 3, March 1999, Pages 1099-1103

[70] Boillat, P. et al. *Neutron imaging of fuel cells - Recent trends and future prospects* Current Opinion in Electrochemistry, Volume 5, Issue 1, October 2017, Pages 3-10

[71] T. Bucherl and C. L. Gostomski. *Fission Neutron Tomography of a 280-L Waste Package.* 11th World Conference on Neutron Radiography, Sydney, Australia, Sep. 2018.

[72] Online source, video: https://www.youtube.com/watch?v=VESMU7JfVHU

[73] Stelzner J. et al. *The application of 3D computed tomography with X-rays and neutrons to visualize archaeological objects in blocks of soil.* Studies in Conservation. Volume 55, Issue 2, 2010, Pages 95-106.

[74] Fiori F. et al. *Non-destructive characterization of archaeological glasses by neutron tomography* . Physica B. Volume 385-386, 15 November 2006, Pages 1206-1208.

[75] A. Fedrigo *Imaging investigation of Chinese bimetallic sword fragment from 2nd-1st century BCE* 11th World Conference on Neutron Radiography, Sydney, Australia, Sep. 2018.

[76] M.Laab *New insights into the tooth structure of pelycosaurs by means of neutron toography* 11th World Conference on Neutron Radiography, Sydney, Australia, Sep. 2018.

[77] S. Olsen and K. Sheedy *Official or Illegal? Tomographic analysis of plated silver coins from Ancient Greece .* 11th World Conference on Neutron Radiography, Sydney, Australia, Sep. 2018.

[78] F. Salvemini *Neutron Imaging, a key scientific analytical tool for the cultural heritage project at ANSTO.* 11th World Conference on Neutron Radiography, Sydney, Australia, Sep. 2018.

[79] J. Bevitt. *Neutron micro-CT as a non-destructive tool for Palaeontology in Australia* 11th World Conference on Neutron Radiography, Sydney, Australia, Sep. 2018.

[80] A.Koliji et al. *Experimental study of flow and deformation in aggregated soils using neutron tomography.* Adv.X-ray Tomogr. Geomater.(2010)341-348.

[81] Perfect E. et al. *Neutron imaging of hydrogen-rich fluids in geomaterials and engineered porous media: A review* Earth-Science Reviews. 129, pp. 120-135

[82] P.Vontobel,E.Lehmann and W.D.Carlson, *Comparison of x-ray and neutron tomography investigations of geological materials* . IEEE Trans. Nucl. Sci.52(1) (2005) 338-341.

[83] M. Extegarai et al. *Investigation of Hydromechanical processes in porous rock using 4D Neutron imaging.* 11th World Conference on Neutron Radiography, Sydney, Australia, Sep. 2018.

[84] P. Christe et al. *Three-dimensional petrographical investigations on borehole rock samples: a comparison between X-ray computed- and neutron tomography.* Acta Geotech. 2 (2007) 269.

[85] Masschaele et al. *High-speed thermal neutron tomography for the visualization of water repellents, consolidants and water uptake in sand and lime stones.* Rad. Phys. Chem. 71 (2004) 807.

[86] R. Satija et al. *In situ neutron imaging technique for evaluation of water management systems in operating PEM fuel cells.* Journal of Power Sources. Volume 129, Issue 2, 22 April 2004, Pages 238-245.

[87] R. Ziesche et al. *Dynamic lithium diffusion in lithium batteries studied by rapid neutron tomography.* 11th World Conference on Neutron Radiography, Sydney, Australia, Sep. 2018.

[88] S. Zimnik et al. *Neutron Imaging of Li-Ion batteries with fission and thermal neutrons.* 11th World Conference on Neutron Radiography, Sydney, Australia, Sep. 2018.

[89] L. G. Butler et al. *Neutron radiography, tomography, and diffraction of commercial lithium-ion polymer batteries.* Physics Procedia 43 ( 2013 ) 331 - 336.

[90] A. Tremisn et al. *In-situ diagnostic of crystal growth by energy-resolved neutron imaging.* 11th World Conference on Neutron Radiography, Sydney, Australia, Sep. 2018.

[91] Y. Kiyanagi et al. *Comparison of crystallographic structures of Japanese swords in Muromach and modern periods by using pulsed neutron imaging.* 11th World Conference on Neutron Radiography, Sydney, Australia, Sep. 2018.

[92] I. Stepanov et al. *Investigation of ancient copper alloy and ferrous artefacts from South-eastern Arabia.* 11th World Conference on Neutron Radiography, Sydney, Australia, Sep. 2018.

[93] Eberhardt J.E. et al. *Fast-neutron/gamma-ray radiography scanner for the detection of contraband in air cargo containers* . Proceedings of SPIE - The International Society for Optical Engineering. Volume 6213, 2006, Article number 621303.

[94] G. Chen and R. C. Lanza *Fast Neutron Resonance Radiography for Security Applications.* Application of Accelerators in Research and Industry - Sixteenth International Conference.

[95] Sinha V., Srivastava A., Lee H.K., Liu X. *Feasibility studies on explosive detection and homeland security applications using a neutron and X-ray combined computed tomography system* . Proceedings of SPIE. Volume 8710, 2013, Article number 87100W.

[96] Buffler, A. *Contraband detection with fast neutrons* . Radiation Physics and Chemistry. Volume 71, Issue 3-4, October 2004, Pages 853-861

[97] T. Gozani and D. Straellis. *Advances in neutron based bulk explosive detection.* Nucl. Instrum. Meth. B 261 (2007) 311.

[98] E. H. Lehmann et al. Non-destructive analysis of nuclear fuel by means of thermal and cold neutrons. Nuclear Instruments and Methods in Physics Research A 515 (2003) 745-759

[99] A. Agrawal, et al. *Study of hydride blisters in Zr-alloy using neutron tomography.* J.Nucl.Mater.421(1-3)(2012) 47-53.

[100] W.J.Richards, G.C.McClellan, D.M.Tow. *Neutron tomography of nuclear fuel bundles.* Mater.Eval.40(12)(1982)1263-1267.

[101] R. Zboray and H. M.Prasser. *Optimizing the performance of cold-neutron tomography for investigating annular flows and functional spacers in fuel rod bundles.* Nucl.Eng.Des.260(2013) 188-203.

[102] J.L. Kickhofel et al. *Cold neutron tomography of annular coolant flow in a double sub channel model of a boiling water reactor.* Nucl. Instrum. Methods Phys. Res. Sect.A. 651(1)(2011)297-304.

[103] T. Gozani *The role of neutron based inspection techniques in the post 9/11/01 era.* Nucl. Instrum. Meth. B 213 (2004) 460.

[104] G. Gaukler et al. *Detecting nuclear materials smuggling: using radiography to improve container inspection policies.* Ann Oper Res (2011) 187:6587

[105] Y. Liu et al. *Nuclear material identification by photoneutron and X-ray radiography.* In proceedings of the 2011 IEEE Nuclear Science Symposium Conference Record, Valencia, Spain, 23-29 October 2011, pp. 305-307 [https://doi.org/10.1109/NSSMIC.2011.6154504].

[106] W. L. Raas et al. *Neutron Resonance Radiography for Explosives Detection: Technical Challenges.* 2005 IEEE Nuclear Science Symposium Conference Record

[107] J. Mullens et al. *Neutron radiography and fission mapping measurements of nuclear materials with varying composition and shielding.* Manuscript. Oak Ridge National Laboratory.

[108] E. H. Lehmann and W. Wagner. *Neutron imaging at PSI: a promising tool in materials science and technology.* Appl Phys A (2010) 99: 627-634. DOI 10.1007/s00339-010-5606-3

[109] J. Hartman et al. *3D imaging using combined neutron-photon fan-beam tomography: A Monte Carlo study.* Appl. Radiat. Isot. 111 (2016) 110.

[110] *Neutron imaging at the spallation source SINQ. Information for potential users and customers.*

[111] V. Sinha et al. *Design and Development of a Neutron/X-Ray Combined Computed Tomography System at S&T Missouri* .

[112] Combined Gamma-Ray/Neutron Imaging System for Detecting Nuclear Material. Manuscript (2013) Radiation Monitoring Devices Inc.

[113] De Beer F. and Ameglio L. *Neutron, X-ray and dual gamma-ray radiography and tomography of geomaterial - A South African perspective.* Leading Edge (Tulsa, OK) Volume 30, Issue 6, June 2011, Pages 666-672.

[114] A. Poitrasson-RiviÃ¨re et al. *Dual-particle imaging system based on simultaneous detection of photon and neutron collision events.* Nuclear Instruments and Methods in Physics Research A 760 (2014) 40-45.

[115] R.T. Lopes and W.W. Pereira. *A comparative study of tomographies using gamma rays and neutrons in non-destructive testing.* Nucl. Instrum. Meth. 353 (1994) 142.

[116] R. Ziesche et al. *4D imaging of lithium-batteries using correlative neutron and X-ray tomography with a virtual unrolling technique.* Nature Communications. https://doi.org/10.1038/s41467-019-13943-3

[117] *Tomographic Image Reconstruction.* 41st Annual Meeting of the American Association of Physicist in Medicine. July 25-29, 1999 Nashville, USA.

[118] R. Gordon et al. *Algebraic Reconstruction Techniques (ART) for three-dimensional electron microscopy and X-ray photography* Volume 29, Issue 3, December 1970, Pages 471-476, IN1-IN2, 477-481

[119] W. V. Aarle, W. J. Palenstijn, J. D. Beenhouwer, T. Altantzis, S. Bals, K. J. Batenburg, J. Sijbers. *The ASTRA Toolbox: A platform for advanced algorithm development in electron tomography.* Ultramicroscopy 157 (2015) 35-47.

[120] P. Gilbert *Iterative methods for the three-dimensional reconstruction of an object from projections.* J. Theor. Biol. 36 (1972) 105.

[121] Georges Louis Leclerc comte de Buffon. *Essai d'arithmÃ©tique morale.* 1977.

[122] N. Metropolis *The beginning of the Monte Carlo method.* Los Alamos Science (1987 Special Issue dedicated to Stanislaw Ulam).

[123] R. Eckhardt. *Stan Ulam, John Von Neumann and the Monte Carlo method.* Los Alamos Science (1987 Special Issue dedicated to Stanislaw Ulam).

[124] J. F. Briesmeister *MCNP - A General Monte Carlo N-Particle Transport Code.* . LA-13709-M Manual. March 2000.

[125] https://geant4.web.cern.ch/

[126] https://mcnp.lanl.gov/

[127] Los Alamos National Laboratory. Los Alamos, NM, USA. https://www.lanl.gov/.

[128] Goorley, T. et al. *Initial MCNP6 Release Overview*. Nuclear Technology, 180, pp 298-315 (Dec 2012).

[129] Goorley, T. MCNP6.1.1-Beta Release Notes. LA-UR-14-24680 (2014).

[130] https://www-nds.iaea.org/exfor/endf.htm

[131] R. Schulze et al. *The ANCIENT CHARM project at FRM II: three-dimensional elemental mapping by prompt gamma activation imaging and neutron tomography.* J. Anal. At. Spectrom. 28 (2013) 1508

[132] C.M. Whitney et al. *Gamma-neutron imaging system utilizing pulse shape discrimination with CLYC*. Nucl. Instrum. Meth. A 784 (2015) 346.

[133] J.E. Eberhardt et al. *Fast neutron and gamma-ray interrogation of air cargo containers*. In proceedings of International Workshop on Fast Neutron Detectors and Applications (FNDA 2006). University of Cape Town, Cape Town, South Africa, 3-6 April 2006.

[134] A. Enqvist et al. *Gamma-Ray and Fast Neutron Imager with Thermal Neutron Detection Capability for Detecting Shielded and Bare Nuclear Materials*. In proceedings of the 2015 IEEE International Symposium on Technologies for Homeland Security (HST), Waltham, MA, U.S.A., 14-16 April 2015.

[135] T. Kamiyama et al. *Accelerator based neutron tomography cooperating with X-ray radiography*. Nucl. Instrum. Meth. A 651 (2011) 28.

[136] B. Schillinger, E. Lehmann and P. Vontobel. *3D neutron computed tomography: requirements and applications*. Physica B 276-278 (2000) 59.

[137] B. Schillinger. *Estimation and measurement of $L/D$ on a cold and thermal neutron guide*. Nondestr. Test. Eval. 16 (2001) 141.

[138] M.J. Radebe et al. *Evaluation procedures for spatial resolution and contrast standards for neutron tomography*. The 7th International Topical Meeting on Neutron Radiography (ITMNR-7). Volume 43, P.C. Hungler ed., Elsevier B.V. (2013) [Phys. Procedia 43 (2013) 138].

[139] *SCIONIX scintillation detectors*. https://scionix.nl/

[140] M.J. Schrapp et al. *Data Fusion in neutron and X-ray computed tomography*. J. Appl. Phys. 116 (2014) 163104.

[141] R. Gordon. *A Tutorial on ART (Algebraic Reconstruction Techniques)*. IEEE Trans. Nucl. Sci. 21 (1974) 78.

[142] D. Verhoeven. *Limited-data computed tomography algorithms for the physical sciences*. Appl. Opt. 32 (1993) 3736.

[143] P.M. Subbarao et al. *Performance of iterative tomographic algorithms applied to non-destructive evaluation with limited data*. NDT&E Int. 30 (1997) 359.

[144] E. Olivera et al. *Comparison among tomographic reconstruction algorithms with limited data*. In proceedings of the 2011 International Nuclear Atlantic Conference (INAC 2011), Belo Horizonte, MG, Brazil, 24-28 October 2011.

[145] H.M. O'D. Parker and M.J. Joyce. *The use of ionising radiation to image nuclear fuel: A review*. Prog. Nucl. Energy 85 (2015) 297.

[146] G. Nebbia et al. *Performance of a tagged neutron inspection system (TNIS) based on portable sealed generators*. Nucl. Instrum. Meth. A 533 (2004) 475.

[147] D.L. Chichester et al. *The API 120: A portable neutron generator for the associated particle technique*. Nucl. Instrum. Meth. B 241 (2005) 753.

[148] M. Mendes et al. *Can laptops be left inside passenger bags if motion imaging is used in X-ray security screening?*. Frontiers in Human Neuroscience. October 2013, Vol.7, Article 654.

[149] M. Mendes et al. *Why laptops should be screened separately when conventional x-ray is used*. Proceedings International Carnahan Conference on Security Technology, pp. 267-273.

[150] F. Croce et al. *Nanocomposite polymer electrolytes for lithium batteries*. Letters to Nature. Vol. 394; 30 July 1998.

[151] P. P. Prosini et al. *The two-phase battery concept: a new strategy for high performance lithium polymer batteries*. Journal of Power Sources, Vol. 97, pp. 786-789.

[152] W. H. Meyer. *Polymer Electrolytes for Lithium-Ion Batteries*. Advanced Materials. 1998, 10, No. 6.

[153] E. Lehmann et al. *Neutron imaging methods for the investigation of energy related materials*. EPJ Web of Conferences 104, 01007 (2015).

[154] B. D. Sowerby et al. *Recent Developments in Fast Neutron Radiography for the Interrogation of Air Cargo Containers*. IAEA Conference, Vienna 4-8 May 2009.

[155] M. Licata and M. Joyce. *Concealed nuclear material identification via combined fast-neutron / $\gamma$-ray computed tomography (FNGCT): a Monte Carlo study*. Journal of Instrumentation. Jan 2018, 13 PO2013. 16 p.

[156] *Eljen Technology*. https://eljentechnology.com/

[157] *Hybrid Instruments Ltd. Real-Time Analysis*. http://www.hybridinstruments.com/

[158] M. J. Joyce et al. *Portable, Fast-Neutron Tomography with an Isotopic Source and Organic Scintillation Detector*. IEEE Nuclear Science Symposium, Abstract 2147, San Diego, US (2015).

[159] Schnitzler, H. U., et al. *From spatial orientation to food acquisition in echolocating bats.* TRENDS in Ecology and Evolution Vol.18 No.8 August 2003.

[160] Simmons, J. A., et al. *Echolocation and Pursuit of Prey by Bats*. Science Vol. 203, 5 January 1979.

[161] Schnitzler, H. U., Kalko, E.K.V. *Echolocation by insect-eating bats.* Bio Science Vol. 51, Issue 7, 2001, Pages 557-569.

[162] Griffin, D. R. et al. *The echolocation of flying insects by bats*. Animal Behaviour Volume 8, Issue 3-4, October 1960, Pages 141-154.

[163] Yovel, Y., et al. *Plant Classification from Bat-Like Echolocation Signals*. PLoS Comput Biol 4(3): e1000032. doi:10.1371/journal.pcbi.1000032.

[164] Elfes, A. *Sonar-Based Real-World Mapping and Navigation.* IEEE Journal on Robotics and Automation Volume 3, Issue 3, June 1987, Pages 249-265.

[165] *Radio Detection and Ranging*. Nature. Vol. 152, pages 391-392 (1943).

[166] Zhan, H. et al. *Scale model experimental validation and calibration of the half-space green's function born approximation model applied to cross-well radar sensing*. IEEE Transactions on Geoscience and Remote Sensing. Vol. 45, Issue 8, August 2007, Pages 2423-2427.

[167] Gilman, M. et al. *Modeling radar targets beyond the first Born approximation*. In: Transionospheric Synthetic Aperture Imaging. Applied and Numerical Harmonic Analysis. Birkhauser, Cham.

[168] H. Seiler. *Secondary electron emission in the scanning electron microscope*. Journal of Applied Physics 54, R1 (1983); https://doi.org/10.1063/1.332840.

[169] Miyadera, H., et al. *Imaging Fukushima Daiichi reactors with muons*. AIP Advances 3, 052133 (2013); https://doi.org/10.1063/1.4808210

[170] Tanaka, H., *Development of a two-fold segmented detection system for near horizontally cosmic-ray muons to probe the internal structure of a volcano*. Nuclear Instruments and Methods in Physics Research, Section A. Vol. 507, Issue 3, 21 July 2003, Pages 657-669.

[171] Morishima, K., et al. *Discovery of a big void in Khufu's Pyramid by observation of cosmic-ray muons*. Nature Vol. 552, Issue 7685, 21 December 2017, Pages 386-390.

[172] Wrobel, N., et al. *Innovative X-ray Backscatter Technique for Security Applications: Detection of Dangerous Materials*. 11th European Conference on Non-Destructive Testing (ECNDT 2014), October 6-10, 2014, Prague, Czech Republic.

[173] Towe, B. C., and Jacobs, A. M. *X-ray Backscatter Imaging.* IEEE Transaction on Biomedical Engineering, Vol. BME-28, N.9, September 1981.

[174] Kolkoory, S., et al. *New X-ray Backscatter Imaging Technique for Nondestructive Testing of Aerospace components.* 11th European Conference on Non-Destructive Testing (ECNDT 2014), October 6-10, 2014, Prague, Czech Republic.

[175] Walker, J. L., and Richter J. D. *Nondestructive Evaluation of Foam Insulation for the External Tank Return to Flight.* Collection of Technical Papers, AIAA/ASME/SAE/ASEE 42nd Joint Propulsion Conference Volume 4, 2006, Pages 2991-2997.

[176] Balamesh, A., et al. *Feasibility of a New, Moving Collimator for Industrial Backscatter Imaging.* Research in Non-destructive Evaluation Volume 29, Issue 3, 3 July 2018, Pages 143-155.

[177] *Neutron/Gamma Probes for simultaneous measurements of soil bulk density and water content*, from *Neutron and gamma probes, their use in agronomy.* IAEA-TCS-16 ISSN 1018-5518. August 2002.

[178] Oresegun, M. O. *Radiation safety of soil neutron moisture probes. Comparison of Soil Water Measurement Using the Neutron Scattering, Time Domain Reflectometry and Capacitance Methods.* IAEA-TECDOC-1137, IAEA, Vienna (2000), 139-146.

[179] Rogante, M. *Neutron examination techniques applied to pipelines.* Oil and Gas Journal. Volume 103, Issue 36, 26 September 2005, Pages 59-64.

[180] Majid, S.A. *Determination of wax deposition and corrosion in pipelines by neutron back diffusion collimation and neutron capture gamma rays.* Applied Radiation and Isotopes. Vol. 74, April 2013, Pages 102-108.

[181] Vanier, P. E. et al. *Thermal neutron backscatter imaging.* IEEE Nuclear Science Symposium Conference Record Volume 1, 2004, Pages 201-205.

[182] Hasan, N.M. *The use of a neutron backscatter technique for in-situ water measurement in paper-recycling industry.* Applied Radiation and Isotopes. Vol. 67, Issue 7-8, July 2009, Pages 1239-1243.

[183] Bom, V. R. et al. *DUNBLAD, the Delft University Neutron Backscatter LAndmine Detector, a status report.* AIP Conference Proceedings 680, 935 (2003); https://doi.org/10.1063/1.1619862.

[184] Nesic, S. *Key issues related to modelling of internal corrosion of oil and gas pipelines. A review.* Corrosion Science 49 (2007) 4308-4338.

[185] Xie, M. and Tian, Z. *A review on pipeline integrity management utilizing in-line inspection data.* Engineering Failure Analysis 92 (2018) 222-239.

[186] Dai, L. et al. *Analysis and Comparison of Long-Distance Pipeline Failures. Journal of Petroleum Engineering.* 2017, Article ID 3174636, 7 pages. (2017). https://doi.org/10.1155/2017/3174636.

[187] Sheikh, A. K. et al. *Statistical Modeling of Pitting Corrosion and Pipeline Reliability.* Corrosion Science 46, Issue 3, 190-197, (1990).

[188] Ossai, C. I. et al. *Predictive Modelling of Internal Pitting Corrosion of Aged Non-Piggable Pipelines.* Journal of The Electrochemical Society, 162 (6) C251-C259 (2015).

[189] Caleyo, F, et al. *Probability distribution of pitting corrosion depth and rate in underground pipelines: A Monte Carlo study.* Corrosion Science 51 1925-1934, (2009).

[190] Alamilla J.L., and Sosa, E. *Stochastic modelling of corrosion damage propagation in active sites from field inspection data.* Corrosion Science 50 1811-1819, (2008).

[191] Dobmann, G. et al. *State of the art of in-line non-destructive weld inspection of pipelines by ultrasonics.* Russian Journal of Nondestructive Testing. Vol 43 (11) 2007 pages 755-761.

[192] Lei, H. et al. *Ultrasonic Pig for Submarine Oil Pipeline Corrosion Inspection.* Russian Journal of Nondestructive Testing, 2009, Vol. 45, No. 4, pp. 285-291.

[193] Kondo, M. et al. *Ultrasonic corrosion inspection of crude pipeline.* Corrosion, paper No 525, 1999.

[194] Suga, N. and Schlegel, P. *Neural Attenuation of Responses to Emitted Sounds in Echolocating Bats.* Science 07 Jul 1972: Vol. 177, Issue 4043, pp. 82-84. DOI: 10.1126/science.177.4043.82177.

[195] Stavroulakis, P. I. et al. *Suppression of backscattered diffraction from subwavelength moth-eye arrays.* Optic Express, January 2013 / Vol. 21, No. 1.

[196] Ntelezos, A. et al. *The anti-bat strategy of ultrasound absorption: the wings of nocturnal moths (Bombycoidea: Saturniidae) absorb more ultrasound than the wings of diurnal moths (Chalcosiinae: Zygaenoidea: Zygaenidae).* The Company of Biologists Ltd, Biology Open (2017) 6, 109-117 doi:10.1242/bio.021782

[197] EJ-301 material data sheet https://eljentechnology.com/products/liquid-scintillators/ej-301-ej-309. Eljen Technology, Sweetwater, Texas, USA (2014).

[198] Gordon, R. and Coumans, J.. *Combining multiple imaging techniques for in vivo pathology: a quantitative method for coupling new imaging modalities.* Med.Phys Vol. 11 N.1. Jan/Feb 1984.

[199] Taylor, G. C. and Thomas, D. J. *Neutron scatter characteristics of the low-scatter facility of the Chadwick Building NPL.* NPL Report. 1998, CIRM 17.

[200] McConn, R. J. et al. *Radiation Portal Monitor Project, Compendium of Material Composition Data for Radiation Transport Modelling.* PIET-43741-TM-963. PNNL-15870 Rev. 1.

[201] F. Azaiez et al. *The ALTO Facility in Orsay.* Nuclear Physics News, 23:2, 5-10, (2013). DOI: 10.1080/10619127.2013.797270

[202] The IPN ALTO Facility. http://ipnwww.in2p3.fr/.

[203] Greenberg, R.R. et al. *Neutron activation analysis: A primary method of measurement.* Spectrochimica Acta - Part B Atomic Spectroscopy 66(3-4), pp. 193-241.

[204] Marc Litz et al. *Neutron-Activated Gamma-Emission: Technology Review* Army Research Laboratory. Adelphi, MD 20783-1197. ARL-TR-5871 January 2012.

[205] Richard M. Lindstrom. *Prompt-Gamma Activation Analysis.* J. Res. Natl. Inst. Stand. Technol. 98, 127 (1993)

[206] Kazmierczak et al. *A Simple Approach to Data Analysis for the Detection of Hazardous Materials by Means of Neutron Activation Analysis.* Proceedings of the II Symposium on Applied Nuclear Physics and Innovative Technologies, Krakow, September 24-27, 2014

[207] Perlman, I. et al. *Pottery Analysis by neutron activation.* Archaeometry 11(1), pp. 21-38.

[208] Dams, R. et al. *Nondestructive Neutron Activation Analysis of Air Pollution Particulates.* Analytical Chemistry. 42(8), pp. 861-867.

[209] Failey, M.P., Anderson, D.L., Zoller, W.H., Gordon, G.-E., Lindstrom, R.M. *Neutron-Capture Prompt Gamma-Ray Activation Analysis for Multielement Determination in Complex Samples.* Analytical Chemistry 51(13), pp. 2209-2221.

[210] Simonits, A. et al. *Single-comparator methods in reactor neutron activation analysis.* Journal of Radioanalytical Chemistry 24(1), pp. 31-46.

[211] Marchkesbery, W.R. et al. *Instrumental neutron activation analysis of brain aluminum in Alzheimer disease and ageing.* Annals of Neurology. 10(6), pp. 511-516.

[212] Jacobs, J.W.et al. *A well-tested procedure for instrumental neutron activation analysis of silicate rocks and minerals.* Journal of Radioanalytical Chemistry 40(1-2), pp. 93-114.

[213] A C Sharma et al. *Neutron stimulated emission computed tomography: a Monte Carlo simulation approach.* Phys. Med. Biol. 52 (2007) 6117-6131. doi:10.1088/0031-9155/52/20/003

[214] M. Gierlik et al. *SWAN Detection of explosives by means of fast neutron activation analysis.* Nuclear Instruments and Methods in Physics Research A834 (2016) 16-23.

[215] N. Pietralla et al. *Absolute level widths in Al below 4 MeV* Phys. Rev. C. n51 Vol. 2 (1995).

[216] S. Mellemxa and R. Vf. Finlay *Neutron inelastic scattering from 54,56-Fe* Phys. Rev. C. n33 Vol. 2 (1986).

[217] *Neutron Imaging: A Non-Destructive Tool for Materials Testing.* IAEA-TECDOC-1604.

[218] J. Medalia. *Detection of Nuclear Weapons and Materials: Science, Technologies, Observations* . CRS Report for US Congress. Congressional Research Service. 7-5700. R40154.

[219] J. Medalia *L-3 CAARS: A Low-Risk Dual-Energy Radiography System* CRS Report for US Congress. Congressional Research Service. 7-5700. R40154. Pages 31-41.

[220] B. Henderson et al. *Experimental demonstration of multiple monoenergetic gamma radiography for effective atomic number identification in cargo inspection.* Journal of Applied Physics. 123, 164901 (2018).

[221] J. Medalia *SAIC CAARS: A Higher-Risk, Higher-Benefit Dual-Energy Radiography System* CRS Report for US Congress. Congressional Research Service. 7-5700. R40154. Pages 42-47.

[222] P. Marleau et al. *Advances in Imaging Fission Neutrons wih a Neutron Scatter Camera.* 2007 IEEE Nuclear Science Symposium Conference Record. 1-4244-0923-3/07

[223] J. Brennan et al. *Applying the Neutron Scatter Camera to Treaty Verification and Warhead Monitoring.* 2010 IEEE Nuclear Science Symposium Conference Record. 978-1-4244-9105-6/10.

[224] N. Mascarenhas *Results with the Neutron Scatter Camera.* IEEE Transactions on Nuclear Science. V56 N3. June 2009.

[225] N. Mascarenhas et al. *Field portable fast neutron imager for SNM detection.* 2009 IEEE Nuclear Science Symposium Conference Record. 9781-4244-3962-1/09.

[226] T.A. Wellington et al. *Recent Fast Neutron Imaging Measurements with the Fieldable Nuclear Materials Identification System.* Physics Procedia 66 (2015) 432-438.

[227] I. Dioszegi et al. *Gamma/neutron analysis for SNM signatures at high-data rates (greater than $10^7$ cps) for single-pulse active interrogation.* Proceedings of SPIE. The International Society for Optical Engineering Volume 8018, 2011, Article number 80180D

[228] P. Marleau et al. *Time encoded fast neutron/gamma imager for large standoff SNM detection.* IEEE Nuclear Science Symposium Conference Record. 2011, Article number 6154118, Pages 591-595.

[229] P. Pietsch and V. Wood. *X-Ray Tomography for Lithium Ion Battery Research: a practical guide.*

[230] O. O. Taiwo et al. *Microstructural degradation of silicon electrodes during lithiation observed via operando X-ray tomographic imaging.* J. Power Sources 342, 904-912 (2017).

[231] S. Risse et al. *Multidimensional operando analysis of macroscopic structure evolution in lithium sulfur cells by X-ray radiography.* Phys. Chem. Chem. Phys. 18, 10630-10636 (2016).

[232] Siegel, J. B. et al. *Neutron imaging of lithium concentration in LFP pouch cell battery.* J. Electrochem. Soc. 158. A523-A529 (2011).

[233] Zhou, H. et al. *Probing multiscale transport and inhomogeneity in a lithiumion pouch cell using in situ neutron methods.* ACS Energy Lett. 1, 981-986 (2016).

[234] M. Lanz et al. *In situ neutron radiography of lithium-ion batteries during charge/discharge cycling.* Sources 101, 177-181 (2001).

[235] J. M. La Manna et al. *Improving material identification by combining x-ray and neutron tomography.* Dev. XRay Tomogr. XI 1039104, 1-7 (2017).

[236] E. Lehmann et al. *Recent applications of neutron imaging methods.* 8th International Topical Meeting on Neutron Radiography, Beijing, China, 4-8 September 2016.

[237] F. Pino et al. *The light output and detection efficiency of the liquid scintillator EJ-309.* Applied Radiation and Isotopes. 89 (2014) 79-84.

[238] J. Medalia *AS&E CAARS: Using Backscattered X-Rays to Detect Dense Material* CRS Report for US Congress. Congressional Research Service. 7-5700. R40154. Pages 49-53.

[239] C. Broglia and D. Ellis. *Effect of alteration, formation absorption, and stand-off on the response of the thermal neutron porosity log in Gabbros and Basalts: Example from deep sea drilling project-ocean drilling program sites.* Journal of Geophysical research, vol95 NO B6 pp 9171-9188.

[240] M. A. Blackston and P. A. Hausladen. *Fast-Neutron Elastic-Scatter Imaging for Material Characterization.* 978-1-4673-9862-6/15 IEEE.

# List of Figures

# List of Tables